Thermal Stress Effects in Intermetallic Matrix Composites

P.K. Wright and M.D. Sensmeier
GE Aircraft Engines
Cincinnati, Oiho

D.S. Kupperman
Argonne National Laboratory
Argonne, Illinois

and

H.N.G. Wadley
University of Virginia
Charlottesville, Virginia

NASA

Thermal Stress Effects
in
Intermetallic Matrix Composites

NAS3-25790

P.K. Wright and M.D. Sensmeier
GE Aircraft Engines
Cincinnati, Ohio 45215-6301

D.S. Kupperman
Argonne National Laboratory
Argonne, Illinois 60439

and

H.N.G. Wadley
University of Virginia
Charlottesville, Virginia 22903

Abstract

Intermetallic matrix composites develop residual stresses from the large thermal expansion mismatch ($\Delta\alpha$) between the fibers and matrix. This work was undertaken to: establish improved techniques to measure these thermal stresses in IMC's; determine residual stresses in a variety of IMC systems by experiments and modeling; and, determine the effect of residual stresses on selected mechanical properties of an IMC.

XRay Diffraction (XRD), Neutron Diffraction (ND), Synchrotron XRD (SXRD), and Ultrasonics (US) techniques for measuring thermal stresses in IMC were examined and ND was selected as the most promising technique. ND was demonstrated on a variety of IMC systems encompassing Ti- and Ni-base matrices, SiC, W, and Al_2O_3 fibers, and different fiber fractions (V_f). Experimental results on these systems agreed with predictions of a concentric cylinder model.

In SiC/Ti-base systems, little yielding was found and stresses were controlled primarily by $\Delta\alpha$ and V_f. In Ni-base matrix systems, yield strength of the matrix and V_f controlled stress levels.

The longitudinal residual stresses in SCS-6/Ti-24Al-11Nb composite were modified by thermomechanical processing. Increasing residual stress decreased ultimate tensile strength in agreement with model predictions. Fiber pushout strength showed an unexpected inverse correlation with residual stress. In-plane shear yield strength showed no dependence on residual stress. Higher levels of residual tension led to higher fatigue crack growth rates, as suggested by matrix mean stress effects.

1. Summary

Intermetallic matrix composites develop residual stresses due to the large thermal expansion mismatch between the reinforcing fibers and the matrix. This work was undertaken to: a) Establish improved techniques to measure these thermal stresses in IMC's; b) Determine residual stresses in a variety of IMC systems; c) Evaluate the predictions of models for thermal stresses, and; d) Determine the effect of residual stresses on selected mechanical properties of an IMC system.

XRay Diffraction (XRD), Neutron Diffraction (ND), Synchrotron XRD (SXRD), and Ultrasonics (US) techniques for measuring thermal stresses in IMC were examined and ND was selected as the most promising technique. The neutron diffraction method was demonstrated on a variety of IMC systems encompassing Ti- and Ni-base matrices, SiC, W, and Al_2O_3 fibers, and different fiber fraction (V_f) and thermomechanical processing. ND (and XRD) results on these systems agreed with predictions of a temperature dependent elastic-plastic concentric cylinder model.

In the SiC/Ti-base systems, little or no yielding was found, and the stresses were controlled primarily by the thermal expansion mismatch and V_f. In the Ni-base matrix systems, yielding of the matrix occurred well above room temperature, and the yield strength of the matrix and V_f controlled stress levels.

The longitudinal residual stresses developed in a SCS-6/Ti-24Al-11Nb composite were modified by thermomechanical processing. These residual stress levels influenced the room temperature longitudinal ultimate strength inagreement with a model based on a the rule of mixtures. Fiber pushout strength showed an unexpected inverse correlation with longitudinal residual stress. In-plane shear yield strength showed no dependence on residual stress. Higher levels of residual tension led to higher fatigue crack growth rates, as suggested by matrix mean stress effects.

1

2. Introduction

2.1 Problem Statement

The stringent demands for greatly increased thrust-to-weight ratio in the next generation of aircraft engines have mandated the development of higher strength, higher operating temperature, higher modulus, but lightweight materials. It is recognized that such materials will be composites with structural capabilities tailored to the application. In addition to identifying the composite material system and the required processing techniques, behavior models for component design and life prediction will need to be developed and verified.

Intermetallic matrix composites (IMC) is one class of materials that shows promise for meeting advanced propulsion system needs. These materials are aimed at applications from 650C to above 1300C, and several ongoing programs are pursing the development and application of these composites in the aerospace industry. One of the key issues limiting progress in applying these materials is the mismatch in thermal expansion coefficient between the fiber and the matrix which leads to the generation of thermal residual stresses in the composite upon cooling from the consolidation temperature or from elevated temperature use. These residual stresses can cause cracking of the composite, or can alter its performance capability through their influence on mechanical properties.

While considerable research is being conducted to minimize thermal residual stresses in composites by developing fibers with higher thermal expansion (closer to most matrices), and by developing interfacial coating systems which can accomodate the expansion mismatch between fiber and matrix, it is inevitable that some residual streeses will be generated during processing or use. In order to successfully apply intermetallic matrix composites these residual stresses need to be accurately determined and their effect on mechancial properties understood. This understanding will lead to a physically based approach to composite strength and life prediction which is required for confident use of the materials in advanced propulsion components.

2.2 Background

2.2.1 Residual Stress Measurement in IMC

Most residual stress measurement in IMC has been performed using conventional Xray diffraction methods (sin^2-psi) on SCS-6 fiber/titanium aluminide matrix composites. Cox et. al. (1990) measured longitudinal (fiber direction) matrix stresses in SCS-6/Ti-25Al-10Nb-3Mo-1V as a function of depth from the surface, and compared these to fiber stresses obtained from measuring the change in length of fibers caused by etching away the matrix. Jayaraman and Rangaswamy (1991) measured matrix stresses as a function of both depth and orientation in SCS-6/Ti-24Al-11Nb. Stress profiles were found to change dramatically as the fiber-matrix interface was approached, and interpretation of the as-fabricated residual stresses was uncertain. Thus there remain significant questions of the effects of material properties, fiber fraction, and processing to be understood.

2.2.2 Residual Stress and Mechanical Property Modeling

Many analytical models for residual stress prediction in IMC have been constructed, particularly in the SCS-6/titanium aluminide system. Concentric cyclinder models have been used because of their simplicity, and refinements which include temperature-dependent properties and plastic deformation in the matrix are available. Finite element models are popular because of the accuracy and flexibility available. Work by Nimmer (1990), for example, predicted the development of high levels of tensile longitudinal and circumferential stress in the matrix, and lower levels of radial matrix and fiber compression. In addition, the effective matrix stresses were higher near the fiber-matrix interface, leading to a tendency for plastic flow (or fracture) to initiate there. Levels of interfacial residual stress large enough to cause matrix yielding were calculated to occur in SCS-6/Ti-24Al-11Nb below about 1200F. Other than the work described in Section 2.2.1, little has been done to directly verify these predictions.

2.3 Program Objectives

The ojectives of this program were to:

a) Establish techniques to measure thermally induced residual stresses in IMC's, with emphasis on obtaining measurements on a microscale, that is, on the scale of the size of the fiber diameter.

b) Use these techniques to determine residual stresses in a variety of IMC systems.

c) Evaluate the predictions of current analytical models for thermal stress in light of these measurements in order to suggest improvements (if necessary).

d) Determine the effect of these residual stresses on the mechanical properties of a representative IMC system.

3

3. Approach

3.1 Overall Approach

This program was performed in three consecutive tasks. In Task 1, one current and three developmental methods for measuring the thermally induced residual stresses were examined using an SCS-6/Ti-24Al-11Nb composite system. Measurements were compared to predictions of a concentric cylinder model for thermal stress, and one technique (neutron diffraction) was selected for further refinement and use in Task 2. In Task 2 several different IMC systems were measured using the selected (neutron diffraction) technique and were compared to predictions of analytical models. The selected IMC systems included SCS-6/Ti-24Al-11Nb processed in several different ways and four other nickel aluminide matrix composite systems. In Task 3 samples of SCS-6/Ti-24Al-11Nb were subjected to different thermomechanical processing to produce different levels of residual stress and different mechanical tests (tension, shear, fatigue crack growth and fiber pushout) were conducted on them to determine the effect of the residual stresses on mechanical properties.

3.2 Task 1 - Selection of Experimental Methods

3.2.1 Selection of Measurement Methods

Several approaches for residual stress measurement exist for homogeneous, crystalline materials. These approaches all have limitations when applied to IMC's. These methods of thermal stress measurement were examined and four were chosen for study. These methods were: conventional Xray diffraction by $\sin^2$-psi method, neutron diffraction (ND), an advanced XRD technique based on synchrotron radiation (SXRD), and ultrasonics (US).

3.2.1.1 Xray Diffraction

Xray Diffraction (XRD) using the $\sin^2$-psi method (Cox, et al., 1990, and Jayaraman and Rangaswamy, 1991) is the most popular of the conventional methods but in its usual form it is limited to relatively small penetration depths and beam sizes much greater than the fiber diameter. Etch techniques can be used to obtain profiles of stress vs. depth, but the complex stress existing around fibers in an IMC make the extraction of information uncertain. However, because of its wide use, conventional XRD was performed to establish a baseline of comparison for the other experimental techniques. These studies were performed at Lambda Research, Inc., Cincinnati, Ohio.

Xray diffraction measurements were taken in the matrix material at the original sample surface and at various depths by etching until the first row of fibers was exposed. Measurements were taken in both the longitudinal (parallel to fiber) and transverse (perpendicular to fiber) directions on both faces of the sample. Raw measurements were corrected for both stress gradients (Koistenin and Marburger, 1959) and sample bending (Moore and Evans, 1958) effects.

3.2.1.2 Neutron diffraction

Neutron radiation has the capability of deep penetration through a material. This gives the potential for interrogating the material in situ without destructive

4

etching.   Neutron diffraction experiments were conducted at the Intense Pulsed Neutron Source at Argonne National Laboratory following the technique outlined by Majumdar et. al. (1991).   The specimen was placed in the diffractometer with the fiber direction oriented at 45° to the beam, and detectors were placed at $\pm$ 90° to the beam as shown in Figure 1.   Since the beam consists of a range of wavelengths, many diffraction peaks were obtained, representing diffraction from different crystal planes.   The spacings from these measurements were compared to those obtained on a stress-free sample, and the residual strain, ε_{hkl}, was calculated as

$$\varepsilon_{hkl} = (d_{hkl}-d_o)/d_o$$

where d_{hkl} and d_o are the measured interplanar spacings in the stressed and unstressed material, respectively, and hkl are the Miller indices of the diffracting planes.   The positions of the two detectors allows measurements to be obtained simultaneously on strains parallel and perpendicular to the fiber directions. Because of the high penetrating power of the beam sampling of the interior of the material is possible, including both the fiber and matrix (fiber and matrix peaks can be separated out by indexing the diffraction patterns).   Since the neutron beam size is appreciably larger than the diameter of the fiber, the average lattice strain in a particular direction of each constituent is obtained.   However, this information can be interpreted to give good estimates of some of the local microstrains using knowledge of the nature of the stress distribution within MMC. Specifically, the longitudinal stresses within both the fiber and matrix are expected from micromechanics analyses to be highly uniform (see Section 3.3.3), so that the ND measurement obtains the fiber stress directly.   In addition, these analyses show that the two transverse stress components within the fiber are equal and also do not vary significantly with position in the fiber.   Thus the transverse fiber stress measured should also accurately represent the radial fiber stress at the fiber-matrix interface, and by equilibrium, should be equal to the matrix radial stress at the fiber-matrix interface.   The interfacial normal stresses are significant quantities in evaluating the load transfer characteristics in MMC with weak bonding, such as SCS-6/Ti-24Al-11Nb.

3.2.1.3 Synchrotron Xray Diffraction

The use of synchrotron radiation for conducting XRD opens up the possibility for both higher spatial resolution and deeper penetration than for conventional XRD. Because the Xray beam is so much more powerful it can be collimated down to a size on the order of that of many IMC fibers, and it can penetrate down to at least the first layer of fibers beneath the surface.   Potential problems requiring attention in applying this teschnique are the specialized nature of the equipment required and the small number of grains within the diffracting volume of the composite. SXRD techniques were explored by the University of Virginia using the Brookhaven Synchrotron through assistance of NIST.   Further details on the advanced XRD method are given in Appendix I.

3.2.1.4 Ultrasonics

Stresses can be measured by ultrasonic methods through the dependence of higher order elastic constants on stress sign and level.   Changes in stress will cause small changes in sound velocity which in principle can be interpreted as residual stress.   Ultrasonics also has the potential for nondestructive penetration
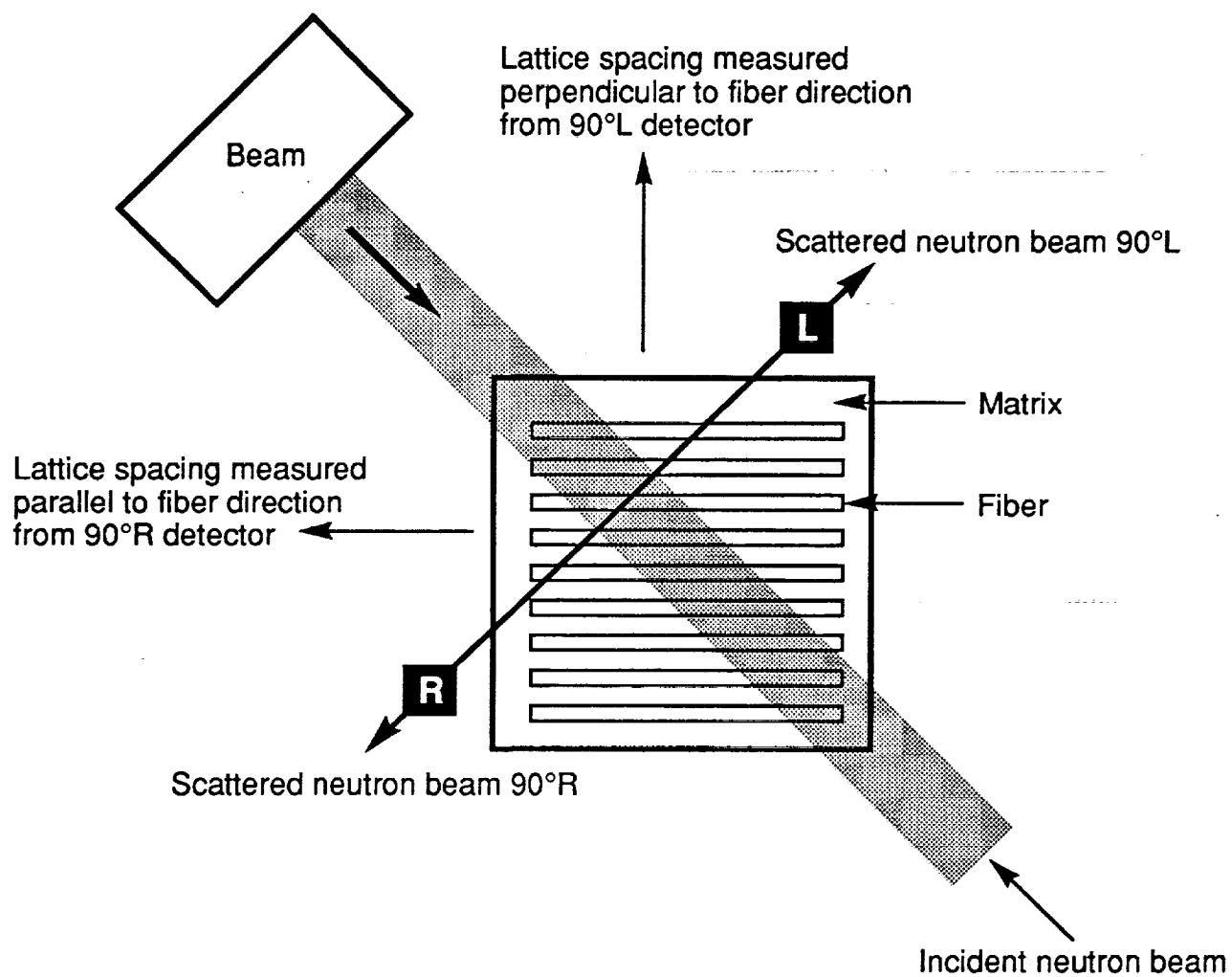
Beam

Lattice spacing measured
perpendicular to fiber direction
from 90°L detector

Scattered neutron beam 90°L

L

Matrix

Fiber

Lattice spacing measured
parallel to fiber direction
from 90°R detector

R

Scattered neutron beam 90°R

Incident neutron beam

Figure 1. Neutron Diffraction.

6

to interrogate around or in the fibers, and techniques exist to create very localized interrogated volumes. An ultrasonic method would be convenient since it would use relatively inexpensive, portable equipment. However, in order to detect residual stresses, very high precision in velocity measurement is required and local fluctuations in modulus must be accounted for. Ultrasonic studies were carried out at University of Virginia. Details of this method are described in Appendix II.

3.2.2 Selection of Material

Samples of a single unidirectional SCS-6/Ti-24Al-11Nb (a/o) composite panel made by Induction Plasma Deposition (IPD) (Gigenrenzer and Wright, 1991) were supplied to each subcontractor for experimental study of the capability of each method and to determine the residual stresses in the panel for comparison to the conventional XRD method and analytical models. In addition, samples of SCS-6 fiber and unreinforced IPD matrix were supplied to help establish a stress-free reference. This panel was made at Textron Specialty Materials by HIPing four fiber-containing IPD monotapes with three fiberless foils at 1010C, 103 MPa for 3 hours. Fiber volume fraction was 25%. A micrograph of this material is shown in Figure 2, and further characterization is given in Gigerenzer and Wright (1991).

3.2.3 Model predictions of stresses and strains

Analytical modeling of the thermal residual stresses expected on the microscale in these composites was conducted using the Concentric Cylinder Model as developed by Hecker (1968). The geometric symmetry element is shown in Figure 3. This model has capability of performing temperature dependent elastic-plastic analysis of the stresses and strains developed during cooling of the composite from processing. The center cylinder was sized to represent the fiber volume fraction and the fiber (elastic) properties shown in Table 1 were assigned to it. These properties were taken from GE studies under AF funding (GE Staff, 1991). Matrix properties were assigned to the outer rings. The purpose of the multiple rings is to follow the development of plastic flow from the fiber-matrix interface outward during the thermal loading history. The matrix properties used are shown in Table 1 and Figure 4. These properties were obtained from GE studies under AF funding (GE Staff, 1991). Both local and average fiber and matrix stresses and strains were computed for the IPD SCS-6/Ti-24Al-11Nb system studied to permit comparison to the experimental data. Finite element analysis of this same composite has also been conducted by Saigal et al. (1992).

3.2.4 Selection of Method for Task 2

The various methods studied in Task 1 were evaluated for their suitability for further use in Task 2. Criteria for selection were:
   a) Maturity of method: how much development is required for confident use?
   b) Accuracy of method: how well do results agree with analytical model predictions or measurements based on the conventional XRD method?
   c) Level of detail about the state of residual stress in the composite: can both fibers and matrix be measured? Can local residual stresses, especially fiber matrix interface values be determined?
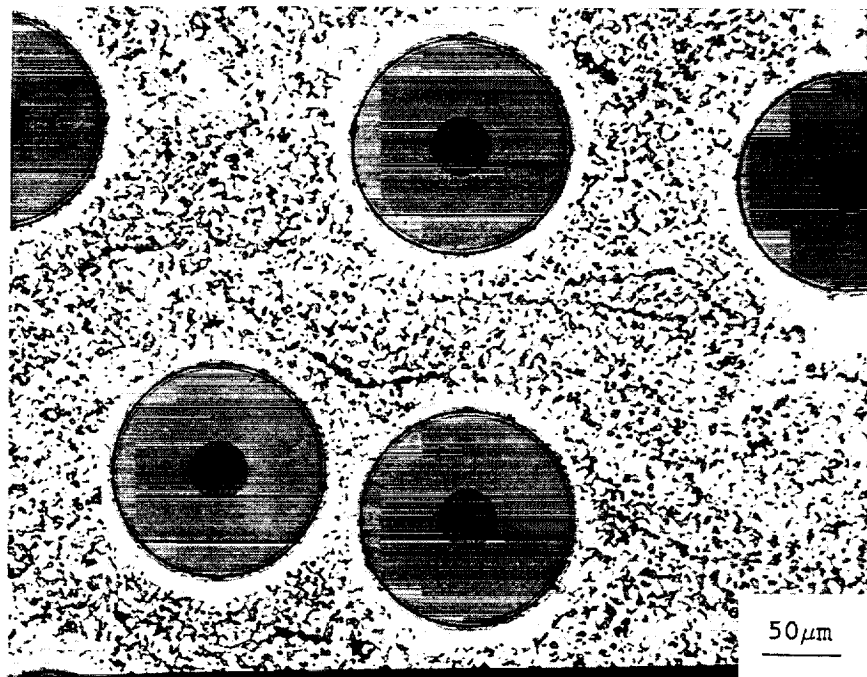The method best fitting these criteria was then selected for use in Task 2.
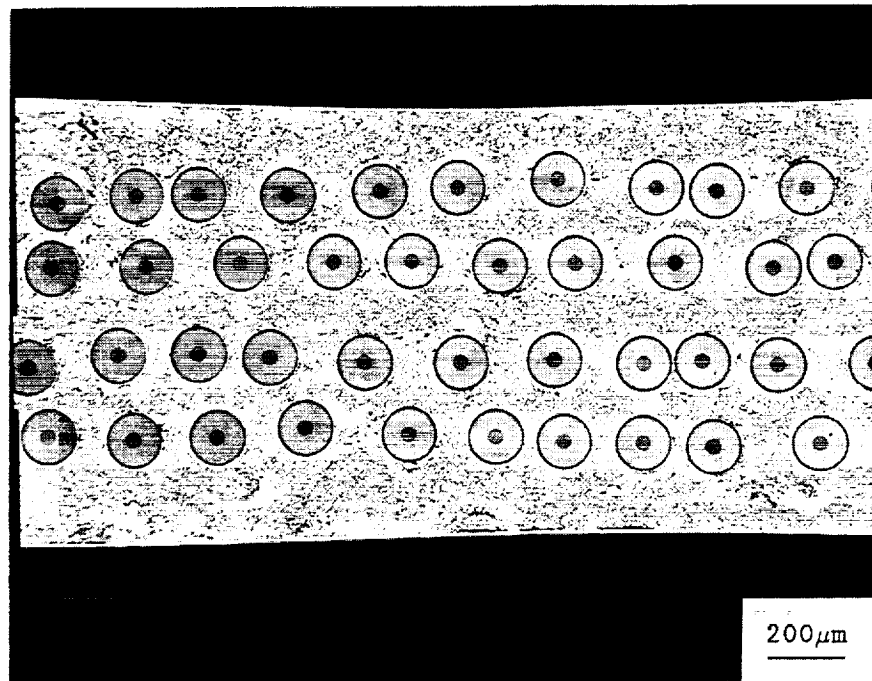
7

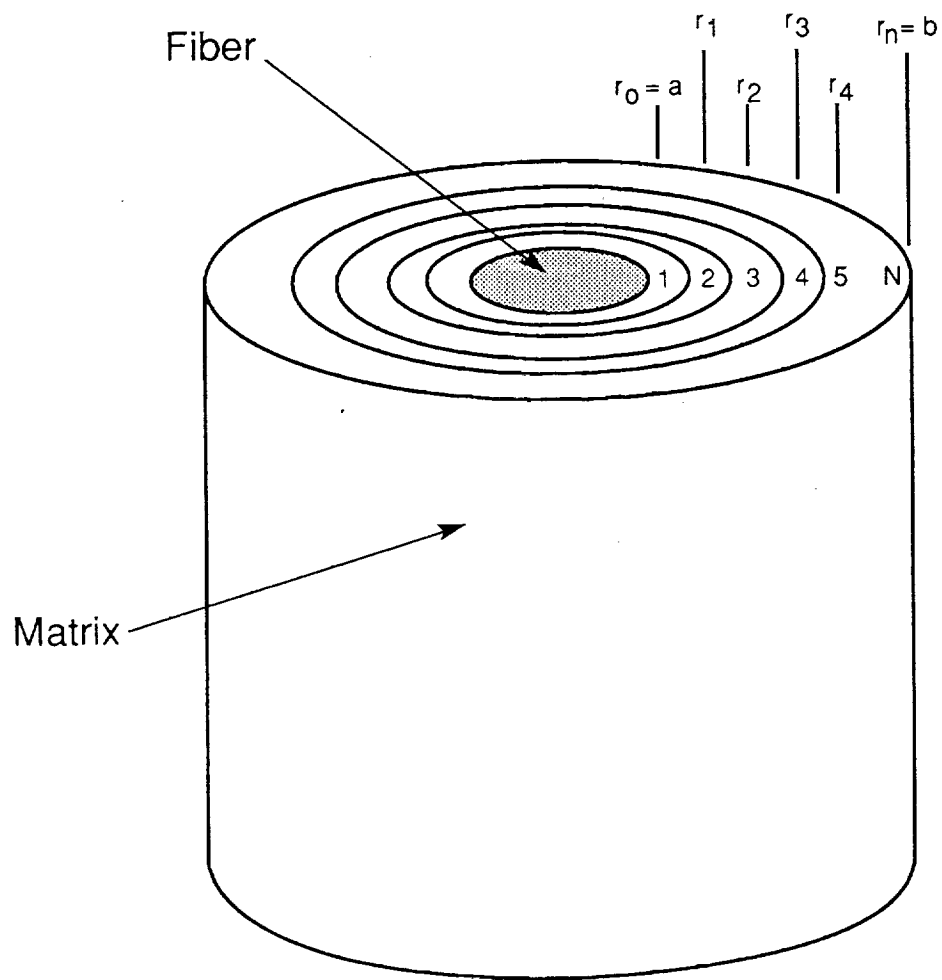Figure 2   Microstructure of IPD SCS-6/Ti-24Al-11Nb Composite Used in Task 1

Figure 3. Geometry of Concentric Cylinder Model Showing Central Fiber and Multiple Matrix Rings.
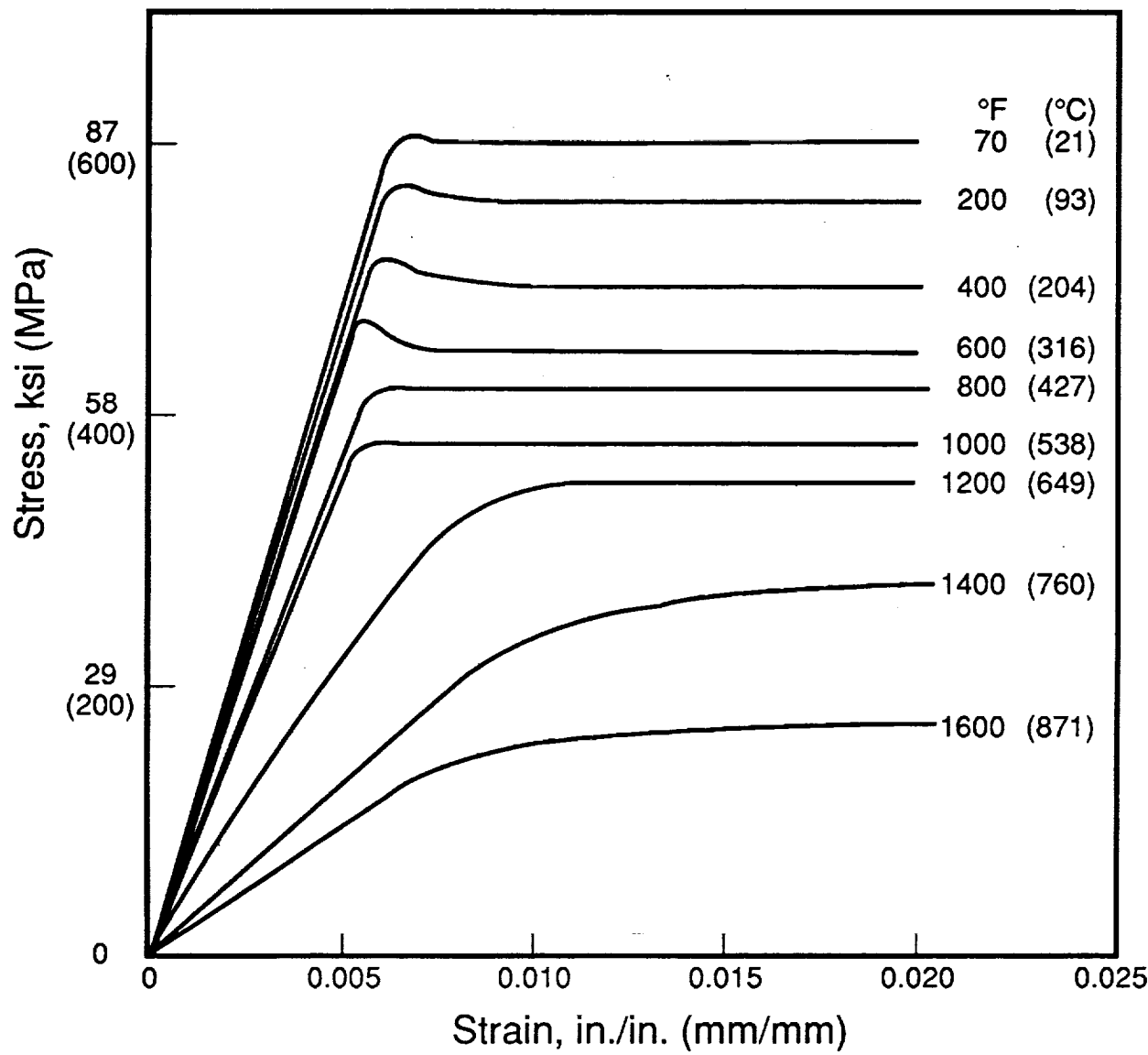
Figure 4   Stress-Strain Properties Used in Analytical Modeling of IPD
            Ti-24Al-11Nb

Table 1

Thermal and Elastic Properties of Fibers and Matrices used for Thermal Stress Analysis

Material	T(°C)	Elastic Modulus (GPa)	Poisson's Ratio	Thermal Expansion* (mm/mm°/C)
SCS-6	20	414	0.30	4.35×10^{-6}
	250	414	0.30	4.35×10^{-6}
	500	414	0.30	4.35×10^{-6}
	750	415	0.30	5.02×10^{-6}
	1000	414	0.30	6.71×10^{-6}
W (ASM, 1979)	20	407	0.28	3.86×10^{-6}
	500	398	0.29	4.20×10^{-6}
	1000	366	0.29	4.60×10^{-6}
	1300	351	0.30	4.90×10^{-6}
Al_2O_3	20	421	0.20	6.02×10^{-6}
	500	413	0.20	9.12×10^{-6}
	1000	405	0.20	10.59×10^{-6}
	1300	346	0.20	10.67×10^{-6}
Ti-24Al-11Nb	20	94,5	0.30	10.11×10^{-6}
	250	90.3	0.30	10.44×10^{-6}
	500	74.5	0.30	12.05×10^{-6}
	750	32.0	0.30	13.77×10^{-6}
	1000	6.5	0.30	16.78×10^{-6}
NiAl and NiFeAl	20	169	0.30	12.91×10^{-6}
	500	155	0.30	15.23×10^{-6}
	1000	128	0.30	17.12×10^{-6}
	1300	81	0.30	17.99×10^{-6}

* tangent value

3.3 Task 2 - Measurement of Stresses in IMC

In this task several different IMC systems were subjected to residual thermal stress measurement to examine the influence of material and processing variables on thermal stress development. These same material and process combinations were modeled using the concentric cylinder model described in Task 1 to examine the capbility of the measurements (and model) to describe residual stress levels.

3.3.1 Selection of Materials

Four different IMC's were selected for study. The first system was an SCS-6/Ti-24Al-11Nb alpha-two titanium aluminide composite with approximately 32% (by volume) fibers, Figure 5. The fibers were oriented unidirectionally in 8 plies. This material was similar to that used in Task 1, except that it was fabricated using a foil-fiber process at Textron Specialty Materials Division. This material was examined in three different process conditions: a) as-fabricated (HIPed at 1010C, 103 MPa, for 1 hour); b) after thermal cycling 100 times between RT and 649C in
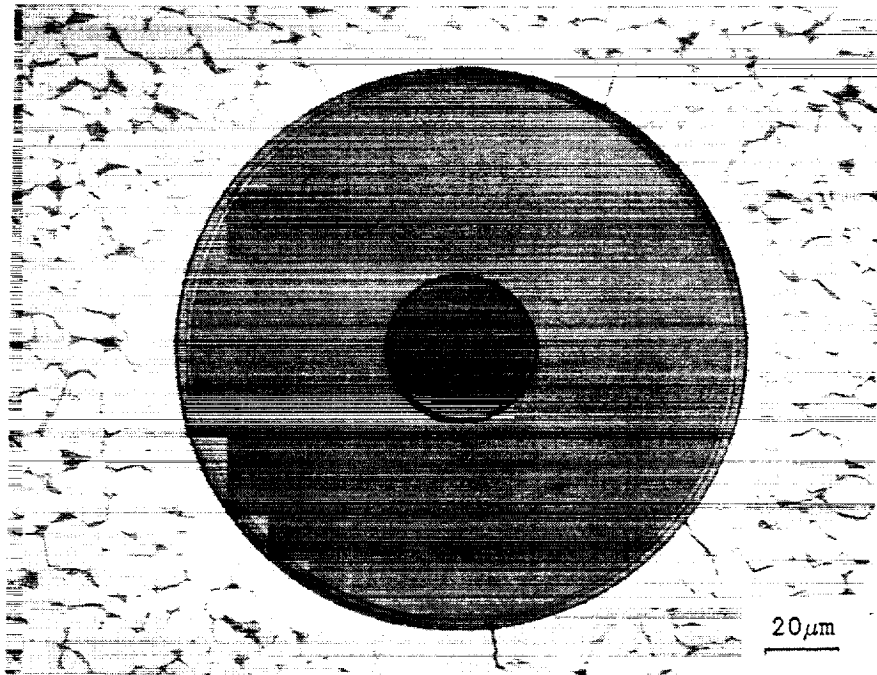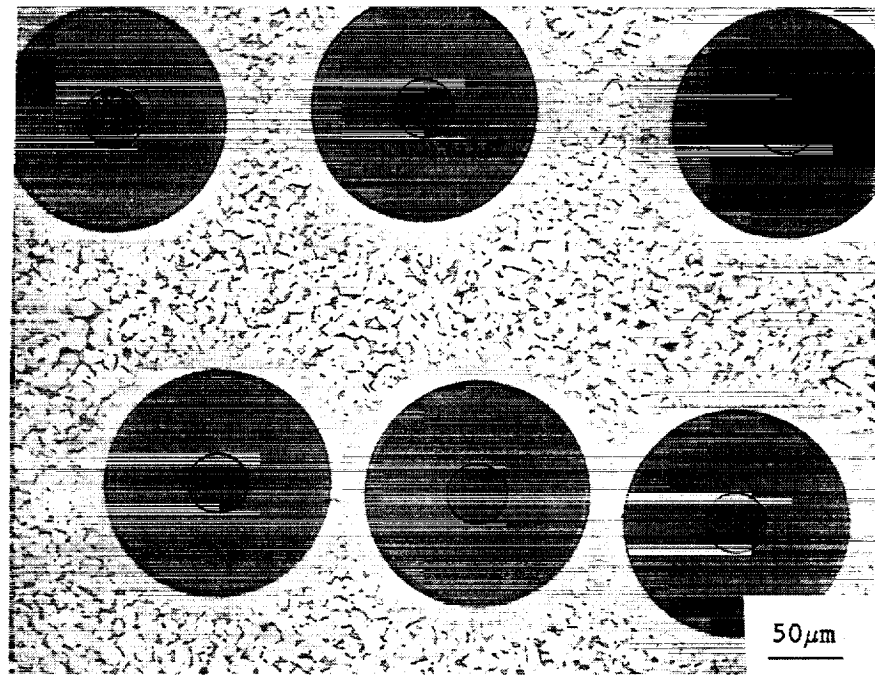
11

Figure 5   Microstructure of Foil-Fiber SCS-6/Ti-24Al-11Nb Used in
Task 2

air; c) after cooling in liquid nitrogen and returning to room temperature. The rationale for treatments b) and c) are as follows:

Treatment b): Cyclic application for the thermal stresses in the thermal cycling process is expected to lead to some extent of stress relaxation in the composite. This is analogous to cyclic shakedown of stresses in strain controlled fatigue tests.

Treatment c): The liquid nitrogen cooling treatment should reduce stresses by driving the matrix into a greater extent of plastic flow than that produced by cooling to room temperature. This extra plasticity is caused by the larger thermal strain ($\Delta \alpha \Delta T$) to which the composite is subjected. Upon returning to room temperature the matrix unloads elastically from this larger plastic strain level, leading to reduced stress. This process is akin to the process of autofrettage, in which a stress-free metal is plastically deformed locally around a hole, and then unloaded to produce a local residual compression.

Additional neutron diffraction experiments were performed on other IMC:

2) Ni-50Al matrix reinforced by four unidirectional plies of tungsten fibers at 35% V_f. This material was obtained from Drs. Randy Bowman and Mike Nathal of NASA Lewis Research Center, and was fabricated by the powder cloth method, hot pressed, and HIPed. Further details of the material fabrication are available from Bowman and Noebe (1990). The microstructure of this material is shown in Figure 6.

3) Ni-50Al matrix reinforced by four unidirectional plies of single crystal Al_2O_3 (Saphikon) fibers at 30% V_f; This material was obtained from Drs. Randy Bowman and Mike Nathal of NASA Lewis Research Center, and was fabricated by the powder cloth method, hot pressed, and HIPed. Further details of the material fabrication are available from Bowman and Noebe (1990). The microstructure of this material is shown in Figure 7.

4) Ni-10Fe-25Al matrix reinforced by ten unidirectional plies of single crystal Al_2O_3 (Saphikon) fibers at 10% V_f. This material was manufactured by GE-Aircraft Engines by hot pressing a compact of fibers and powder at 1121C and HIPing at 1121C. Its microstructure is shown in Figure 8.

5) Ni-10Fe-25Al matrix reinforced by six unidirectional plies of single crystal Al_2O_3 (Saphikon) fibers at 6% V_f. This material was processed identically to material 4 and is illustrated in Figure 9.

Samples of fiber and unreinforced matrix materials consolidated in the same fashion as the composites were also obtained.

3.3.2 Analytical modeling method

The concentric cylinder model used in Task 1 was also used for predicting the residual stresses and strains in the selected composite systems. The only change was in the modification of the input material properties used, as appropriate to each system:
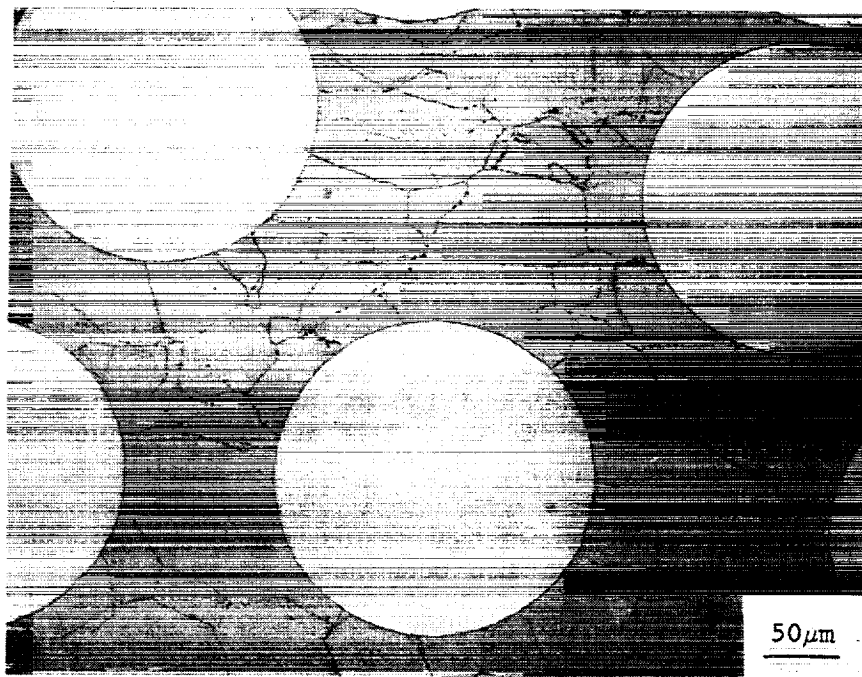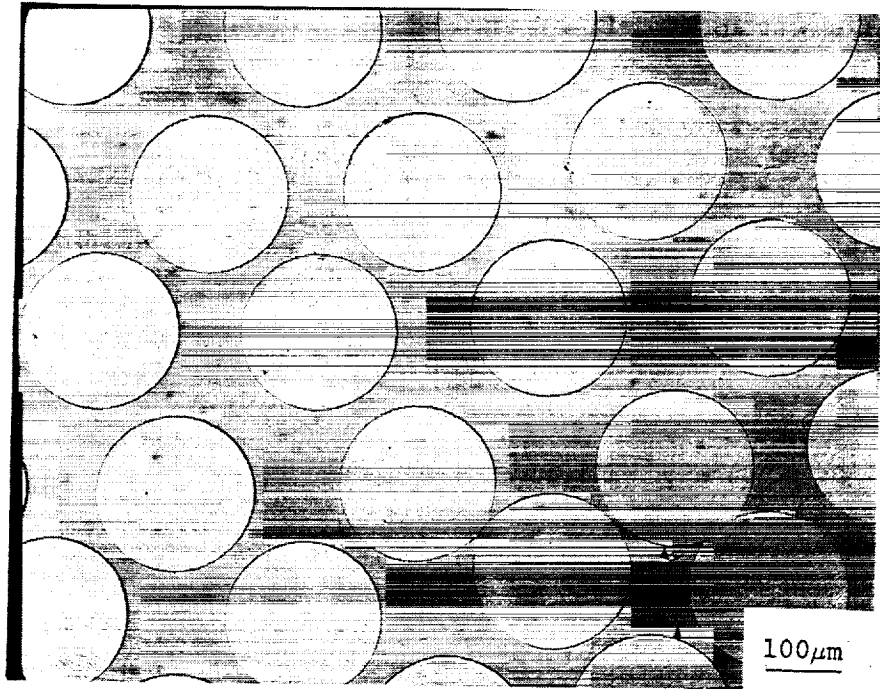
13

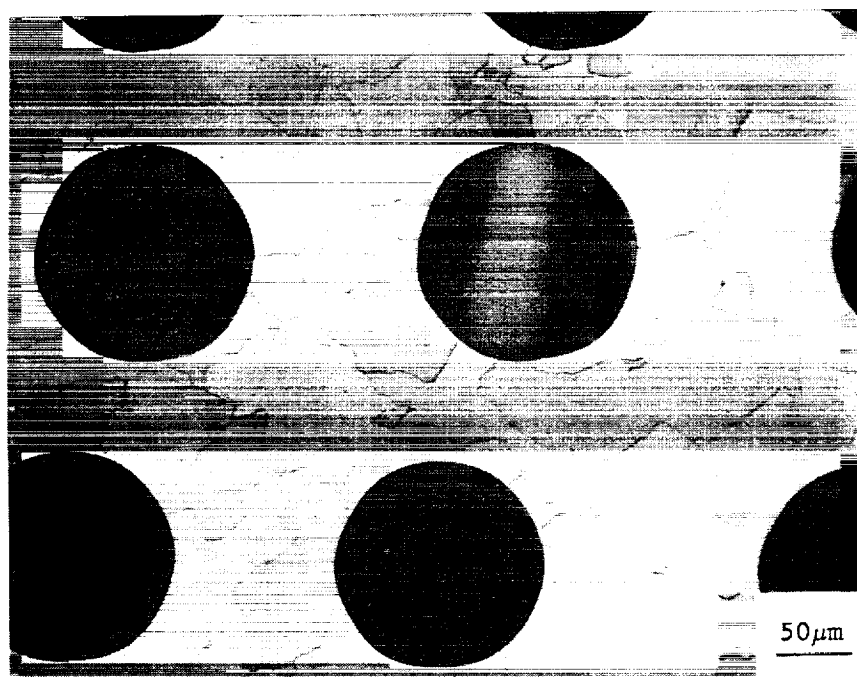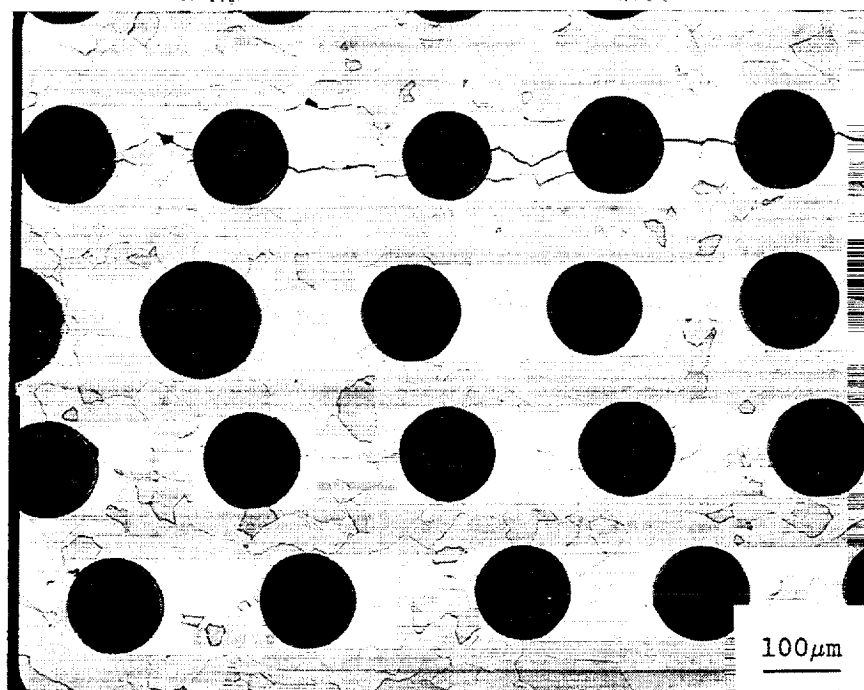Figure 6   Microstructure of W/NiAl Used in Task 2

14

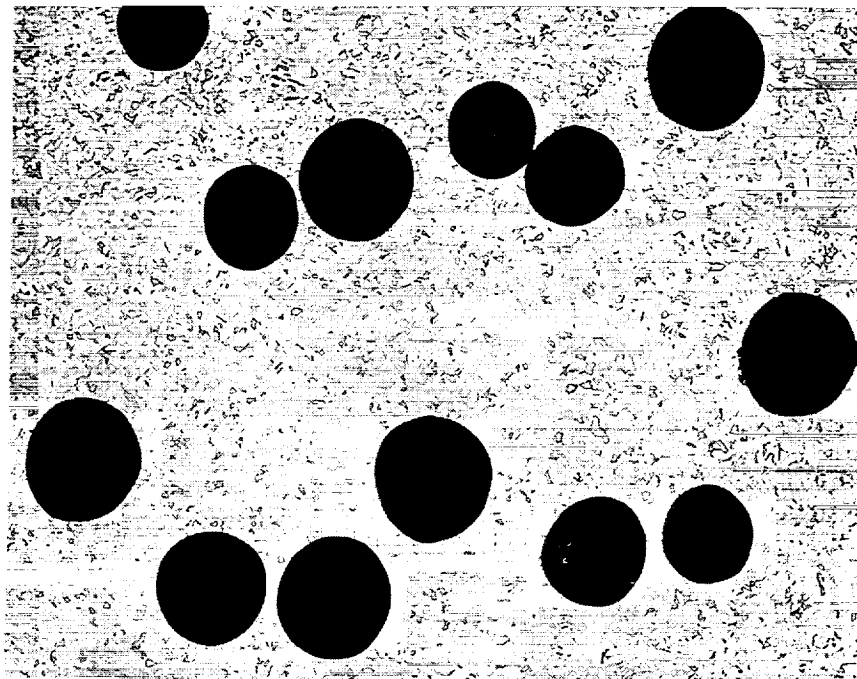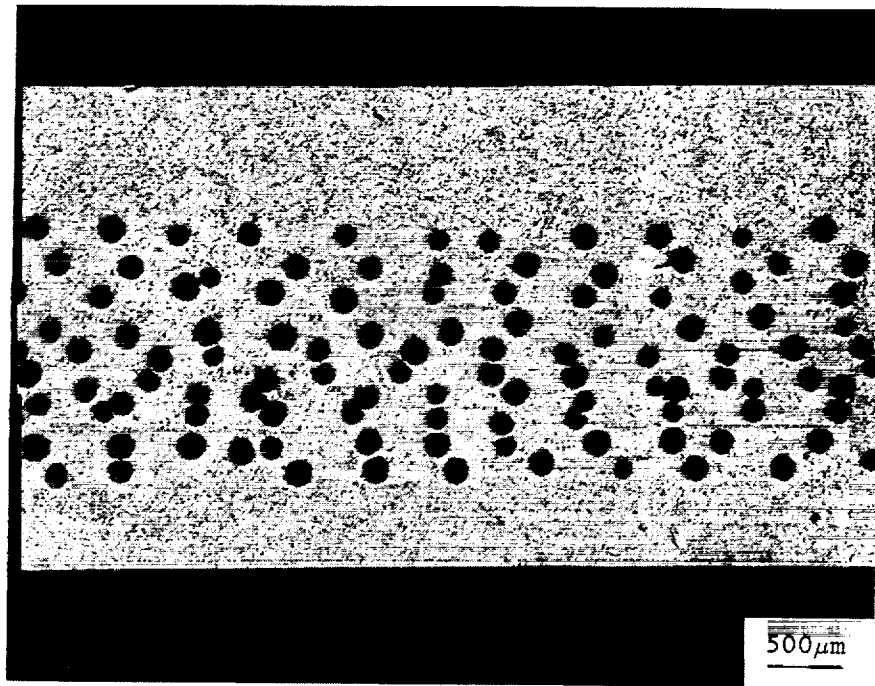Figure 7   Microstructure of Al_2O_3/NiAl Used in Task 2

Figure 8   Microstructure of Al_2O_3/NiFeAl (10% V_f) Used in Task 2
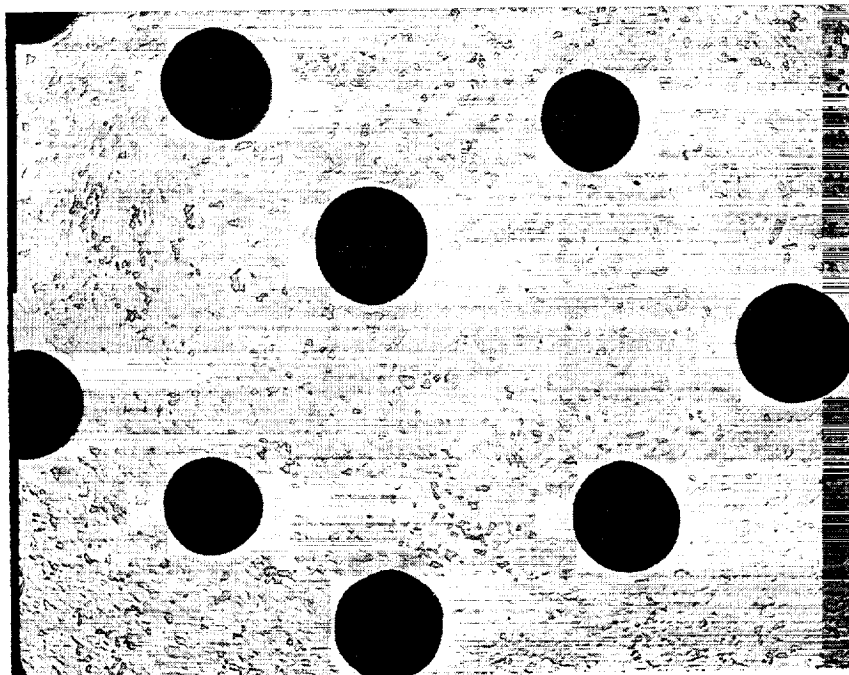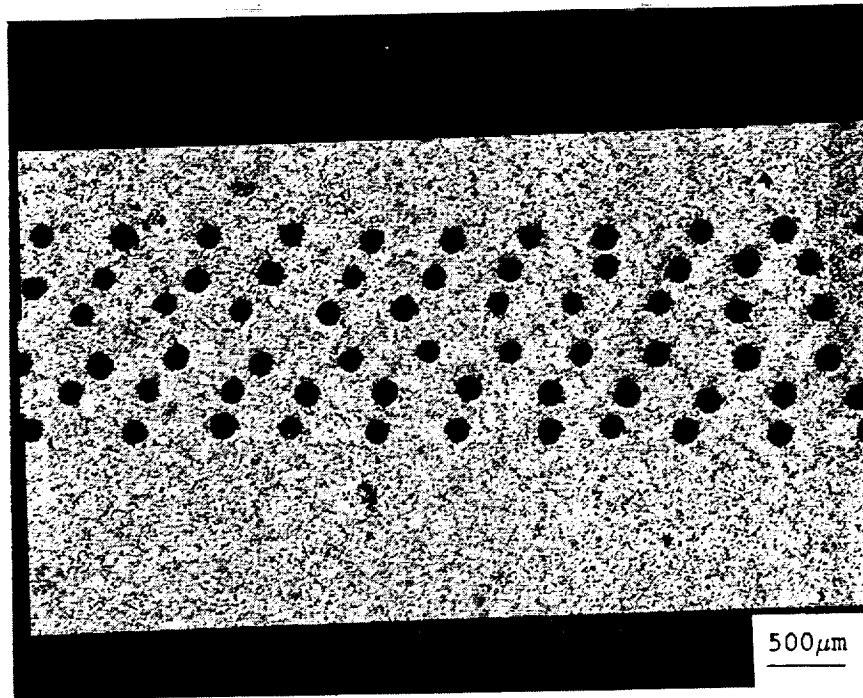
Figure 9   Microstructure of Al$_2$O$_3$/NiFeAl (6% V$_f$) Used in Task 2

1) Foil-fiber SCS-6/Ti-24Al-11Nb:

a) As-fabricated SCS-6/Ti-24Al-11Nb: The fiber properties were identical to those shown in Table 1, while the matrix properties used were different from Task 1, since the matrix material was from foil instead of sprayed powder. Matrix stress-strain behavior was estimated from stress-strain data from fiberless panels presented in Gambone (1990). These curves are shown in Figure 10 and show slightly lower strength than the IPD matrix.

b) Thermal cycled SCS-6/Ti-24Al-11Nb: Fiber properties were identical to those shown in Table 1. Matrix physical properties were as shown in Table 1, but stress-strain behavior was modified to account for the thermal cycling. Instead of trying to trace the entire history of cooldown plus 100 thermal cycles, the matrix cyclic stress-strain response after thermal cycling was approximated and used in the model. This cyclic stress strain behavior was estimated from out-of-phase TMF stress strain response of wrought (unreinforced) Ti-24Al-11Nb from DeLuca et al. (1990) and is shown in Figure 11. Note that, as expected, the cyclic flow stresses for this condition are slightly lower than for as-fabricated material.

c) Liquid nitrogen cooled SCS-6/Ti-24Al-11Nb: Properties used were the same as 1) a) except that the fiber and matrix properties were extended to -196C by extrapolation (no data was found to substantiate these data below ambient temperature). Extrapolated matrix yield strengths are shown in Figure 12.

2) W/NiAl: Fiber properties were taken from ASM (1979), and are listed in Table 1. Matrix properties are listed are Table 1, and stress-strain response is shown in Figure 13. These properties were obtained from Bowman and Noebe (1990) and Noebe, et al. (1990).

3) Al_2O_3/NiAl: Fiber properties were taken from internal GE data sources, and are shown in Table 1. Matrix properties were the same as for material 2.

4) and 5) Al_2O_3/NiFeAl: These two systems differed only by fiber fraction. Fiber properties were as used for material 3, and matrix properties were estimated from limited data from internal GE sources. Stress-strain behavior assumed for the model is shown in Figure 14.

3.4 Task 3 - Effect of Thermal Stresses on Mechanical Properties

In Task 3 samples of SCS-6/Ti-24Al-11Nb were subjected to different thermomechanical processing to produce different levels of residual stress. Four different mechanical tests (tension, shear, fatigue crack growth and fiber pushout) were conducted on samples with these levels of residual stress to determine the effect of the residual stresses on mechanical properties.

3.4.1 Selection of Material

SCS-6/Ti-24Al-11Nb was selected as the material system on which to conduct the Task 3 residual stress modification and mechanical testing since of the materials studied it was the most mature, i.e., it could be obtained in large enough quantities and with high enough confidence in the process control to make consistent material from panel to panel. Four panels of 4 ply unidirectional material with 30 ± 2% fiber volume fraction were made by Textron Specialty Materials Division by

18

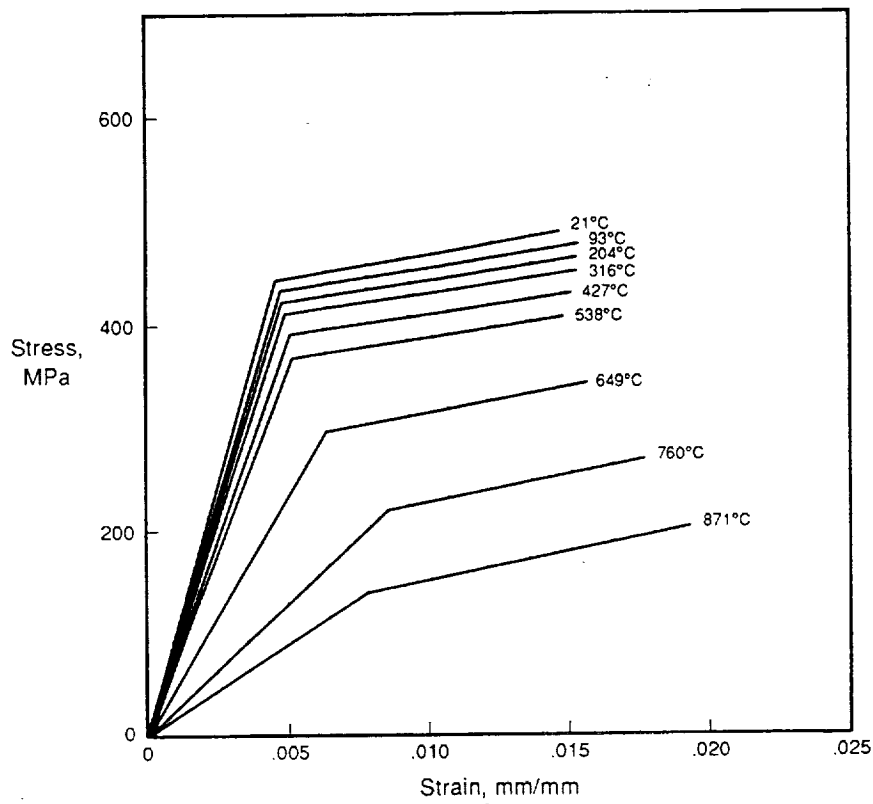Figure 10. Stress-Strain Behavior of Ti-24Al-11Nb
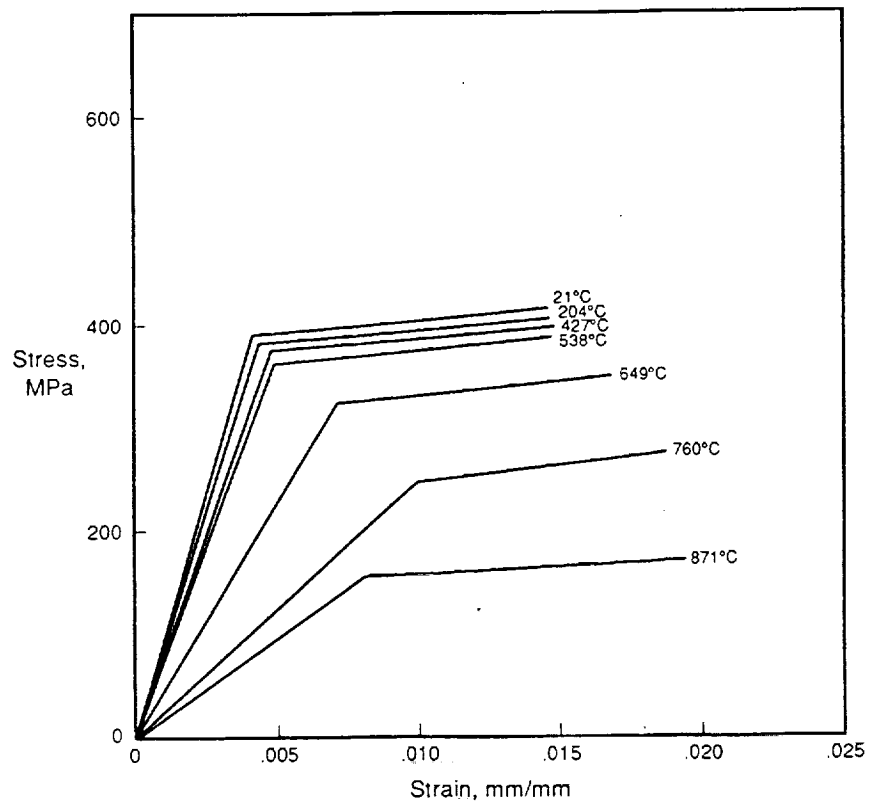Foil Matrix (Gambone, 1990)

Figure 11. Stress-Strain Behavior of Ti-24Al-11Nb Foil
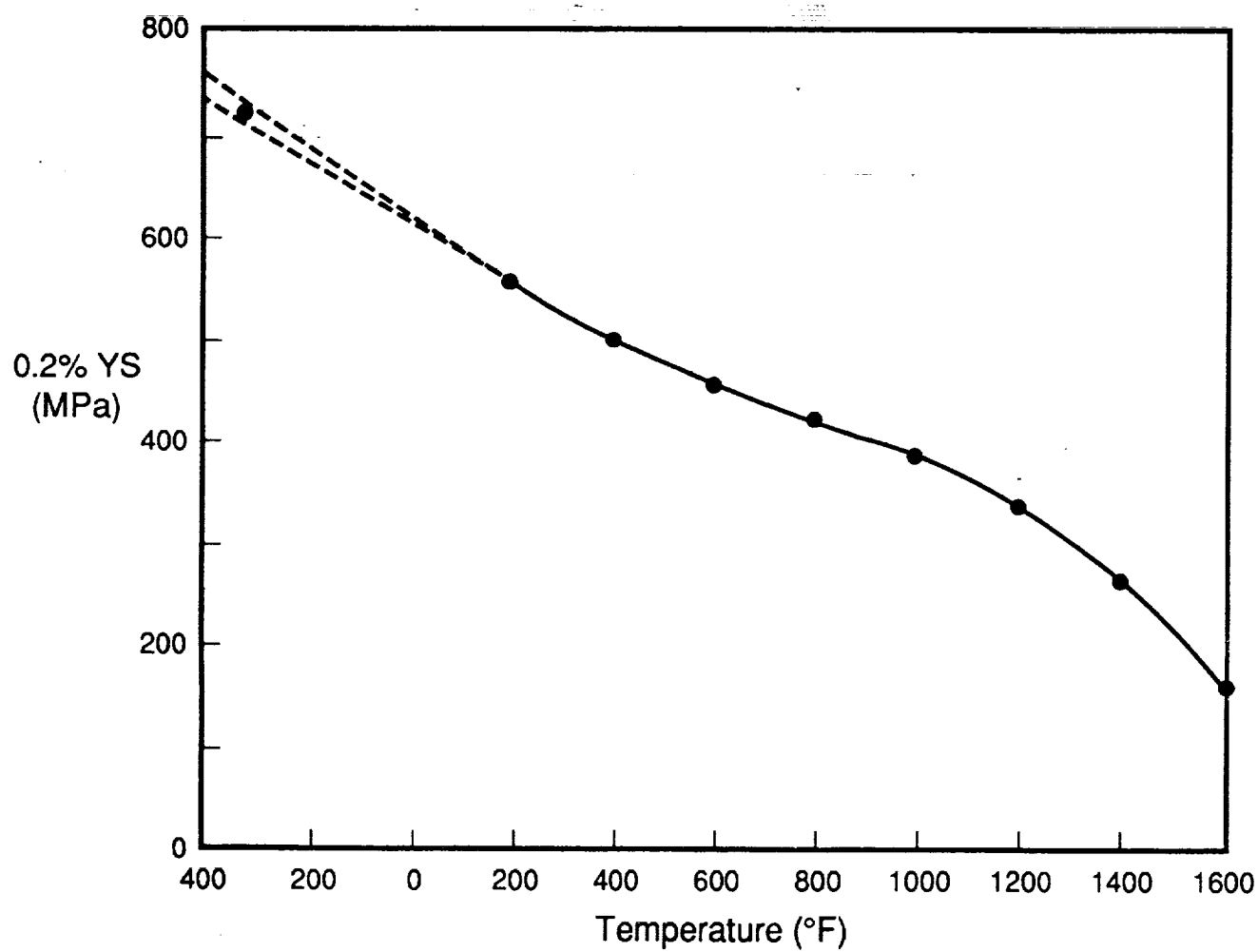Matrix Adjusted for Cyclic Relaxation

19

Figure 12   Yield Strength of Ti-24Al-11Nb Extrapolated to Liquid Nitrogen
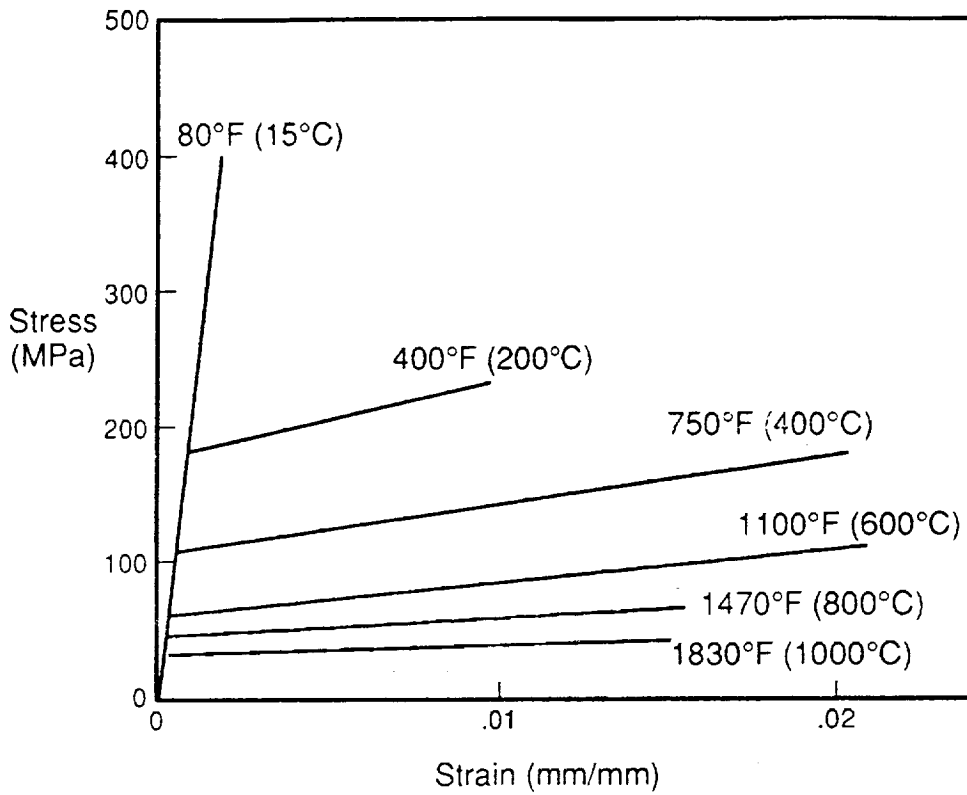Temperature for Modeling

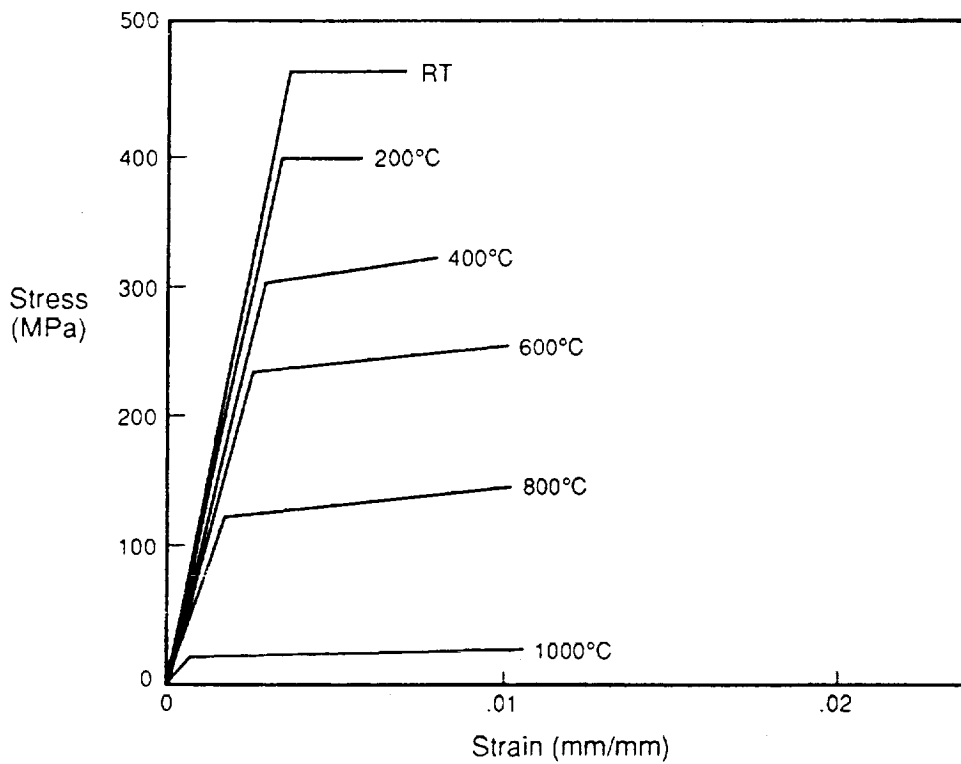Figure 13 Stress-Strain Behavior of NiAl Used for Modeling

Figure 14 Stress-Strain Behavior of NiFeAl Used for Modeling

2 1

the foil-fiber process. Typical microstructure and fiber distribution were similar to that shown in Figure 5.

3.4.2 Selection of Processing to Modify Thermal Stresses

One-half inch wide strips were cut from these panels parallel to the fibers, and were subjected to various thermomechanical treatments:
1) Free thermal cycling between 93 and 650°C for 100 cycles;
2) The treatment shown in Figure 15a involving cooling from high temperature under tension: a) heating to 850°C with an induction coil and stabilizing temperature, b) loading to 689 MPa tension while holding at 850°C, c) cooling to room temperature under load, and d) removing the tensile stress at room temperature;
3) A four step treatment shown in Figure 15b, like treatment 2 except involving loading and cooling under 344 MPa compression.
4) Some samples were also left as-fabricated.

These treatments were chosen based on the following rationale:
1) Free thermal cycling: Cycling materials with a mean stress under strain control usually results in a reduction in mean stress. In these composites the matrix is being cycled from essentially no stress at high temperature to tension at low temperature with the stiff fibers providing constraint that approximates strain control, Figure 16. DeLuca et al. (1990) have showed that under such out-of-phase, R = 1.0 conditions, Ti-24Al-11Nb material will show relaxation of the maximum (low temperature) stress. Thus free thermal cycling was chosen as one means of modifying the residual thermal stress.

2) Cooling under tension: The changes in thermal stress produced by this treatment can best be described through Figure 17a. At room temperature after fabrication the matrix is in tension and the fiber is in compression, as demonstrated in Cox et al. (1990). On heat up to 850C these stresses reduce toward zero as the thermal mismatch from the fabrication temperature is reduced. Application of tension at 850C raises both the fiber and matrix into tension, but the fiber stress is higher than the matrix because its modulus is higher. During the brief hold period under load at 850C the matrix creeps and its stress relaxes back to low levels again while the fiber stress increases. On cooling, thermal stresses are reimposed (tensile for the fiber, compression for the fiber) and at this point the matrix is at about the same stress level as it was after the original cooldown from fabrication. (The fiber, however, is under a much more tensile condition.) When the load is released after reaching room temperature the fiber and matrix unload (go toward compression) and the matrix ends up with a lower tensile stress than it had after fabrication. Since the matrix and the fiber stresses must balance through equilibrium, the fiber stress is also lower (less compressive), as illustrated in Figure 17a.

3) Cooling under compression: This treatment, Figure 17b, works much like cooling under tension, except that the load applied at 850C is compression. After cooling to room temperature the unloading of the compression drives the matrix further up in tension and raises the residual stress above that developed on free cooldown from fabrication. It practice the load applied had to be reduced below that used for the cooling under tension treatment in order to reduce the risk of buckling the samples. It was also found necessary to use a buckling restraint fixture consisting of alumina rods clamped to the faces of the specimen.
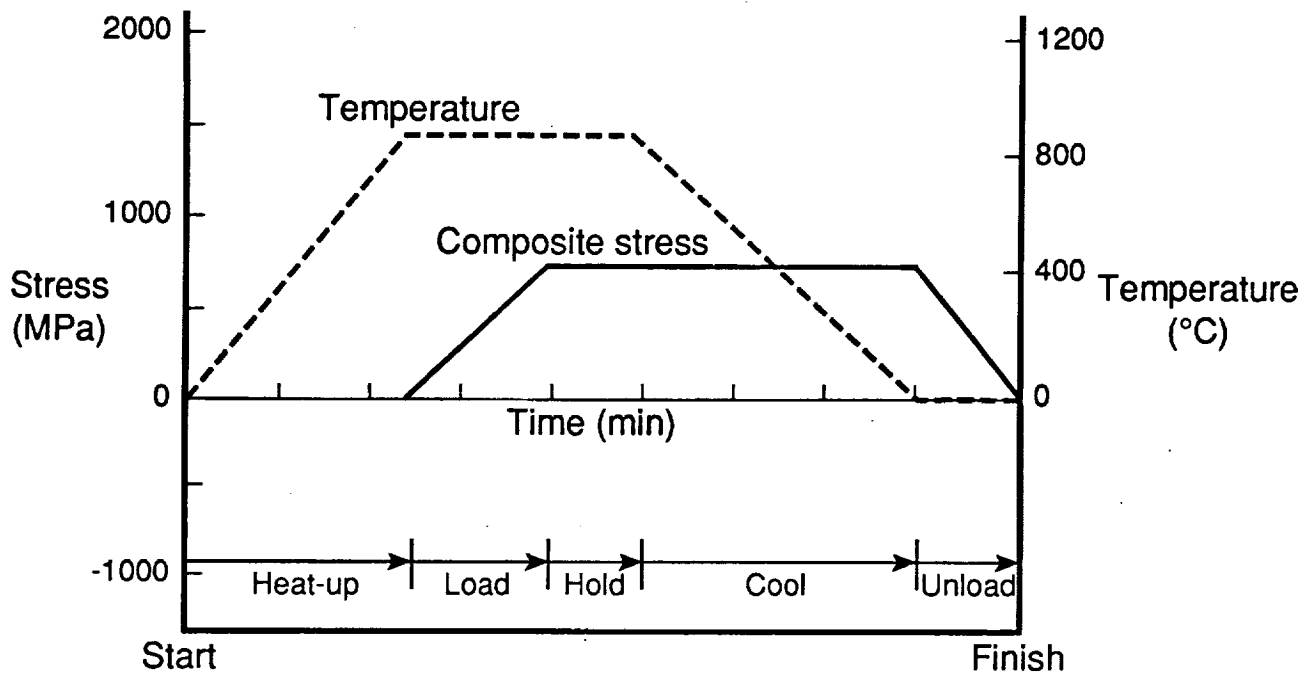
a) Cooling Under Tension Treatment
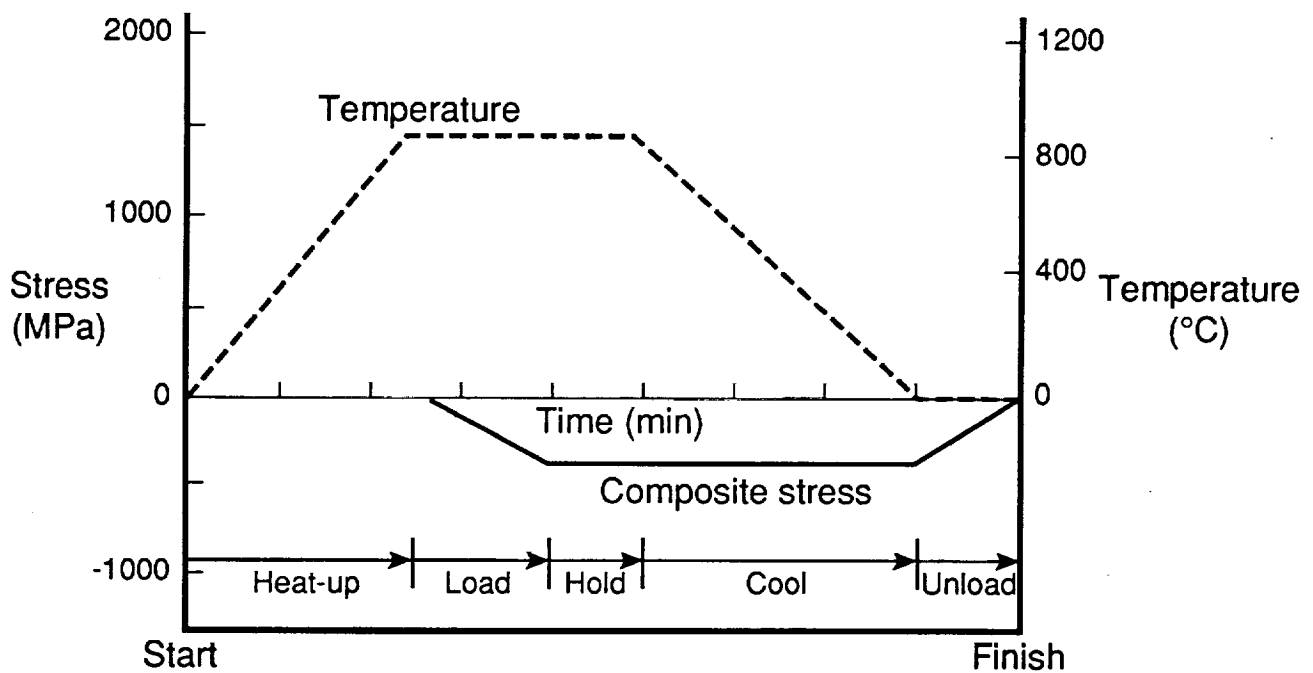
b) Cooling Under Compression Treatment

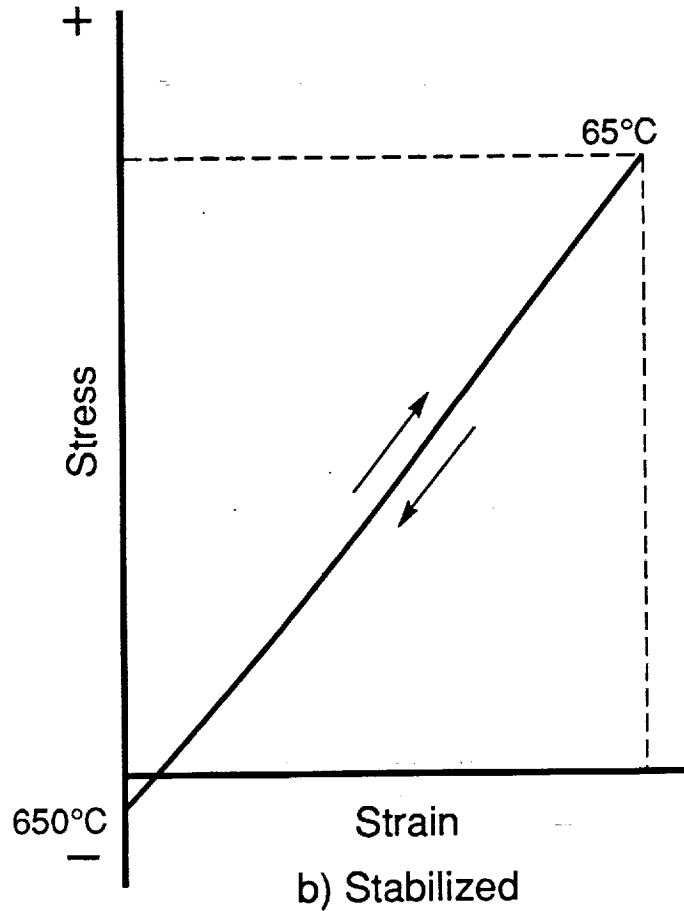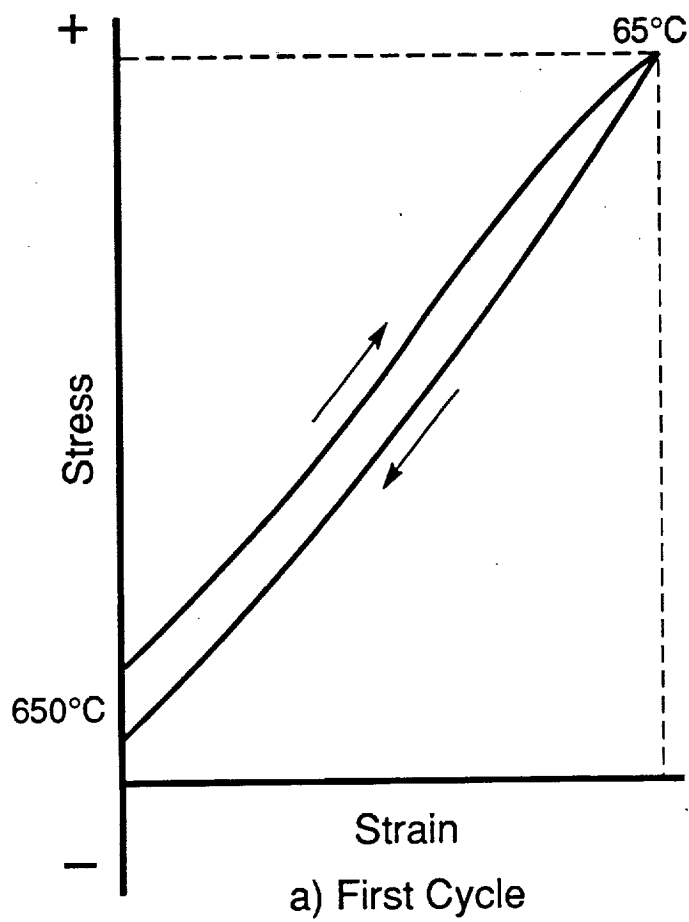Figure 15   Thermomechanical Treatments Used to Modify Residual
Stresses

23

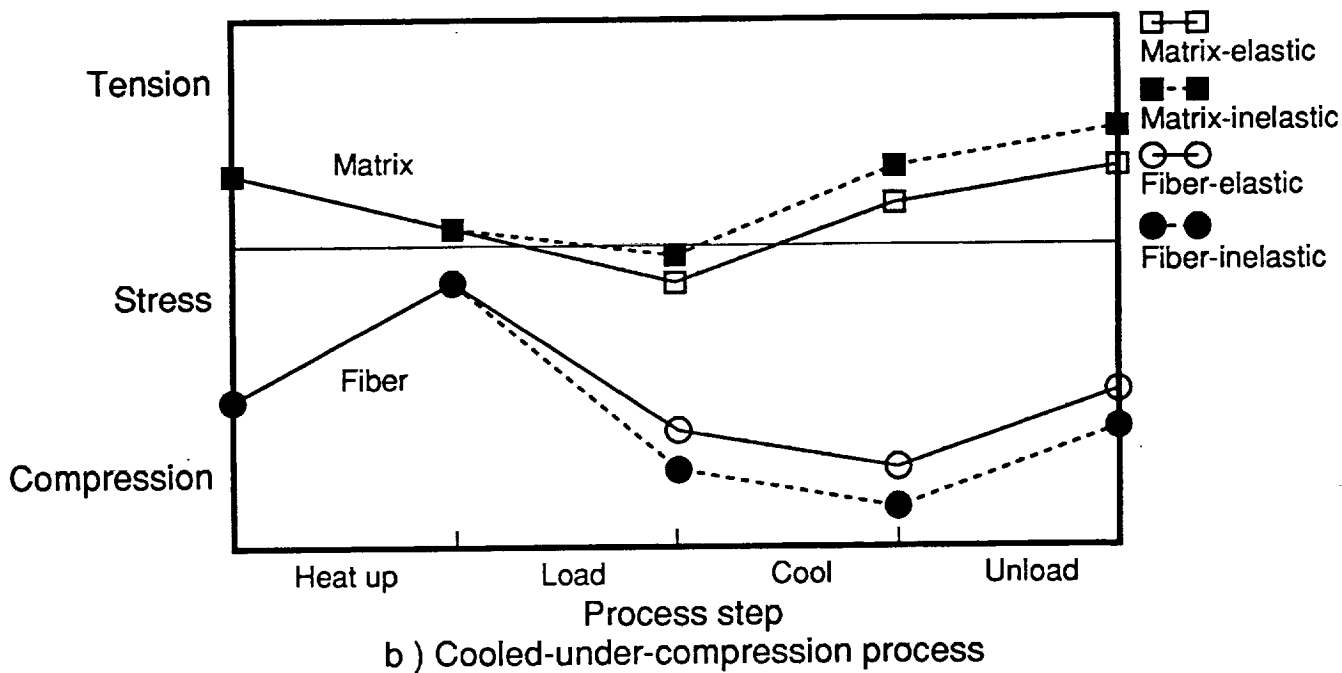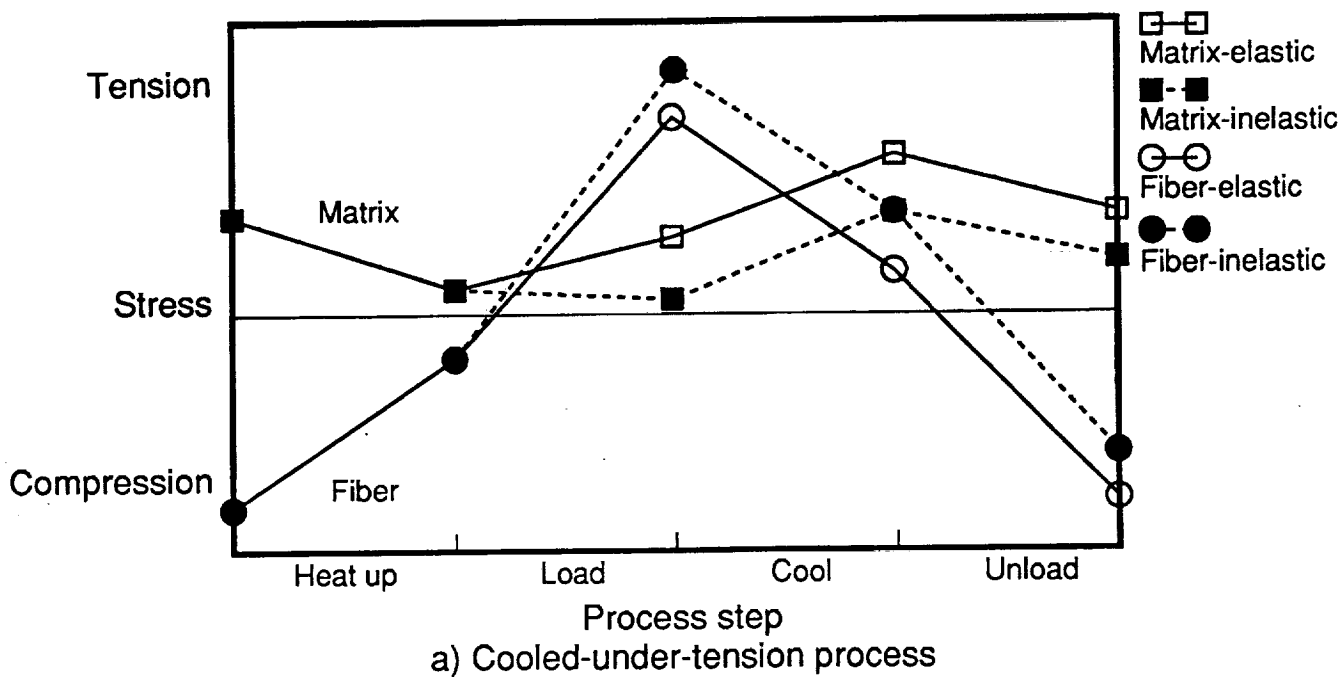Figure 16   Thermal Cycling Reduces Stresses by Shakedown of Mean Stresses

Figure 17 Schematic Fiber and Matrix Stress Histories as a Function of Processing Step. Response for Elastic and Inelastic Behavior are Shown.

25

3.4.3 Selection of test types and conditions

Four different mechanical tests types were selected to evalaute the effects of residual stresses on IMC properties and to compare these results to predictions of analytical property models. These four tests were selected to investigate fiber and matrix/interface dominated properties. The selected tests were: a) longitudinal tension, b) fiber pushout, c) in-plane shear, and d) fatigue crack growth. The rationale for selection and details of test method are given in the following paragraphs.

a) Longitudinal tension: This test was selected because tensile strength in the fiber direction is a primary design property for IMC. While longitudinal tensile strength is generally considered a fiber-dominated property because the strength and stiffness of the fibers are greater than that of the matrix, in IMC the matrix can play a significant role because fiber fraction tends to be fairly low and matrix stiffness high. An effect of thermal residual stresses on longitudinal tensile strength is expected through the modifying effect that an initial stress would have on the strength capability of a brittle constituent. For example, if the fibers are in residual compression after fabrication, then their tensile strength should be enhanced because it would take more applied stress to load them to their breaking stress. Conversely, tensile stress in the matrix would tend to promote earlier matrix failure. Modeling of residual stress effects on longitudinal tensile strength will be dealt with more fully in Section 4.3.2. Tensile tests were conducted at room temperature on specimens machined from the processed blanks to the configuration shown in Figure 18. Testing was performed at Martest, Inc, Cincinnati, OH, at a crosshead rate of 0.05 in/min. Strain was recorded using an extensometer placed in the reduced gage section, and was left on the specimen to failure.

b) Fiber pushout: While not a standard mechanical property of bulk composite material, this test is important because it gives a direct measure of the fiber-matrix interface shear strength. This parameter plays a significant role in other mechanical property models, so it is helpful to determine directly how it is affected by the thermal residual stress states produced in this study. From current understanding of the nature and role of the interface in SCS-6/Titanium composites, the interface is primarily mechanically, rather than chemically bonded (Johnson, et al., 1990, and Wright, et al., 1990). Since the primary mechanical bonding force is the radial interfacial clamping stress induced by a combination of thermal and mechanical loading of the composite, variations in the radial interface stress should influence the interface shear strength: the higher the radial thermal stress, the higher the interface strength. Modeling of this effect will be described more fully in Section 4.3.3.

Fiber pushout testing was conducted at University of Cincinnati by Dr. R. Singh. One piece of each thermomechancial treatment was supplied, and samples of nearly 0.5 mm long parallel to the fibers were cut from these on a wafering saw and ground to 0.38 mm thick (fiber direction). Care was taken to keep the samples flat and the fibers perpendicular to the surface. Cut surfaces were final polished to 1 μm and the samples were ultrasonically cleaned. Each sample was individually mounted with double-sided scotch tape on the micro-slide platform of the pushout apparatus. Crosshead speed of the Instron used to drive the indentor was 0.0127 cm/min. Load vs. time plots were obtained during testing. Approximately ten
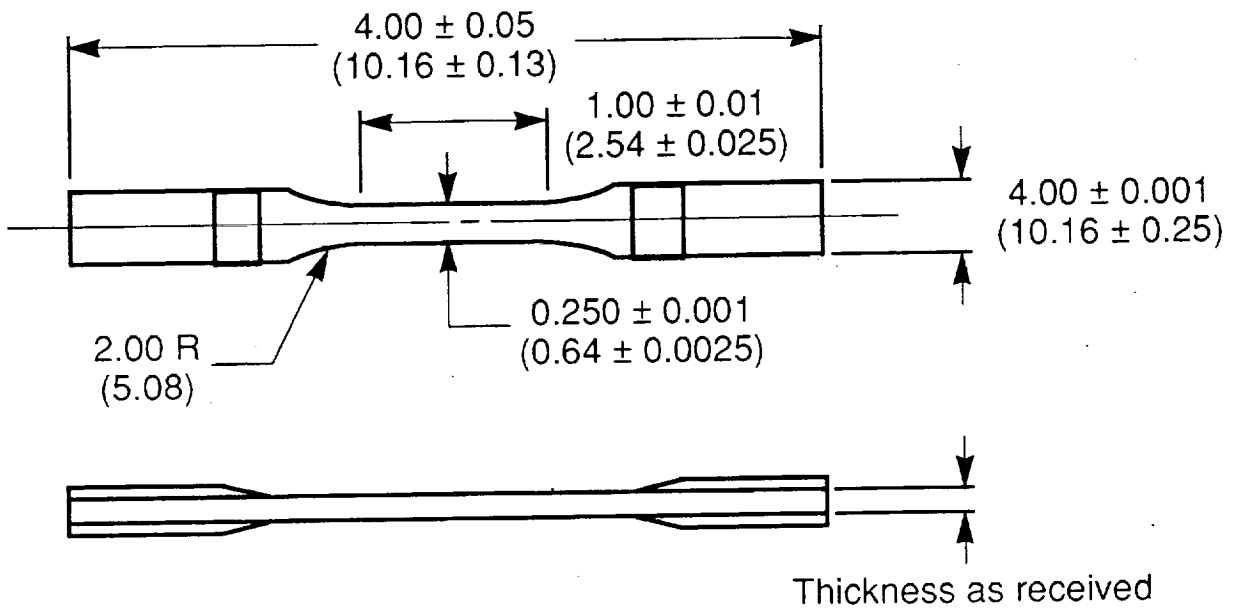
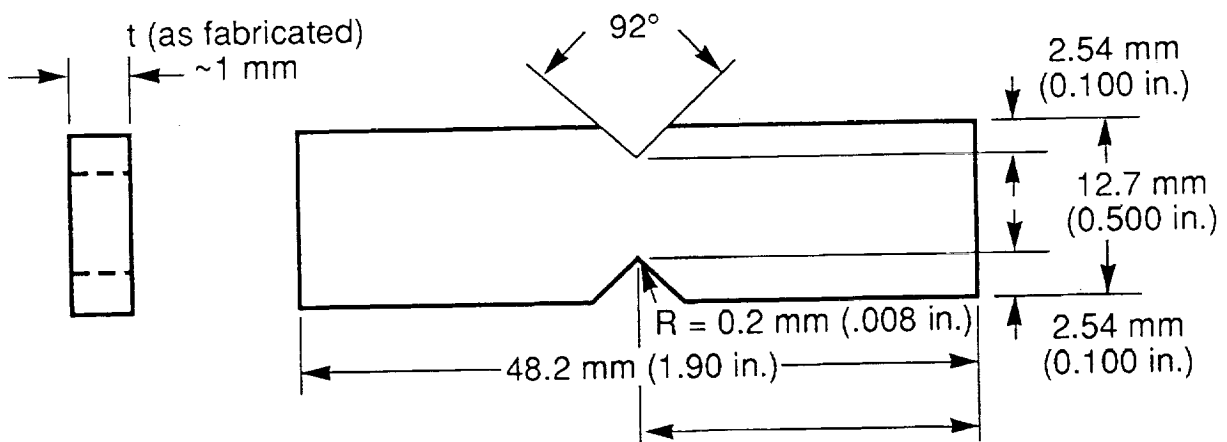Figure 18   Tensile Specimen Configuration.   Dimensions in Inches (cm).

Figure 19   Iosipescu In-Plane Shear Specimen. Dimensions in mm. (in.)

pushouts were done per sample and the average interfacial shear strength, τ_i, was determined by dividing the debonding load by the total interface area (thickness x π x fiber diameter).

c) <u>In-plane shear</u>: This test was selected to evaluate the matrix and fiber-matrix interface dominated property effects, since shear strength tends to be more dependent on these properties than on the fiber properties. Shear was selected over transverse tension because previous work (Wright et al.,1990) had suggested that shear strength would be more sensitive to interface strength variations, and thus indirectly, to residual stress effects on clamping of the interface. It is expected that higher residual stresses would cause tighter clamping of the fiber matrix interfaces and reduce the ease of interface sliding, thereby rasing shear strength. A more extensive discussion of modeling is given in Section 4.3.4. Shear tests were conducted at Cincinnati Testing Laboratory, Cincinnati, OH using the Iosipescu method. The specimen configuration shown in Figure 19 was cut from processed blanks with the fibers parallel to the long axis. A ±45 strain gage rosette was bonded on the gage section between the notches, and tests were conducted at room temperature until failure or maximum load.

d) <u>Fatigue crack growth</u>: This test was selected because fatigue is a primary loading mode in aerospace applications. Fatigue crack growth, rather than fatigue crack initiation, was selected for study because fatigue crack growth behavior is typically more repeatable than initiation and thus easier to characterize difference due to residual stress differences. Effects of residual stress on fatigue crack growth are expected through two different effects: residual stresses in the matrix will affect the mean stress level in the matrix, and thus influence the matrix contribution to crack growth, and residual stresses should influence the extent of matrix clamping of the fiber, which will influence fiber-matrix interface strength. The interface strength in turn should influence the degree of fiber bridging of the matrix crack, thus influence crack tip stress intensity and growth rate, as described in models of fiber bridging (Sensmeier and Wright, 1989, Marshall, et al., 1985, McCartney, 1987, and Ghosn et al., 1992). Fatigue crack growth modeling will be described further in Section 4.3.5.

Straight-sided specimens of the same overall size as the tensile samples (Figure 18) were tested at GE at room temperature. Cracks were initiated from a center notch 2.5 mm long. Specimens were instrumented for electrical potential measurement of crack growth using the method implemented at GE (Van Stone and Richardson, 1985) and crack growth was monitored as cycling occurred. Two specimens of each process were tested, one at 345 MPa, and one at 552 MPa. R-ratio was 0.05 and frequency was 0.33hz.

28

4. Results and Discussion

4.1 Task 1 - Selection of Experimental Method for Residual Stress Measurement

4.1.1 Results of Xray Diffraction

The residual stresses measured by Xray diffraction in the matrix of the SCS-6/Ti-24Al-11Nb composite are shown in Table 2 and Figure 20. Detailed results are given in Appendix III. These results are for both longitudinal and transverse matrix stresses on both sides of the composite sample. At the surface, there appears to be some variability in the stresses, but at depths of 33 and 75 microns, the results are fairly consistent and constant with depth. Tensile stresses were found in both longitudinal (315MPa average) and transverse (200MPa average) directions. Longitudinal tensile stresses of this magnitude have been reported in these materials by Cox et al. (1991) and by Jayaraman and Rangaswamy (1991). The variations in surface stresses found here are most likely the result of chemical contamination or surface finishing; it was noted that the Xray peak widths at the surface were broader than subsurface, indicating the presence of disturbed material at the surface. The averages of the measurements at the two subsurface locations are listed in Table 2 for comparison to the neutron diffraction and analytical model results. Elastic strain values corresponding to these stresses are also presented for purposes of comparison. Attempts were made to obtain diffraction data from the fibers but were not successful.

Table 2
Measured and Calculated Average Thermal Strains and Stresses in
IPD SCS-6/Ti-24Al-11Nb (V_f = .25)

		XRD	ND	Analysis
Matrix	Longitudinal Strain (m/m) Transverse Strain (m/m)	+.0032 +.0012	+.0037 -.0002	+.0029 -.0004
	Longitudinal Stress (MPa) Transverse Stress (MPa)	+315 +200	+ 430 - 160	+ 330 - 90
Fiber	Longitudinal Strain (m/m) Transverse Strain (m/m)		-.0022 +.0009	-.0020 +.0003
	Longitudinal Stress (MPa) Transverse Stress (MPa)		- 1220 - 770	- 998 - 270

4.1.2 Results of Neutron Diffraction

The residual strains and stresses measured by neutron diffraction are also shown in Table 2 and Figure 21. (The stresses were obtained using the average strains in Hooke's Law with the elastic constants given in Table 1.) Like the Xray diffraction results, they indicate the presence of substantial matrix tension in the longitudinal direction and a lower level of matrix tension in the transverse direction. Quantitatively, the average longitudinal matrix stress measured by neutron diffraction is slightly higher than that measured by Xray diffraction and the transverse stress is lower. In addition to the matrix strains, the fiber strains could be clearly detected, and these are also reported in Table 2. As expected, the fiber is in compression, with the compressive strains and stresses being larger in the longitudinal direction than in the transverse.
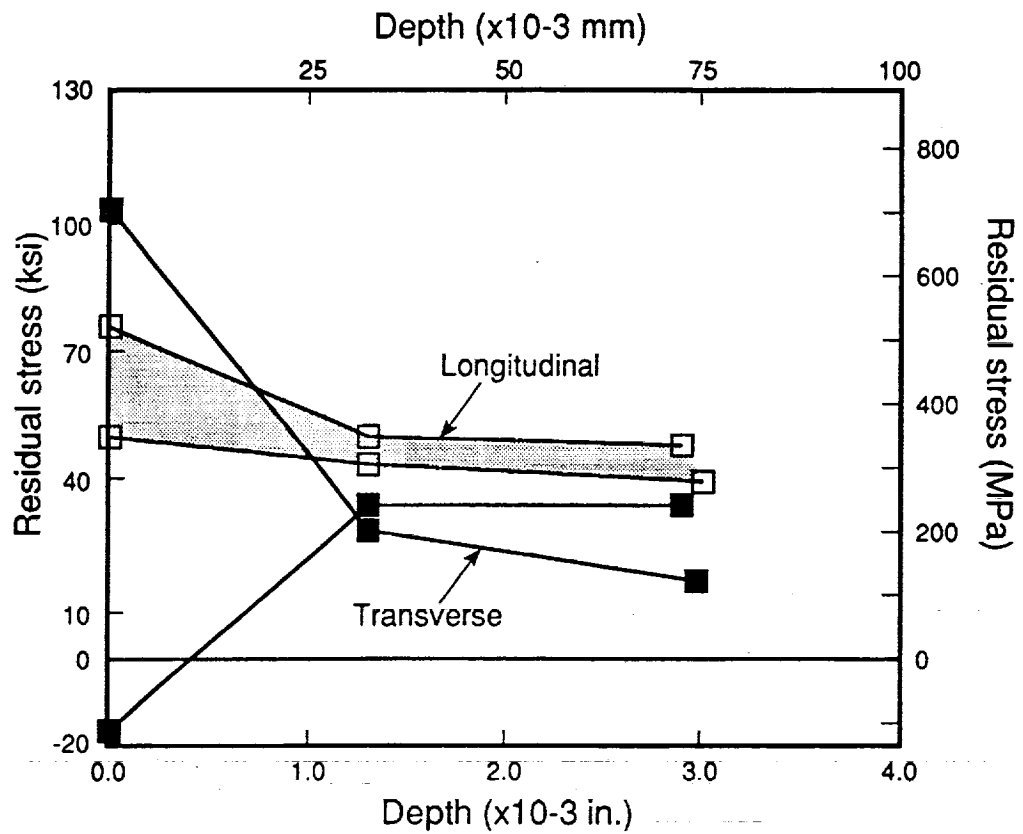
29

Figure 20 Matrix Residual Stresses Determined in SCS-6/Ti-24-11Nb by
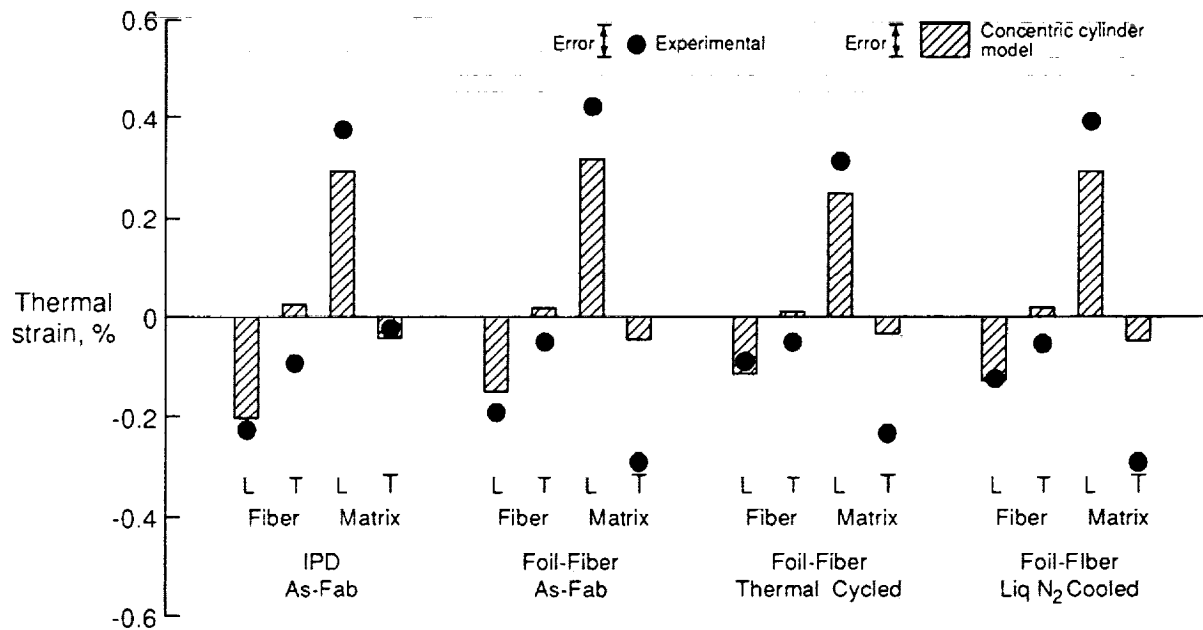XRay Diffraction.

Figure 21. Comparison of Thermal Strains in SCS-6/Ti-24Al-11Nb
Composites Measured by Neutron Diffraction vs Predicted
by Concentric Cylinder Model.

4.1.3 Results of Synchrotron XRay Diffraction

To examine the feasibility of SXRD, experiments were conducted on a sample with a single imbedded 800 micron diameter Al_2O_3 fiber in a matrix of CP Ti. The incoming and diffracted X-ray beams were collimated down to 50-100 microns thick by 1000 microns wide (Figure 22) so that only a small volume of material was interrogated. Residual strains were calculated by measuring the energy shift in a diffracting peak as compared to a stress-free reference peak obtained in the matrix far from the isolated fiber. The beam was positioned so that it was adjacent to the fiber-matrix interface by checking for the disappearance of any SiC peaks, and then diffraction data was taken as a function of distance from the interface by translating the specimen. Figures 23 and 24 present the hoop and radial strain profiles for this sample, plotted along with expected strain distributions obtained from an elastic concentric cylinder model ($V_f \approx 0$). Generally good agreement is seen between the measured and predicted values, although considerable scatter in data was obtained. The scatter was reduced somewhat by using the average of shifts for several different peaks, as plotted in Figures 23 and 24. However, the major factor contributing to scatter was the relatively small number of grains within the diffracting volume. If only a few grains are diffracting, their average location within the volume is likely to be different than the volume center, leading to a geometric contribution to diffraction angle which will be interpreted as a peak shift or strain (Figure 25). For the matrix grain size (10-20 microns) and diffracting volume, this error could be equivalent to a strain of about 0.001.

Experiments were also performed on samples with single SCS-6 fibers in Ti-24Al-11Nb. Hoop strains are shown in Figure 26. Note the spatial scale is much smaller than for Figures 23 and 24. The strains measured show reasonable agreement with expected values at distances greater than about 75 microns from the fiber-matrix interface, but closer in, the measured strains are far less than expected. It is possible that this is real; in this sample a 10 micron thick beta-depleted zone was seen around the interface, Figure 27, and the radial cracking observed would lower strains in the vicinity. Diffusion of interstitials from the interface may also have altered the local lattice spacing and affected the apparent strain values.

4.1.4 Results of Ultrasonics

Strategies for US measurement of thermal stresses were also investigated. US methods depend on higher order change in elastic properties (and hence wave velocities) due to the nonlinear form of the interatomic potential. In order to achieve reasonable accuracy, it was felt necessary to develop an approach in which the relative velocity change would be greater than 1 part in 1000. Using a concentric cylinder model to describe the state of stress around a fiber in a composite, the effect of these stresses on the higher order elastic terms was investigated analytically to identify velocity effects which might meet the required criterion. Two promising configurations were identified. Figure 28 shows that a shear wave travelling parallel to the fiber near the fiber-matrix interface should develop a relatively large velocity change. The difference in velocity of the two polarized shear waves, v_{s1} and v_{s2}, should be particularly large. This is important because it would allow the automatic cancellation of compositional or microstructural variations in elastic properties along the sound path. An alternate configuration (the "creeping ray" method) Figure 29 would utilize rays backscattered perpendicular to a fiber. Again, the difference in polarized shear waves, v_{s1} and v_{s3}, would be used as a measure of stress. These
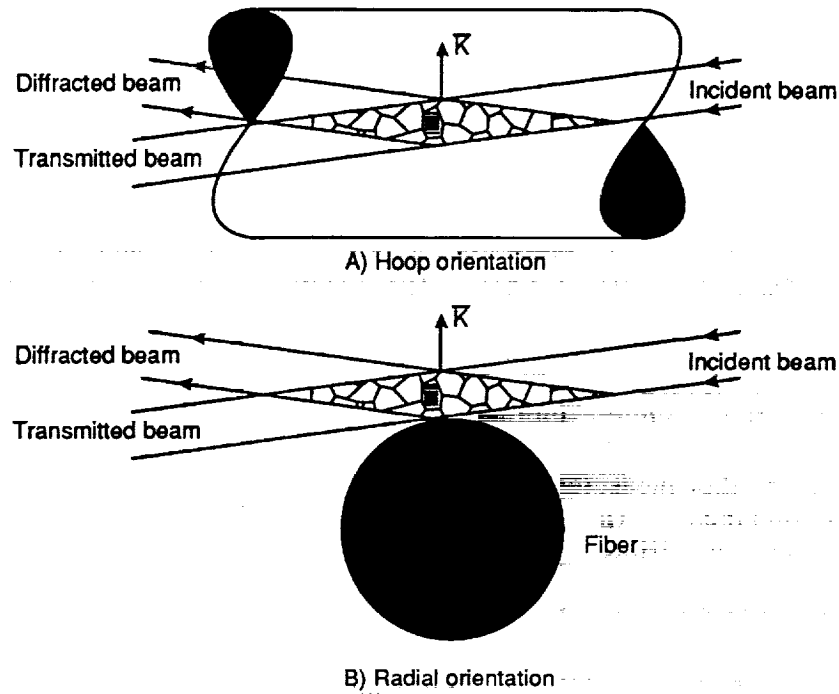
Figure 22   Hoop and radial strain measurement geometries for SXRD.
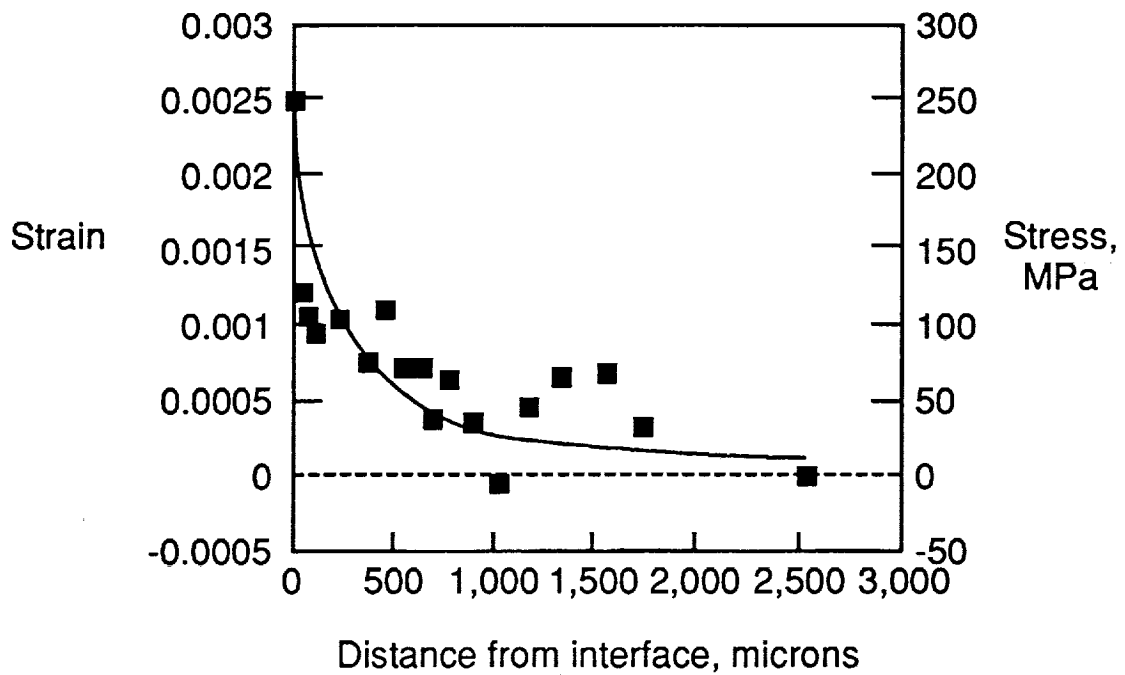
Figure 23   Residual hoop strain profile, single 800 micron Al_2O_3 fiber in CP Ti.
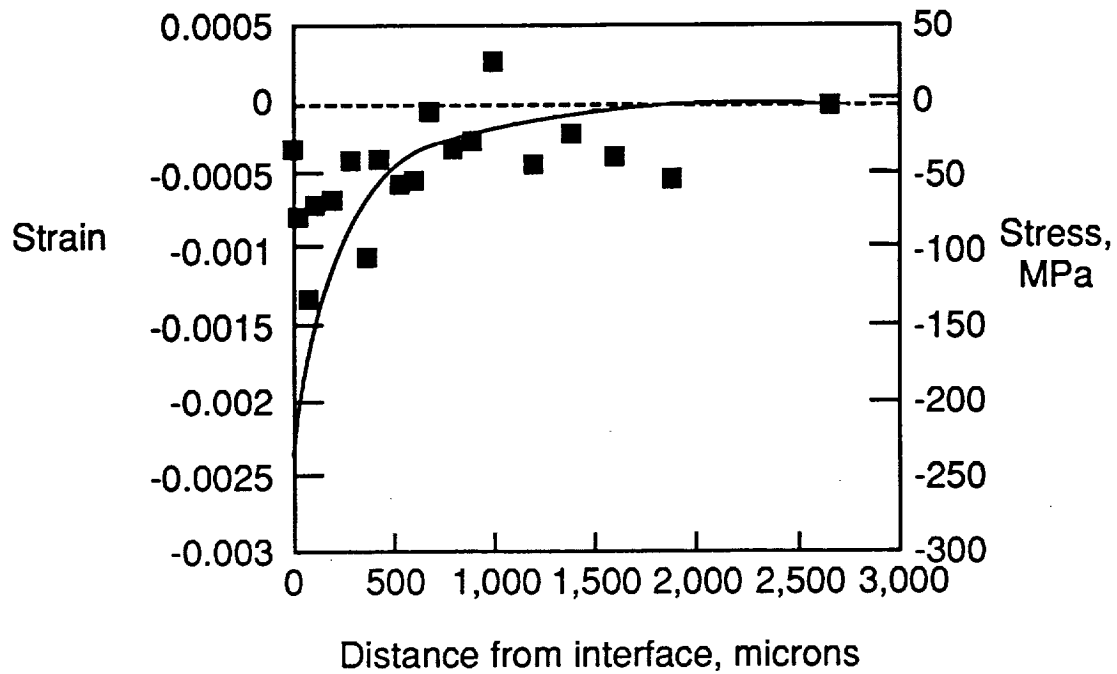
Figure 24 Residual radial strain profile, single 800 micron Al_2O_3 fiber in CP Ti.
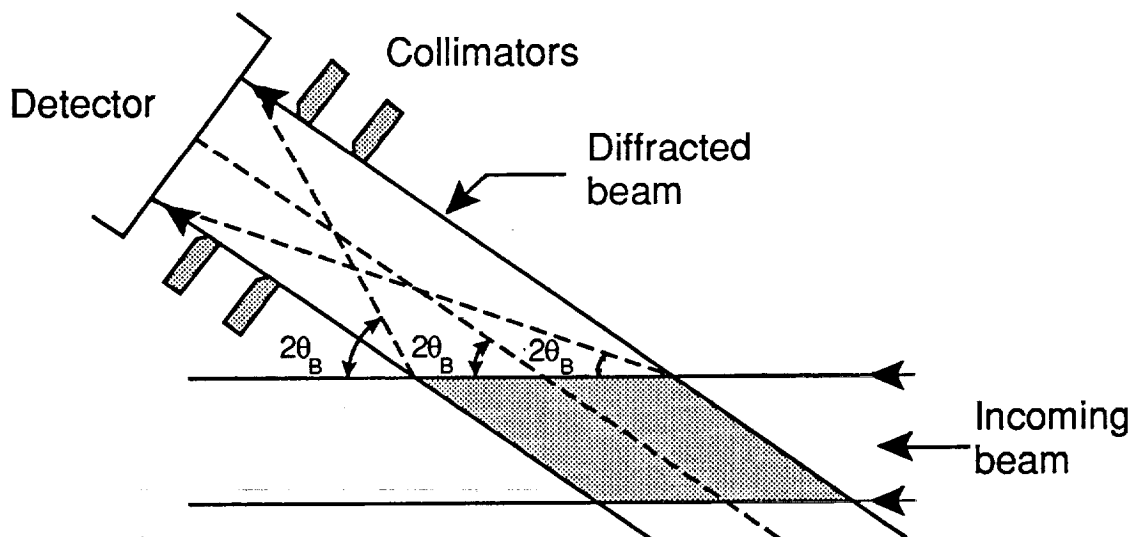
Figure 25 X-ray probe schematic showing maximum variations in θ arising from diffraction from the edges of the diffracting volume.

33
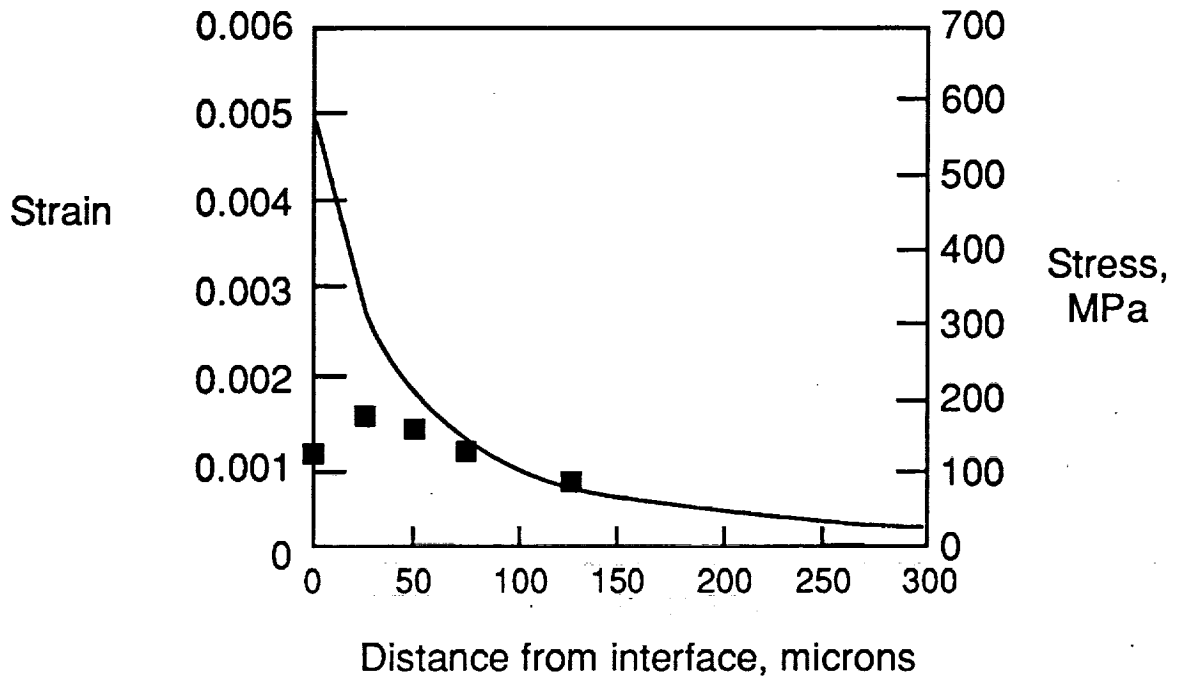
Figure 26 Residual hoop strain profile, single fiber SCS-6/Ti-24Al-11Nb sample.
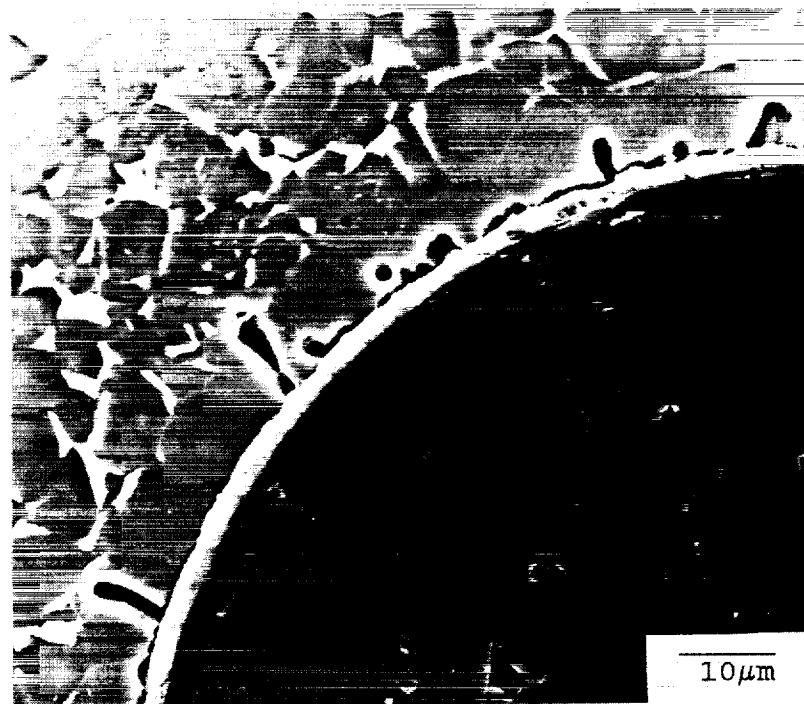
Figure 27 Fiber/matrix interface of single fiber SCS-6/Ti-24Al-11Nb composite of Figure 7. Note cracks in beta-depleted layer next to fiber.
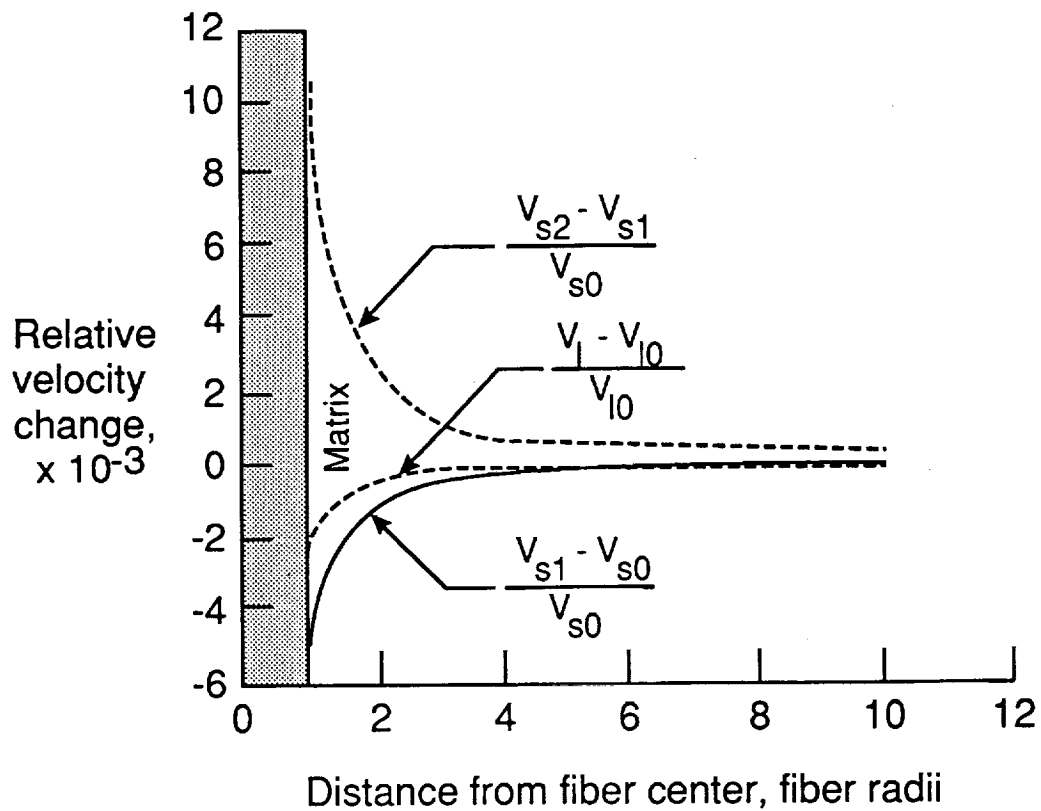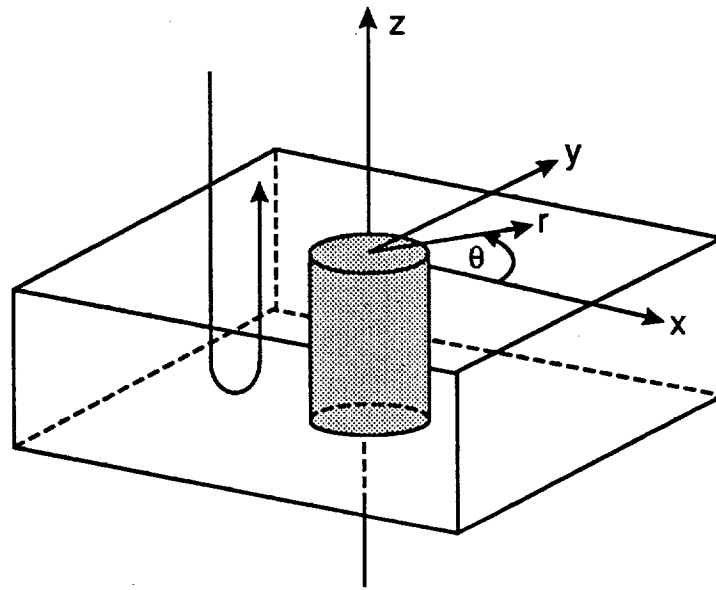
Figure 28   US pulse-echo configuration and predicted wave velocity differences.
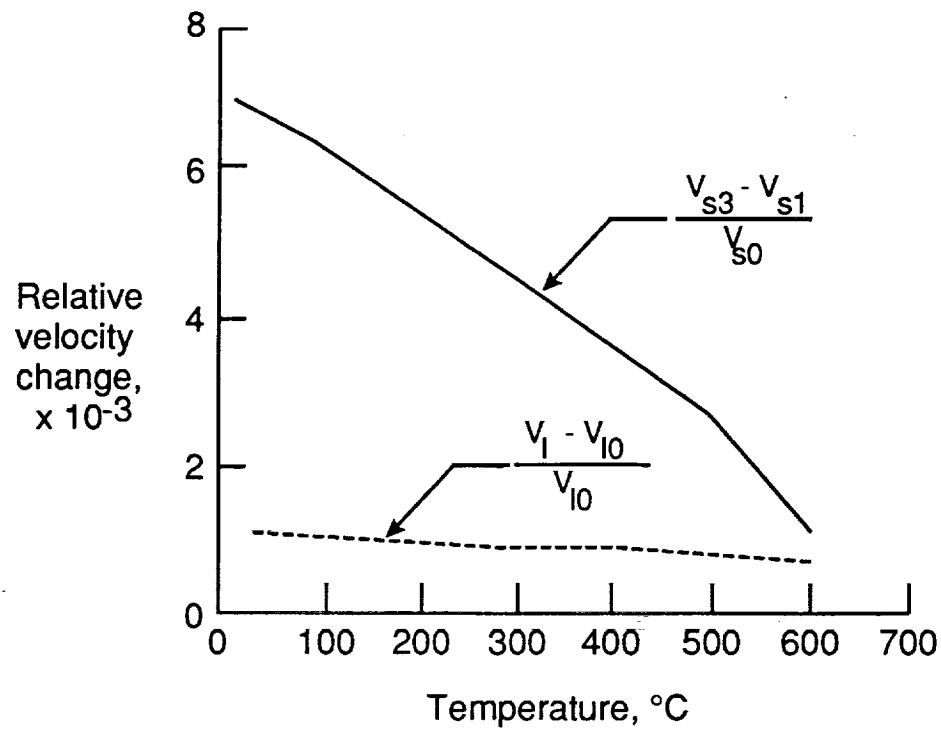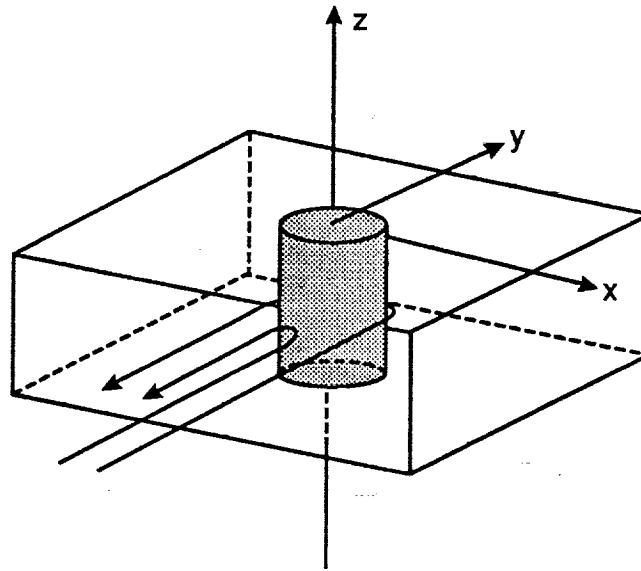
Figure 29   US "creeping-ray" method and predicted wave velocity differences.

approaches will require further efforts in order to determine whether they represent experimentally viable approaches.

4.1.5 Results of Analytical Modeling

Thermal residual stresses and strains predicted for the IPD SCS-6/Ti-24Al-11Nb composite studies in Task 1 are shown in Figure 30 as a function of radial position (distance outward from the axis of the fiber). Because of the radial symmetry of this model, there is no circumferential variation in any of the stresses. As stated above, the stresses in the fiber are compressive and independent of radial location. The longitudinal (z) stresses are considerably higher than the radial (r) and circumferential (θ) stresses. The matrix longitudinal stress and strain are also independent of r, but are tensile in sign. Note that because of equilibrium condition imposed, the radial stress at the fiber-material interface is the same in the fiber and matrix, and the radial stress at the outer radius is zero. Finite element analysis of similar composites (Saigal et al., 1992) shows general similarity of predictions; the stresses now become somewhat dependent on circumferential position, and only the average instead of the local radial matrix stress goes to zero at the outer boundary of the symmetry element. For the material properties and consolidation temperature assumed, the model predicts a small amount of yielding (about 0.24% strain) in the matrix of SCS-6/Ti-24Al-11Nb.

The average longitudinal and transverse stresses and strains predicted by the concentric cylinder model for the IPD SCS-6 Ti-24Al-11Nb composite are given in Table 2 in comparison with the experimental values obtained. These averages were obtained by taking the z, r, and θ coordinate stresses in each cylinder ring, transforming them to a rectangular z, x, and y coordinate system, and then averaging over the volume of each phase (fiber, or matrix). For cases in which plastic flow was observed, the strains reported are elastic strain, since this is what is sensed by the diffraction experiments. In the fiber, the average longitudinal and transverse stresses and strains are the same as the local values shown in Figure 30, since the stresses and strains are predicted to be uniform throughout the fiber. The same is true for the matrix longitudinal stresses and strains. In the matrix transverse direction, however, the radial dependence of stress and strain causes the average values to differ from the local values. In addition, the averaging is done in an x, y, z coordinate system to be consistent with the way the neutrons travel through the composite. Thus at some points the radial components are in the x-direction and at other points the hoop components are in the x-direction. Thus the average transverse values are not simply related to the local values.

Comparison of Table 2 and Figure 30 shows that the average matrix transverse stresses are predicted to be tensile reflecting the dominance of the hoop component over the radial component, and the average matrix transverse strains are predicted to be compressive.
Note that even though the average transverse matrix strain is slightly negative, the average transverse stress is positive because of the strong Poisson effects from the large axial matrix strain component. This effect comes from the Hooke's Law relationship between strain (measured by neutron diffraction) and stress (calculated using elastic constants):

$$\sigma_L^i = \frac{v^i E^i}{(1+v^i)(1-2v^i)} (\varepsilon_L^i + \varepsilon_T^i + \varepsilon_N^i) + \frac{E^i}{(1+v^i)} (\varepsilon_L^i) \quad\ldots\ldots\ldots\ldots\ldots(1a)$$
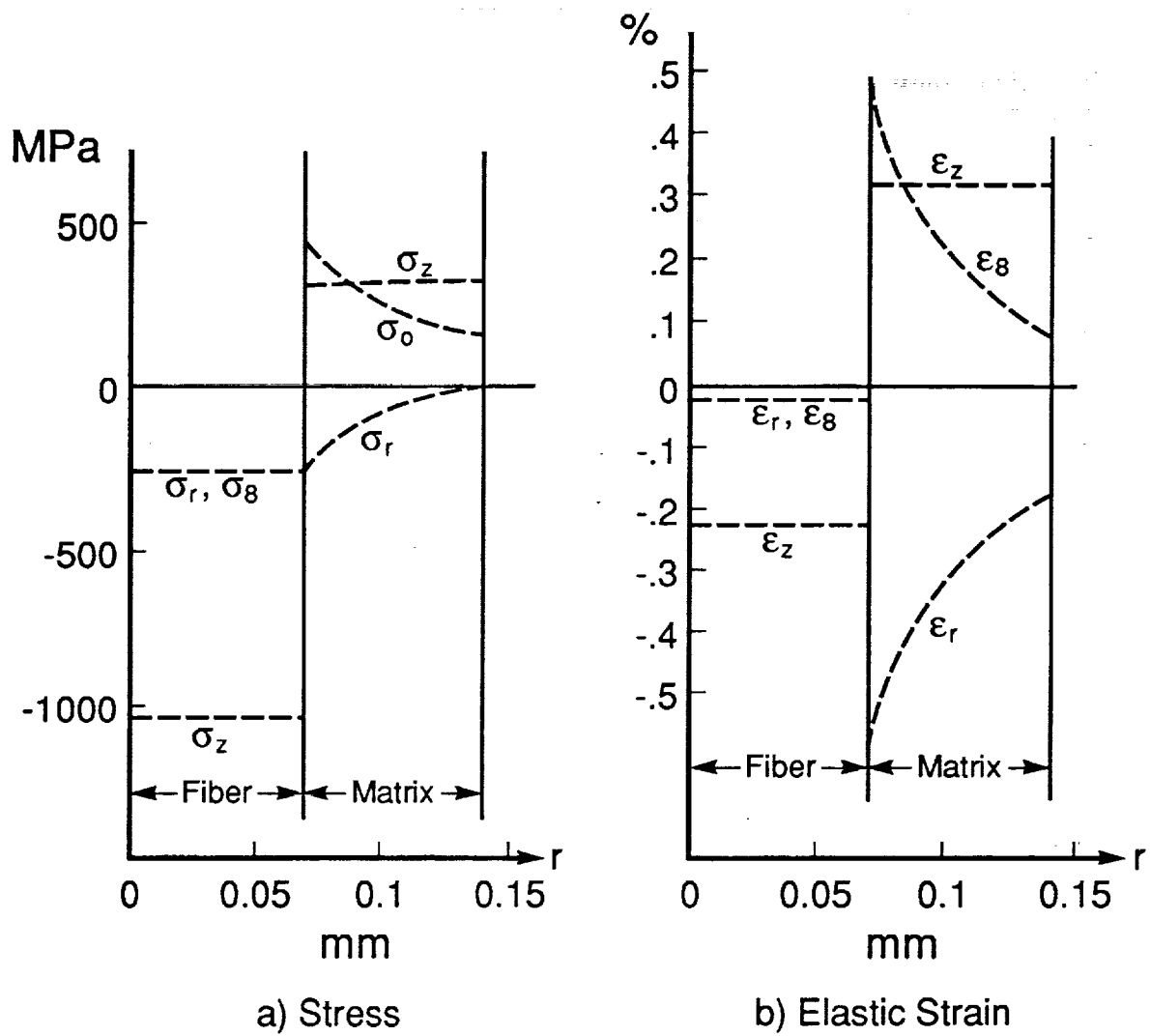
Figure 30   Fiber and Matrix Stresses and Strains Calculated by
Concentric Cylinder Model for SCS-6/Ti24Al-11Nb (Vf = .25).

$$\sigma_T^i = \frac{v^i E^i}{(1+v^i)(1-2v^i)} (\varepsilon_L^i + \varepsilon_T^i + \varepsilon_N^i) + \frac{E^i}{(1+v^i)} (\varepsilon_T^i) \quad ....(1b)$$

Here, σ_L^i and σ_T^i are the average longitudinal and transverse stresses, respectively, listed in Table 2 for the fibers (i = f) and matrix (i = m) phases. E^i and v^i are the elastic constants at room temperature listed in Table 1, and $\varepsilon_L^i, \varepsilon_T^i$, and ε_N^i are the average measured strains in either the fiber (i = f) or matrix (i = m) in the three principal material directions: longitudinal, transverse, and through-thickness. It was assumed that the composite was transversely isotropic, so $\varepsilon_N^i = \varepsilon_T^i$. If ε_L^i is much larger than ε_T^i, as it is in most of the cases here, then the first term in Equation 1b will dominate the value of σ_T^i. Thus even if ε_T^i is slightly negative, σ_T^i can be positive.

4.1.6 Comparison of Results and Selection of Method

Comparison of XRay and ND

The Xray and ND methods can be compared through the measurements on SCS-6/Ti-24Al-11Nb (Table 2). Only matrix measurements can be compared because of the inability of the Xray method to detect fiber strains. In the longitudinal direction the xray and ND results are fairly close (differing by a strain of 0.05% with a likely experimental error of +/- 0.03% strain). The transverse strains are quite different in magnitude and sign (tensile for Xray, compressive for ND). This difference is quite likely due to the difference in volume of the composite sampled: the Xray method senses only the outer surface, while the ND method averages the whole volume. In the outer surface of the composite (relatively far from the fibers), the transverse direction stresses and strains (rectilinear coordinate system) are more likely to be representative of the θ direction in Figure 30, i.e., tension, while in averaging the whole volume regions representing both θ (tension) and r (compression) will be seen resulting in a net stress or strain near zero. In addition, the ND method has the advantage of giving information about the fiber without ambiguities about the effect of removing matrix material layers. The fiber transverse stress measurements, given in Table 2, are a direct measurement of the interfacial radial stress, which is a significant parameter in many mechanical property models. The ND method does, however, require a separate stress-free reference specimen in order to obtain the unstressed lattice parameter, and thus is more sensitive to subtle variations in experimentation. Overall, however, the ND method appears to be accurate and useful.

Comparison of Experimental and Analytical Results

Comparison of the ND and Analytical columns in Table 2 indicates generally good agreement between the two. Looking in more detail, the strains and stresses observed in the fiber by the neutron diffraction method are typically slightly smaller (less compressive) than predicted by the concentric cylinder model. The matrix stresses also tend to be slightly higher (more tensile). While the difference for the transverse matrix values is large on a percentage basis, it is only slightly more than the likely experimental error in measurement. One check on the validity of the measurements can be obtained by comparing the fiber and matrix longitudinal stresses through the rule of mixtures. Since the next externally imposed stress on the composite is zero, the fiber, σ_L^f, and matrix, σ_L^m, longitudinal stresses should be related:

$$\sigma_L^f V_f + \sigma_L^m (1 - V_f) = 0 \qquad (2)$$

Performing this check for the neutron diffraction data shows that the summation of Equation (2) gives a net stress of 17 MPa, a value that is within the experimental error of the measurements. Thus it appears that the experimental data are valid, and that the average transverse stresses are in actuality slightly higher than predicted by the concentric cylinder model used. Results of finite element calculations of residual stresses in the same composites performed by Saigal et al. (1992) show better agreement of the predicted matrix transverse stresses with the experimental measurements and support this view.

Based on these results and the selection criteria presented in Section 2.2.4, the neutron diffraction method was selected for use in Task 2.

4.2 Task 2 - Measurement of Stresses in IMC

4.2.1 Results of As-Fabricated SCS-6/Ti-24-11

The results from the as-fabricated foil-fiber SCS-6/Ti-24Al-11Nb composite are shown in Table 3a and Figure 21. The SCS-6/Ti-24Al-11Nb composite shows somewhat lower fiber strains and stresses than reported for the IPD composite studied in Task 1, but higher matrix values, especially in the transverse direction. Except for the transverse matrix values, the differences are small and are within experimental error, although the analytical results presented below suggest that the differences may be real. The difference in transverse strains between the IPD and foil-fiber materials are so large as to require other explanation. Perhaps the strong crystallographic typically present in foils and absent in IPD material is reponsible for this.

A temperature dependent experiment was also carried out on this material. Lattice parameters for various crystallographic directions were measured by ND as a function of temperature from room temperature to 900C parallel and perpendicular to the fiber axis. The strains obtained are shown in Figure 31. The strains parallel to the fiber show the expected decrease with increasing temperature up to 800C where they essentially vanished. The transverse direction matrix strains do not go to zero at 800C, however, suggesting that some unaccounted for factor such as crystal texturing exists, and that the actual transverse matrix strains are much lower (by about 0.001) than shown in Figure 31.

40
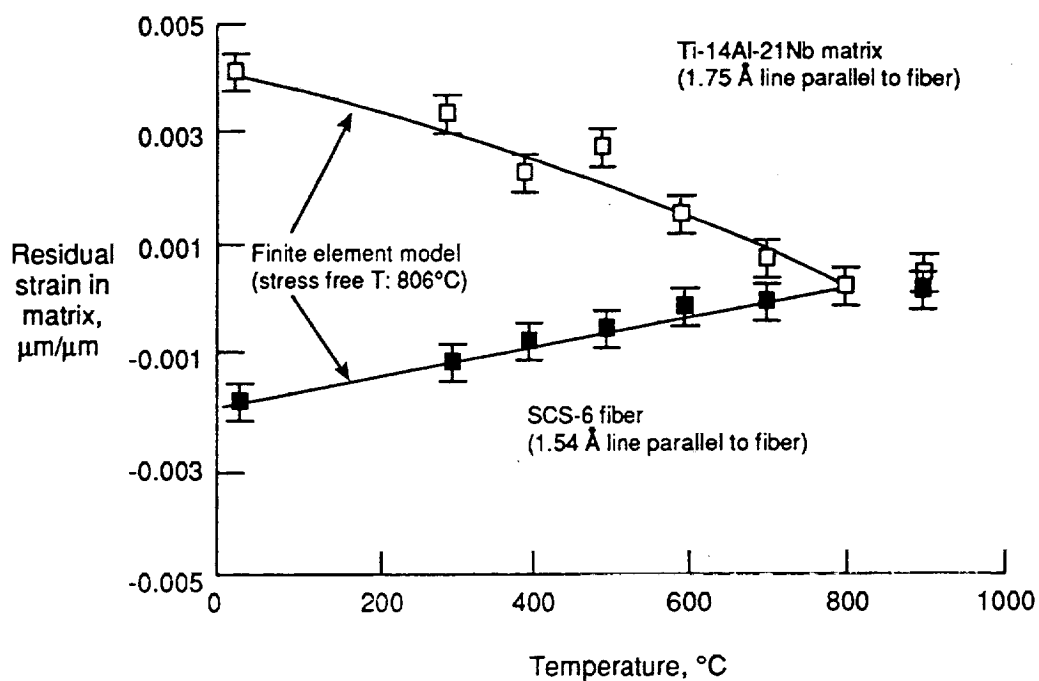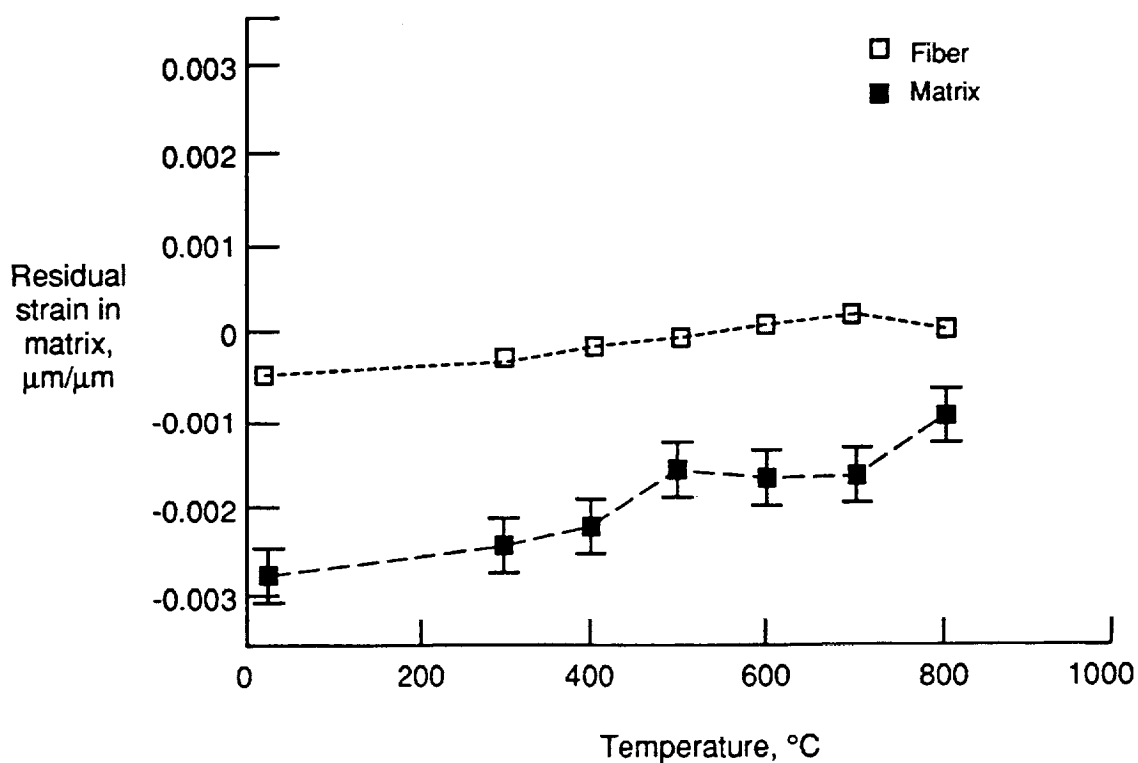
Figure 31   Thermal Strains Determined by ND in SCS-6/Ti-24Al-11Nb
as a Function of Temperature.

4.2.2 Results of Thermal cycled SCS-6/Ti-24Al-11Nb

The neutron diffraction measurements from this sample are shown in Table 3b and Figure 21. Compared to the as-fabricated results described in Section 4.2.1, all thermal strain values except those for the transverse fiber direction were reduced by 20 to 60%. The signs and the relative sizes of the strains remained similar to the as-fabricated material.

4.2.3 Results of Liq N$_2$ cooled SCS-6/Ti-24Al-11Nb

The results from this sample are shown in Table 3c and Figure 21. Fiber and matrix strains in the longitudinal direction were reduced by about 8 to 35% compared to the as-fabricated condition, while the transverse strains were unchanged. Thus the liquid nitrogen cooling was less effective in reducing the residual stress than thermal cycling was.

4.2.4 Results of W/NiAl

Residual strains were measured by neutron diffraction in this system; the average strains and stresses obtained are shown in Table 3d and Figure 32. Despite the larger thermal expansion and higher stress-free temperature compared to SCS-6/Ti-24Al-11Nb, the strains and stresses were actually lower. The trend among the stresses and strains were similar however: longitudinal tension in the matrix, longitudinal compression in the fiber, and transverse compression in the fiber and (on average) transverse tension in the matrix.

4.2.5 Results of Al$_2$O$_3$/NiAl

Neutron diffraction results for this system are also shown in Table 3e and Figure 32. Even though the thermal expansion coefficient of the alumina fiber is considerably greater than that of the tungsten fiber (i.e., a better match for the matrix), the residual stresses and strains are approximately the same as the W/NiAl system.

4.2.6 Results of Al$_2$O$_3$/NiFeAl

Neutron diffraction results for these two composites are shown in Table 3f and 3g and in Figure 32. Results are similar to those obtained for the Al$_2$O$_3$/NiAl system except that the fiber longitudinal strains (compression) are much greater, and the matrix longitudinal strains (tensile) are slightly greater. The matrix transverse strains are small but tensile in these materials as opposed to small but compressive in Al$_2$O$_3$/NiAl. The trend in fiber strains are related to volume fraction fiber; the smaller the fiber fraction the higher the strain in the fiber. Since the fiber longitudinal strains increase with decreasing volume fraction, it would be expected that matrix longitudinal strain would decrease. This is generally observed in comparing the NiAl and NiFeAl matrix materials.

42

Table 3
Measured and Calculated Average Thermal Strains and Stresses in IMC's

a) As-fabricated SCS-6/Ti-24Al-11Nb (V$_f$ = .30)

		ND	Analysis
Matrix	Longitudinal Strain (m/m)	+.0042	+.0031
	Transverse Strain (m/m)	-.0029	-.0004
	Longitudinal Stress (MPa)		+ 360
	Transverse Stress (MPa)		+ 100
Fiber	Longitudinal Strain (m/m)	-.0019	-.0015
	Transverse Strain (m/m)	-.0005	+.0002
	Longitudinal Stress (MPa)		- 725
	Transverse Stress (MPa)		- 205

b) Thermal cycled SCS-6/Ti-24Al-11Nb (V$_f$ = .30)

		ND	Analysis
Matrix	Longitudinal Strain (m/m)	+.0031	+.0025
	Transverse Strain (m/m)	-.0023	-.0003
	Longitudinal Stress (MPa)		+ 285
	Transverse Stress (MPa)		+ 85
Fiber	Longitudinal Strain (m/m)	-.0008	-.0011
	Transverse Strain (m/m)	-.0005	+.0001
	Longitudinal Stress (MPa)		- 575
	Transverse Stress (MPa)		- 175

c) Liquid nitrogen cooled SCS-6/Ti-24Al-11Nb (V$_f$ = .30)

		ND	Analysis
Matrix	Longitudinal Strain (m/m)	+.0039	+.0029
	Transverse Strain (m/m)	-.0029	-.0004
	Longitudinal Stress (MPa)		+ 320
	Transverse Stress (MPa)		+ 80
Fiber	Longitudinal Strain (m/m)	-.0012	-.0013
	Transverse Strain (m/m)	-.0005	+.0002
	Longitudinal Stress (MPa)		- 650
	Transverse Stress (MPa)		- 165

d) W/NiAl (V$_f$ = .35)

		ND	Analysis
Matrix	Longitudinal Strain (m/m)	+.0013	+.0017
	Transverse Strain (m/m)	-.0005	-.0001
	Longitudinal Stress (MPa)	+ 198	+ 345
	Transverse Stress (MPa)	- 36	+ 102
Fiber	Longitudinal Strain (m/m)	-.0012	-.0013
	Transverse Strain (m/m)	+.0001	+.0001
	Longitudinal Stress (MPa)	- 584	- 640
	Transverse Stress (MPa)	- 170	- 190

43

e) $Al_2O_3/NiAl$ ($V_f = .30$)

		ND	Analysis
Matrix	Longitudinal Strain (m/m)	+.0014	+.0014
	Transverse Strain (m/m)	-.0004	-.0002
	Longitudinal Stress (MPa)	+ 240	+ 295
	Transverse Stress (MPa)	+ 6	+ 80
Fiber	Longitudinal Strain (m/m)	-.0011	-.0015
	Transverse Strain (m/m)	+.0003	+.0000
	Longitudinal Stress (MPa)	- 445	- 690
	Transverse Stress (MPa)	+ 47	- 190

f) $Al_2O_3/NiFeAl$ (10% V_f)

		ND	Analysis
Matrix	Longitudinal Strain (m/m)	+.0022	+.0014
	Transverse Strain (m/m)	+.0005	-.0003
	Longitudinal Stress (MPa)	+ 730	+ 220
	Transverse Stress (MPa)	- 305	+ 42
Fiber	Longitudinal Strain (m/m)	-.0040	-.0044
	Transverse Strain (m/m)	+.0002	+.0002
	Longitudinal Stress (MPa)	- 1825	- 1980
	Transverse Stress (MPa)	- 280	- 380

g) $Al_2O_3/NiFeAl$ (6% V_f)

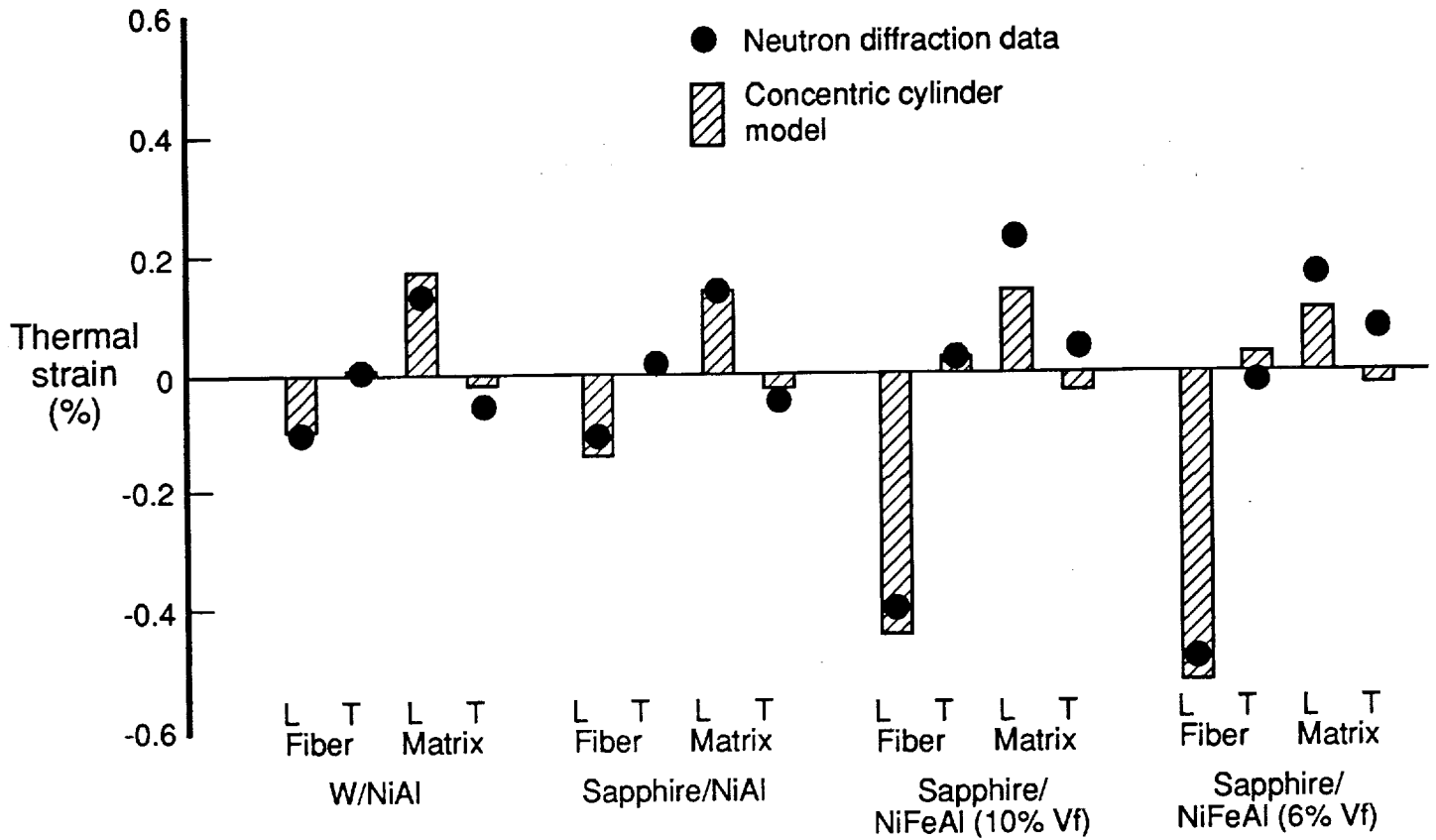|		ND	Analysis
Matrix	Longitudinal Strain (m/m)	+.0017	+.0010
	Transverse Strain (m/m)	+.0008	-.0002
	Longitudinal Stress (MPa)	+ 437	+ 145
	Transverse Stress (MPa)	+ 343	+ 25
Fiber	Longitudinal Strain (m/m)	-.0047	-.0052
	Transverse Strain (m/m)	-.0001	+.0003
	Longitudinal Stress (MPa)	- 2220	- 2305
	Transverse Stress (MPa)	- 610	- 410

44

Figure 32   Thermal Strains in Nickel Aluminide Composites Measured
by Neutron Diffraction vs. Concentric Cylinder Model.

4.2.7 Analytical Model Results and comparisons

The average longitudinal and transverse stresses and strains predicted by the concentric cylinder model for the composites studied are given in Table 3 in comparison with the experimental values obtained. For systems in which plastic flow was observed, the strains reported are elastic strain, since this is what is sensed by the diffraction experiments.

Predictions of strains and stresses for the foil-fiber SCS-6/Ti-24Al-11Nb material are shown in Table 3a and were quite similar to those presented in section 3.1.5 for IPD SCS-6/Ti-24Al-11Nb. The fiber stresses and strains were slightly smaller in magnitude, and the matrix stresses and strains were slightly larger. This is due to the slightly higher fiber volume fraction in the foil-fiber material (0.32 vs. 0.25).

Concentric cylinder model predictions were also performed for the two NiAl matrix composites using the properties shown in Table 1 and Figure 2. The predicted average stresses and elastic strains are shown in Table 3b and c and Figure 32. Unlike the SCS-6/Ti-24Al-11Nb system, both of these composites show extensive yielding in the NiAl matrix during cooldown. Figure 33 shows the predicted radial distribution of stress and strain in Al_2O_3/NiAl after cooling to RT. The matrix longitudinal stress is reduced near the fiber due to yielding and the stress levels are generally less than for SCS-6/Ti-24Al-11Nb. In the W fiber system the matrix shows more total strain than in the Al_2O_3 fiber system due to the higher thermal expansion mismatch. However, because of matrix yielding the predicted final matrix stresses in these systems are limited by the flow stress of the matrix at room temperature, and are thus more similar than expected without plasticity. Note that the model calculations for the two NiAl composites were performed at slightly different volume fraction fibers to match the different fiber fractions actually present in the samples tested. The higher fiber fraction in the W fiber composite tends to lower the fiber stresses since there is more fiber present to balance the matrix stresses. The fiber fraction difference has a minor effect on the matrix stresses because of matrix yielding.

The predicted stresses and strains for the NiFeAl matrix composites are shown in Table 3d and e. Like the NiAl composites, these materials show substantial yielding in the matrix. The matrix stresses are predicted to be lower in the NiFeAl composites, which must reflect the influence of volume fraction fiber, since the NiFeAl yield strength is higher than that of NiAl. This influence is seen more clearly in comparing the 10% and 6% V_f materials in Table 3d and e, respectively. The fiber stresses in the NiFeAl composites are predicted to be substantially greater than for the other composites; this also is a volume fraction effect.

Comparison of the ND and Analytical columns in Table 3 indicates generally good agreement between the two. This is illustrated in Figure 34. Of the 32 pairs of strain measurements and predictions, 18 are within 10% or are within the estimated experimental error of 0.03% strain. Another 11 are within 20%. Three pairs of data deviate by more than 100%, and all of these are for matrix transverse strain. Thus it can be said that 50% of the time the experimental and analytical results agreed with 10%.

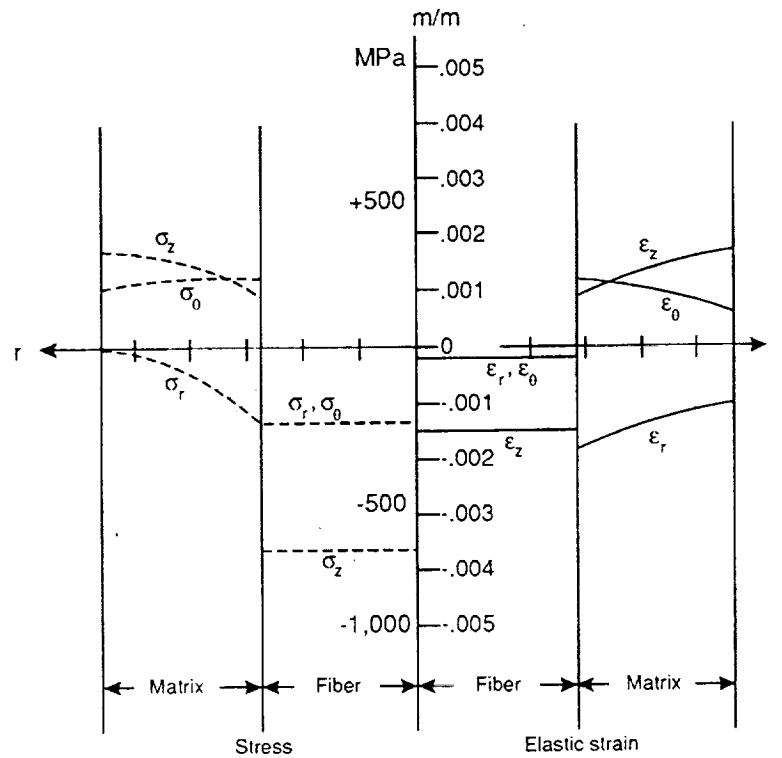46

Figure 33   Fiber and Matrix Stresses and Elastic Mechanical Strains
Calculated by Concentric Cylinder Model for $Al_2O_3/NiAl$
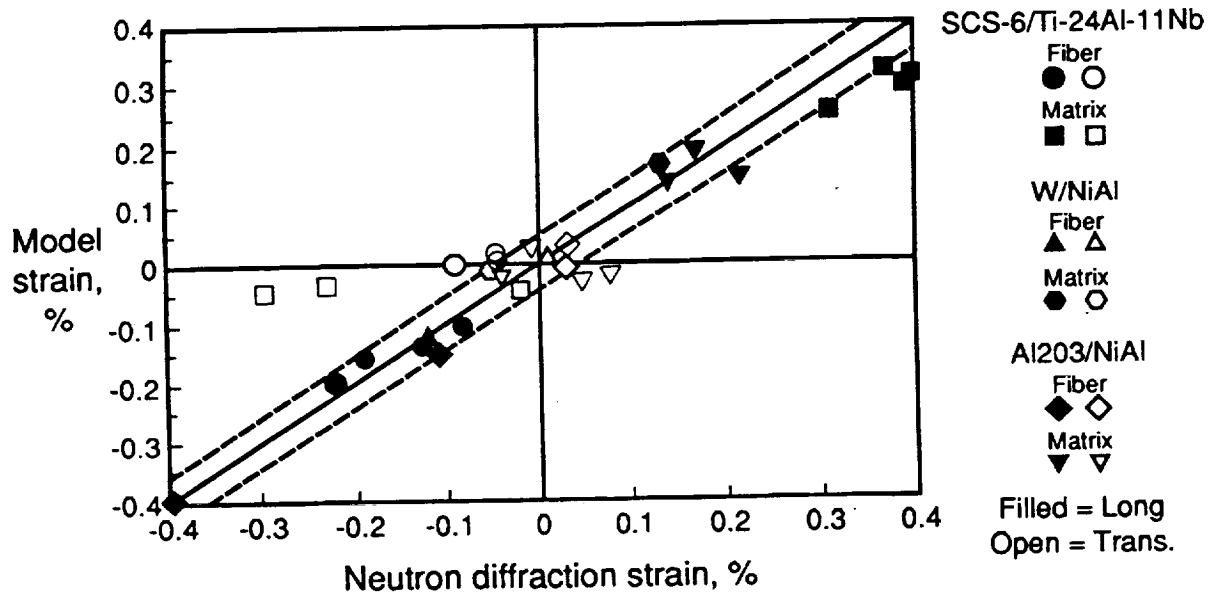$(V_f = .30)$.

Figure 34   Comparison of Neutron Diffraction Results with Concentric
Cylinder Model Predictions.

Sensitivity Study

Because of the uncertainty in some of the material properties assumed for the concnetric cyclinder model calculations, a small parametric study was conducted to determine the sensitivity of the model prediction to what were felt to be the key material variables: fiber volume fraction, matrix yield strength, matrix thermal expansion coefficient, and matrix elastic modulus. This study also had the benefit of examining the effect of changing one of these variables at a time, since most of the real materials systems examined had several different variables changed at once. To simplify the data comparisons, only one Ti-base system, foil-fiber SCS-6/Ti-24Al-11Nb, and one Ni-base system, $Al_2O_3/NiAl$, were studied. Each of the selected variables were changed in these two systems up or down by reasonable variations felt likely to be possible. The variables and their ranges were: volume fraction fibers, V_f ($\pm$ 0.05); matrix coeffecient of thermal expansion, α ($\pm$ 10%); matrix yield strength, YS ($\pm$ 15%); and matrix modulus, E ($\pm$ 5%). α, YS, and E were changed uniformly across the full temperature range used in the analyses. These variations, and the average fiber and matrix stresses and elastic strains predicted are shown in Table 4. Plots of the percentage change in stress resulting from each change in independent variable are shown in Figure 35. Figure 35a shows that the longitudinal fiber stress in both composite systems is most sensitive to a 0.05 change in V_f The change is negative because an increase in Vf causes a decrease in fiber stress. Variation in longitudinal matrix stress, Figure 35b, is different for the two systems studied. In the SCS-6/Ti-24Al-11Nb system, longitudinal matrix stress is most sensitive to α, while in $Al_2O_3/NiAl$, it is most senstivie to YS, with α a close second. This difference between systems is probably due to the difference in matrix yielding. The Ti-matrix system is mostly elastic, while the NiAl-matrix system shows extensive yielding, thus increasing its dependence on yield stress. In the transverse direction, the variation in both the fiber, Figure 35c, and matrix, Figure 35d, transverse stresses were most dependent on V_f and YS in both composite systems.

Some caution must be used in assigning relative importance to the different variables since the calculations incorporated different levels of each variable which were felt to be probable ranges of uncertainty. Nevertheless, it is interesting that in all cases but one V_f was an important variable, and in three cases YS was important. E never showed up as a significant variable, and α was dominant only once.

4.3 Task 3 - Effects of Thermal Stresses on Mechanical Properties

4.3.1 Results of Thermomechanical Processing Trials

Residual Stresses

The residual stresses in SCS-6/Ti-24Al-11Nb samples after the thermomechanical processing described in Section 2.4.2 are shown in Table 5. These stresses were measured by Xray diffraction at Lambda Research, Inc. These are stresses parallel to the fiber direction, in the direction of stress during tensile testing. The matrix stress in the as-fabricated condition ranged from 400 to 470 MPa, somewhat higher than obtained from other measurements on this type composite (Cox et al, 1990, and Jayaraman and Rangaswamy,1991). As expected, thermal cycling did reduce the matrix longitudinal stress, to about 380 MPa. Cooling under tension reduced matrix stresses further: in one case to 295 MPa, in another to 360 MPa. Finally, cooling

48

Table 4
Results of Analytical Study of the Sensitivity
of Residual Stresses and Strains
to Likely Variations in Input Model Parameters

Matrix	Fiber	Fab temp	Param.	Param. Value	Average Residual Elastic Mechanical Strain (%)				Average Residual Stress (ksi)			
					Matrix		Fiber		Matrix		Fiber	
					Axial	Trans	Axial	Trans	Axial	Trans	Axial	Trans
F3 Ti-14Al-21Nb	SCS-6	1850F	Vol.Frac.	0.33	+0.313	-0.038	-0.145	+0.018	+51.8	+14.8	-105.1	-30.0
				0.28	+0.297	-0.041	-0.174	+0.024	+48.4	+12.8	-124.4	-32.9
				0.38	+0.326	-0.035	-0.121	+0.013	+54.6	+16.6	-89.1	-27.1
			Matrix CTE	Baseline	+0.313	-0.038	-0.145	+0.018	+51.8	+14.8	-105.1	-30.0
				Baseline-10%	+0.269	-0.030	-0.125	+0.014	+44.9	+13.5	-91.2	-27.4
				Baseline+10%	+0.349	-0.046	-0.162	+0.021	+57.0	+15.4	-115.7	-31.2
			Matrix YS	Baseline	+0.313	-0.038	-0.145	+0.018	+51.8	+14.8	-105.1	-30.0
				Baseline-15%	+0.298	-0.040	-0.138	+0.018	+48.7	+13.1	-98.8	-26.6
				Baseline+15%	+0.321	-0.036	-0.149	+0.017	+53.5	+15.9	-108.7	-32.3
			Matrix E	Baseline	+0.313	-0.038	-0.145	+0.018	+51.8	+14.8	-105.1	-30.0
				Baseline- 5%	+0.321	-0.038	-0.141	+0.017	+50.4	+14.4	-102.2	-29.3
				Baseline+ 5%	+0.307	-0.038	-0.149	+0.018	+53.1	+15.0	-107.8	-30.5
NASA NiAl	Al2O3 (Sapphire)	2300F	Vol.Frac.	0.25	+0.140	-0.020	-0.183	-0.000	+40.4	+10.2	-121.2	-30.7
				0.20	+0.134	-0.022	-0.232	+0.004	+38.0	+8.7	-152.1	-35.0
				0.30	+0.148	-0.019	-0.151	-0.004	+43.5	+12.1	-101.4	-28.2
			Matrix CTE	Baseline	+0.140	-0.020	-0.183	-0.000	+40.4	+10.2	-121.2	-30.7
				Baseline-10%	+0.129	-0.018	-0.169	-0.002	+37.6	+9.9	-112.7	-29.8
				Baseline+10%	+0.153	-0.023	-0.198	+0.000	+43.9	+10.9	-131.7	-32.6
			Matrix YS	Baseline	+0.140	-0.020	-0.183	-0.000	+40.4	+10.2	-121.2	-30.7
				Baseline-15%	+0.129	-0.019	-0.168	+0.000	+37.1	+9.3	-111.2	-27.8
				Baseline+15%	+0.154	-0.022	-0.201	-0.002	+44.7	+11.6	-134.0	-34.8
			Matrix E	Baseline	+0.140	-0.020	-0.183	-0.000	+40.4	+10.2	-121.2	-30.7
				Baseline- 5%	+0.148	-0.021	-0.184	-0.000	+40.8	+10.4	-122.3	-31.3
				Baseline+ 5%	+0.136	-0.019	-0.186	-0.000	+41.2	+10.5	-123.6	-31.6
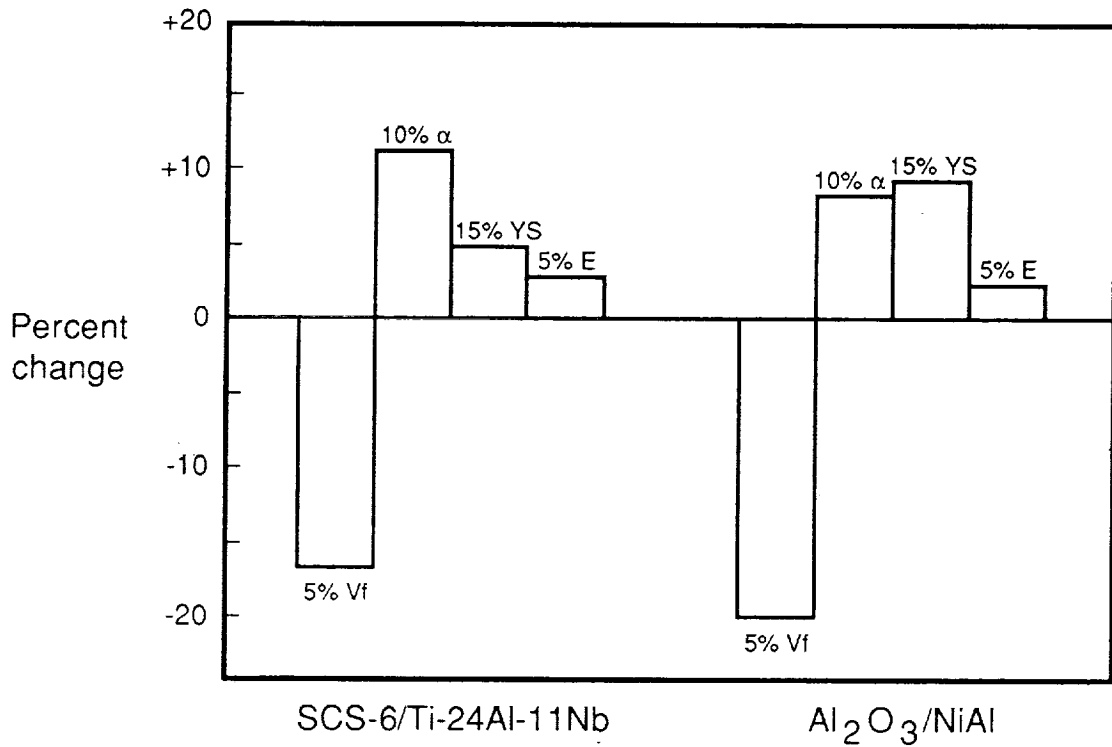
a) Longitudinal Fiber Stress
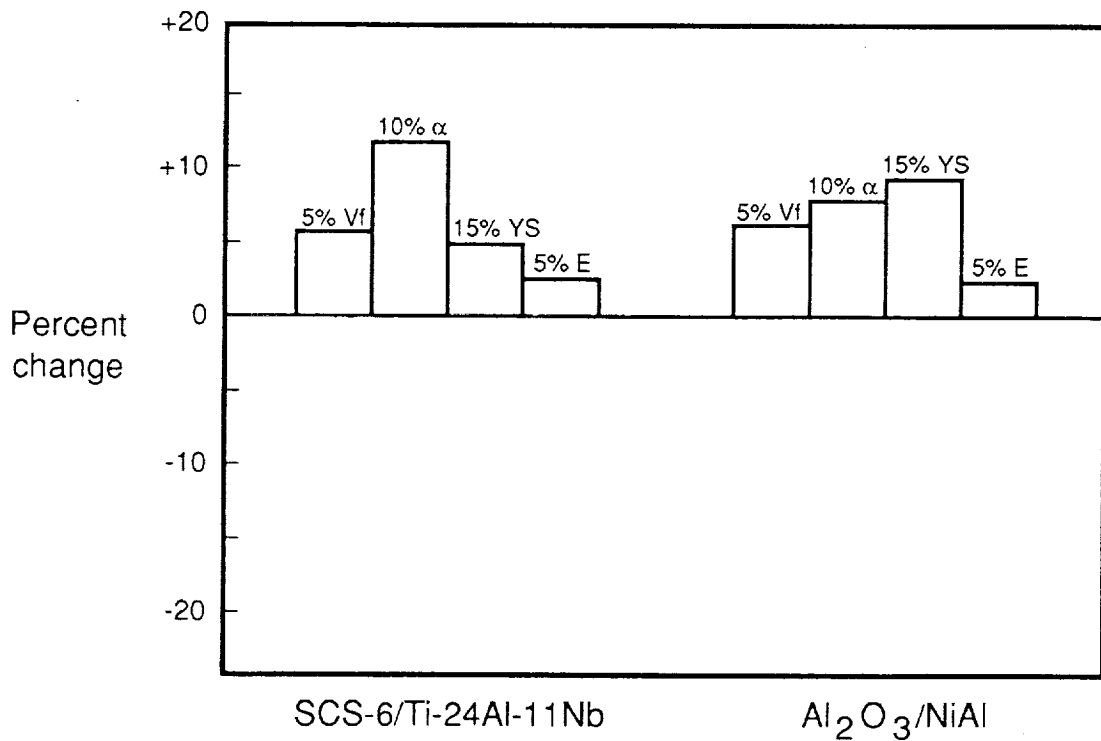
b) Longitudinal Matrix Stress

Figure 35   Sensitivity Analysis Results Showing Effects of Changes in
V_f, α, YS, and E on Residual Stress in SCS-6/Ti-24Al-11Nb and
Al_2O_3/NiAl.
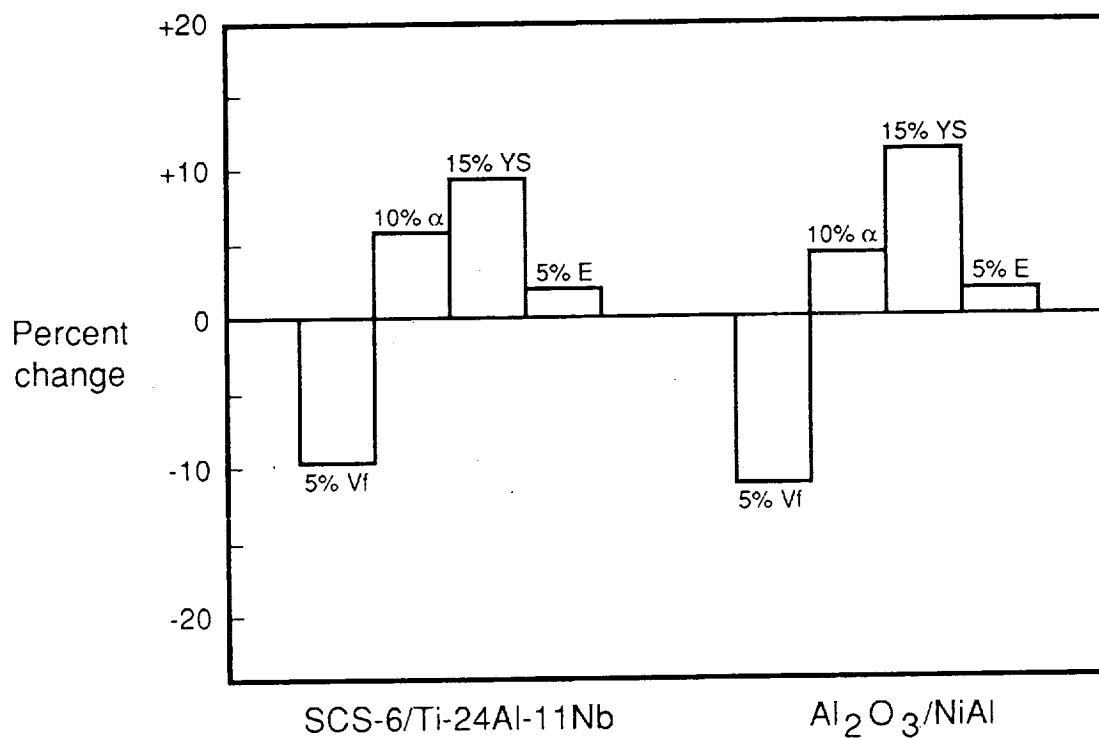
c) Transverse Fiber Stress

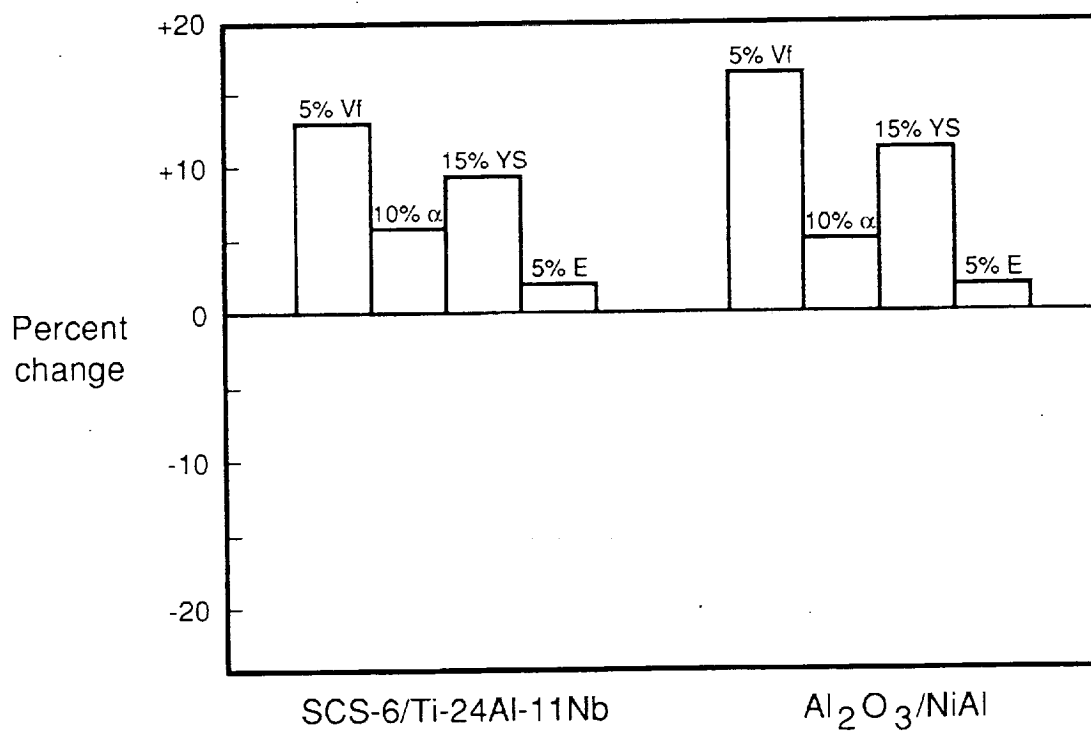d) Transverse Matrix Stress

Figure 35   Sensitivity Analysis Results Showing Effects of Changes in V_f, α, YS, and E on Residual Stress in SCS-6/Ti-24Al-11Nb and Al_2O_3/NiAl.

under compression increased matrix stress levels as expected, to about 535 MPa.
Overall, a range of residual matrix stress of about 200 MPa was produced by the
various treatments.

Table 5
Residual Matrix Longitudinal Stresses
in SCS-6/Ti-24Al-11Nb after Thermomechanical Treatment

Treatment	Residual Stress (MPa)
As-fabricated	399 ± 100
	463 ± 60
	470 ± 105
Free thermal cycled	376 ± 34
	383 ± 35
Cooled under tension	295 ± 63
	360 ± 18
Cooled under compression	555 ± 26
	520 ± 41

4.3.1.2 Modeling of Thermomechanical Processing

The "cooled in tension" and "cooled in compression" thermomechanical processes
described in Section 3.4.2 were analyzed using the concentric cylinder model
described in Section 3.2.3. Fiber and matrix properties were the same as used for
the as-fabricated foil-fiber SCS-6/Ti-24Al-11Nb composite studied in Task 2 (Section
4.2.7). Fiber fraction was taken as 0.25 and 850C was used as the stress-free
temperature. The model was taken step-wise through each of the two processes: 1)
heat to 850C (remove residual stresses); 2) apply longitudinal load (689MPa tension
or 275MPa compression) at 850C; 3) cool under load to 21C; 4) remove load. The
stresses in the composites at each step are shown in Table 6. For the "cooled in
tension" process, the average longitudinal stresses are zero on heating to 850C
since this was used as the stress free temperature. After applying the load at 850C,
the fiber and matrix go into tension, although the fiber carries the largest portion
of the load since the matrix is weak at 850C. After cooling under load the
longitudinal stresses redistribute, the matrix stress increasing and the fiber stress
decreasing due to their different thermal contraction. Both fiber and matrix stress
at this point are higher than for free cooling to room temperature (compare to
Figure 30), and matrix yielding is predicted to have occurred. Removing the
mechanical load at 21C reduces the fiber and matrix stress substantially. Note,
however, from Table 7 that the radial interface stress (-243MPa) is but little
changed from the value calculated for free cooling from fabrication (-248MPa).
The final stress distribution predicted for the composite element is shown in
Figure 36a. The fluctuation in matrix hoop and axial stress near the interface are
the result of matrix yielding during cooldown under load.
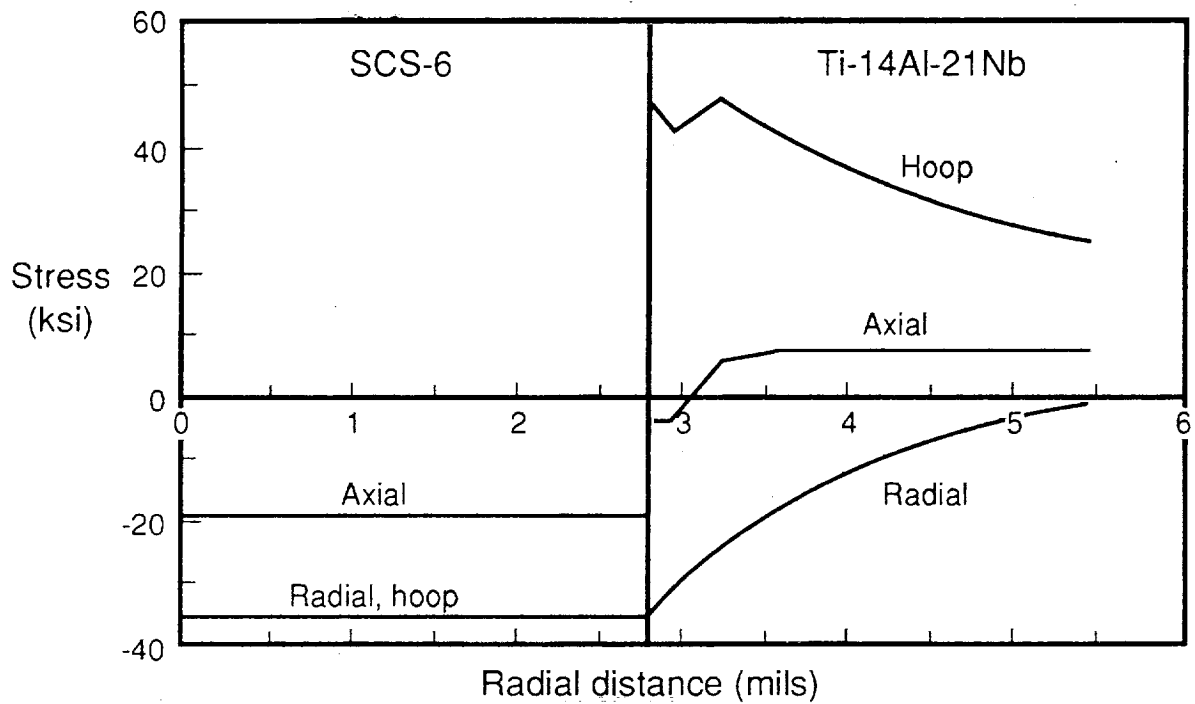
a) Cooled in Tension from 850C
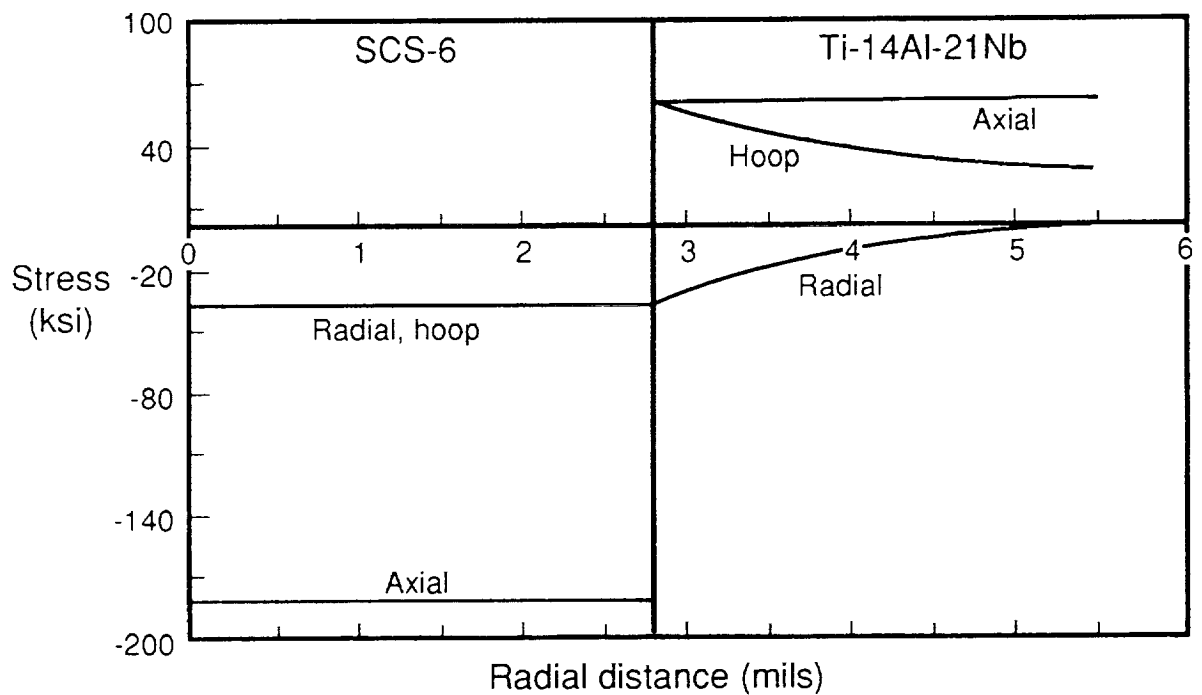
b) Cooled in Compression from 850C

Figure 36   Residual Stresses in SCS-6/Ti-24Al-11Nb After
           Thermomechanical Processing as Predicted by Concentric
           Cylinder Model

53

Table 6
Longitudinal Fiber and Matrix Stresses Predicted during Thermomechanical Processing

a) Cooled in Tension

Temp (^{o}C)	Composite stress (MPa)	Matrix stress (MPa)	Fiber stress (MPa)
850	0	0	0
850	689	113	2419
21	689	418	1504
21	0	44	-133

b) Cooled in Compression

Temp (^{o}C)	Composite stress (MPa)	Matrix stress (MPa)	Fiber stress (MPa)
850	0	0	0
850	-276	-45	-968
21	-276	265	-1900
21	0	415	-1244

Table 7
Final Interface Stress State (in Matrix) Calculated by Concentric Cylinder Model

Process	σ_r (MPa)	σ_θ (MPa)	σ_z (MPa)
Cooled in Tension	-243	+325	-26
Cooled in Compression	-258	+430	+415
As Fabricated	-206	+278	+238

The changes in fiber and matrix stress with process step during the "cooled in compression" process are also shown in Table 6 and the final stress distribution is given in Figure 36b. Note that longitudinal fiber and matrix stresses are predicted to be increased over those established by free cooling. However, as in the "cooled in tension" case, the radial fiber-matrix interface stress (Table 7) is hardly changed at all (-258MPa).

4.3.2 Results of Tensile Tests

4.3.2.1 Experimental Results

Tensile test results for samples subjected to these treatments are shown in Table 8 and ultimate tensile strength is plotted against matrix residual stress level in Figure 37. As-fabricated specimens had an average strength of about 1180 MPa, which is on the low side but within the typical range for this material (Gambone, 1990). (Rule of Mixtures suggests strength should be about 1400 MPa, assuming a fiber strength of 3450 MPa, a matrix strength of 550 MPa, and a fiber fraction of 0.3.) Thermally cycled material had a higher strength, averaging about 1365 MPa, and the cooled under tension material had a similar average strength, 1345 MPa. In comparison, the cooled under compression material, with the highest matrix residual stress, had the lowest tensile strength, 1070 MPa. Thus there is a distinct correlation between matrix residual stress and composite tensile strength: the lower the matrix residual stress, the higher the composite strength. (The strength of the cooled under tension material is not higher than the thermal cycled material; this will be discussed below.)

Table 8
Longitudinal Tensile Properties of
SCS-6/Ti-24Al-11Nb for Various Thermomechanical Treatments

Treatment	UTS (MPa)	Modulus (GPa)
As Fabricated	1225 1100	208 163
Free Thermal Cycled	1310 1420	206 189
Cooled in Tension	1420 1269	184 172
Cooled in Compression	1220 917	176 154

In addition to the differences in ultimate strength, the stress-strain curves had different appearances as a function of residual stress level. Figure 38a shows the stress-strain response typical of lower levels of residual stress (free thermal cycled) for which a fairly long region of fully elastic reponse was seen before the stress-strain curve bent over due to matrix yielding or cracking. The stress-strain response for high levels of residual stress (cooled in compression) is illustrated in Figure 38b, and shows a significantly earlier bend-over of the curve.

Analytical Model

The effect of matrix residual stress on composite strength can be rationalized through the following model of composite strength, illustrated in Figure 39. Invoking equilibrium of forces, the residual stresses in the fiber direction (from either cooldown or process modification) must balance as follows:

$$\sigma_c = 0 = \sigma_f^r V_f + \sigma_m^r (1 - V_f) \qquad (3)$$

where σ_c is the external composite stress, σ_f^r is the residual stress in the fiber, σ_m^r is the residual stress in the matrix, and V_f is the fiber volume fraction. The
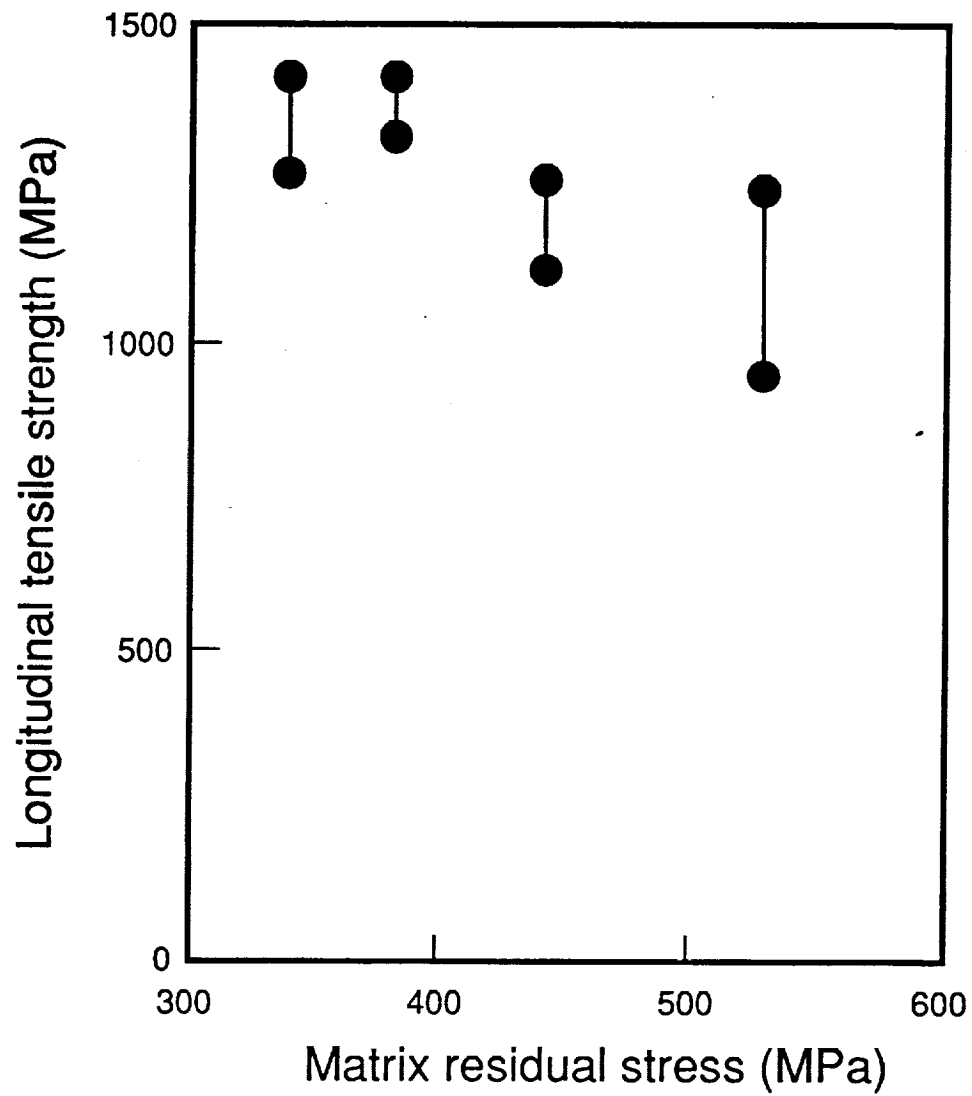
55

Figure 37 Influence of Thermal Residual Stress on Longitudinal
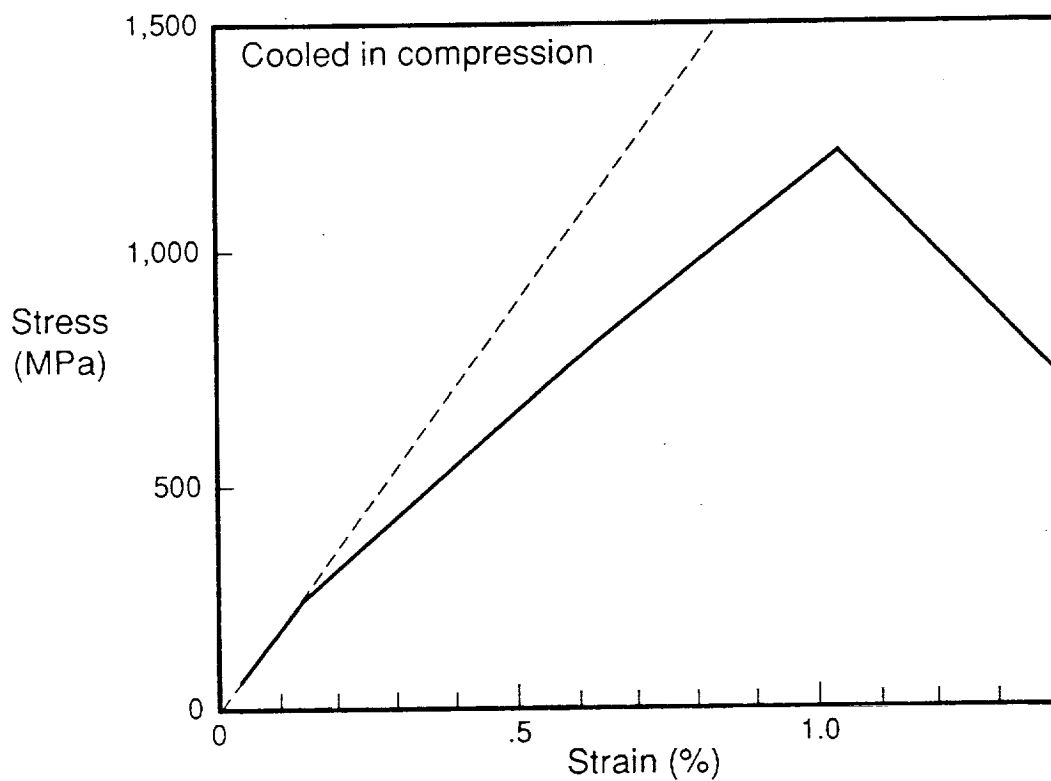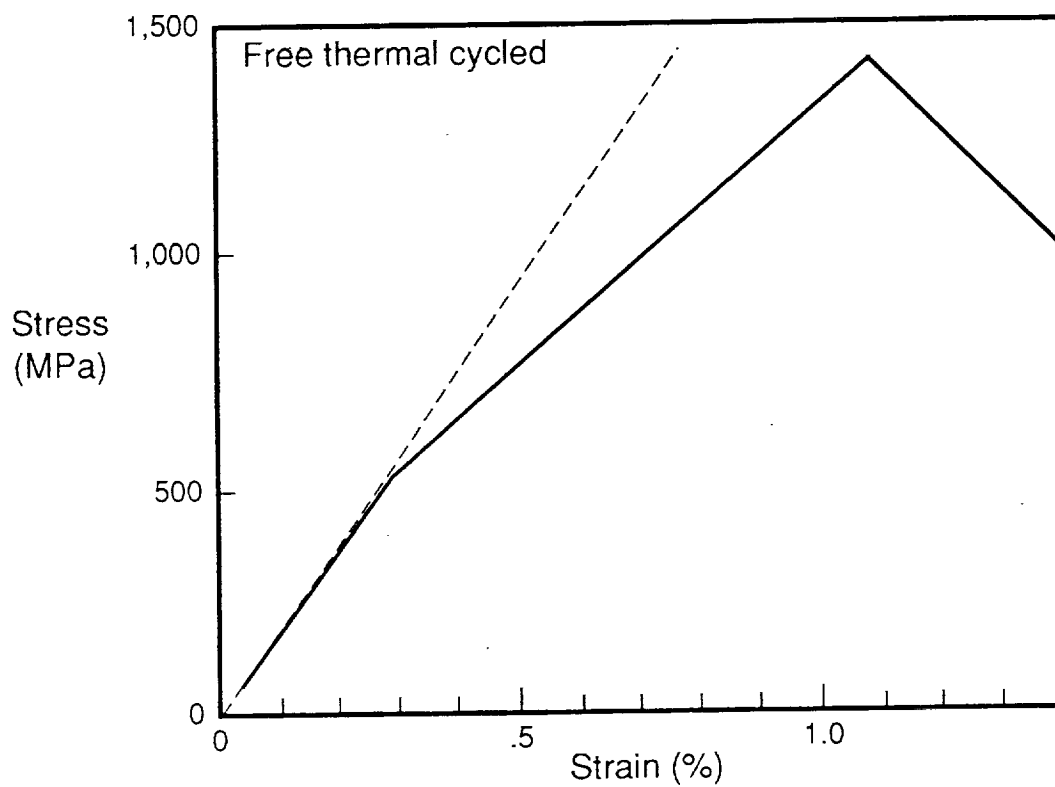Tensile Strength of SCS-6/Ti-24Al-11Nb.

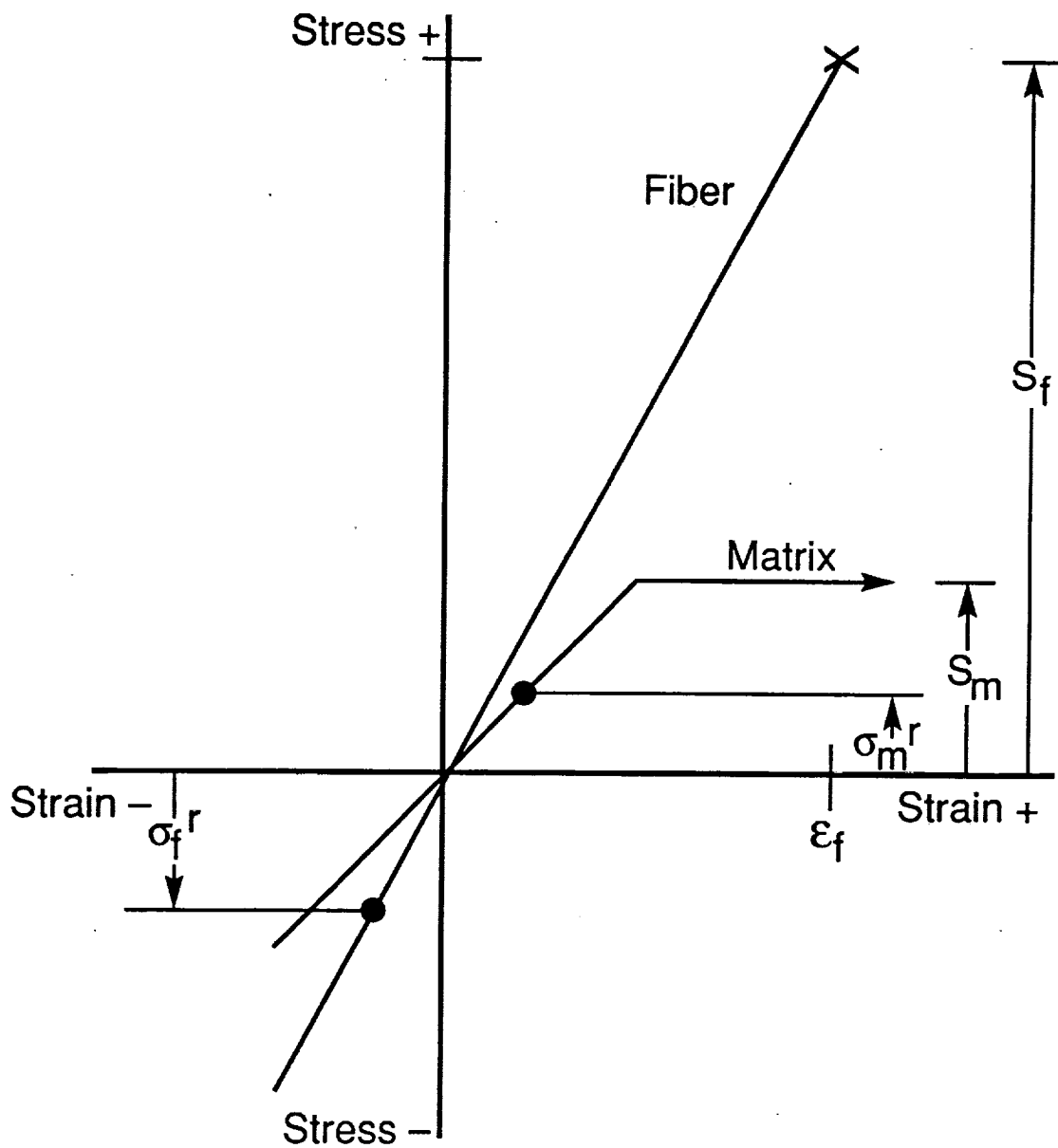**Figure 38** Shape of Tensile Stress-Strain Curves for Different Residual Stress levels.

Figure 39   Effect of Residual Stress on Longitudinal Composite
             Tensile Stress - Strain Response. High Matrix Ductility.

values of σ_f^r and σ_m^r are plotted in Figure 39 on the stress-strain curves for each material, and represent the starting point for mechanical loading. The effect of these residual stresses will depend on which constituent controls composite failure. One possible condition is that the fibers control failure; that is, the failure strain of the matrix is sufficiently greater than that of the fibers so that the fibers reach their failure strain first. Under this condition, the composite stress at failure, S_c, can be written, including the residual stress terms, as:

$$S_c = (S_f - \sigma_f^r) V_f + (S_m - \sigma_m^r) (1 - V_f) \qquad (4)$$

where S_f and S_m are the strength of the fiber and matrix, respectively, in freestanding form. Note that since the fiber residual stress, σ_f^r, is compressive (negative), the effective fiber strength $(S_f - \sigma_f^r)$ increases due to residual stresses. Note, however, that the effective matrix strength decreases. In fact, the positive contribution to composite strength due to the fiber residual strength, $\sigma_f^r V_f$, is exactly balanced by the loss of strength due to the matrix, $\sigma_m^r (1 - V_f)$, since these two are equal but opposite in sign from Equation 3. As a result, when the matrix is ductile, residual stresses should have no effect on composite strength.

Now consider the case when the matrix is not more ductile than the fiber, Figure 40. The same residual stress starting points are plotted for the fiber and matrix. Now, however, the factor controlling failure is the matrix strain to fracture, ϵ_m. The matrix residual stress places the matrix at a starting strain level of σ_m^r/E_m, where E_m is the matrix modulus. Thus the amount of strain capability remaining is $\epsilon_m - \sigma_m^r/E_m$. Since the strain in the matrix due to mechanical loading is the same as that in the fiber, the effective stress in the fiber at matrix failure is now $E_f(\epsilon_m - \sigma_m^r/E_m)$. This quantity is shown graphically in Figure 40, and is less than the fiber strength, S_f. Inserting this new effective fiber strength into Equation 4 gives:

$$S_c = (E_f[\epsilon_m - \sigma_m^r/E_m])V_f + (S_m - \sigma_m^r)(1 - V_f) \qquad (5)$$

Here the fiber and matrix residual stress terms do not cancel out; in fact, the σ_m^r terms in each part of the strength equation act to reduce composite strength. This equation, strictly speaking, is for matrix failure, and whether composite failure occurs simultaneously or after further load can depend on V_f and other factors such as whether matrix cracks propagate into the fibers or are diverted around them. Nevertheless, the onset of substantial matrix cracking will limit the composite strength to a value near V_fS_f, or about 1035 MPa. Thus if the matrix ductility is low, residual stresses should degrade the composite strength below what is normally termed "Rule of Mixtures" strength, with a lower limit of about V_fS_f.

4.3.2.3 Evaluation of Model

The SCS-6/Ti-24Al-11Nb composite tested here appears to be acting in the manner expected for a low ductility matrix. This is not too surprising, since ductility of Ti-24Al-11Nb at room temperature is generally quite low. This statement is supported by the post-test observation on the tensile specimens that multiple matrix cracking was commonly observed in the gage sections.
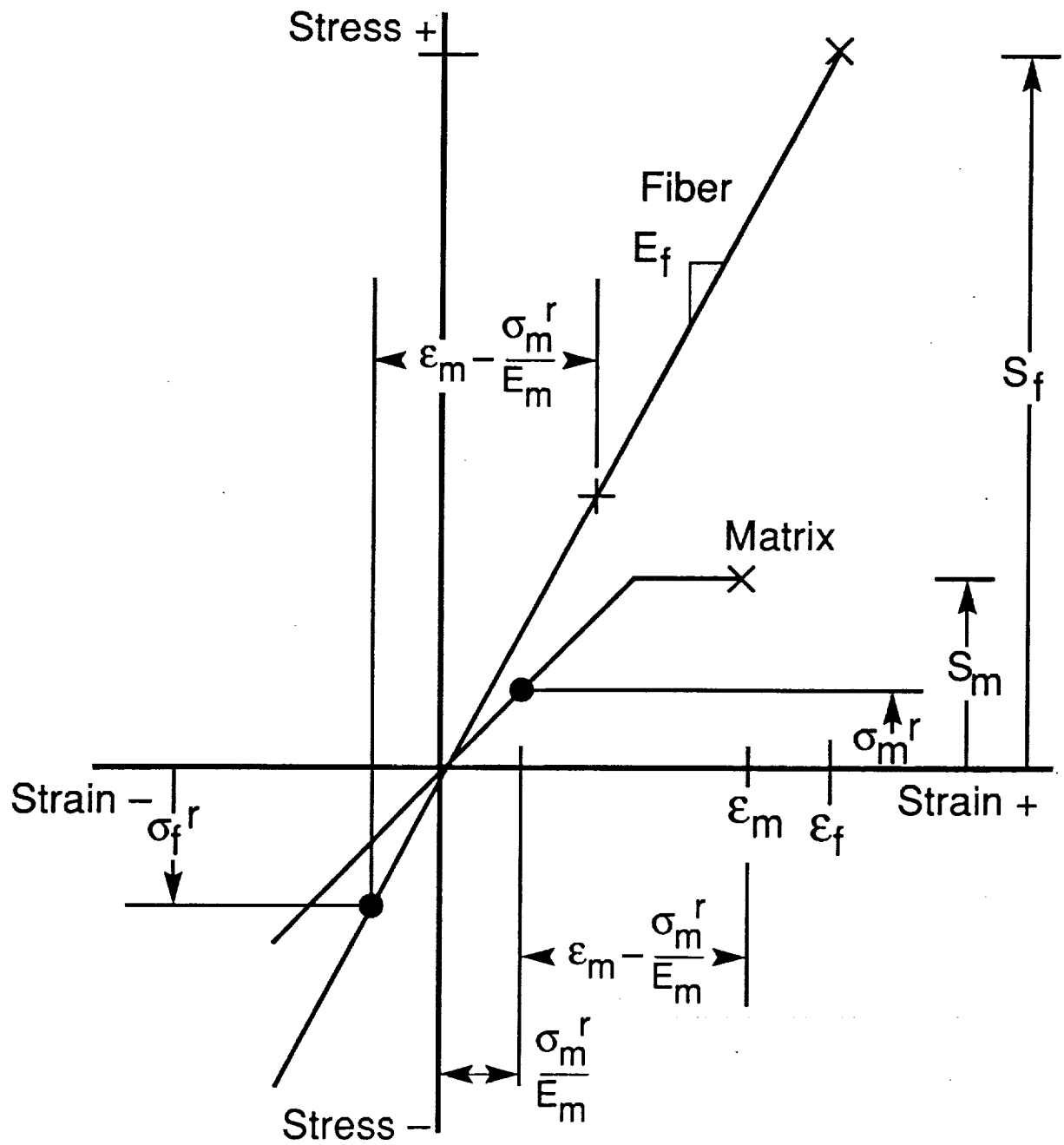
Figure 40   Effect of Residual Stress on Longitudinal Composite Tensile
Stress - Strain Response. Low Matrix Ductility.

The strength levels predicted by Equation 5 are highly sensitive to the value of ε_m. The ductility of the Ti-24Al-11Nb foil is likely to be approximately .01 to .02. If we assume $\varepsilon_m = .014$, and insert the extreme values of residual stress found in this study into Equation 5, we find that for $\sigma_m{}^r = 330$ MPa, $S_c = 1389$ MPa and for $\sigma_m{}^r = 530$ MPa, $S_c = 986$ MPa. Other parameters were set at $V_f = 0.3$, $S_m = 450$ MPA, and values for E_f and E_m from Table 1. Actual strengths measured (Table 8) were 1365 and 1070 MPa, respectively. The strengths calculated from Equation 5 show approximately the same dependence on residual stress as does the actual strengths, supporting the validity of Equation 5.

It is possible, if ε_m is large, to calculate strengths from Equation 5 greater than those obtained from Equation 4. These values should be considered invalid, since the matrix ductility is now large enough so that the more usual fiber controlled failure process described by Equation 4 limits the composite strength. In the present case, ε_m may be high enough so that for the lowest residual stress conditions (cooled under tension and thermally cycled) fiber controlled failure is occurring. This would explain the lack of difference in strength between these two conditions.

4.3.3 Results of Fiber Pushout Tests

4.3.3.1 Experimental Results

During fiber pushout testing load elongation behavior showed a relatively linear rise, a short load drop at debonding, and a gradual decrease of load, as illustrated in Figure 41. This is similar to other pushout results on SCS-6/Ti-24Al-11Nb. The average and standard deviation of the results for each treatment are shown in Table 9.

Table 9
Fiber Pushout Results

Treatment	Interface Shear Stength (MPa)
As Fabricated	86 ± 8
Free Thermal Cycled	62 ± 15
Cooled in Tension	137 ± 12
Cooled in Compression	59 ± 25

Post-test observation of the pushout specimens showed that the as fabricated and free thermal cycled fibers failed along the outer coating-reaction layer interface, Figure 42a. The cooled in tension fibers, however, failed along the fiber-inner coating interface, Figure 42b. The fibers in the cooled in compression sample appear to have failed at either the interface between the two coating layers, or at the outer coating-reaction layer interface. The higher interface strength in the cooled in tension specimen thus appears to be associated with the different failure mode observed.

22.43 (N) = 103.99 MPa
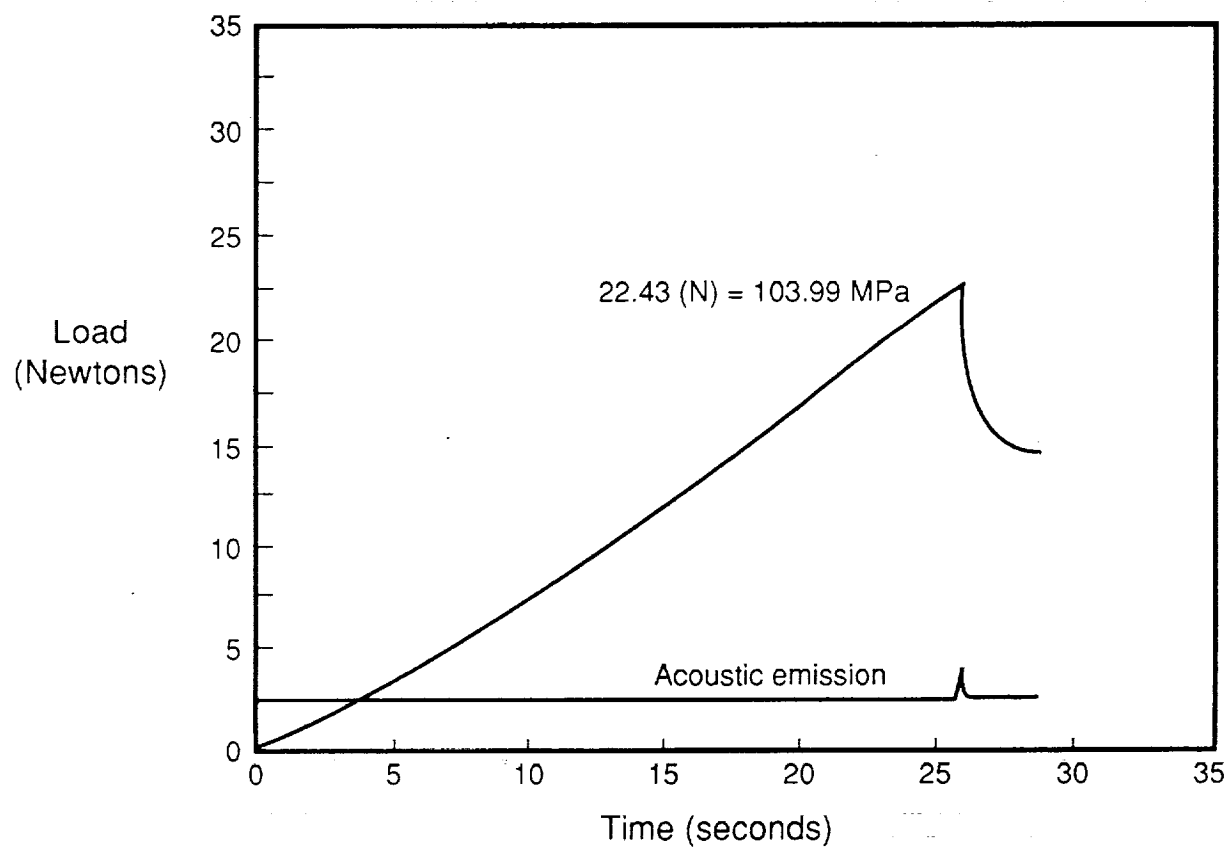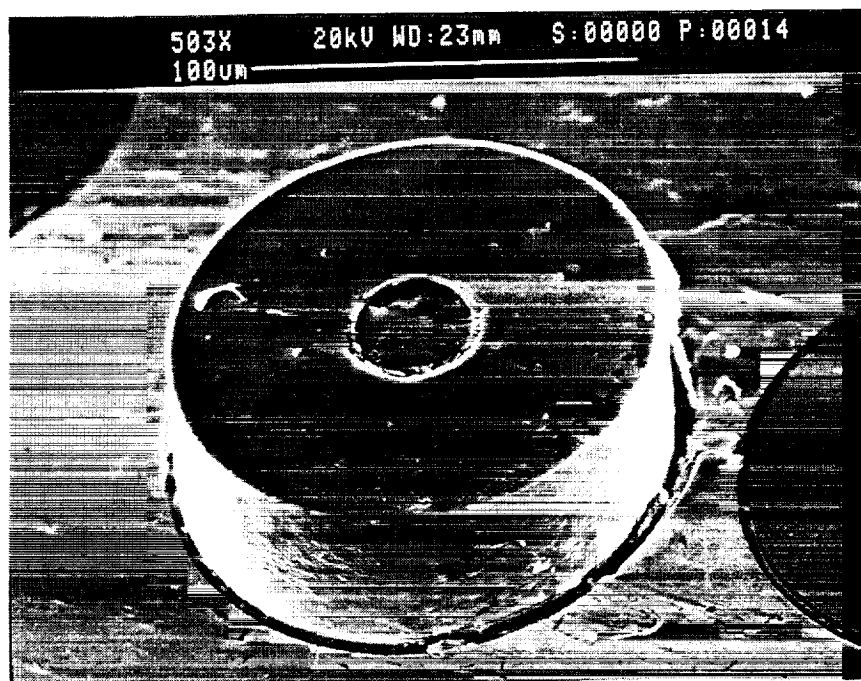
Acoustic emission

Figure 41   Typical Load-Time Response During Fiber Pushout Test

a) As-Fabricated, Showing Fiber Coating Retained on Fiber

b) Cooled in Tension, Showing Fiber Coating Retained on Matrix

Figure 42   Pushed out Fibers in SCS-6/Ti-24Al-11Nb Showing
Different Failure Morphologies.

4.3.3.2 Analytical Model

The simplest model for inteface shear strength assumes that the interface is frictionally bonded. This results in a simple dependence of the interfacial shear strength, τ_i, on the interfacial residual clamping stress, σ_r^r:

$$\tau_i = \mu \sigma_r^r \qquad\qquad (6)$$

where μ is the interface frictional coefficient.

4.3.3.3 Evaluation of Model

To test this model the measured interfacial strear strengths were plotted against the interfacial clamping stress. The slope of this plot should be positive linear, with a value equal to the friction coefficient. Since σ_r^r was not measured directly (only the longitudinal matrix stress was measured), it is assumed that σ_r^r is directly proportional to the longitudinal matrix stress, σ_m^r. This plot is shown as Figure 43, and shows that instead of increasing with σ_m^r, the interface strength decreases. This would imply a negative friction coefficient! This seems physically unrealistic so other effects must be interfering. Two possible explanations are:

1) The assumption that $\sigma_r^r \propto \sigma_m^r$ may not be valid. Results from analytical modeling of the modification of residual stress by the thermomechanical processing suggest that the change in radial interface stress caused by the processing could be negligible (Table 7).

2) The process of making thin samples for pushout testing may significantly alter the residual stresses from the as-processed state. Significant stress relief is expected at the cut specimen surfaces, and relief should occur at least one fiber diameter deep. Since the samples are only about five fiber diameters thick, a large portion of the clamping stresses may be removed or altered.

However, Ghosn, et al. (1992) have shown that although effect 2) will change absolute values of interface shear strength somewhat, the change should be proportional in all cases. Therefore effect 1) is the likely cause of the failure of the frictional model in this case.

4.3.4 Results of In-Plane Shear

Table 10
In-Plane Shear (Iosipescu) Test Results
SCS-6/Ti-24Al-11Nb at RT

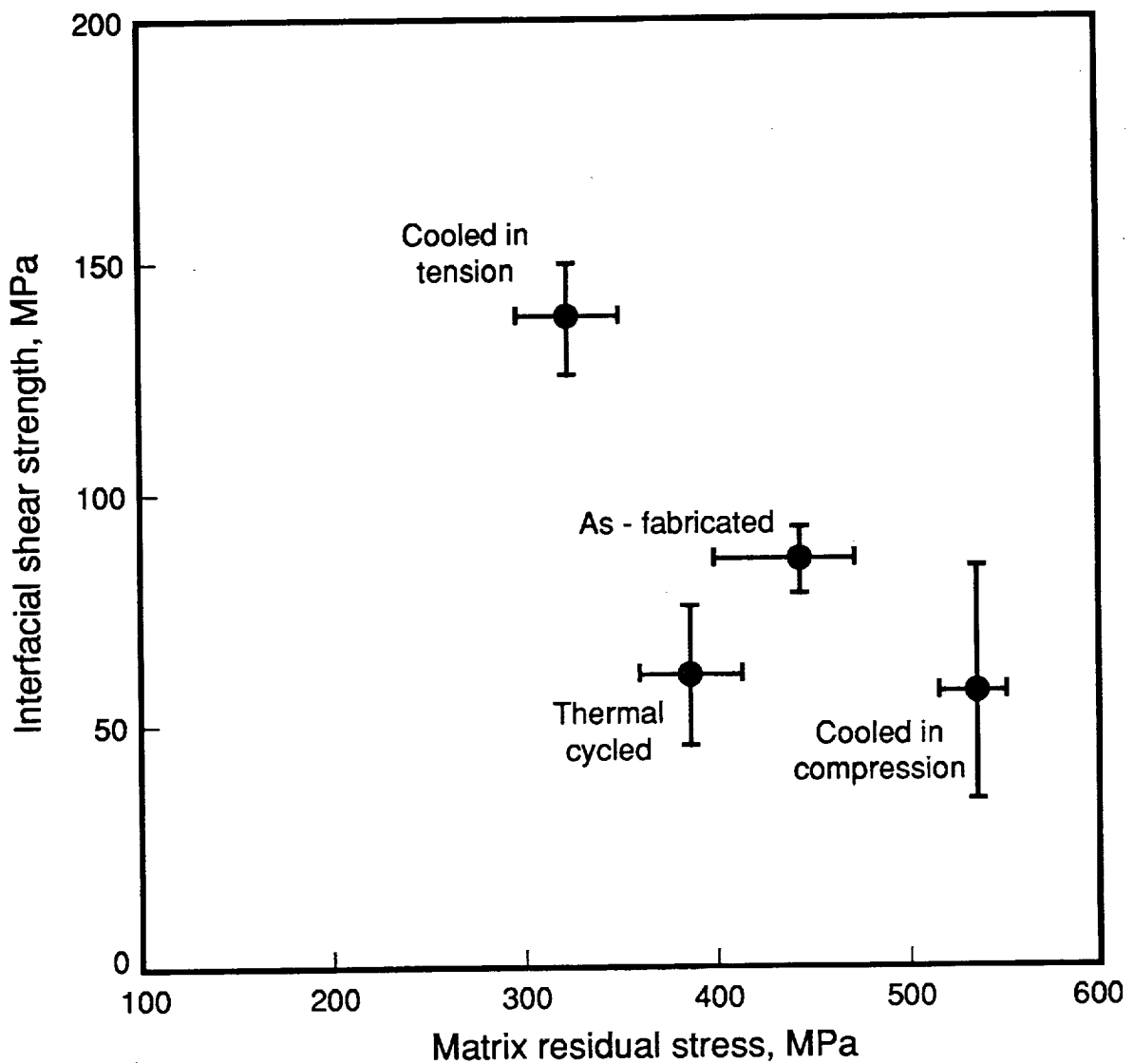| Process	Shear Yield Strength (MPa)
As Fabricated	269
	256
Free Thermal Cycled	233
	255
Cooled in Tension	257
	223
Cooled in Compression	227
	205

64

Figure 43 Correlation Between Fiber/Matrix Interfacial Shear-Strength
and Residual Matrix (Longitudinal) Stress

Results of the in-plane shear testing are shown in Table 10. In-plane shear testing produced stress-strain curves of the typical shape shown in Figure 44. The elastic modulus, G, averaged 91.0 GPa. Once yielded, the curve bent over rapidly to produce additional plastic deformation with little hardening. This is unlike the behavior seen for transverse tension in these composites (Nimmer, et al, 1991) where a bilinear region wass seen which can be attributed to fiber-matrix interface separation prior to large scale matrix plasticity.

Since many of the specimens did not fracture cleanly in two (Figure 45) but cracked along the fiber direction out of the notches, the ultimate shear strength values are of questionable value. Therefore, the 0.2% shear yield strength (SYS) is the most meaningful strength measure obtained in this test. SYS showed only small variations from process to process (Table 10). Figure 46 illustrates that the dependence of SYS on matrix residual stress is weak or non-existent. A poor correlation of SYS with fiber push out stress was also observed (Figure 47).

4.3.4.2 Analytical Model

The shear stength model was based on a simple geometric idealization of the composite into 3 subsections as shown in Figure 48. Subsection **a** represents the fiber, subsection **b** represents the portion of the matrix between the fibers in a direction perpendicular to the plane of the shear, and subsection **c** represents the matrix between the fibers in the plane of the shear. By treating these three subsections as a set of springs in a parallel/series arrangement, the shear stress-strain response of this model can be predicted. The detailed derivation is presented in Appendix IV. Four regimes of behavior were considered: 1) fully elastic, with no slip at the fiber-matrix interface; 2) elastic with interface slip; 3) plastic matrix, elastic fiber with interface slip 4) plastic matrix, elastic fiber with no interface slip. From Appendix IV, the composite shear stress (τ_c)-shear strain (γ_c) behaviors for these cases are represented by the following equations:

$$\tau_c = \frac{G_m[G_f\sqrt{V_f} + G_m(1 - \sqrt{V_f})]}{[\sqrt{V_f} + (1 - \sqrt{V_f})^2]G_m + \sqrt{V_f}(1 - \sqrt{V_f})G_f} \gamma_c \tag{7}$$

$$\tau_c = 2\tau_i\sqrt{V_f} + G_m\gamma_c \tag{8}$$

$$\tau_c = 2\tau_i\sqrt{V_f} + \tau_m(1 - \sqrt{V_f}) \tag{9}$$

$$\tau_c = \tau_m \tag{10}$$

where G_f and G_m are the fiber and matrix shear modulus, respectively, V_f is the fiber volume fraction, τ_i is the interface shear stength, and τ_m is the matrix shear yield strength. These stress-strain relationships are plotted in Figure 49, and show the following characteristics: There is an initial fully elastic modulus (Regime 1) given by Equation 7. The extent of the fully elastic behavior is a function of the interfacial shear strength, τ_i, and the matrix shear strength, τ_m. For weak interface behavior, Regime 2, (0 < τ_i< τ_m) Equation 8 applies and the slope of the shear stress-shear strain curve is decreased by the addition of interface sliding. For τ_i = 0, the intial region represented by Equation 7 is suppressed altogether, while for increasing τ_i the break in the stress-strain curve rises. At some point
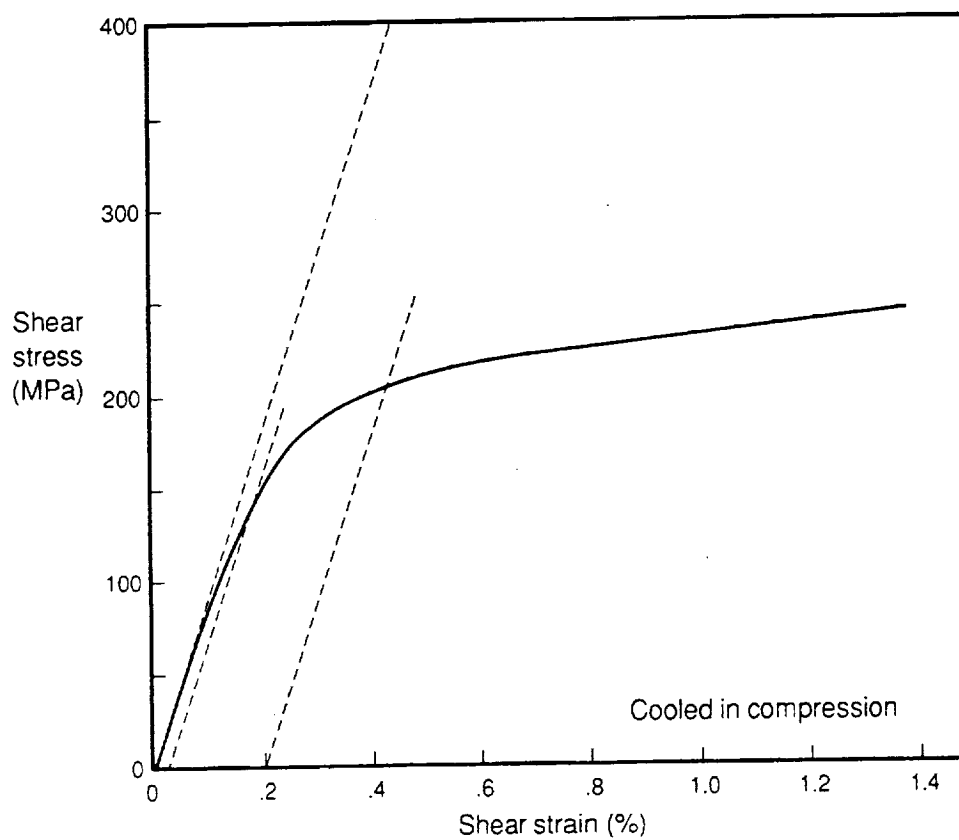
Figure 44   Typical Shear Stress-Strain Curve from RT Iosipescu Test
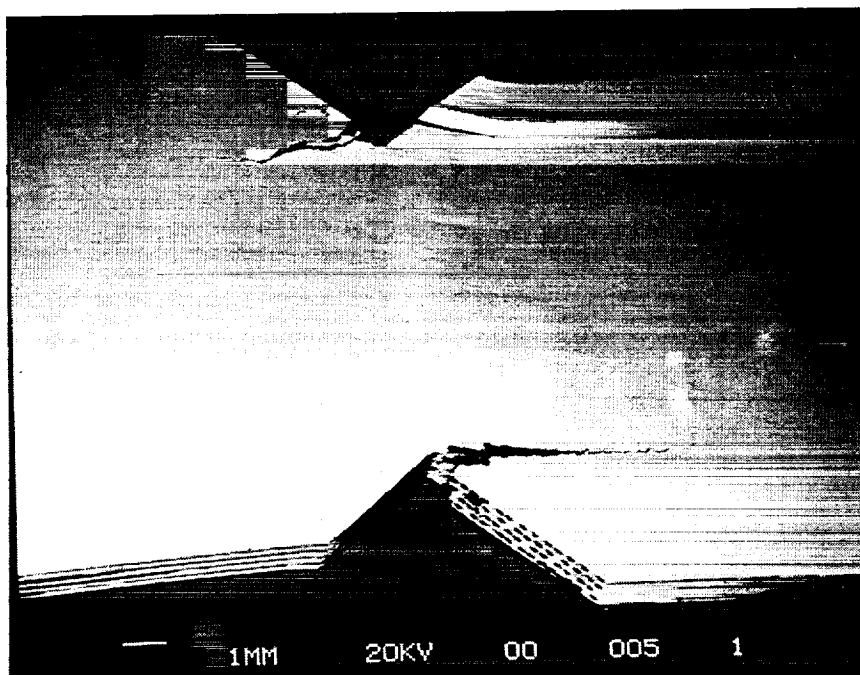
Figure 45   Failure Mode for Iosipescu Shear Test of SCS-6/Ti-24Al-11Nb
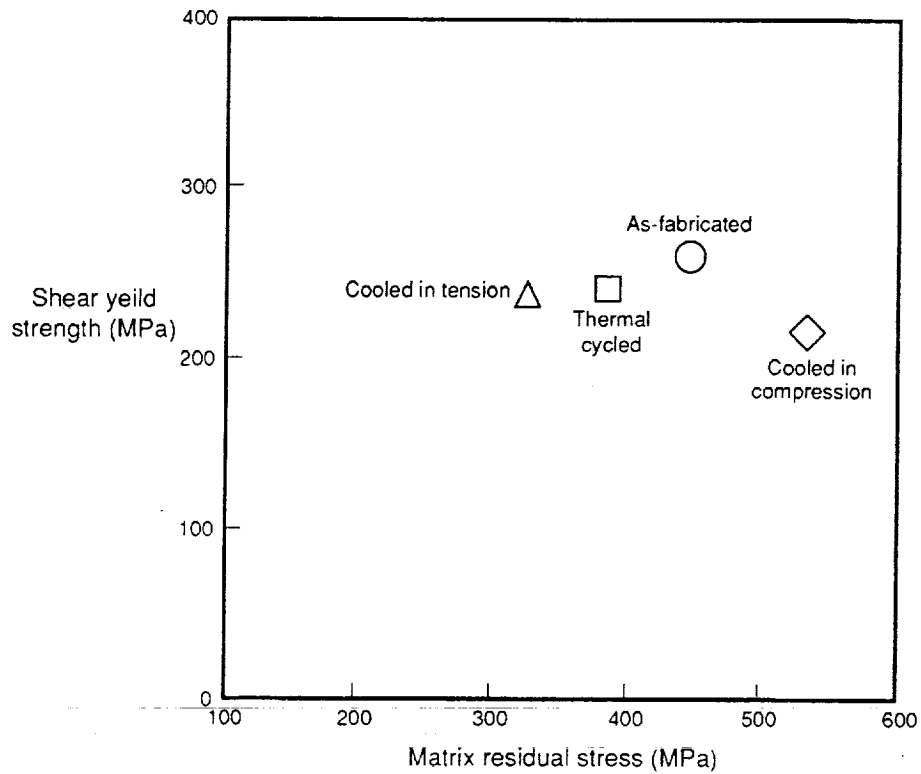
Figure 46   In-Plane Shear Yield Strength is Independent of Matrix Residual Stress
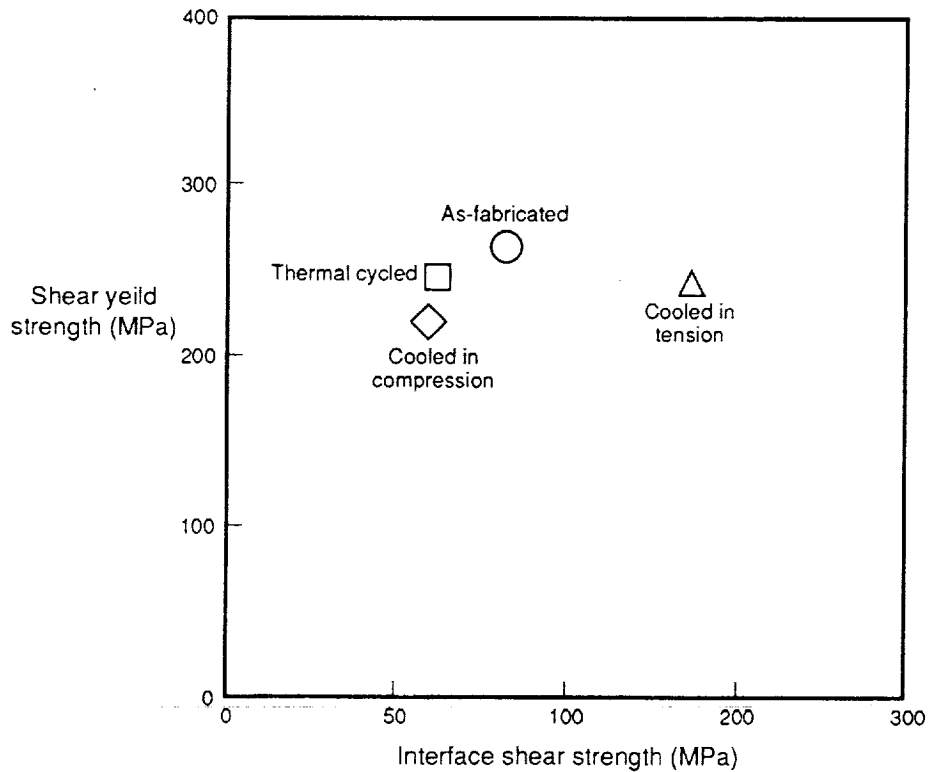
Figure 47   In-Plane Shear Stress is Independent of Interface Shear Strength

68
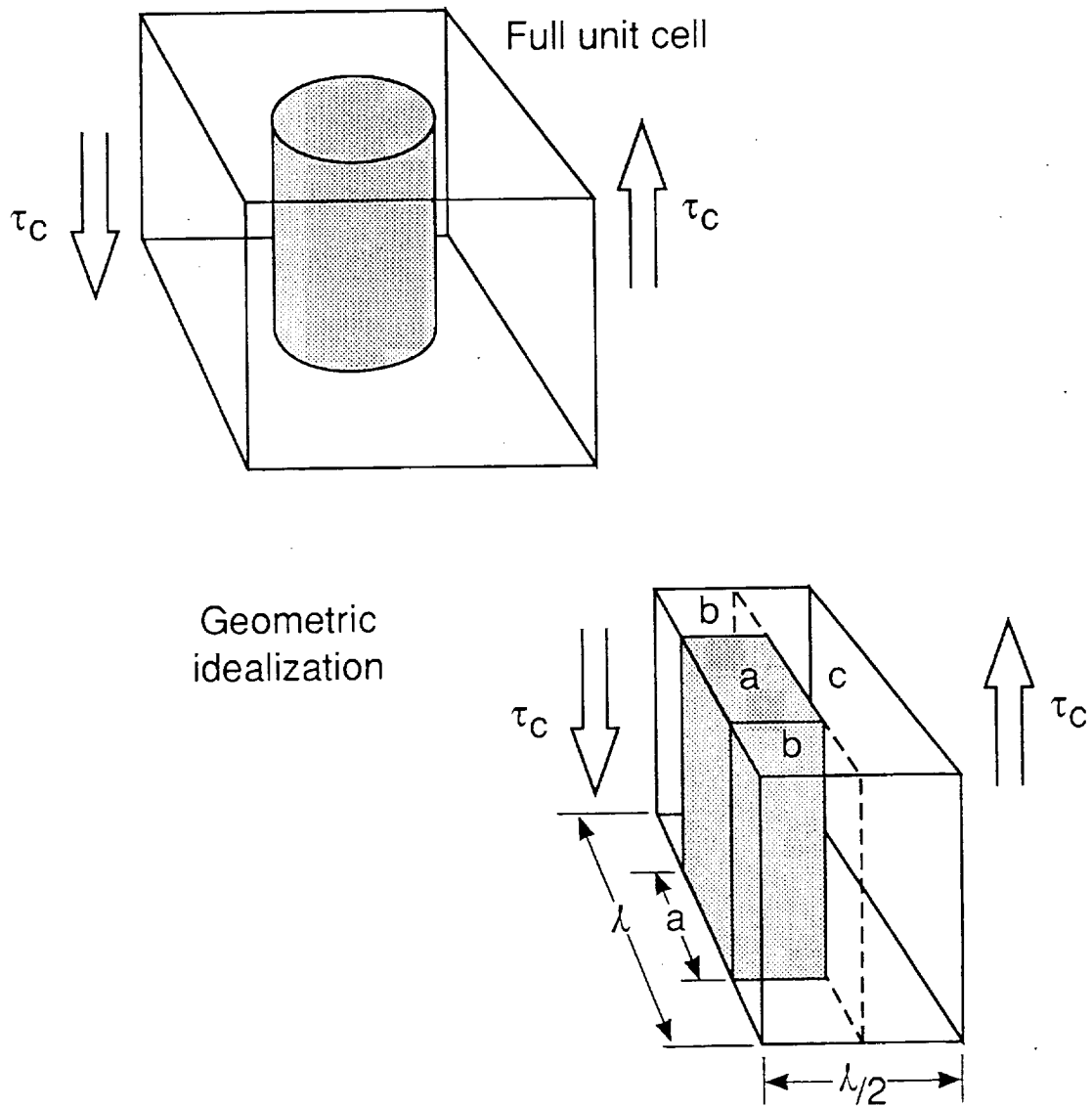
Figure 48. Geometric Model Used for In-Plane Shear Stress Model.
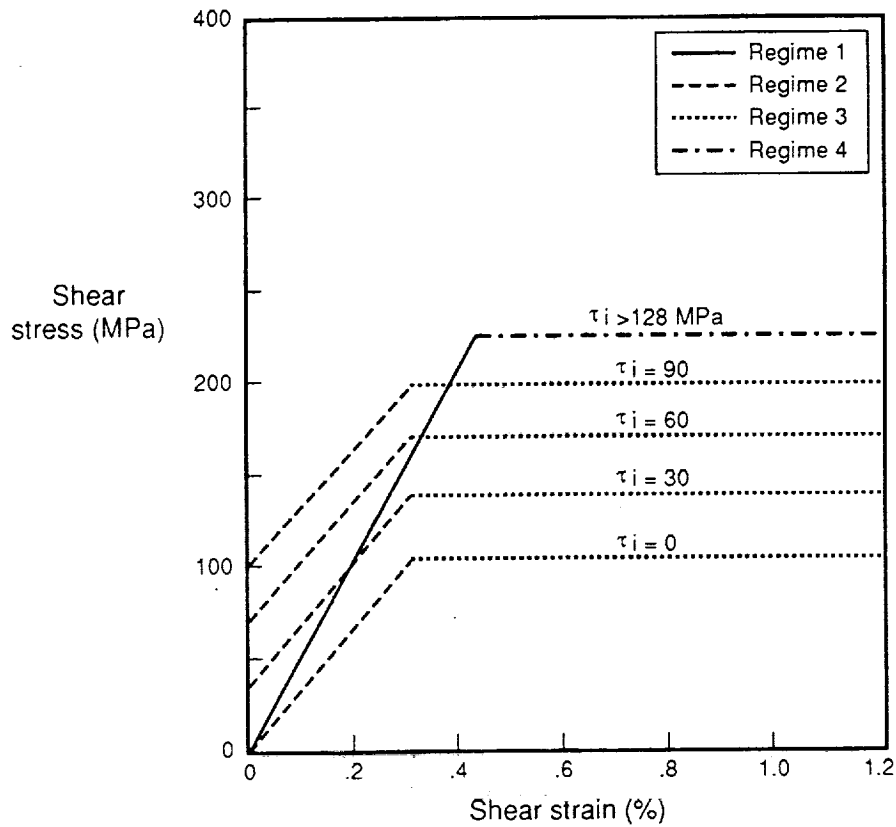
Figure 49   In-Plane Shear Model Stres-Strain Predictions for Various
Levels of Interfacial Shear Strength
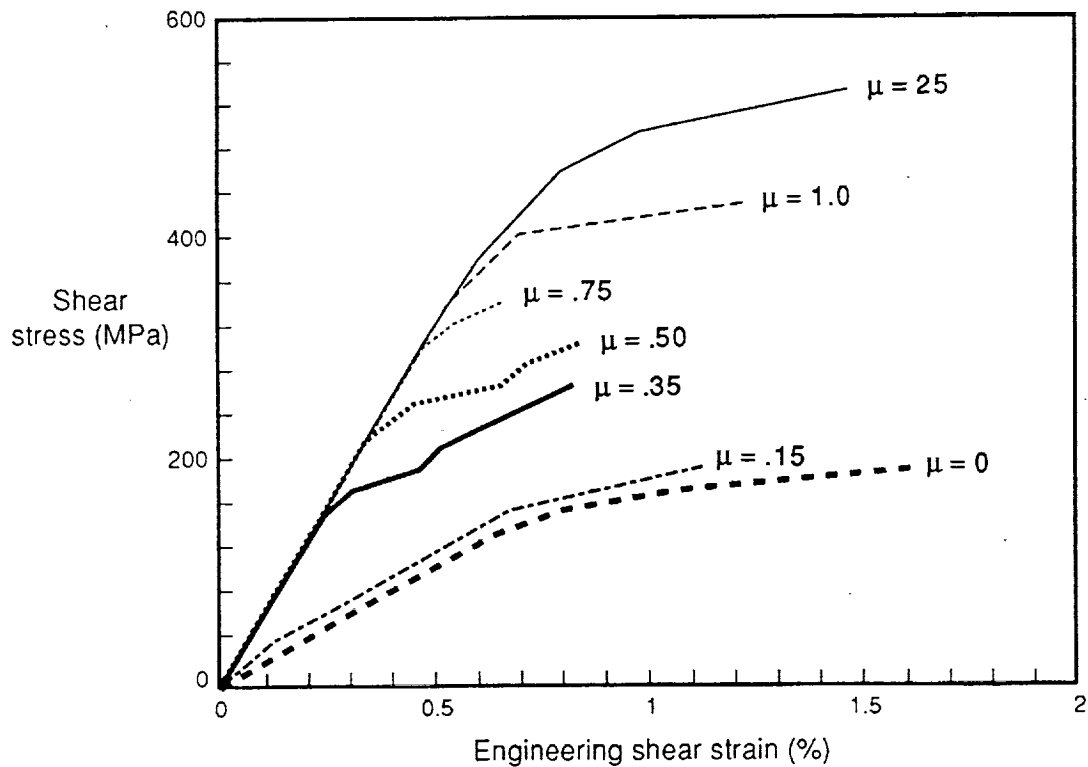
Figure 50   Predictions of Nimmer's FEM Model of In-Plane Shear Stress-
Strain Response for Various Levels of Interface Friction

matrix yielding occurs, Regime 3. For the case where $\tau_i < \tau_m/2$, Equation 9 applies, and for the assumption made here of non-strainhardening plastic matrix behavior, the stress-strain curve becomes flat. If $\tau_i > \tau_m/2$, then interface sliding never occurs, Regime 4. The uppermost envelope of behavior represented by Equations 7 and 10 is then traced.

The influence of thermal residual stress enters this model in two ways: 1) through its effect on apparent matrix yield strength, and 2) through its effect on interface shear strength. The first effect arises from the fact that the matrix is already partially stressed toward yield due to the thermal residual stresses. In the presence of these residual stresses, the addition of an applied shear stress from mechanical loading will tend to lead to matrix yielding at lower applied stresses than if no residual stresses were present. Thus increasing the thermal residual stressses should lower the effective matrix yield strength, τ_m, and lower the composite shear yield strength (Equations 9 and 10). The second effect arises through the influence of radial residual clamping stresses on the shear strength of a frictionally bonded fiber-matrix interface ($\tau_i = \mu\sigma_r^r$, where μ is the interface friction coefficient and σ_r^r is the radial interface clamping stress). The higher the residual stresses, the higher the clamping shoud be, and the higher the composite shear strength should be (Equations 8 and 9). Thus to some extent the two effects are counteracting.

4.3.4.3 Evaluation of Model

The fiber push measurements indicate interface strengths from 59 to 137 Mpa, at or below one-half the matrix shear strength (approximately 250 MPa, estimated as one-half the matrix tensile yield strength). Therefore, some interface slip should occur during loading. However, from the predicted response of Equations 7 through 10, and the interface strength values observed, the behavior should consist of a combination of Regimes 1 and 3 for the lower τ_i conditions, or Regimes 1 and 4 for the higher τ_i conditions. Because the matrix strength of Ti-24Al-11Nb is so low, little or no Regime 2 behavior is expected. Thus a two-part shear stress-strain curve is predicted (Figure 49), much like that observed experimentally (Figure 44). However, the level of the composite shear stress predicted for the low τ_i conditions is much lower than observed.

The model itself appears to be in good agreement with a more sophisticated finite element method model analyzed by Nimmer (GE Staff, 1991) using SCS-6/Ti-6Al-4V. In this model, thermal residual stresses are included, and the shear stress-strain response was analyzed with various interfacial friction coefficients. Figure 50 shows the response predicted by Nimmer's model and it is quite similar to the current model: a two or three-part curve is predicted depending on whether the interface strength (friction) is high or low respectively.

A possible explanation for the lack of agreement in Regime 3 is that the interface shear strength may actually be higher than measured from the fiber pushout test. Analysis of the pushout test by Ghosn, et al. (1992) shows that the maximum shear stress at the ends of the interface, which is the quantity controlling debonding, can be considerably higher than the average shear stress obtained by dividing the apllied load by the interface area. This discrepancy is a factor of about 2.5 for the pushout specimen thickness used in this study. If the true interface shear stress is

2.5 times higher than the pushout values reported here, then the model shows (Figure 49) that interface sliding in shear stress-strain behavior should not be observed and that the full strength given by Regime 4 shoud by obtained. This would cause SYS to be independent of τ_i as observed. Note that for higher strength matrices the model consisting of Eq. 7 - 10 predicts that more sensitvity to τ_i should be seen.

4.3.5 Results of Fatigue Crack Growth Tests

4.3.5.1 Experimental Results

Fatigue crack tests were conducted at room temperature at both 345 and 552 MPa (50 and 80 ksi) for each thermomechanical process. At 345 MPa the cracks continuously decelerated as they grew (Figure 51), leading to da/dN - $\Delta K_{applied}$ curves that trend downward (Figure 52) instead of the usual rising crack growth rate with increasing ΔK that is seen in most homogeneous materials. At 552 MPa there is more of a tendency for the crack growth rate to accelerate (Figure 53), and the da/dN - $\Delta K_{applied}$ curves tend to be flatter or even rising (Figure 54).

The cracks in all cases grew out of the notches perpendicular to the applied stress. In the cooled in compression samples, aditional matrix cracking occured over the unnotched portion of the gage section, but these were ignored in the analysis since other studies have indicate no strong effect of multiple cracking on growth rate.

A cross plot of crack growth rate at constant $\Delta K_{applied}$ vs. residual matrix stress is shown in Figure 55. There is a general trend of increasing crack growth rate with increasing matrix residual stress for both 345 and 552 MPa stress levels, but in both cases the as-fabricated test appears out of line. At higher stress the as-fabricated growth rate is much lower than the general trend; as lower stress the situation is just the opposite.

A similar correlation of crack growth rate with interfacial strength is shown as Figure 56. Here the trend is for decreasing crack growth rate with increasing interface strength. Again the as-fabricated data points do not fall on the trend lines established by the other conditions.

4.3.5.2 Analytical Modeling

The fatigue crack growth response of the SCS-6/Ti-24Al-11Nb material was modeled using the crack growth model of Sensmeier and Wright (1990) This model is based on the fiber bridging mechanics of Marshall, Cox and Evans (1985). It iteratively solves for the matrix crack tip stress intensity which is entered into the matrix fatigue crack growth rate law to establish the number of cycles required for an increment of crack advancement. The bridging conditions are re-evaluated for fiberbreakage by comparing the fiber stress to the fiber breaking strength, and the extent of bridging is adjusted, if necessary, before re-incrementing crack growth. The model was modified in two ways for the current predictions:

72

Figure 51   Crack length vs. Cycles at 345 MPa Shows Deceleration

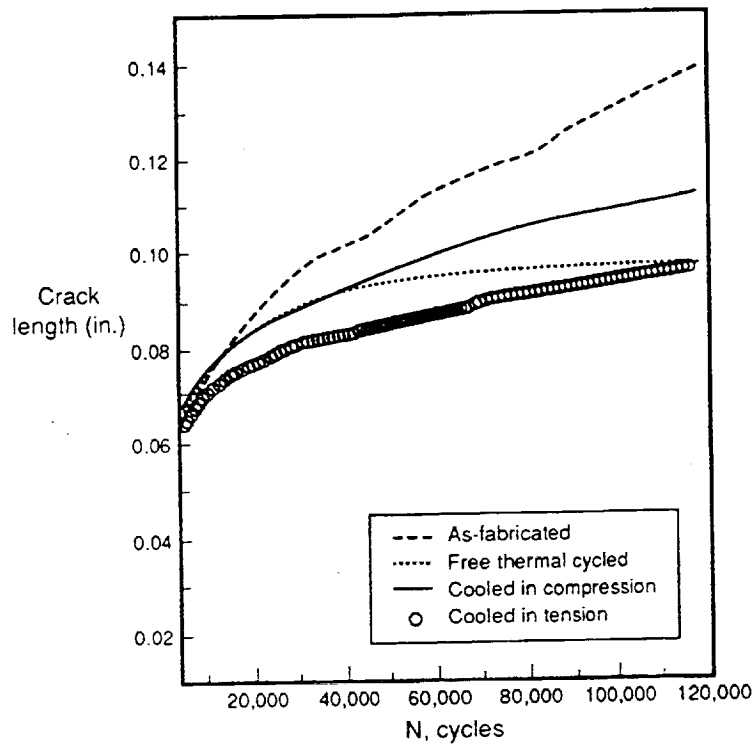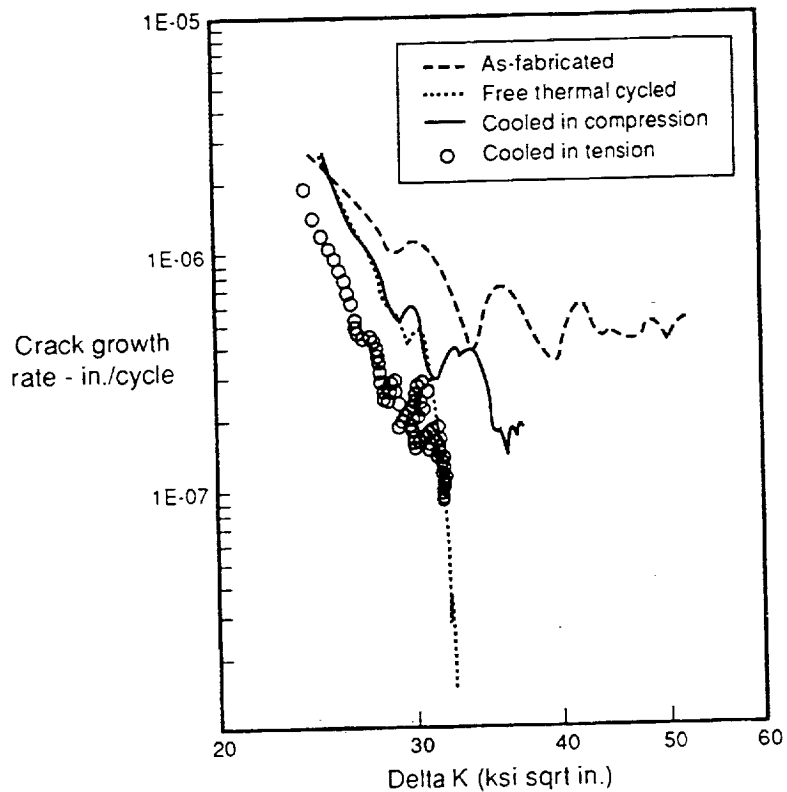Figure 52   Crack Growth Rate vs. $\Delta K_{applied}$ for 345 MPa

73
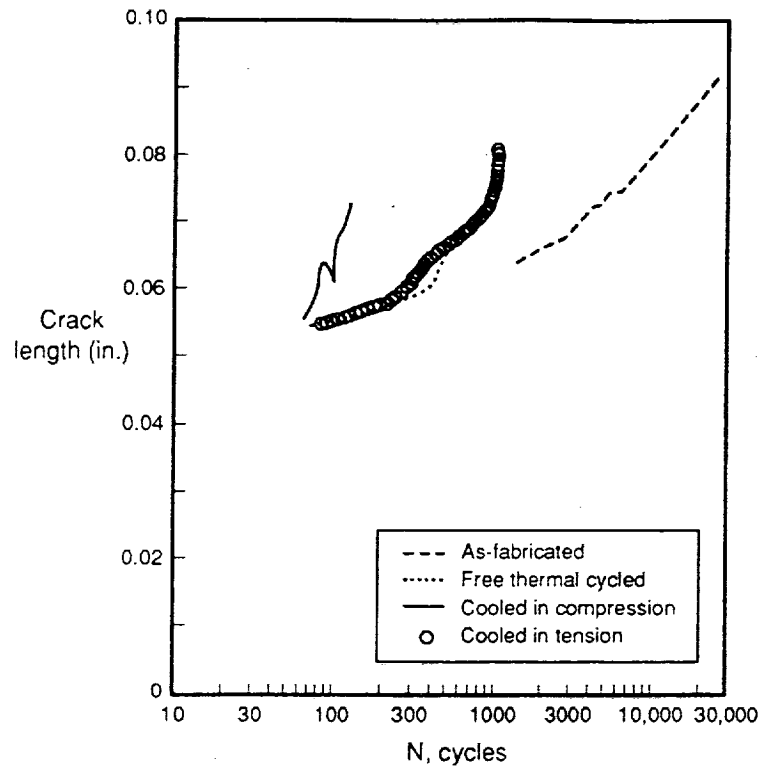
Figure 53   Crack length vs. Cycles for 552 MPa Shows Acceleration
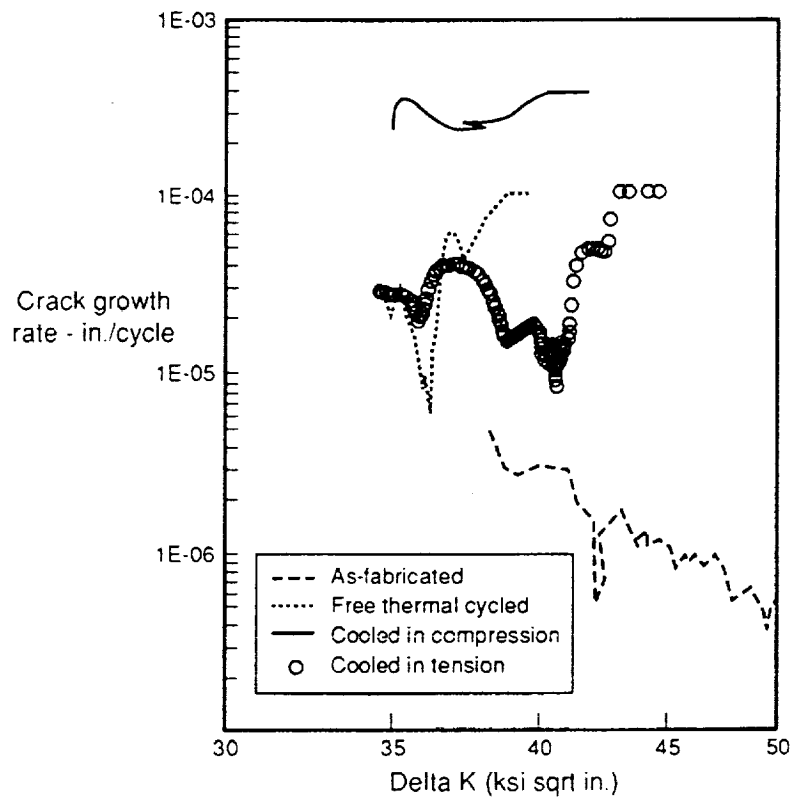
Figure 54   Crack Growth Rate vs. $\Delta K_{applied}$ for 552 MPa
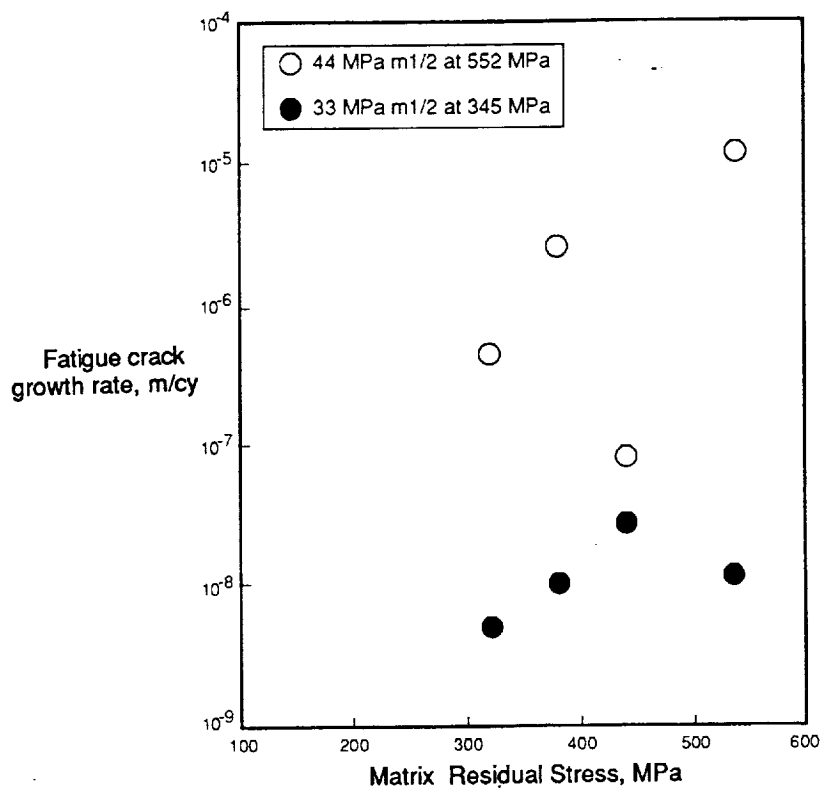
Figure 55 Correlation Between Fatigue Crack Growth Rate
and Residual Matrix (Longitudinal) Stress
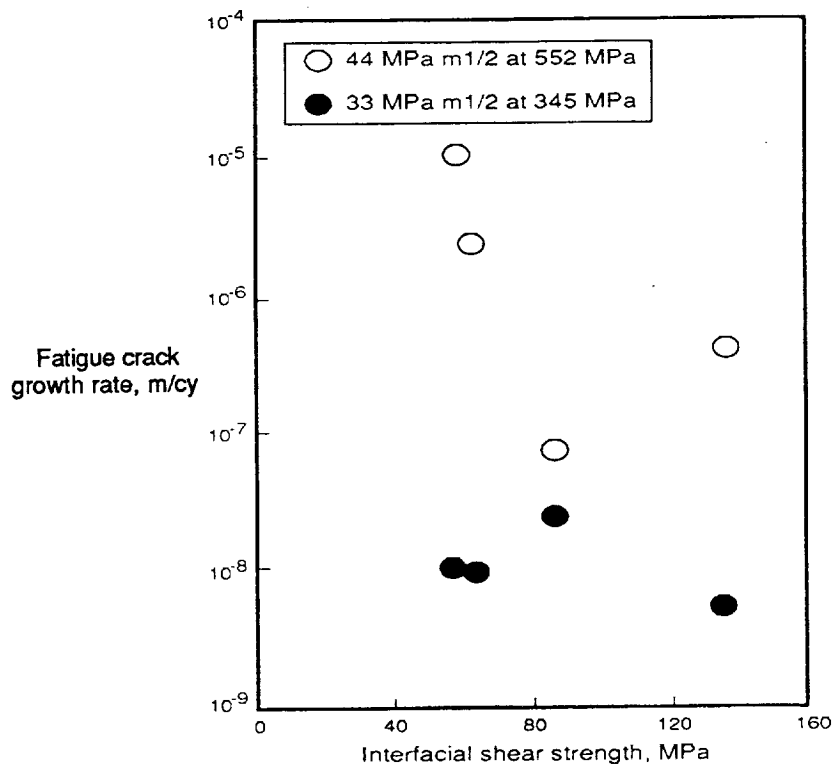
Figure 56 Dependence of Fatigue Crack Growth of SCS-6/Ti-24Al-11Nb
on Fiber Matrix Interfacial Shear Strength.

1)   The crack tip stress intensity range, ΔK, was substituted for the maximum crack tip stress intensity K according to the mechanics of reversed sliding formulated by McMeeking and Evans (1990):

$$\Delta K = 2K_{(\Delta\sigma/2)} \qquad (11)$$

where $K_{(\Delta\sigma/2)}$ is the maximum crack tip stress intensity at a stress level of $\Delta\sigma/2$. This properly accounts for the reverse frictional effects on crack closure which reduces the effective ΔK during cyclic loading.

2)   The effect of residual stresses on crack growth was accounted for by altering the matrix crack growth law by the mean stress in the matrix:

$$da/dn = 2.9234 \times 10^{-11}(\Delta K_{eq}) \quad (in/cy) \qquad (12)$$

where:

$$\Delta K_{eq} = \Delta K(1-R)^{-0.49} \qquad (13)$$

and R is the ratio of minimum to maximum matrix stress in a fatigue cycle.   This mean stress dependance was determined from measurements of DeLuca, et al. (1990).   R was calaculated as follows:

$$R = \frac{\sigma_m{}^r}{(\Delta\sigma_m + \sigma_m{}^r)} \qquad (14)$$

where $\sigma_m{}^r$ is the residual stress measured in the matrix and $\Delta\sigma_m$ is the stress range imposed by mechanical loading on the matrix (not on the whole composite).

Additionally, the fiber-matrix interfacial sliding stress for each process condition (Table 9) was used in the calculations.   Other parameters used were:

$$Vf = 0.30$$
$$Sf = 550 \text{ ksi}$$

The resulting da/dn vs. $\Delta K_{applied}$ behavior predicted at 345MPa and 552MPa is shown in Figures 57 and 58, respectively.

Both figures show cracking under strongly bridged conditions, with crack growth rates decreasing rapidly with growth (increasing ΔK applied).   At both stress levels the model as applied predicts some difference between the four different residual stress (and interface strength) cases examined, in the order of: cooled in tension, as-fabricated, thermal cycled, and cooled in compression .

4.3.5.3   Evaluation of Model

The model predictions shown in Figures 57 and 58 indicate an effect of residual stress on crack growth rate.   At 345 MPa maximum stress, the range of growth rates is about a factor 6 (at about 11 MPa-m$^{1/2}$) and at 552 MPa the range is about a factor of 100 (at 20 MPa-m$^{1/2}$).   These ranges are similar to those observed experimentally: about a factor of 10 at 345 MPa and a factor of 100 at 552 MPa.

76
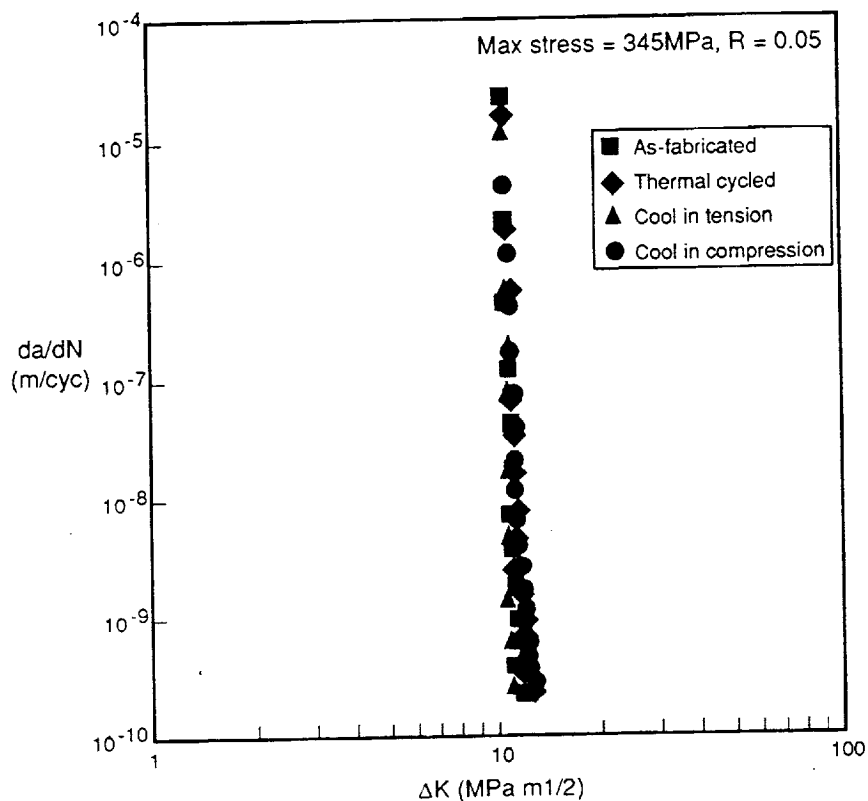
Figure 57   Crack Growth Model Predictions for 345 MPa Max. Stress
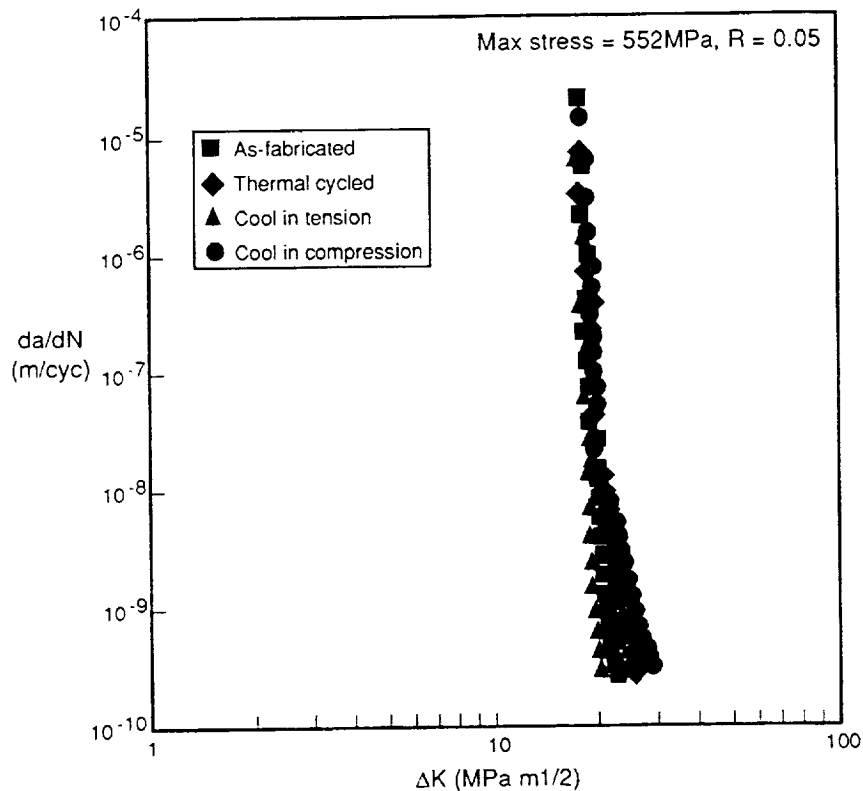
Figure 58   Crack Growth Model Predictions for 552 MPa Max. Stress

Furthermore, the rank order of crack growth rate as a function of residual stress as predicted by the model (cooled in tension, as-fabricated, thermal cycled, cooled in compression) is similar to that observed experimentally (cooled in tension, thermal cycled, cooled in compression) with as-fabricated either highest (at 345 MPa) or lowest (at 552 MPa). The as-fabricated crack growth rate behavior certainly seems anamolous since in comparison to the others it shows no consistent ranking. This behavior is not understood.

Aside from the qualitative agreement in ranking order, however, the predictions of the model for crack growth rates and curve shape are badly matched to the expedrimental ones. At 345 MPa maximum stress, the model does predict bridging behavior with decreasing crack growth rates, as observed, but the rate of decrease predicted is much faster than observed, and occurs at lower ΔK applied levels. At 552 MPa, the model again predicts extensive bridging and a rapid decrease in crack growth rate. The tests at 552 Mpa show little or no decrease in crack growth rate, and growth rates in general much higher than predicted from the model. Evidently the model over-predicts the extent of fiber bridging and thus under-predicts the crack growth rates. Several possible reasons for the discrepancy exist. Within the context of the model, it may be that the interfacial sliding strength values used are low, or that the fiber strength value was high. The inplane shear strength modeling results also suggest that the interface strength is higher than given by the push out tests. The level of fiber strength used in the model was satisfactory to describe crack growth behavior in an SCS-6/Ti-6Al-4V composite, but measurements of fibers extracted from SCS-6/Ti-24Al-11Nb panels have shown a tendency for lower fiber strengths. Other models for fatigue crack growth are also available and these may give better agreement with observed behavior.

5. Summary and Conclusions

5.1 Task 1 - Experimental Methods for Thermal Stress Measurement

The capability of XRD, ND, SXRD, and US techniques for measuring residual thermal stresses in IMC was examined with emphasis on obtaining stress distributions at a microscale. ND was selected as the most promising technique because it could develop information about the state of stress in both the fiber and the matrix with no method development required. While direct information about the local internal stress variations could be obtained, an indirect measure of the interfacial radial stress in the matrix could be obtained through measurement of the transverse fiber stress. SXRD and US techniques hold potential for small scale microstress measurement but considerable additional development is required to provide consistent and verifiable results.

ND (and XRD) experimental results on SCS-6/Ti-24Al-11Nb were found to agree with predictions made by a temperature dependent elastic-plastic concentric cylinder model. This agreement was generally within that expected from the experimental error and the assumptions made in modeling.

5.2 Task 2 - Analytical Models for Thermal Stress Prediction

The neutron diffraction method was demonstrated on a variety of IMC systems encompassing three matrix compositions, three fibers, four fiber fractions, and three thermomechanical processing conditions. The ND method generally gave results in good agreement with analytical predictions. The best agreement was found with the longitudinal fiber and matrix stresses and strains, while the poorest agreement was found with the transverse matrix stress predictions. This is consistent with the observation that the longitudinal strains were large, while the transverse strains were small, near the limit of experimental resolution.

In the materials studied several different potential factors contributed to the development of thermally induced stresses: thermal expansion of the constituent materials, elastic modulus, matrix yield strength, volume fraction fiber, and temperature difference between cooldown and ambient. While not all of these were investigated so as to individually isolate their contributions, nevertheless, the combination of experimental results and analytical modeling allows some observations to be made:

1) In the SCS-6/Ti-24Al-11Nb system, little or no yielding was predicted, and the stresses were controlled by the fiber-matrix thermal expansion mismatch, the elastic properties of the fiber and matrix, and to a large extent, the volume fraction fiber.

2) In the NiAl and NiFeAl matrix systems, yielding of the matrix occurred well above room temperature, and the fiber-matrix thermal expansion mismatch had a smaller influence on the stresses at room temperature. The yield strength of the matrix controlled stress levels under such conditions, with important contributions from V_f.

3) While thermal expansion mismatch between fiber and matrix is the overall driving force for thermal stress generation, its effect on constituent stress level can be overshadowed by the occurrence of significant levels of plastic

79

deformation in the matrix. The thermal expansion mismatch is a direct contributor to _total_ strain levels, but once the total strain level developed exceeds the matrix yield strain, the stress (and _elastic_ strain) stays relatively constant at a level dictated by the yield strength. This explains why the stresses in the NiAl and NiFeAl composites are all fairly similar and lower than SCS-6/Ti-24Al-11Nb even though their thermal expansion mismatches ($\Delta\alpha\Delta T$) are greater than that of SCS-6/Ti-24Al-11Nb: the yield strengths of the Ni-base matrices are lower than that of Ti-24Al-11Nb (see Figure 2). For situations where the matrix stresses are near or below yield (SCS-6/Ti-24Al-11Nb), reducing thermal expansion mismatch should be effective in reducing residual stresses.

4) Elastic modulus is expected from the models to directly influence thermal stress levels, so long as the constituents are both elastic. However, once matrix yielding begins, the influence of modulus will diminish in the fashion described above for thermal expansion mismatch. In the cases studied here elastic modulus did not appear to play an important role in final stress levels.

5) Matrix yield strength becomes the major controlling factor in thermal stress levels when thermal strains are above yield.

6) As fiber volume fraction is decreased, matrix stresses decrease and fiber stresses increase. This is a direct consequence of the equilibrium condition of Equation 3, which expresses the balance between fiber and matrix stresses. The two NiFeAl matrix composites show this directly. A comparison of these two to the Al_2O_3/NiAl system is more difficult since the volume fraction change is accompanied by a change in matrix yield strength. The volume fraction is higher in the NiAl system, which should increase matrix stress, but the yield strength is lower, which reduces stress. The effects of volume fraction are less confounded in the Al_2O_3 fibers which remain elastic: the stresses increase uniformly as volume decreases. Analytical studies of the sensitivity of residual stress calculations to the major variables showed that fiber volume fraction was generally an important factor in setting stress levels.

7) The temperature from which cooldown is started had little effect on the results of these models. Although temperature change is a major driving factor in the development of thermal stresses, the temperature dependent properties used in this model inhibit the development of significant thermal stresses until the composite is well below its peak temperature. In reality, creep relaxation effects would also occur, so that the major portion of the stresses are developed in the lower half to two-thirds of the temperature excursion.

5.3 Task 3 - Influence of Thermal Stresses on Mechanical Properties

1) The longitudinal residual stresses developed in a SCS-6/Ti-24Al-11Nb composite from fabrication can be modified (raised or lowered) by thermomechanical processing. Compared to the as-fabricated state, free thermal cycling and cooling from high temperature under tension reduced the matrix tensile stresses, and cooling from high temperature under compression increased the matrix tensile stress. A range of matrix residual stresses spanning 200 MPa (around an as-fabricated residual stress of 430 MPa) were achieved. No attempt was made to optimize the thermomechanical treatments used; larger changes may be possible. Although only longitudinal matrix residual stresses were measured, the results of this study suggest that only the longitudinal stresses were substantially altered by

this processing. The transverse residual stresses appear to have been unaltered, or altered in a manner not directly correlated to the change in longitudinal stresses.

2) The residual stress levels in the composite influenced the room temperature longitudinal ultimate strength in this composite. Reductions in matrix residual tension increased composite strength, and vice versa. The composite strength changes were related to residual stress changes through a model based on a modification of the rule of mixtures, assuming that the composite strength was limited by matrix cracking due to low ductility. It was also demonstatrated that for high matrix ductility (when composite strength is limited by fiber strain to failure) residual stress levels are expected to have no influence on composite longitudinal ultimate tensile strength.

3) Fiber pushout strength was found to show an inverse correlation with matrix longitudinal residual stress. This finding is at odds with a frictional model of fiber-matrix interface shear strength and appears to be due to the lack of correlation between longitudinal and transverse (radial) stresses resulting from processing. Modeling and experimental stress measurement of the thermomechanically processed specimens were not complete enough to fully understand the stress states produced by the thermomechanical processing. It appears that the changes in fiber-matrix interface stress were different or much less than the changes in longitudinal matrix stress which occurred.

4) In-plane shear yield strength showed no correlation to residual stress. A model for in-plane shear strength of a frictionally bonded fiber composite was developed and used to analyze the composite shear strength response. Competing effects of residual stress on interface strength and matrix effective yield strength apparently cancel each other and lead to a lack of dependence of shear yield strength on residual stress level.

5) Fatigue crack growth in a direction perpendicular to the fibers showed a dependence on matrix residual stress: higher levels of residual tension led, on the whole, to faster crack growth rates. This is in agreement with the trend expected based on matrix mean stress effects. However, the observed behavior was only qualitatively similar to that expected from models of fatigue crack growth based on fiber bridging models. Since other experiments have served to support the models, it is likely that the incomplete description of material properties and stress states in the thermomechanically processed condition has prevented accurate evaluation of the model.

5.4 Recommendations for Further Research

1) The complete residual stress state produced by the thermomechanical processes studied here needs to be measured by neutron diffraction to document the fiber-matrix interface stresses (transverse fiber stress). This should be accompanied by more detailed modeling of the stress changes occuring during thermomechancial processing.

2) The stress changes observed need to be more thoroughly related to changes in the interfacial sliding strength.

3) Alternative methods for less (or non) destructive measurement of fiber-matrix interface strength such as ultrasonics should be evaluated so that changes in the interface can be more confidently measured.

4) Demonstration of the capability to implement items 1) and 2) above should be conducted by examining a wider range of thermomechanical processing, including thermomechanical fatigue cycling, to determine the changes in internal stress that accompany thermomechanical histories which are of importance to advanced engine applications. This will help verify TMF life models currently being proposed for IMC.

6. References

ASM Handbook Committee, "Properties and Selection: Nonferrous Alloys and Pure Metals," Metals Handbook Ninth Edition, Vol. 2, American Society for Metals, 1979, pp 816-820.

Bowman, R.R., and Noebe, R.D., "Processing and Mechanical Evaluation of Continuous Fiber Reinforced NiAl Composites", HITEMP Review 1990, NASA Conference Publication 10051, 1990, pp 40-1 to 40-14.

Cox, B. N., James, M.R., Marshall, D.B., and Addison, R.C. "Determination of Residual Stresses in Thin Sheet Titanium Aluminide Composites", Met. Trans., Vol. 21A, 1990, pp 2701-2707.

DeLuca, D.P., Cowles, B.A., Haake, F.K., Holland, K.P., "Fatigue and Fracture of Titanium Aluminides", AF Wright Research and Development Center Report, WRDC-TR-89-4136, February, 1990.

Gambone, M.L., "Fatigue and Fracture of Titanium Aluminides", AF Wright Research and Development Center Report, WRDC-TR-89-4145, Vol. II, February, 1990.

General Electric Staff, "Titanium Aluminide Composites", NASP Contractor Report 1112, Interim Technical Report No. 4, January, 1991.

Ghosn, L.J., Kantzos, P., Eldridge, J.I, and Wilson, R., "Analysis of Interfacial Failure in SCS-6/Ti-based Composites During Fiber Pushout Testing", HITEMP Review 1992, Vol. II, NASA-CP-10104, Oct. 1992, pp.27-1 to 27-12.

Gigerenzer, H., and Wright, P.K., (1991), "Plasma Sprayed SCS-6/Titanium Aluminide Composite Test Panles", Titanium Aluminide Composites, P.R. Smith, S.J. Balsone, and T. Nicholas, Eds., WL-TR-91-4020, pp.251-264.

Hecker, S.S., "Elastic-Plastic Analysis of Composite Cylinders in Axial Tension", PhD Thesis, Case Western Reserve University, 1968.

Jayaraman, N. and Rangaswany, P., "Residual Stress in Ti_3Al-SCS-6 Fiber Reinforced Metal Matrix Composites", Titanium Aluminide Composites, P.R. Smith, et.al., Eds, WL-TR-91-4020, February, 1991.

Johnson, W.S., Lubowinski, S.J., and Highsmith, A.L., "Mechanicla Characterization of Unnotched SCS6/Ti-15-3 Metal Matrix Composites at Room Temperature", Thermal And Mechanical Behavior of Ceramic and Metal Matrix Composites, ASTM STP 1080, J. Kennedy, et al. Eds., ASTM ,1990.

Koistinen, D.P., and Marburger, R.E., (1959), Trans. ASM, Vol. 51, p537.

Majumdar, S., Singh, J.P., Kupperman, D., and Krawitz, A.D., 1991, "Application of Neutron Diffraction to Measure Residual Strains in Various Engineering Composite Materials", Trans ASME: J. Eng. Mater. Technol., Vol. 113, pp 51-59.

Marshall, D.B., Cox, B.N., and Evans, A.G., Acta Metall., vol. 33, 1985, p.2013.

McCartney, L.N., "Mechanics of Matrix Cracking in Brittle-Matrix Fiber Reinforced Composites", Proc. Roy. Soc., Lond., A409, 1987, pp. 329-350.

McMeeking, R.M., and Evans, A.G., "Matrix Fatigue Cracking in Fiber Composites", Mech. Materials, vol 9, 1990, p217.

Moore, M.G., and Evans, W.P., (1958), "Mathematical Corecction for Stress in Removed Layers in Xray Diffraction Residual Stress Analysis", Trans. SAE, Vol. 66, pp 340-345.

Nimmer, R.P., "Fiber Matrix Interface Effects in the Presence of Thermally Induced Residual Stresses", J. Comp Tech Res. Vol 12,1990, pp.63-75.

Nimmer, R.P., Bankert, R.J., Russell, E.S., Smith, G.A., and Wright, P.K, "Micromechanical Modeling of Fiber/Matrix Interface Effects on Transversely Loaded SiC/Ti-6-4 Metal Matrix Composites" J. Comp. Technol. & Res., Vol. 13, 1991, pp 3-13.

Noebe, R.D., Bowman, R.R., Cullers, C.L., and Raj, S.V., (1990), "Flow and Fracture Behavior of Binary NiAl with Prospects for Future Alloy Development", HITEMP Review 1990, NASA Conference Publication 10051, pp. 20-1 to 20-19.

Saigal, A., Kupperman, D.S., and Majumdar, S., "Residual Strains in Titanium Matrix, High Temperature Composites", Material Science and Engr., Vol. A150, 1992, pp 59-66.

Sensmeier, M.D., and Wright, P.K., "The Effect of Fiber Bridging on Fatigue Crack Growth in Titanium Composites", Fundamental Relationships Between Microstructures and Mechanical Properties of Metal Matrix Composites, Ed. M.N. Gungor and P.K. Liaw, TMS, 1990, pp. 441-457.

Van Stone, R.H., and Richardson, T.L., ASTM STP 877, Philadelphia, 1985, pp.148-166.

Wright, P.K., Nimmer, R., Smith, G., Sensmeier, M., and Brun, M., "The Influence of the Interface on Mechanical Behavior of Ti-6Al-4V/SCS-6 Composites", Interfaces in Metal-Ceramics Composites, Ed. R.Y. Lin, R.J. Arsenault, G.P. Martins, and S.G. Fishman, TMS, 1990, pp. 559-581.

7. Appendices

Appendix I - University of Virginia. Report on Synchrotron XRD

RESIDUAL STRAIN GRADIENT DETERMINATION IN METAL MATRIX COMPOSITES BY SYNCHROTRON X-RAY ENERGY DISPERSIVE DIFFRACTION

Todd A. Kuntz and Haydn N.G. Wadley
Department of Materials Science
University of Virginia, Charlottesville, Virginia

and

David R. Black
National Institute of Standards and Technology
Gaithersburg, Maryland

ABSTRACT

An x-ray technique for the measurement of internal residual strain gradients near the continuous reinforcements of metal matrix composites has been investigated. The technique utilizes high intensity white x-ray radiation from a synchrotron radiation source to obtain energy spectra from small ($10^{-3}mm^3$) volumes deep within composite samples. The peak positions satisfy Bragg's law and allow determination of the lattice parameter. As the probe volume is translated, the peaks of the spectra shift and are used to infer lattice spacing changes and thus strains with a precision of 10^{-3}-10^{-4} (depending on the sample grain size/probe volume ratio). The viability of the technique was first tested using a model system with $800\mu m$ Al_2O_3 fibers and a commercial purity titanium matrix. In this system, which remained elastic on cooling, good agreement was observed between the measured residual radial and hoop strain gradients and those estimated from a simple elastic concentric cylinders model. The technique was then used to assess the strains near (SCS-6) silicon carbide fibers in a Ti-14Al-21Nb matrix. Reasonable agreement between measured and calculated strains was seen provided the probe volume was located $50\mu m$ or more from the fiber/matrix interface. Close to the interface, the measured elastic strains were smaller than anticipated, because of relaxation by plasticity and radial cracking on sample cooling.

1. INTRODUCTION

Low density titanium based metal and intermetallic matrix composites reinforced with silicon carbide and aluminum oxide fibers are attracting interest for high temperature aerospace applications [1]. In all the systems of interest, the fibers have a smaller coefficient of thermal expansion than the matrix and thus

86

residual stress gradients are created in the matrix during cooling after high temperature fabrication [2]. The radial stress component in the matrix is compressive and has its greatest magnitude at the fiber/matrix interface. The hoop stress in the matrix is tensile and is also of greatest magnitude at the interface. The stresses are frequently sufficient to cause matrix plastic deformation [3,4] or even radial cracking in low ductility systems [5].

These stresses play a very important role in the mechanical properties of composites. For instance, the radial compressive stress controls both the transverse tensile properties (resulting in bilinear behavior) of ductile matrix composites [6] and the longitudinal toughness of brittle matrix systems by affecting the the fiber pull out stress [7,8]. The stresses also add to those imposed during loading and result in premature deformation and fracture [9-11]. It is thus important to develop ways to measure these stresses (or strains) and to test the validity of the many models that seek to predict them [6,10-14]. This is gathering importance as researchers seek to use the models to optimize the interface of fiber reinforced composites in order to reduce the residual stress [15,16].

A technique widely used for many years to measure the state of residual stress (actually strains) at the surfaces of a body [17-19] is the $\sin^2\psi$ x-ray diffraction method. However, this technique is not useful for measuring the strains inside a composite sample, particularly the rapidly varying strain fields around a fiber. This is because conventionally generated x-rays are strongly absorbed by most engineering materials, penetrating only a few microns. Efforts to overcome this have included surface measurements, followed by the mechanical or electrochemical removal of a thin layer of surface material, after which another measurement is made [20]. In this way, insight into the strains as a function of depth can be obtained. Unfortunately, the internal strains are altered by the destructive removal of surface layers and the validity of compensation methods for this effect are unclear. Neutron diffraction has been used for residual stress measurement, taking advantage of the high penetration of neutrons in engineering materials [21-23]. While an internal strain is measured, large diffracting volumes are required (because available neutron sources provide relatively low intensities) and only bulk average stresses are determined over a much larger volume than the reinforcement of many of today's composite materials.

Energy dispersive diffractometry using high intensity white synchrotron radiation offers the promise of both good penetration (through several millimeters of titanium for example) and potentially high spatial resolution [24]. The work reported here explores the feasibility of using this technique for residual strain

87

measurement in a metal matrix composite. The intent has been to measure the diffraction from volumes smaller than the reinforcing fiber, to determine the lattic parameter in the probe volume, and then scan the probe away from the fiber. The strain (or stress) profile can then be compared with, for example, concentric cylinder elastic [14] and recently developed elastic-plastic models [26].

2. MEASUREMENT PRINCIPLE

Energy dispersive diffractometry, based on Bragg diffraction, utilizes a solid state detector to analyze the distribution of diffracted x-ray energies from a polychromatic (white radiation) incident beam, Fig. 1. The intrinsic germanium detector is positioned at a fixed scattering angle 2θ so that diffraction is detected from a volume defined by the incident and scattered beams. The energy of the diffracted peaks satisfy Bragg's Law:

$$E_{hkl} = \frac{hc}{\lambda} = \frac{hc}{2\sin\theta} \cdot \frac{1}{d_{hk\ell}} \qquad (1)$$

where E_{hkl} is the energy of an {hkl} reflection, h is Plank's constant, λ the wavelength, d_{hkl} the {hkl} lattice spacing and c is the speed of light. For E given in keV and d in Å, the above equation becomes:

$$E_{hkl} = \frac{6.22}{d_{hkl} \sin\theta} \qquad (2)$$

Thus for a known experimentally fixed, scattering angle 2θ, each crystallographic plane with a lattice spacing d_{hkl} diffracts at a particular energy E_{hkl}. Measurement of a peak energy at the fixed angle 2θ allows the calculation of lattice spacing. Shifts in peak energy allow the strain, ε, be determined:

$$\varepsilon = \left(\frac{\Delta d}{d}\right)_{hkl} = \left(\frac{\Delta E}{E}\right)_{hkl} \qquad (3)$$

where Δd refers to the change in the lattice spacing and ΔE the resultant peak shift.

Two factors determine the strain measurement capability of the energy dispersive approach; resolution and detectability/sensitivity . The resolution is obtained by differentiation of equation (1):

$$\left|\left(\frac{\delta d}{d}\right)_{hk\ell}\right| = \left|\left(\frac{\delta E}{E}\right)_{hk\ell}\right| + |\cot\theta| \cdot \Delta\theta \qquad (4)$$

88

where δE is the energy resolution of the solid state detector and $\Delta\theta$ the angular divergence (determined by the collimation of the incident/diffracted beams). The energy resolution of an intrinsic germanium detector at 122keV is $\Delta E/E \approx 4 \times 10^{-3}$, and for a typical set-up, $\Delta\theta \approx 2$ milliradians and $\theta \sim 2\text{-}8^0$. Thus, the resolution apparently is only $\sim 1\%$, insufficient for our purpose (we ideally need $10^{-2}\%$ strain resolution). However, it is important to realize that equation (4) is an expression for the ability to resolve two peaks in a single spectrum resulting from nearly identical lattice spacings. The actual strain resolution is determined by the ability to measure the shift in a single peak between two different spectra. This resolution is given in equation (3).

$$\varepsilon = \left(\frac{\Delta d}{d}\right)_{hk\ell} = \left(\frac{\Delta E}{E}\right)_{hk\ell} \tag{5}$$

Therefore, the strain resolution is determined only by the smallest shift in peak energy resolvable. To increase the sensitivity to peak shifts, one can fit the diffraction to a Gaussian plus linear profile. This theoretically sound practice (27-30) has been shown to allow peak shifts of a few eV to be resolved, and depending on $E_{hk\ell}$, sensitivity of $\sim 10^{-4}$ [27].

The intersection of the incident and diffracted beams defines the x-ray probe, which is controlled by collimating the two beams, Fig. 1. In this region, diffraction is measured only from lattice planes which are perpendicular to the diffraction vector $\vec{k}$, which is in the direction of the bisector of the angle formed by the incident and diffracted beams. These planes alone satisfy the Bragg condition for diffraction at the particular scattering angle being used. In this way, the hoop and radial strains can be measured independently, depending on the orientation of the fiber relative to the incident beam, as shown in Figure 2.

A system of slits is employed to collimate both the incident and diffracted beams, allowing precise control of the incident beam cross section, the scattering angle, the dimensions of the x-ray probe and the angular divergence. For the experiments reported here, the probe volume was $50 \times 50 \times 1000 \mu m^3$ with the long dimension arranged parallel to the fiber axis (the direction in which the stress field does not change). These parameters control peak position, peak breadth, count rate and resolution in the strain sensitive direction, all of which are optimized for a particular experiment.

3. EXPERIMENTAL PROCEDURE

3.1 Test Samples

Three model single-fiber samples were fabricated by hot isostatic pressing (HIP) consolidation of either commercially pure titanium powder or an intermetallic Ti-14Al-21Nb (wt%) alloy with either a 800μm polycrystalline alumina fiber or a Textron* silicon carbide (SCS-6) fiber of 142μm diameter (HIP). Titanium powder was provided by Johnson Mattey Inc.*, with an average particle size of 150μm. The Ti-14Al-21Nb intermetallic alloy powder also had a 150μm particle size. It was made by the plasma rotating electrode process (PREP) by Nuclear Metals, Inc.* Samples were HIPed in stainless steel cans in an ABB Minihipper* under the conditions shown in Table 1. Controlled cooling was done at less than 2°C/minute from the hold temperature to 500°C and then cooled to ambient at around 20°C per minute. The resulting sample geometry was a 5-7mm thick flat plate with a single fiber embedded in the plane of the plate. The embedded fiber was at least 2.5mm from any free surface.

Table 1. Composite Test Samples for X-ray Study of Internal Strain Gradients

SAMPLE	MATRIX/FIBER COMBINATION	TEMP (°C)	HIP CONDITIONS PRESSURE (MPa)	TIME (hrs)
HIP0	CP Ti/800μm Al$_2$O$_3$	850	100	4.0
HIP1	PREP Ti-14Al-21Nb/SCS-6	1050	100	4.0
HIP2	PREP Ti-14Al-21Nb/SCS-6	950	205	2.0

3.2 X-Ray Measurement Methodology

All energy dispersive experiments were performed using the NIST materials science beamline, X23A3 at the National Synchrotron Light Source, Brookhaven National Labs, on Long Island, New York. Usable x-ray energies range from 5 to 60 keV, with the critical energy at 8 keV. The uncollimated beam cross section at the sample is roughly 50mm X 5mm.

A nominal scattering angle of ~5 degrees was chosen to insure good energy separation between diffraction peaks in the range between 20 and 60 keV. An EG&G Ortec* high purity germanium solid state detector, with a resolution of 190 eV at 5.9 KeV was used to measure the diffracted energy spectrum. An Ortec 92X Spectrum Master* provided high bias, amplification and analog to digital

conversion. Data acquisition, storage and analysis were performed by Ortec Maestro II* software operating on a Compaq 386s Deskpro* personal computer.

All spectra for a particular geometry, hoop or radial, were acquired during a single fill of the electron storage ring to eliminate peak shifting as a result of source position changes as discussed below. The sample was translated across the probe in steps as small as 50 micrometers in the region close to the interface. The step size was increased to as large as 750 micrometers far from the interface where the strain was expected to be almost constant.

4. RESULTS and DISCUSSION

4.1 C.P. Titanium/Al$_2$O$_3$ System

A typical sequence of x-ray intensity spectra for sample HIP0 are shown in Fig. 3 The first, (Fig. 3a) corresponds to an x-ray probe centered on the fiber matrix interface and both Al$_2$O$_3$ and the (hexagonal) titanium peaks are clearly resolvable. In Fig. 3b the probe volume was radially translated 40μm from the first location. An abrupt drop in the Al$_2$O$_3$ signal is observed for the 50x50μm^2 probe area used here (though it had not completely disappeared). Fig. 3c shows the spectrum after translating a further 40μm. Also shown on the spectra are MnK$_\alpha$ and K$_\beta$ obtained from an Fe^{55} radioactive source. These had energies of 5.909 and 6.502 keV respectively and were used to calibrate the energy (channel number) axis. The sequence shown in Fig. 3 was continued until the probe volume was 2500μm away from the fiber. This was sufficiently far from the fiber that the stresses due to the thermal mismatch would have fallen to a small value, and the spectra at this location was used as a reference from which to calculate peak shifts. The peak shifts of individual Bragg reflections were found to have quite significant random errors; an average peak shift was determined from the 6 to 8 strongest Bragg peaks.

Figures 4 and 5 show the hoop and radial strain profiles as a function of distance from the fiber/matrix interface for the HIP0 sample. Stress values are given on the secondary vertical axis (stresses and strains being related by one dimensional Hooke's law). Also shown is a solid line that represents the predictions of a simple concentric cylinders elastic model for the residual stress gradient created on cooling [25]. The general form of the thermal stresses are given by:

$$\sigma_{hoop} = A\left(1 + \frac{b^2}{r^2}\right) \qquad \sigma_{radial} = A\left(1 - \frac{b^2}{r^2}\right) \qquad (6)$$

where b is the radius of the matrix sleeve, r is distance in the radial direction and A is a constant determined by the fiber and matrix elastic moduli and thermal expansion coefficients, fiber radius, change in temperature and Poisson's ratio for the composite [10]. The thermophysical data used for the elastic calculations are given in Table 2.

Table 2. Thermophysical Data Used for Elastic Concentric Cylinders Model

HIP0

E_m = 100 GPa	ΔT = -830°C
E_f = 365 GPa	v_c = 0.36
α_m = 8.4 X 10-6/°C	matrix sleeve = 2500 μm
α_f = 5.2 X 10-6/°C	fiber radius = 400 μm

HIP1/HIP2

E_m = 110 GPa	ΔT = -1030°C/-930°C
E_f = 390 GPa	v_c = 0.25
α_m = 10.6 X 10-6/°C	matrix sleeve radius (b) = 800 μm
α_f =4.9 X 10-6/°C	fiber radius = 71 μm

Overall, quite good agreement is seen between the measured and predicted values, although there is point to point scatter which we discuss below.

As mentioned above, each data point shown in Figs. 4 and 5 represents an average of all the intense matrix peak shifts of each spectrum. Eight peaks were used for the hoop strain and six for the radial strain measurements. The average standard deviation for the peak shift was 9.5 x 10-4 for the hoop strain and 9.9 x 10-4 for the radial strain. It should be noted that averaging is strictly valid only for an isotropic material, since in an anisotropic material, a constant stress will produce different strains depending on orientation. However, since the anisotropy factor for titanium is only 1.34, averaging was considered to introduce less error than that of the random fluctuation of only a single peak.

Two factors contribute to the random scatter in the individual data points of Figs. 4 and 5, i.e., to the averaged peak shifts. In principle, given sufficient counts, a peak shift can be resolved to a strain of ~10-4 using the Gaussian curve fitting technique [27-29]. In practice, we were unable to always gather enough

counts at each measurement location to give ideal counting statistics because of a combination of our small ($\sim 10^{-3}$mm^3) probe volume, and time constraints associated with the Synchrotron. These time constraints arise from the need for periodic (roughly every 24 hours) reinjection of electrons into the accelerator ring. The electrons may be injected into a different orbit which causes a shift in the x-ray beam position which leads to unacceptable scattering angle and probe volume location shifts. A trade-off between the number of measurement points, and counting statistics was therefore made during data collection. The typical peak height that resulted had 1000 counts.

A more serious contributor to the error were "single grain" effects. They are believed to be the primary contributing factor to the random fluctuations in the data. A schematic diagram illustrating how this effect can occur is shown in Figure 6. A basic assumption of the technique is that all of the grains in the probe are scattering only at a single angle, $2\theta_B$. However, suitably oriented grains at extremes (corners) within the probe volume can scattering at angles either slightly greater or less than the nominal angle $2\theta_B$. The Bragg scattering contributions from these grains tends to shift the peak to either higher or lower energies according to equation (1). We estimate the range of scattering angles between $2\theta_B \pm \Delta$ is large enough to shift a peak by an amount equal to a strain of 0.001 [30]. Thus, if a suitably oriented large grain is located at the edge of the probe, its diffraction will skew the peak position (even with no strain present) resulting in an anomalous peak shift. Only if many randomly oriented grains are present in the probe will enough of them be properly oriented for diffraction so that this divergence contributes only to a peak broadening and not to a shift in peak position. Using typical probe dimensions of 50x50x1000μm^3 and a matrix grain size of 10-20 μm, on the order of 1000 grains are expected in a typical probe. Using solid angles, the probability that diffraction will be observed from any one orientation in a single randomly oriented grain is calculated to be roughly 10^{-6}. Thus it is likely that only a few grains are contributing to any single peak, and there is a substantial probability that they diffract at some angle slightly larger or smaller than the nominal scattering angle. Further evidence for this was observed experimentally by the fact that the intensity of a particular peak varied greatly at different points in the sample.

We notice that the experimentally determined stresses near the fiber-matrix interfaces in Figs. 4 and 5 always tend to lie below the prediction of the elastic model. For example, the radial stress components around 100μm from the interface reached a high of $\sim$130MPa whereas the predicted values were $\sim$180MPa. Likewise, with the exception of the measurement immediately adjacent to the interface, the hoop stress components out to $\sim$150μm were $\sim$50MPa less than the model prediction. Since the residual stresses are below the matrix yield stress

throughout cooling [26], it is unlikely these effects are due to plastic relaxation. Figure 8 shows a micrograph of this region. Although an interfacial reaction had occurred, it is believed not directly responsible for this as it was confined to a 10μm region near the fiber. We believe the difference to have arisen in part from small misorientation errors of the probe volume.

Figure 7 shows schematically the intended alignment of the fiber and probe volume. Recall that the axial dimension of the probe volume was 1000μm for these tests, and therefore a misorientation in either the θ or ψ directions would rotate the probe and change the radial distances it samples. As an example, suppose the probe is positioned correctly 40μm from the interface. The average radial stress then sampled, $\bar{\sigma}_r$, is then;

$$\bar{\sigma}_r = \frac{A}{(r_0 - r_1)} \int_{r_1}^{r_0} (1 - \frac{b^2}{r^2}) dr = 189 \text{MPa}$$

where r_0, r_1 are the radial distances to the outer and inner edges of the probe volume (465 and 415μm) respectively, and is almost the same as the value at r=44μm because of the weak variation in σ_r with r. This equals 189MPa for our test configuration. Suppose, however, the probe were rotated 10° in the θ direction. The central longitudinal axis of the probe volume would then penetrate into the fiber (accounting for the fiber diffraction observed in the tests for probes close to the interface) and shortens the volume of the probe from which matrix diffraction would be sampled (from 1000 to 730μm). The range of radial distances sampled then changes; ranging from r=400μm (where the probe enters the fiber) to r=527μm. The average radial stress sampled in this situation falls from 189 to 173MPa. Rotations of up to 10° in the ψ direction can also reduce the radial stress by a further 10MPa or so.

The remaining discrepancies between the model prediction and the data could be due to a number of effects ignored in modelling including the difference in modulus and α for the reaction products, and perturbations gradients near the fiber. Further work is needed to investigate this.

4.2   Ti-14Al-21Nb SCS-6/System

Two SCS-6/Ti-14Al-21Nb samples containing very widely (serveral millimeter) spaced fibers were also examined. Figure 9 shows the residual hoop strain (stress) profile for sample HIP 1 and Fig. 10 the radial strain (stress) profile for sample HIP 2. In the figures, the square points correspond to the experimentally measured data, and the curve is the prediction of the elastic

concentric cylinders model. Using the same probe volume as before, it was found that because of the much smaller grain size of the samples, the scatter in peak shift data was much less, and the local strains could be obtained from the analysis of a single diffraction peak rather than the average of 6-8 peaks as before.

It can be seen that the residual stress measured 50-150μm and beyond from the interface are in reasonable agreement with the residual stresses calculated from the elastic model. However, closer to the interfaces, the experiments indicate the stresses are significantly less than those of the elastic model. Errors associated with the finite cross section of the probe (50μmx50μm) and up to a 10° misalignment of the probe volume (when nominally located 40μm from the interface) can account for only 30MPa of this difference. Using the data of Lukasak and Koss [31], Pindera has found from elastic-plastic calculations that on cooling, the stresses exceed the matrix yield strength and that significant plastic deformation occurs. The analysis predicted plastic strains of ~4% close to the interface. These resulted in radial stresses of ~380MPa and hoop stresses of only ~190MPa at the interface; a substantial reduction from the predictions of the elastic model, but still greater than those observed in the experiment.

To gain further insight into possible causes of the discrepancy, each sample was sectioned, polished, lightly etched and examined by scanning electron microscopy, Figs. 11 and 12. Sample HIP 1 had transformed to the familiar $\alpha_2 + \beta$ structure of these alloys. A 2-3μm reaction product had formed at the interface during consolidation (1050°C, 4h) and a ß-depleted zone extended about 15μm from the interface. About ten relatively short (5-10μm) radial cracks had formed in the ß-depleted zone. Sample HIP 2 had been deliberately consolidated at a lower temperature (950°C, 2h) to try and minimize this interfacial damage. Only a 1-2μm reaction zone and a few short (<5μm) radial cracks were present. The matrix in this case had transformed to a combination of σ_2, ß and orthorhombic phases (32-36).

These micrographs suggest several possible explanations for the lower than expected stresses. The radial cracking is probably the most important since the crack face separation would allow relaxation of the elastic stress. However, other effects such as volume changes accompanying the silicide/carbide reaction at the interface and impurity profiles near the fiber could contribute. Again, this seems to be an area suited to further study.

5. SUMMARY

Synchrotron x-ray energy dispersive diffractometry has been used to measure thermal residual strains around Al_2O_3 and SCS-6 fibers embedded in

a-2

HIP-consolidated titanium and Ti-14Al-21Nb matrix composites. For the first time, a measurement of the thermal residual strain gradients around ceramic fibers embedded several millimeters within thick metal matrix composites has been accomplished. Using the high intensity white radiation available at the National Synchrotron Light Source at Brookhaven National Laboratory, the measurement of strain to a (grain size limited) precision of 10^{-3} or better from diffracting volumes of order $10^{-3}mm^3$ has been demonstrated. The spatial resolution within the sample was controlled by the probe dimensions and positioning errors. Typically it was $\pm 20\mu m$ though further improvement is feasible. For the model $800\mu m$ diameter Al_2O_3 fiber-titanium matrix system, reasonable agreement between measured and elastic predictions was observed. The agreement between measurement and elastic model predictions for the SCS 6/Ti-14Al-21Nb system was not as good. In particular, the measured stresses near the fiber were substantialy less than those predicted by a simple elastic concentric model. Elastic-plastic models of the problem indicate that in the SCS-6/Ti-14Al-21Nb system, significant plastic strains (~4%) occur on cooling, and these relax the residual strains. However, the most important effect appears to be the radial cracking of the matrix near the fiber.

VI. ACKNOWLEDGMENTS

*Disclaimer: The names of material suppliers and equipment vendors are given in the text to aid the readers evaluation of the experiments. This should not be considered a product endorsements by either the National Institutes of Standards and Technology or the University of Virginia.

VII. REFERENCES

1. Ronald, T.M.F., Adv. Mat. & Proc., 135, 5, pp. 29-37 (1989).

2. G. Garmong, Met. Trans., 5, pp. 2183-2186, (1974).

3. D. C. Dunand and A. Mortensen, Acta Metall. Mater., 39 (2), pp. 127-139, (1991).

4. Poritsky, H., Physics, 5, pp.406-411 (1934).

5. P. K. Brindley, P. A. Bartolotta, and R. A. MacKay, "Thermal and Mechanical Fatigue of SiC/Ti$_3$Al+Nb," Proceedings HIGHTEMP Review, NASA CP 10039, pp. 52-1 to 52-14, (1989).

6. R. P. Nimmer, J. Composites Technology and Research, 12 (2), pp. 65-70, (1990).

7. J. W. Hutchinson and H. M. Jensen, Mech. Mater., 9, pp. 139-163, (1990).

8. D. B. Marshall and W. Oliver, J. Amer. Ceram. Soc., 70, (8), pp. 542-48, (1987).

9. G. Garmong, Met. Trans., 5, pp. 2191-2197, (1974).

10. Chawla, K.K., Metallography, 6, pp. 155-169 (1973).

11. Hecker, S.S., Hamilton, C.H. and Ebert, L.J., J. of Mats., 5, pp. 868-900 (1970).

12. J. D. Eshelby, Proc. Roy. Soc. A, 252, pp. 561-569, (1959).

13. D. Iesan, J. Thermal Stress, 3, pp. 495-508.

14. Y. Mikata and M. Taya, J. Comp. Mat., 19, pp. 554-578, (1985).

15. M. Vedula, R. N. Pangborn, and R. A. Queeney, Composites, Vol.   , pp. 133-137, (1988).

16. S. Arnold, V. K. Arya, M. E. Melis, "Elastic/Plastic Analyses of Advanced Composites Investigating the Use of the Compliant Layer Concept in Reducing Residual Stresses Resulting from Processing," NASA Tech. Memo 103204, Sept. (1990).

17. Cullity, B.D., Elements of X-Ray Diffraction, 2nd Edition, pp. 447-478, Addison-Wesley, Reading, MA, (1978).

18. P. D. Evenschor and V. Hauk, Z. Metall. ed. , 66, pp. 164-168, (1975).

19. K. M. Brown, R. W. Hendricks and W. D. Brewer, "X-ray Diffraction Measurements of Residual Stresses in SiC/Ti Composites," in "Fundamental Relationships Between Microstructure and Mech. Properties of MMC's," TMS (Metals Park), Indianapolis, (1988).

20. Cox, B.N., James, M.R., Marshall, D.B. and Addison Jr., R.C., Met. Trans., 21A, pp. 2701-2707 (1990).

21. Schmank, M.J. and Krawitz, A.D., Met. Trans., 13A, pp. 1069- 1076 (1982).

22. S. R. MacEwen, J. Faber and A. P. L. Turner, Acta Metall., 31 (5), pp. 657-676, (1983).

23. D. Kupperman, Private Communication.

24. Black, D.R., Bechtoldt, C.J., Placious, R.C. and Kuriyama, M., J. of Nondestructive Eval., 5, pp. 21-25 (1985).

25. Chawla, K.K., Composite Materials, Science and Engineering, pp. 189-196, Springer-Verlag, NY, (1987).

26. M. Pindera, Private Communication.

27. C. J. Bechtoldt, R. C. Placious, W. J. Boettinger and M. Kuriyama, Advances in X-ray Analysis, 25, pp. 329, (1982).

28. M. Kuriyama, W J. Boettinger and H. E. Burdette, NBS Special Technical publication 567, p. 479, (1980).

29. M. A. Mariscotti, Nuclear Instruments and Methods, 50, pp. 309-320, (1987).

30.   T. Kuntz, M. Sci. Thesis, University of Virginia, May 1991.

31.   D. A. Lukasak and D. A. Koss, Met. Trans. A, <u>21A</u>, pp. 135-143, (1990).

32.   L. M. Hsiung, T. A. Kuntz and H. N. G. Wadley, Proceedings of Conf. on Low Density High Temperature P/M Alloys, Ed. by N. Saunders and W. E. Frazier, TMS (Detroit), p. 21, 1991.

33.   H. N. G. Wadley, D. M. Elzey, J. M. Duva, L. M. Hsiung, S. Parthasarathi, Y. Lu, K. P. Dharmasena, J. M. Kunze and D. G. Meyer, Proc. of Conf. on First Thermal Structures, in press.

34.   L. M. Hsiung, W. Cai and H. N. G. Wadley, Proc. of International Conference on High-Temperature Aluminides and Intermetallics, ASM (San Diego, CA), September 1991, In Press. Also submitted to J. Mat. Sci. and Eng. (A) for publication.

35.   Baumann, S.F., Brindley, P.K. and Smith, S.D., Met. Trans., <u>21A</u>, pp. 1559-1569 (1990).

36.   Strychor, R., Williams, J.C. and Soffa, W.A., Met. Trans., <u>19A</u>, pp. 225-234 (1988).
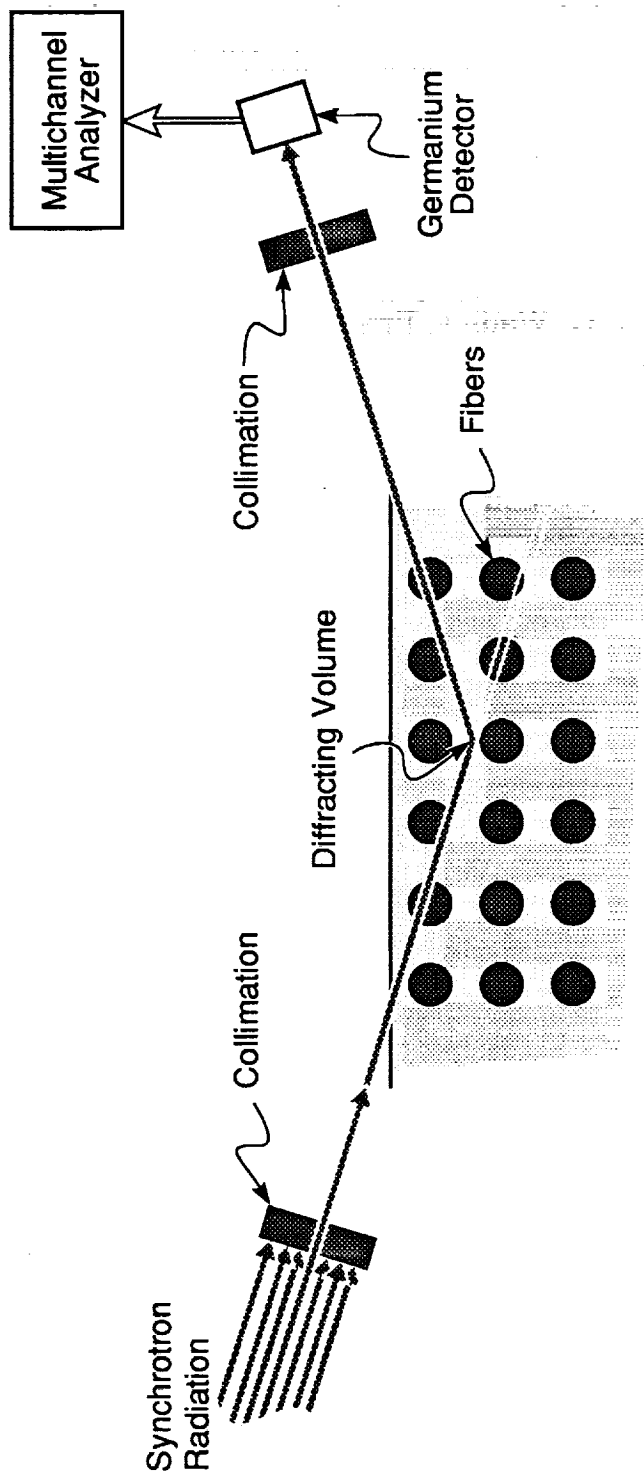
Figure 1. Schematic diagram of the energy disperse x-ray diffraction method.
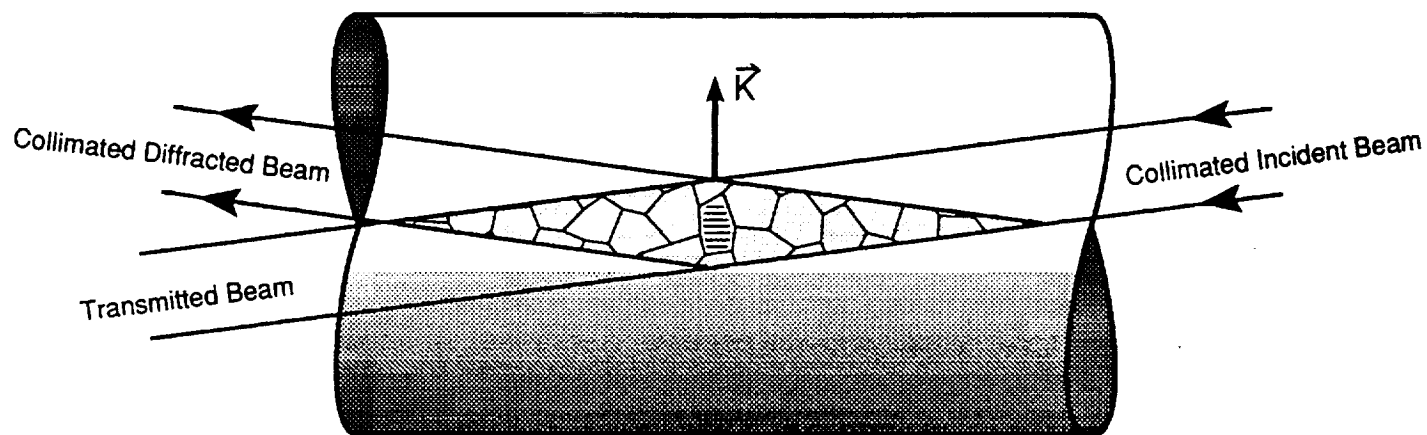
Figure 2. (a) Hoop and (b) radial strain measurement probe geometries.
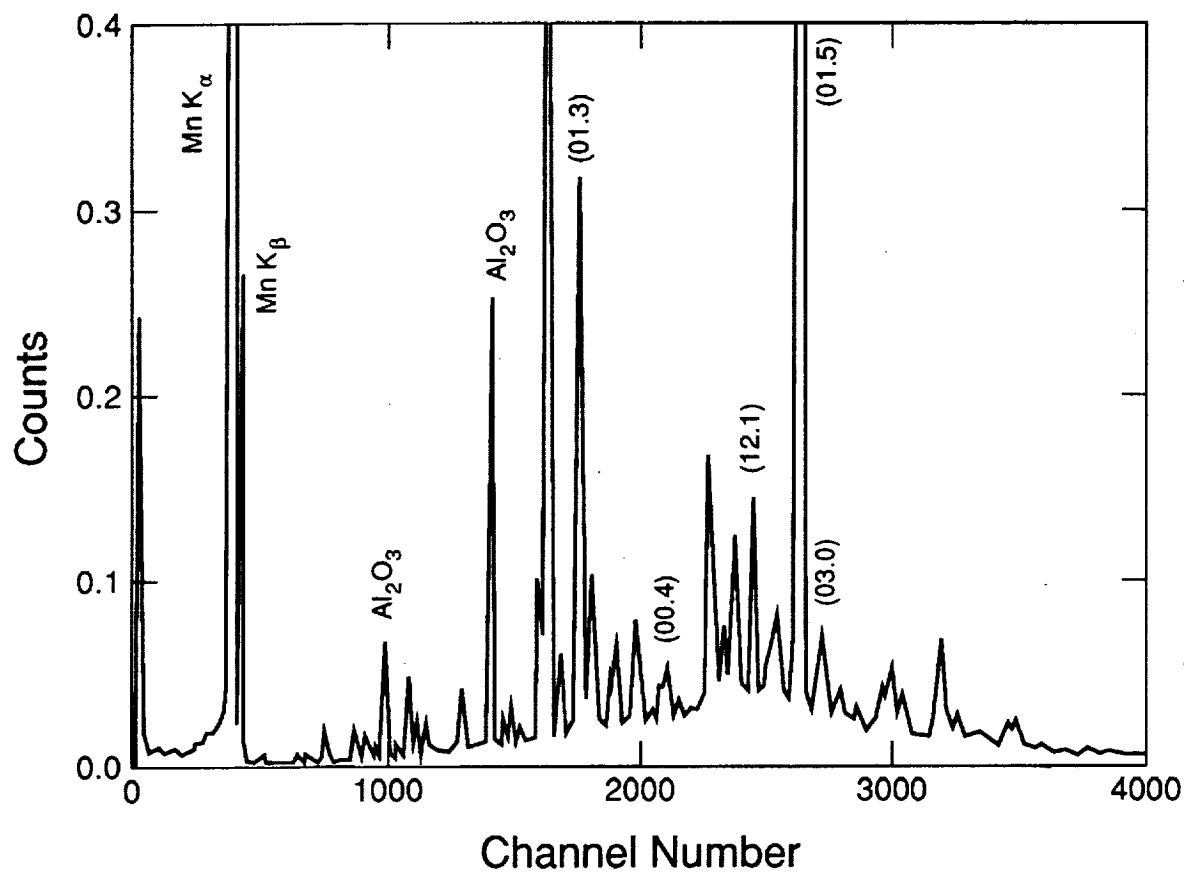
Figure 3a. Typical energy dispersive spectra from the CP Titanium/Al₂0₃ sample probe volume centered on fiber-matrix interface.
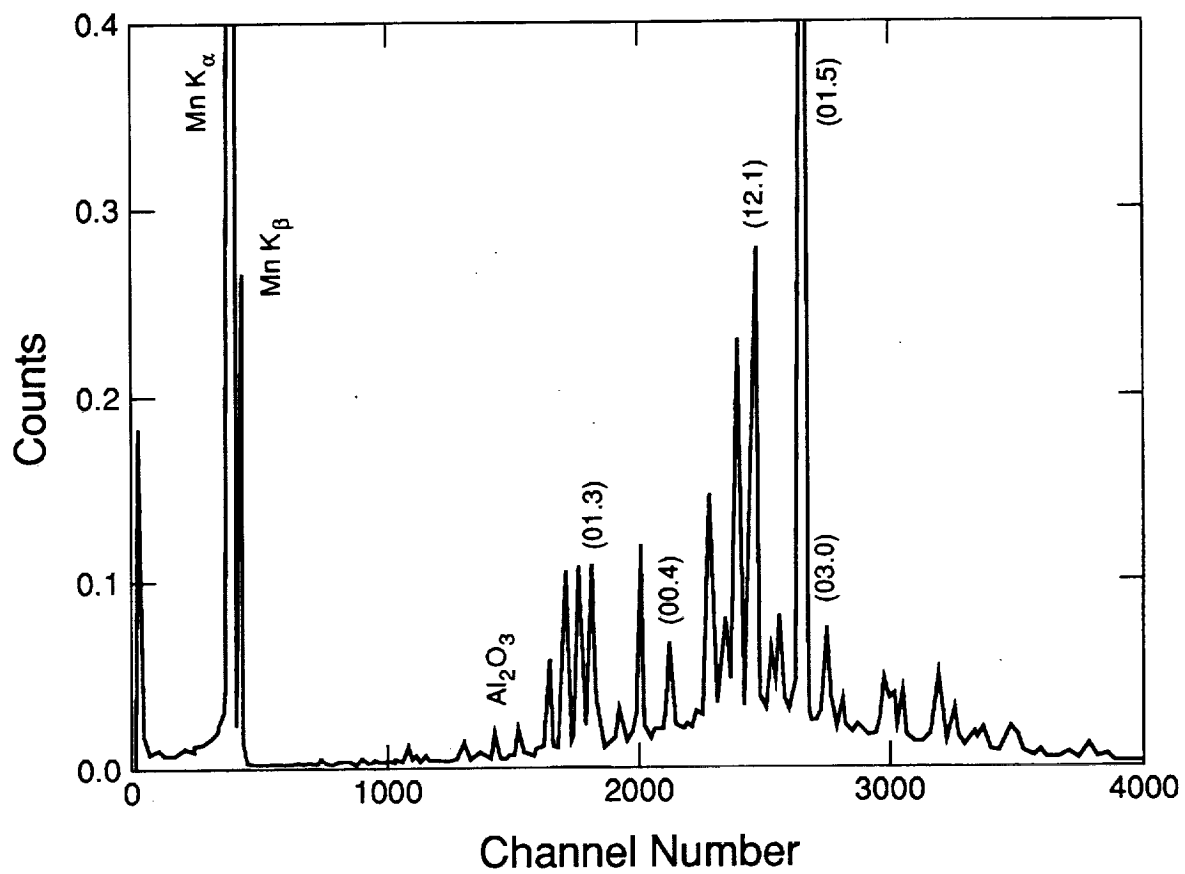
Figure 3b. Typical energy dispersive spectra from the CP Titanium/Al₂O₃ sample translated 40μm into matrix.
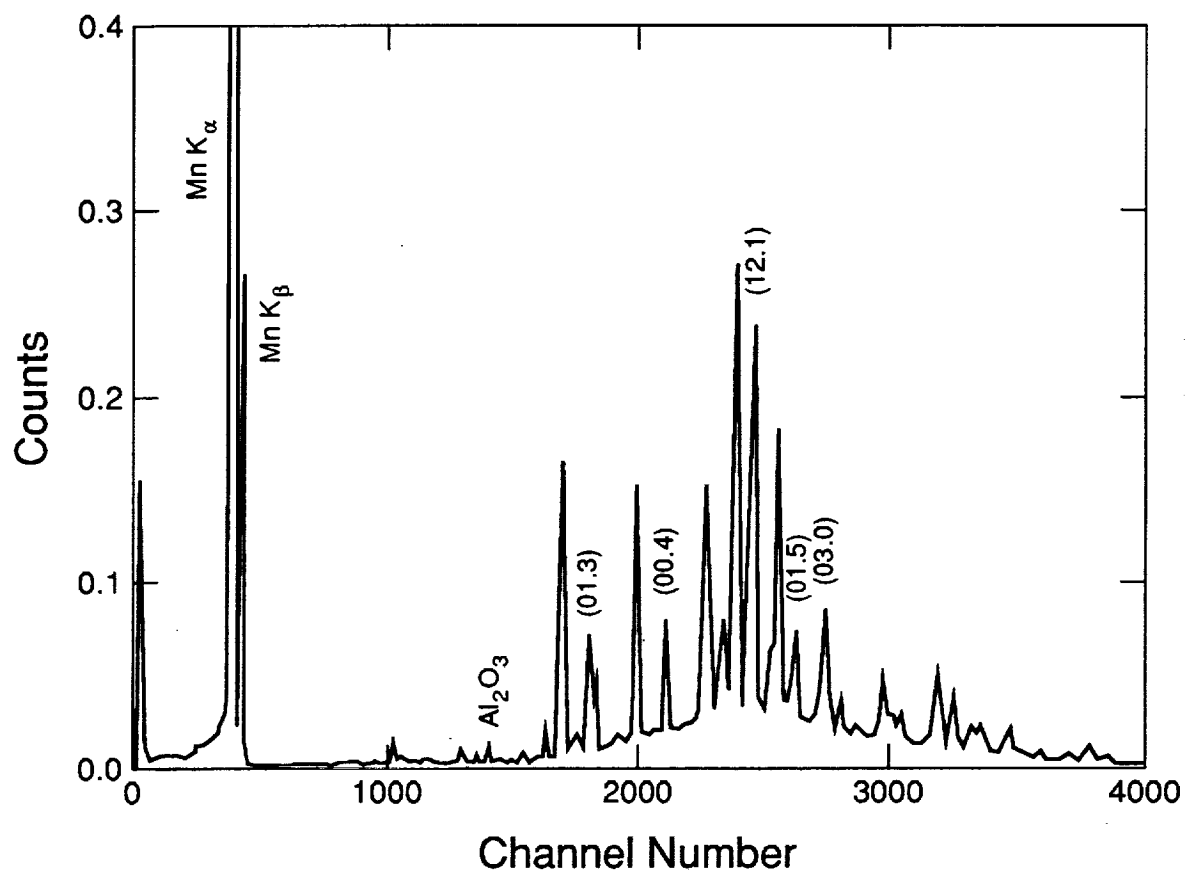
Figure 3c. Typical energy dispersive spectra from the CP Titanium/Al₂0₃ sample translated 80μm into matrix.
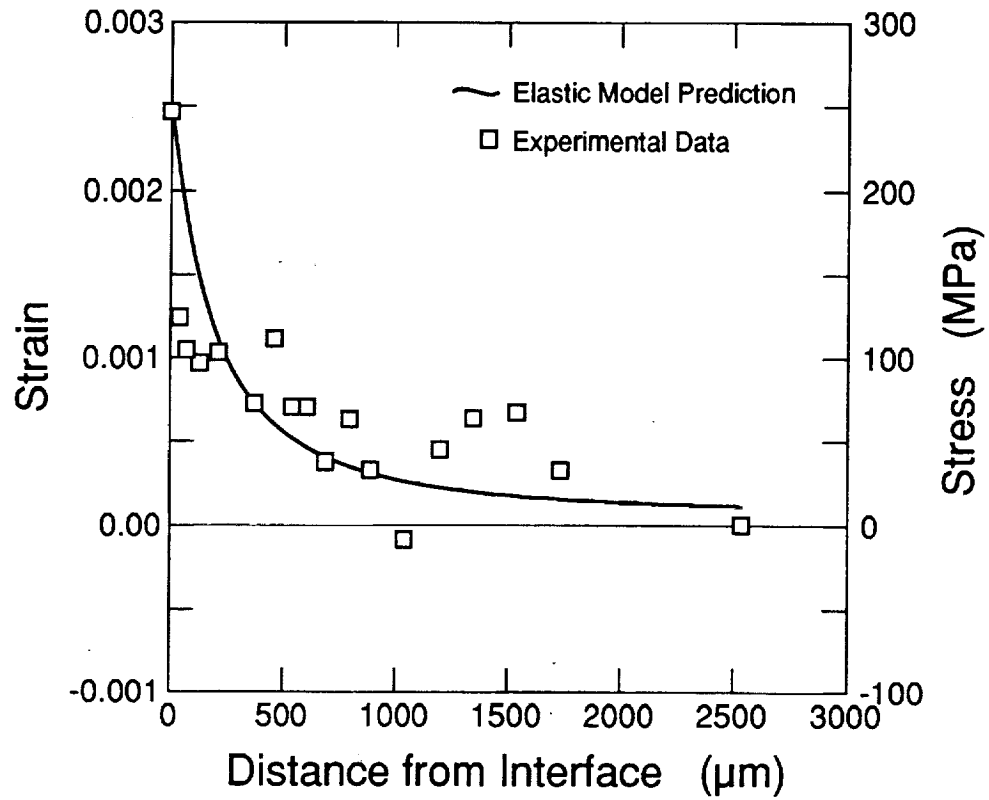
Figure 4. Hoop residual strain profile for the CP Titanium/Al$_2$O$_3$ (HIP0) sample.
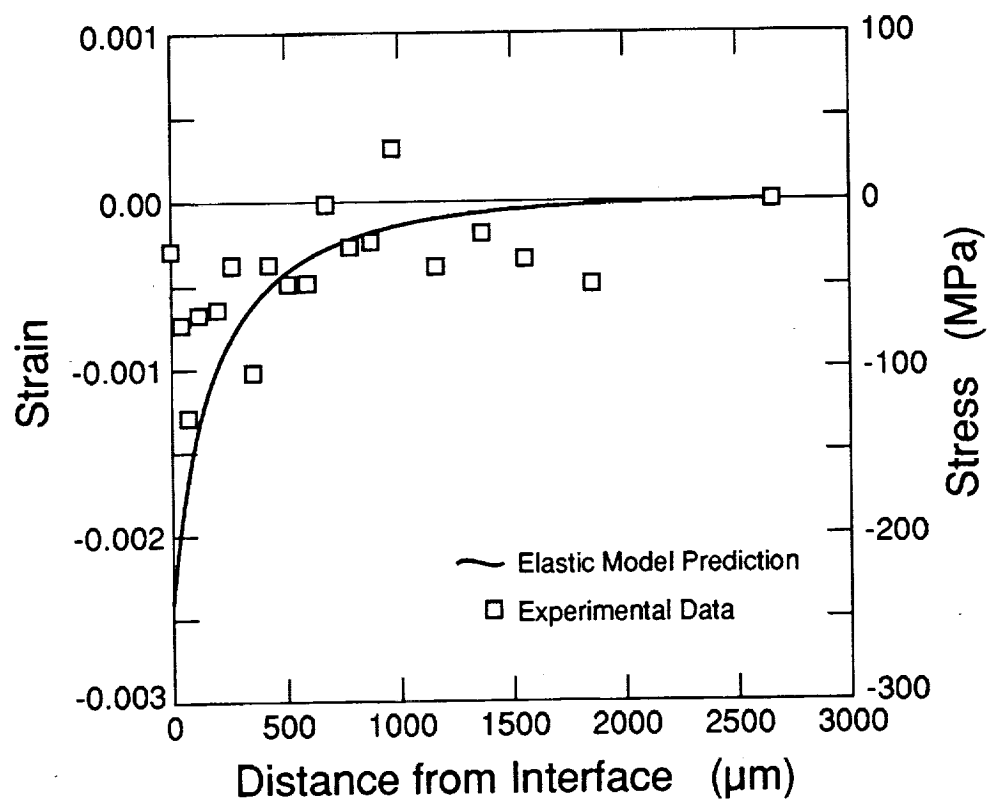
Figure 5. Radial residual strain profile for the CP Titanium/Al$_2$O$_3$ (HIPO) sample.
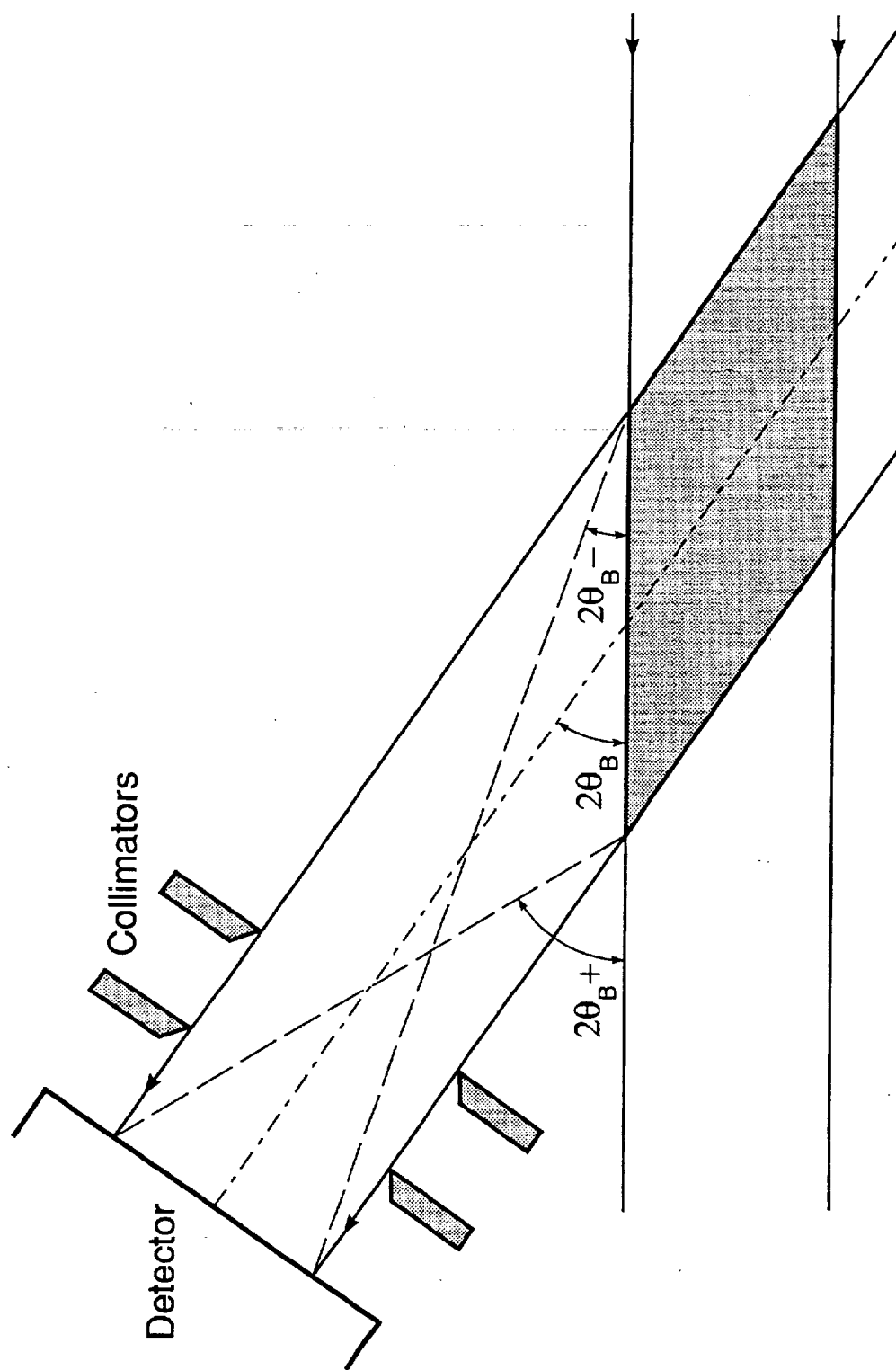
Figure 6. X-ray probe volume schematic diagram showing the range of scattering angles sampled.
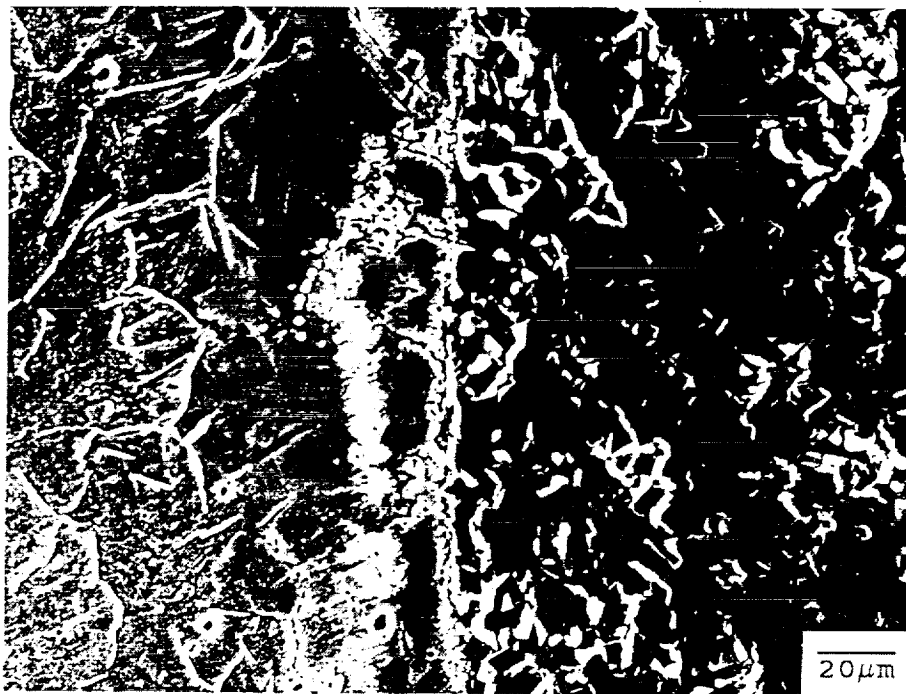
Figure 7. SEM of the interface of the CP Titanium/Al$_2$O$_3$ sample.
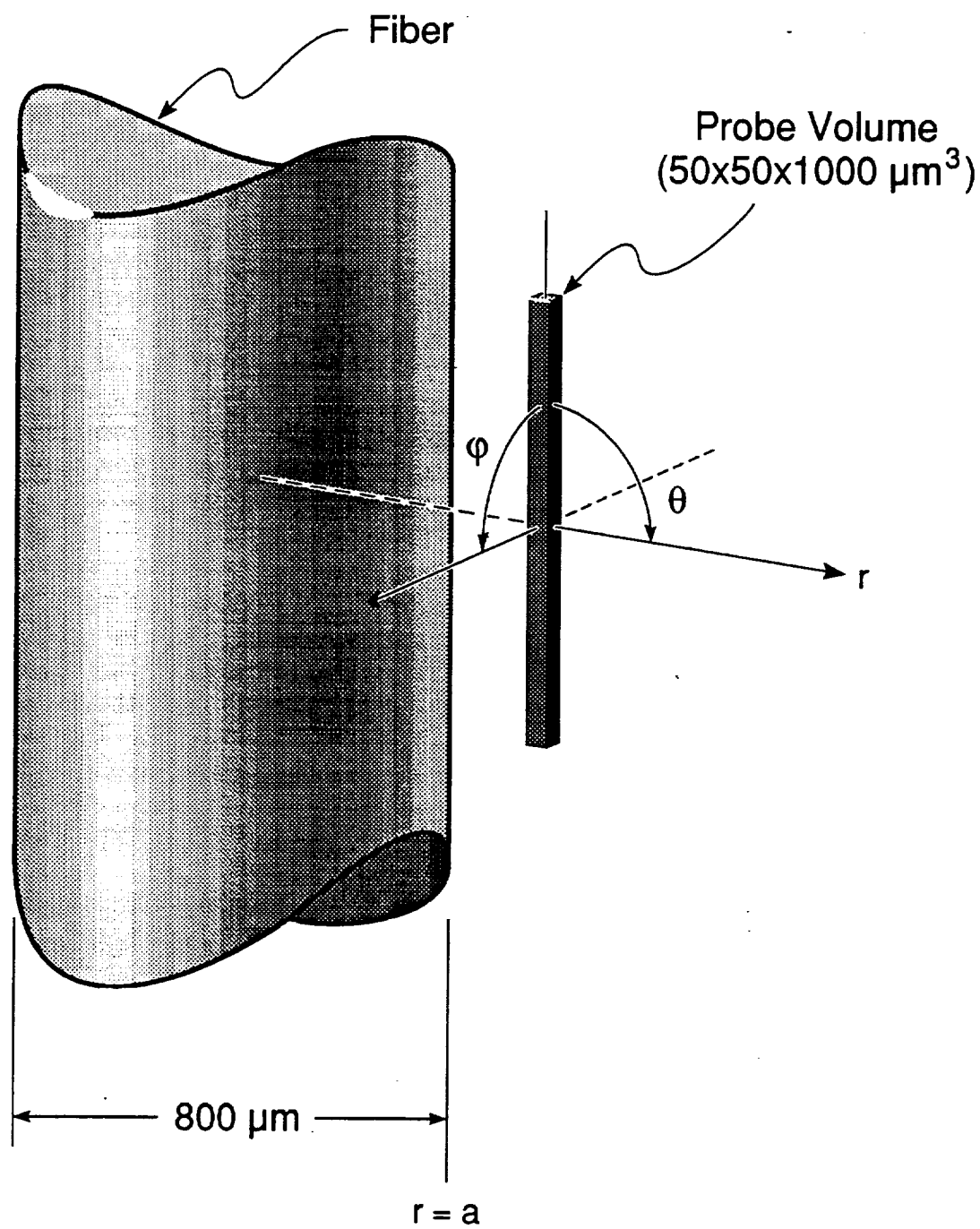
Figure 8. Schematic illustration of probe volume - fiber orientation.
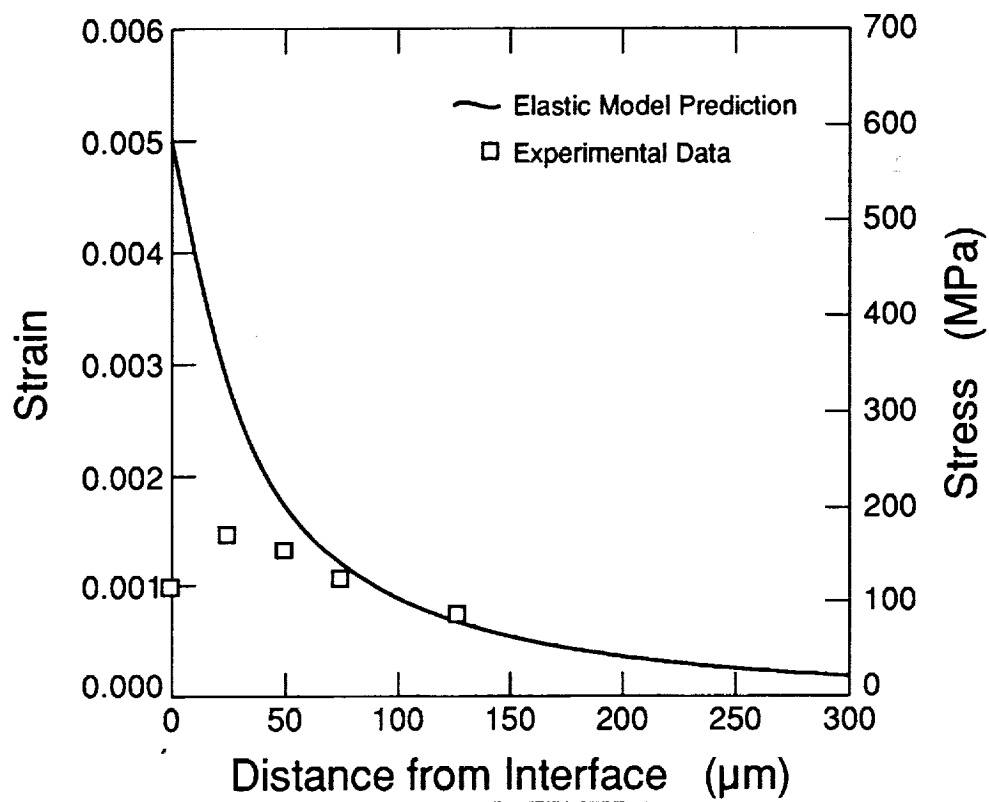
Figure 9. Hoop residual strain profile for the Ti-14Al-21Nb/SCS-6 (HIP1) sample.
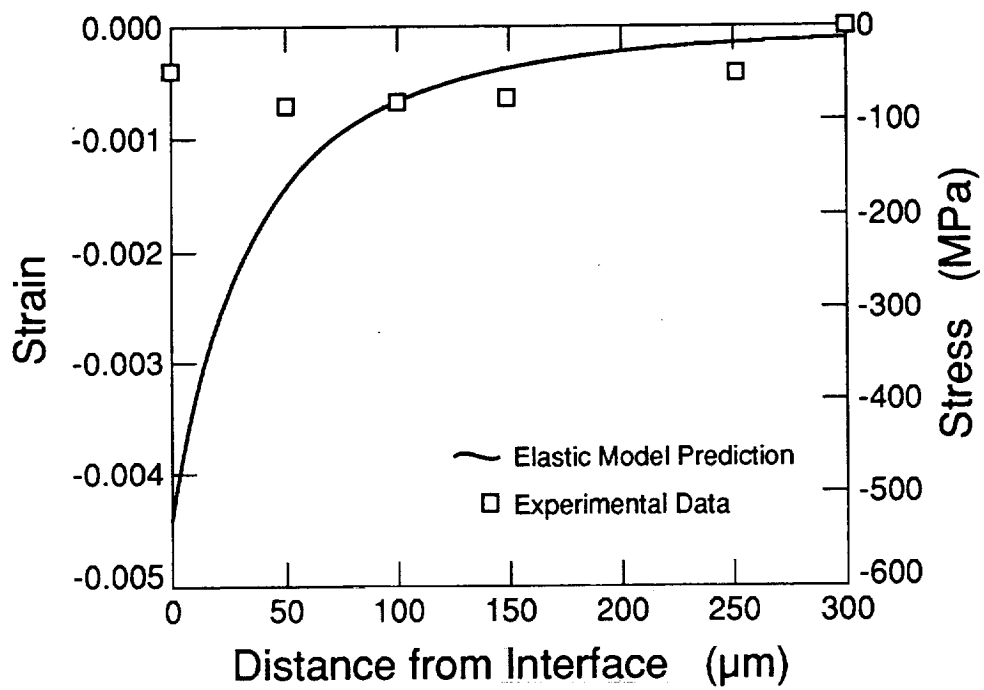
Figure 10. Radial residual strain profile for a Ti-14Al-21Nb/SCS-6 (HIP2) sample.
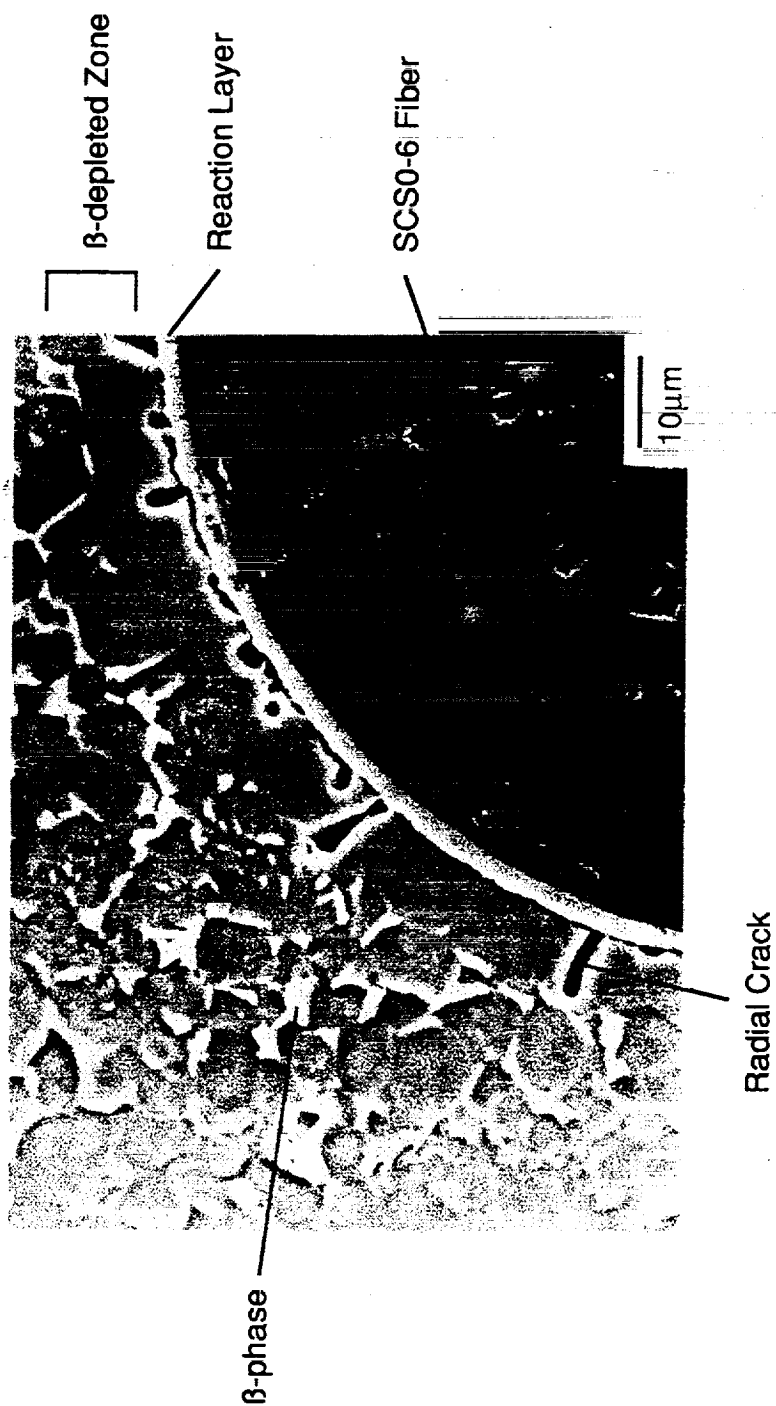
Figure 11. SEM of the interface of sample HIP1.
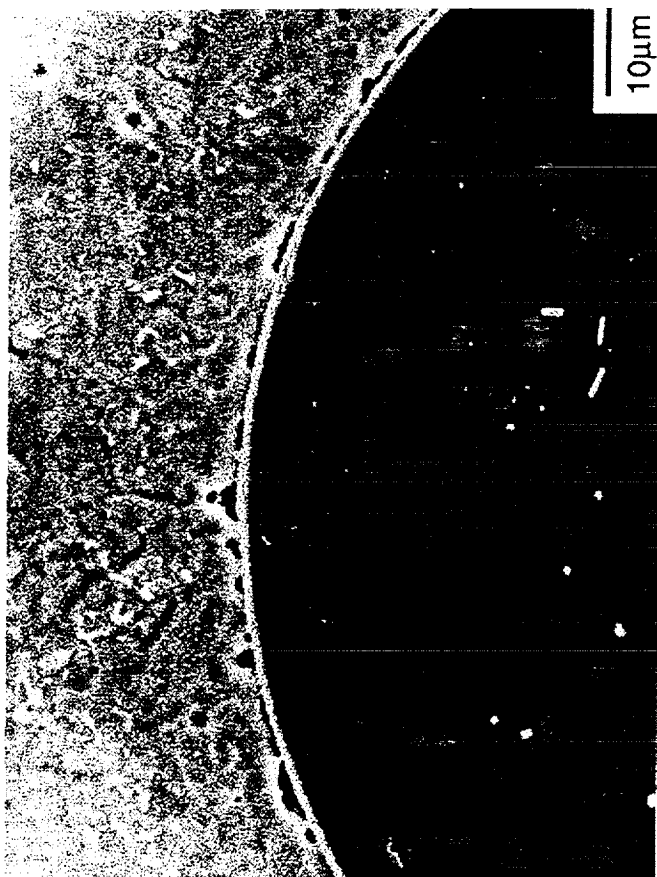
Figure 12. SEM of the interface of sample HIP2.

Appendix II -   University of Virginia Report on Ultrasonics

ULTRASONIC DETERMINATION OF THERMAL RESIDUAL STRESSES IN INTERMETALLIC MATRIX COMPOSITES

Yichi Lu and Haydn N. G. Wadley

Intelligent Processing of Materials Laboratory
School of Engineering and Applied Science
University of Virginia
Charlottesville, Virginia 22903

115

EXECUTIVE SUMMARY

Ultrasonic methods have been investigated as a possible nondestructive evaluation method to determine thermal residual stresses in fiber reinforced intermetallic matrix composites using wave propagation theory and literature data for acoustoelastic constants. Data are available for only a few materials. In order to establish potential concepts, a preliminary study has been conducted for a model composite cell (for which data exist) consisting of an aluminum cylinder (representing the matrix) containing a circular stainless steel inclusion (representing the fiber). We show for the cell that ultrasonic velocity changes caused by a thermal (CTE difference) residual stresses are small but detectable by the Pulse-Echo-Overlap method, provided that one chooses ultrasonic modes whose polarizations are in the directions of larger residual stress components, here σ_r and σ_θ. However, practical difficulties in real composites may swamp the stress effect. In particular, variations in the metal/ceramic ratio sampled by the ray path are thought to be the most severe. An investigation of the use of focused immersion techniques for residual stresses measurements may hold promise since the focused transducers may enable one to better control the metal/ceramic ratio in the volume ultrasonically sampled.

I   INTRODUCTION

Intermetallic matrix composites utilizing continuous silicon carbide/aluminum oxide fibers and α_2-Ti$_3$Al+Nb and γ-TiAl matrices are promising high temperature propulsion materials because of their good specific modulus and high temperature strength. But due to the mismatch in thermal expansion coefficients between the matrix material and the reinforcement (especially the SiC reinforcement), large residual stresses exist in these materials after processing, and they are susceptible to thermal fatigue damage during thermal-mechanical load cycling.

We have investigated the potential of ultrasonic methods for measuring thermal residual stresses. For a linear elastic material without residual stresses, the ultrasonic wave velocity is a constant (independent of stress amplitude) which depends upon the temperature, and microstructural state. Ultrasonic determination of residual stresses is only possible because large residual stresses induce a change in ultrasonic velocity due to the small nonlinear elastic behavior of engineering materials. For many materials, this velocity change can be detected by ultrasonic methods.

Stress induced changes in the ultrasonic velocity are referred to as the acoustoelastic effect. Hughes and Kelly were among the first to report ultrasonic velocity changes (in polystyrene, iron and Pyrex) due to the application of either hydrostatic or uniaxial stresses.[1] Their technique was later used by Egle and Bray to measure the residual stresses in rail steel,[2] by Kino, et al, to map the

stress state near a crack tip,[3] and by Thompson, et al, to separately measure the stress and texture in an orthorhombic material.[4] A comprehensive review on the subject is given in an article by Pao, Sachse, and Fukuoka.[5]

Three ultrasonic wave modes can propagate in bulk solids: one longitudinal and two shear wave modes. All three wave mode velocities are sensitive to the background stress and can be used to detect residual stresses. In what follows, we first give the theoretical background for acousto-elasticity. We then use this insight to discuss and evaluate possible ways to measure the residual stresses in intermetallic matrix composite materials after processing. We are constrained in this by the absence of experimental data for the nonlinear response of these newly emerged alloys, and can only make qualitative statements until these data become available. Our conclusions lead us to believe that the collection of such data could well be worthwhile.

II   ACOUSTOELASTICITY

If a large static deformation is present in an otherwise isotropic, homogeneous medium, the strain energy function W is given by

$$W = \frac{1}{2}\lambda I_1^2 + \mu(I_1^2 - 2I_2) + \frac{1}{6}(m_1 + 6m_2 + 8m_3)I_1^3 - 2(m_2 + 2m_3)I_1I_2 + 4m_3I_3 \tag{1}$$

where I_1, I_2 and I_3 are the first, second and third invariant of the strain tensor given by:

118

$$I_1 = \varepsilon_{11} + \varepsilon_{22} + \varepsilon_{33} \tag{2}$$

$$I_2 = \varepsilon_{11}\varepsilon_{22} + \varepsilon_{22}\varepsilon_{33} + \varepsilon_{33}\varepsilon_{11} - \varepsilon_{12}^2 - \varepsilon_{23}^2 - \varepsilon_{31}^2 \tag{3}$$

$$I_3 = \varepsilon_{11}\varepsilon_{22}\varepsilon_{33} + 2\varepsilon_{12}\varepsilon_{23}\varepsilon_{31} - 6\varepsilon_{11}\varepsilon_{23}^2 - 6\varepsilon_{22}\varepsilon_{31}^2 - 6\varepsilon_{33}\varepsilon_{12}^2 \tag{4}$$

Here, ε is the strain tensor, λ and μ are Lamé elastic constants, and m_1, m_2 and m_3 are so called the third order elastic constants. The last three terms on the right hand side of Eq. (1) ($\sim O(\varepsilon^3)$) can be neglected if the deformation strain is small.

The constitutive relation that relates the stress tensor, σ, and the strain tensor, ε, for a general elastic body is given by :

$$\sigma_{ij} = C_{ijkl}\varepsilon_{kl} \tag{5}$$

where the stiffness tensor C is related to the second derivative of the strain energy function :

$$C_{ijkl} = \frac{\partial^2 W}{\partial\varepsilon_{ij}\partial\varepsilon_{kl}} \tag{6}$$

Since in general, the strain energy W is a cubic function of strain components, Eq. (1), we see that when a relatively large deformation exists, the stiffness tensor C_{ijkl} is a function of the (residual) strain components. For an originally isotropic, linear elastic body, the residual stresses result in anisotropy

119

and nonlinearity, which in turn cause changes in ultrasonic velocity. The usual assumption taken for ultrasonic residual stress work is that a large static deformation exists, and one treats the ultrasonic disturbance, which only causes a small deformation, as a wave motion superimposed on the large deformation. We point out that in this case the equation of motion for the originally isotropic, linear elastic body subjected to a small deformation is unfortunately not applicable.

a)   <u>Homogeneous Deformation</u>

If the deformation is large but homogeneous in the direction of wave propagation, the equation of motion governing the propagation of a superimposed ultrasonic disturbance is linear and is given by

$$(\sigma^r_{jl}\delta_{ik} + C_{ijkl})\frac{\partial^2 u_k}{\partial x_j \partial x_l} = \rho\frac{\partial^2 u_i}{\partial t^2}$$

(7)

where σ^r_{jl} are residual stresses, C_{ijkl} is given by Eq. (6). If the original, undeformed material is isotropic then the problem for the superimposed wave motion becomes anisotropic, since in general the residual stresses are not isotropic, so that the "effective stiffness" $(\sigma^r_{jl}\delta_{ik} + C_{ijkl})$ is not isotropic. The changes in velocity of the ultrasound is the consequence of the residual stresses and the anisotropy. If the original, undeformed material is also anisotropic, then

the problem will be further complicated by the added anisotropy. These changes in velocity can sometimes be detected ultrasonically, and serve as a way of detecting/measuring the homogeneous deformation.

Let us consider a plane wave propagating in the z direction, (the direction in which the deformation is homogeneous). the particle displacement components are :

$$u_i = d_i \exp[ik(z - vt)], \qquad i=1, 2, 3 \tag{8}$$

where d_i are the unit displacement vector components, k and v are the wavenumber and the velocity, respectively. Substituting Eq. (8) into Eq. (7) and using Eqs. (5) and (6) yields an equation for the change to the ultrasonic velocity of each of the bulk waves permitted to propagate in the body:

$$\frac{v_{Lz} - v_{L0}}{v_{L0}} = \frac{1}{2(\lambda + 2\mu)}\left[(\lambda + m_1 + 2m_2)\varepsilon_{kk} + 2(2\lambda + 5\mu + 2m_2 + 4m_3)\varepsilon_{zz}\right] \tag{9}$$

$$\frac{v_{Sx} - v_{S0}}{v_{S0}} = \frac{1}{2\mu}\left[(\lambda + m_2)\varepsilon_{kk} + 2(\mu + m_3)(\varepsilon_{xx} + \varepsilon_{zz}) + 2\mu\varepsilon_{zz}\right] \tag{10}$$

$$\frac{v_{Sy} - v_{S0}}{v_{S0}} = \frac{1}{2\mu}\left[(\lambda + m_2)\varepsilon_{kk} + 2(\mu + m_3)(\varepsilon_{yy} + \varepsilon_{zz}) + 2\mu\varepsilon_{zz}\right] \tag{11}$$

where $\varepsilon_{kk}=\varepsilon_{xx}+\varepsilon_{yy}+\varepsilon_{zz}$ is the dilatation, $v_{L0} = \sqrt{(\lambda + 2\mu)/\rho}$ is the velocity for the

longitudinal wave, and $v_{S0} = \sqrt{\mu / \rho}$ is the velocity for the shear wave in a unstressed body, v_{Lz} is the velocity for the longitudinal wave, and v_{Sx}, and v_{Sy} are velocities for the shear waves polarized in the x and y directions, respectively, in the stressed body. The residual strain state can be obtained if the relative velocity changes can be measured and one knows the values of the second and third order elastic constants for the material of interest (ie. λ, μ, m_1, m_2, and m_3).

When a shear wave propagates across a stressed body in the direction of a principal strain, say ε_{zz}, the wave will be split into two shear waves polarizing in the two other principal strain directions (the so called acoustoelastic birefringence effect). The two shear waves propagate with velocities given by Eqs. (10) and (11), from which a simple equation can be obtained :

$$\frac{v_{Sx} - v_{Sy}}{v_{S0}} = \frac{\mu + m_3}{\mu}(\varepsilon_{xx} - \varepsilon_{yy}) \tag{12}$$

Having obtained the strain components, the stress components can be readily obtained using the linearized stress-strain relation:

$$\sigma_{ij} = \lambda \varepsilon_{kk} \delta_{ij} + 2\mu \varepsilon_{ij} \qquad i=x, y, z \tag{13}$$

where δ_{ij} is the Kronecker delta, $\delta_{ij} = 1$ if $i = j$, $\delta_{ij} = 0$ if $i \neq j$.

b) Inhomogeneous Deformation

For a continuous fiber reinforced composite, the matrix stresses vary with the radial distance from the fiber. In this case, the large deformation is inhomogeneous in the radial direction. If an ultrasonic disturbance is superimposed on the inhomogeneously deformed body, the governing equation of motion is given by

$$(\sigma^r_{jl}\delta_{ik} + C_{ijkl})\frac{\partial^2 u_k}{\partial x_j \partial x_l} + \frac{\partial C_{ijkl}}{\partial x_j}\frac{\partial u_k}{\partial x_l} = \rho\frac{\partial^2 u_i}{\partial t^2} \tag{14}$$

The problem now is not only anisotropic, but also nonlinear since $\partial C_{ijkl}/\partial x_j \neq 0$. To determine the nature of wave propagation we have to solve a second order, nonlinear partial deferential equation. We are unaware of any available method to tackle this problem, and conclude that a precise simulation is not possible at this time. These types of differential equation usually lead to dispersive wave propagation. For weak inhomogeneities one can make a local homogeneous approximation, and obtain rough estimates of likely effects of a large deformation upon ultrasonic propagation in a composite. It is this approach that has been considered below.

III NUMERICAL EXAMPLE

Before any residual stress state can be determined ultrasonically one must know the values of Lamé constants λ and μ, the third order elastic constants m_1, m_2 and m_3, and the density ρ. Lamé constants λ and μ and the density ρ can be

measured on the unstressed material. A simple way to find the third order material constants is to load a specimen with a known stress state (eg uniaxially), and measure the relative velocity change for the longitudinal wave, and for the shear waves polarizing in the directions parallel and perpendicular to the loading direction. One then readily obtains the third order material constants by substituting the relative velocity changes into Eqs. (9-11). Published results for the third order elastic constants are available for only a few materials, and none are the intermetallic alloys and fibers of interest. As an example case, we choose aluminum as the matrix material, and stainless steel as the fiber.

The material constants used are listed in Table I.[11,12] The thermal linear expansion coefficients for aluminum and stainless steel are $24 \times 10^{-6}/°C$ and $12 \times 10^{-6}/°C$, respectively, and the densities are 2.7 g/cm^3 and 7.8 g/cm^3, respectively.

Table I Material Constants GPa

	λ	μ	m1	m2	m3
Aluminum	58.82	24.41	1.0	364.0	332.0
Stainless Steel	107.4	81.9	-13.0	-200.0	-200.0

We first present the residual stress field around a single fiber and then estimate the perturbation to the velocity for a cylindrical cell of the composite containing a single fiber.

(a)   <u>Thermal Stress Problem</u>

Consider a solid cylinder with a radius b containing a cylindrical inclusion of radius a, Fig. 1, the cylinder length is assumed to be much larger than the inclusion radius. For a temperature difference $\Delta T = T - T_0$, where T_0 is the processing temperature and T is the current (room) temperature, the elastic thermal stresses in the matrix (the residual stresses we seek to measure) are given by :[6]

$$\sigma_r = \frac{p}{(1-(a/b)^2)}\left(\frac{a^2}{r^2} - \frac{a^2}{b^2}\right), \qquad b \geq r \geq a \tag{15}$$

$$\sigma_\theta = \frac{-p}{(1-(a/b)^2)}\left(\frac{a^2}{r^2} + \frac{a^2}{b^2}\right), \qquad b \geq r \geq a \tag{16}$$

$$\sigma_z = -\frac{c_1 + 2c_2}{c_2 + c_3}\left(\frac{(a/b)^2}{1-(a/b)^2}\right)p, \qquad b \geq r \geq a \tag{17}$$

where

$$p = \frac{c_2 + c_3}{c_1 c_3 - 2c_2^2}(\alpha_m - \alpha_f)\Delta T \tag{18}$$

is the radial compressive stress at the inclusion-matrix interface, α_m and α_f are the linear thermal expansion coefficients for the matrix and the fiber,

respectively,

$$c_1 = \frac{1-v_f}{E_f} + \frac{v_m}{E_m} + \left(\frac{1+(a/b)^2}{1-(a/b)^2}\right)\frac{1}{E_m} \qquad (19)$$

$$c_2 = \frac{v_f}{E_f} + \left(\frac{(a/b)^2}{1-(a/b)^2}\right)\frac{v_m}{E_m} \qquad (20)$$

$$c_3 = \frac{1}{E_f} + \left(\frac{(a/b)^2}{1-(a/b)^2}\right)\frac{1}{E_m} \qquad (21)$$

E_m and E_f are Young's moduli, v_m and v_f are Poisson's ratios of the matrix and the fiber, respectively. Figure 2 shows the variation of stresses as functions of radial distance r. For this problem, the calculated values of the compressive radial stress σ_r and the tensile circumferential stress σ_θ near the inclusion-matrix interface are well beyond the yield stress for pure aluminum (~ 40 MN/m^2), but for our purposes we will assume the matrix to remain elastic. The axial stress σ_z is constant, which may not be true for metal matrix composites containing a large number of reinforcements, (see for example Nimmer, et al[7]).

(b)   Relative Velocity Changes Due to the Residual Stresses

The local relative velocity changes due to the residual stresses are usually small, so that accurate velocity measurement techniques are required. The Pulse-Echo-Overlap (PEO) Method[14] has a time of flight measurement accuracy of 1 part

in 10^4 and a stress resolution of 20 MPa has been reported,[10] which is significantly better than the level required for composites (for instance ± 70 MPa would be acceptible). To use this method, the time of flight for ultrasonic signals are determined by overlapping the signals at the beginning and end of the ultrasound path. The overlapping is performed on the face of an oscilloscope by driving the repetition period of pulses at a frequency such that the period of the pulse frequency is equal to the time of flight.

We have analysed two setups to measure the residual stresses.

1) Pulse-Echo or Pulse-Catch setup (Fig. 3).

This setup can be used for each of the three wave modes. All three modes propagate in the direction of the fiber. To calculate the relative velocity changes, Eqs. (15-17) are first used to obtain the strain components according to :

$$\varepsilon_{xx} = -\frac{1}{2(3\lambda + 2\mu)}(\sigma_r + \sigma_\theta + \sigma_{zz}) + \frac{1}{2\mu}\sigma_r \qquad (22)$$

$$\varepsilon_{yy} = -\frac{1}{2(3\lambda + 2\mu)}(\sigma_r + \sigma_\theta + \sigma_{zz}) + \frac{1}{2\mu}\sigma_\theta \qquad (23)$$

$$\varepsilon_{zz} = -\frac{1}{2(3\lambda + 2\mu)}(\sigma_r + \sigma_\theta + \sigma_{zz}) + \frac{1}{2\mu}\sigma_z \qquad (24)$$

since the problem studied here is axisymmetric. These are then substituted into Eqs. (9-11) to obtain the relative velocity changes for three wave modes. Figure 4 shows the relative velocity changes for all three wave modes as well as the one for

acoustoelastic birefringence for $\Delta T = -500$ °C. We see that the relative velocity change for the longitudinal wave mode is constant. This is because the axial stress σ_z, and the sum of σ_r and σ_θ are constant, see Eq. (9). Two shear wave modes show large relative velocity changes near the interface (~ 10%), since in the directions of polarization (r and θ), the residual stresses σ_θ and σ_r have large values. Notice that the radial strain is compressive while the circumferential strain is tensile. The acoustoelastic birefringence measurement is extremely attractive in this case. By measuring the relative shear wave velocity changes in radial and circumferential directions, respectively, the birefringence results in a relative velocity change as high as 20 % near the interface. By measuring the relative velocity changes along the radial direction, one might even be able to map the stress variations in the matrix material.

Assuming rays propagate parallel with the interface (r=1.2a), Fig. 5 shows the relative velocity changes as functions of the temperature difference ΔT (ignoring temperature dependence of the moduli and density). When the temperature difference is larger than 200 °C, the relative velocity change for the birefringence measurement is larger than 5 %, which can be easily detected by the PEO method.

Since for the pulse-echo or pulse-catch setup in which the wave propagates parallel to the inclusion axis, the shear wave modes show larger relative velocity changes, we therefore suggest the use of shear wave modes and the birefringence measurement to measure the residual stresses in this axial propagation configuration.

2)   Creeping Ray setup (Fig. 6).

It may be easier to make ultrasonic measurements normal to the fibers as

opposed to the simpler to interpret axial measurement (e.g. in uniaxial plates).

In this case, a creeping ray may be of some interest. The existence of the creeping

ray was discovered more than forty years ago. The physical explanation of the

creeping ray is that any ray tangent to the inclusion boundary is bent around the

inclusion, and the boundary points act as Huygens sources reradiating

ultrasound. The signal due to this ray, though much smaller in amplitude

compared to other rays, is often detectable.[13]

The creeping ray propagates with the velocity of the incident wave in the

matrix material.[13] Since the ray path is near the interface (matrix side), the

velocity depends only on the local mechanical properties of the matrix material

near the interface. The creeping ray setup can be used to measure the crucial

stresses σ_θ and σ_r near the interface. To calculate the relative velocity changes,

we can determine the velocity v_0 as the one measured far away from the fiber.

Suppose that rays propagate approximately with the speed v_0 from $y = -b$ to $y = 0$,

Fig. 7, the residual stresses thus only affect the time of flight along the ray path

from the point $(-a, 0)$ to the point $(a, 0)$. Notice that creeping rays always

propagate with the velocity of incident wave, the ray path can be assumed to be

staight with a length of $a\pi$, so that the velocity affected by the residual stresses is

determined as :

$$v = \frac{t - t'}{\pi a} \qquad (25)$$

where $t' = 2b/v_0$. Figure 8 shows the relative velocity changes as functions of the temperature difference ΔT. We see for this case that the longitudinal wave mode and one shear wave mode polarizing in the direction normal to the inclusion axis show larger relative velocity changes. This is again because in the directions of polarization of these two waves (circumferential for the longitudinal wave and radial for the shear wave), the residual stresses σ_θ and σ_r have large values, which severely change the local stiffness. Another shear wave mode polarized in the z direction shows only a very small change, resulting from small residual stress level of σ_z. The former two wave modes polarizing in the circumferential and the radial directions are suggested for the residual stress measurement for this setup configuration.

IV DISCUSSION

The relative velocity change $\Delta v/v_0$ due to residual stresses in CTE mismatched systems is proportional to $|\Delta \alpha \Delta T|$. For the problem studied here, where aluminum was chosen as the matrix material, and stainless steel as the fiber, $\Delta \alpha = 12 \times 10^{-6}/°C$. For the γ-TiAl and SiC fibers, $\alpha_m \approx 10 \times 10^{-6}/°C$, $\alpha_f \approx 5 \times 10^{-6}/°C$, so that $\Delta \alpha = 5 \times 10^{-6}/°C$. Since the processing temperature for the γ intermetallic matrix composite materials is between 1000 ~ 1100 °C, the temperature difference $\Delta T \sim 1000$ °C is about twice as we have used in the

130

calculation ($\Delta T = -500$ °C). So even though the difference in the thermal expansion coefficients for the Ti-Al intermetallic material is only about half of that we have used in our calculation, we expect that the velocity changes for the intermetallic matrix be about the same scale as those studied here, provided that the (presently unknown) third ordered elastic constants are similar to those of aluminum.

Our conclusions above were based on a model containing only a single fiber (inclusion). For a composite with a large number of fibers, the residual stress distribution is quite different[7] and the fiber-fiber interaction must be considered. The fiber-matrix interface condition may add extra complexities to the problem. For wave propagating in the direction normal to the fiber axis, only the creeping signal scattered by the nearest fiber can be clearly identified. Those signals scattered from more distant fibers may be too complex to be resolved (we would need to know their locations in the composite to the same order as the precision of the velocity measurement, i.e. 1 part in 10^4 or so).

The stress resolution can often be achieved to a level of 20 MPa in homogeneously strained body. Propagation of ultrasound in the axial direction could potentislly result in stress determination to this accuracy provided one has a good spatial resolution. The spatial resolution is controlled by the size of the transducers used. The smallest common (unfocused) piezoelectric transducers is about 5 mm in diameter and the beam will sample many fibers. Because the wave velocity in fibers is much greater than that in the matrix, this results in measured or apparent velocities that are controlled more by the fraction of fibers in the sampled path than the perturbation (due to stress) of the matrix. In order to sample a smaller volume of materials, we suggest the use of focused

piezoelectric transducers operating in a water bath. For example, using a spherically focused transducer with element size of 20 mm, operating at 25 MHz, one can obtain a spacial resolution of about 100 μm, comparable to a single fiber size. Figure 9 shows an example of the recommended setup.

V   SUMMARY

In conclusion, we argue that the relative velocity changes caused by thermal residual stresses can be detected by the PEO method. To do so, one must first have determined the third order elastic constants of the composite materials of interest. To effectively measure the residual stresses, one must select wave modes that polarize in the directions in which the residual stresses have their largest values. For the problem studied here, the acoustoelastic birefringence measurement is the most effective way to determine the residual stress state. To achieve a higher spatial resolution, high frequency, focused immersion transducers are suggested.

Further research activities to address the practical issues should include the measurement of the third order elastic constants for the intermetallic alloys of interest, experiments on a model system with known residual stress states to verify the approximate theory. Finally, analytical theory and experimental techniques must be developed for ultrasonic testing on real composites.

REFERENCES

1. "Second-Order Elastic Deformation of Solids," D. S. Hughes and J. L. Kelly, Physical Review, 92(5), 1145-1149, (1953).

2. "Measurement of Acoustoelastic and Third-order Elastic Constants for Rail Steel," D. M. Egle and D. E. Bray, J. Acoust. Soc. Am. 60(3), 741-744, (1976).

3. "Acoustic Measurements of Stress Field and Microstructure," G. S. Kino, et al., J. NDE, 1(1), 67-77, (1980).

4. "Angular Dependence of Ultrasonic Wave Propagation in a stressed, Orthorhombic Continuum: Theory and Application to the Measurement of Stress and Texture," R. B. Thompson, S. S. Lee and J. F. Smith, J. Acoust. Soc. Am. 80(3), 921-931, (1986).

5. "Acoustoelasticity and Ultrasonic Measurements of Residual Stresses," Y. Pao, W. Sachse and H Fukuoka, in "Physical Acoustics," 17, eds., W. P. Mason and R. N. thurston, (1984).

6. D. Brooksbank and K. W. Andrews, "Tessellated Stresses Associated with Some Inclusions in Steel," J. Iron & Steel Inst., 207, 474-483, (1969).

7. "Fiber-Matrix Interface Effects in the Presence of Thermally Induced Residual Stresses," R. P. Nimmer, J. Comp. Tech. Res., 12(2), 65-75, (1990).

8. "Acoustoelastic Effect of Rayleigh Surface Wave in Isotropic Material," M. Hirao, H. Fukuoka and K. Hori, J. Appl. Mech., 48, 119-124, (1981).

9. "The Measurement of Ultrasonic Velocity," E. P. Papadakis, in "Physical Acoustics," 19, eds., R. N. Thurston and , A. D. Pierce, (1990).

10. "Residual Stress Determination Using Acoustoelasticity," J. J. Dike and G.

C. Johnson, J. Appl. Mech., **57**, 12-17, (1990).

11. M. Hirao, H. Fukuoka and K. Hori, J. Appl. Mech., **48**, 119, (1981).

12. A. V. Clark, R. B. Mignogna and R. J. Sanford, "Acousto-elastic Measurement of Stress and Stress Intensity Factors Around Crack Tip," Ultrasonics, **21**, 57-64, (1983).

13. Y. H. Pao and W. Sachse, "Interpretation of Time Records and Power Spectra of Scattered Ultrasonic Pulses in Solids," J. Acoust. Soc. Am., 56(5), 1478-1486, (1974).

14. E. P. Papadakis, in "Physical Acoustics: Principles and Methods," **12**, eds. W. P. Mason and R. N. Thurston, Academic Press, New York, 277-374, (1976).
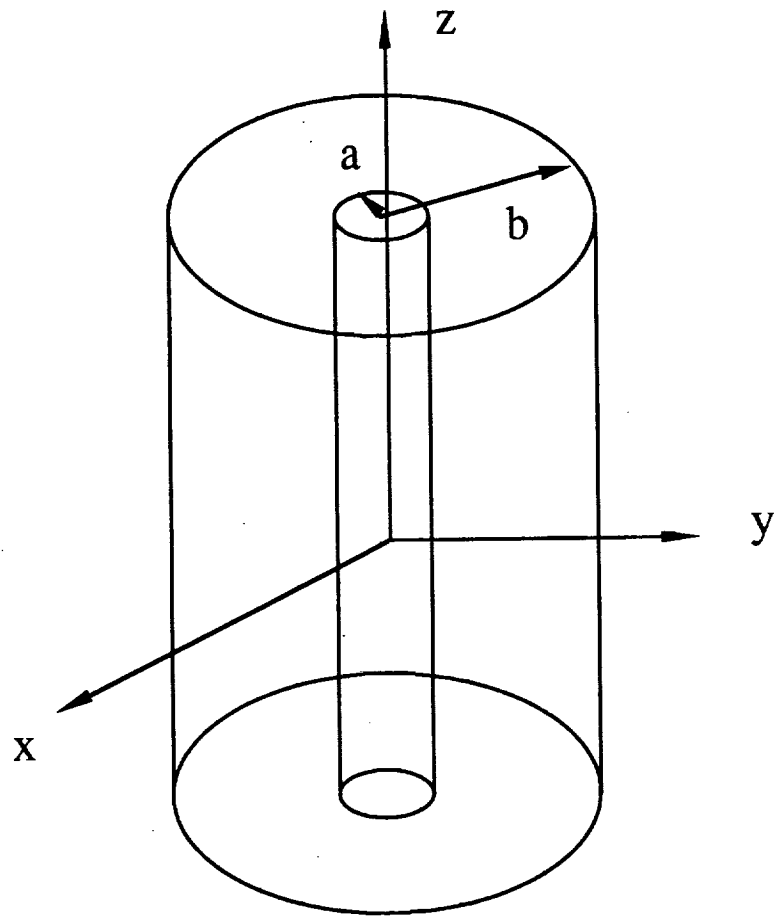
Fig.1   A cylindrical cell of a composite containing a single fiber.
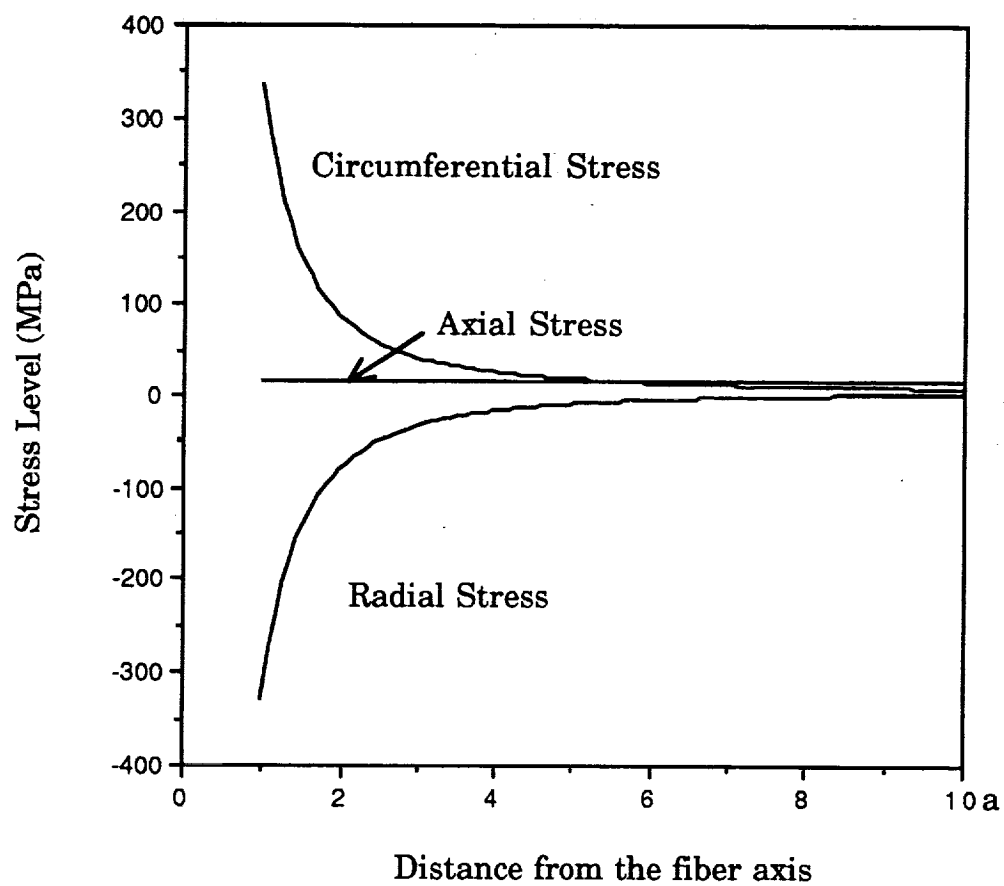
Fig. 2   Residual stresses as functions of the radial distance from the fiber axis.

PULSE - ECHO METHOD
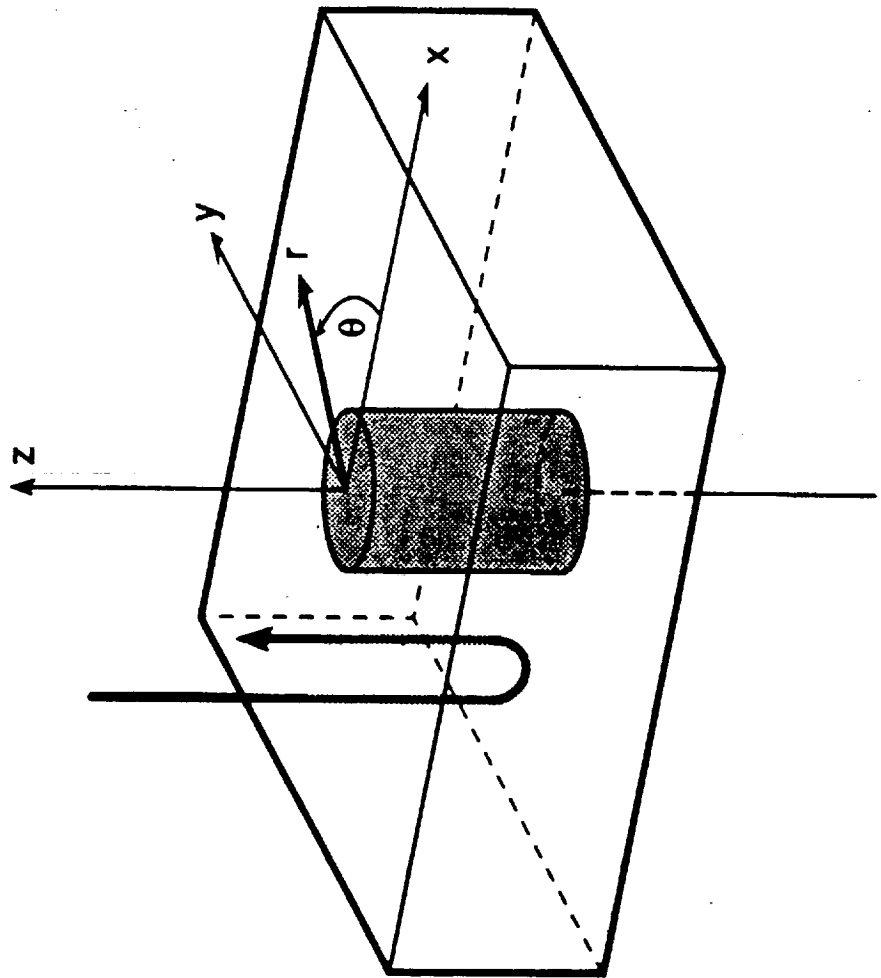
Fig. 3   Pulse-Echo or Pulse Catch setup.
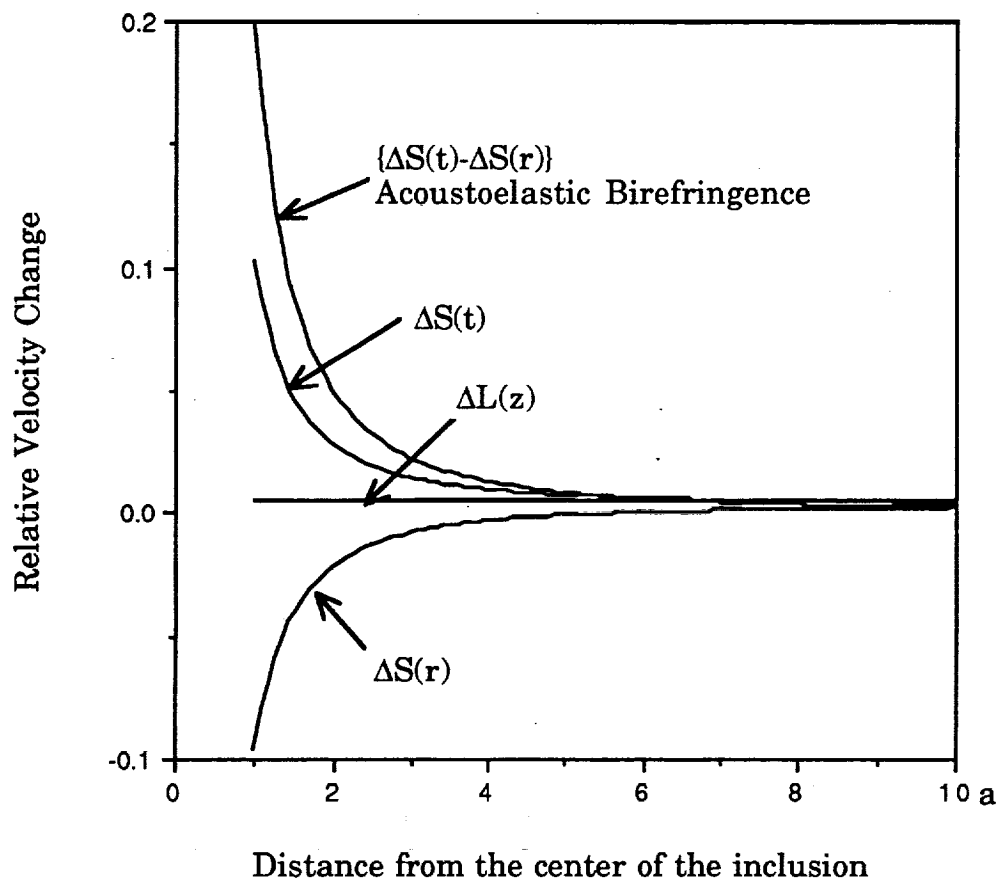
Fig. 4   Relative velocity changes as functions of the radial distance; $\Delta L(z)$ is for the longitudinal wave mode propagating in the z direction, $\Delta S(t)$ and $\Delta S(r)$ are for the shear wave modes polarized in the tangential and radial directions, respectively.
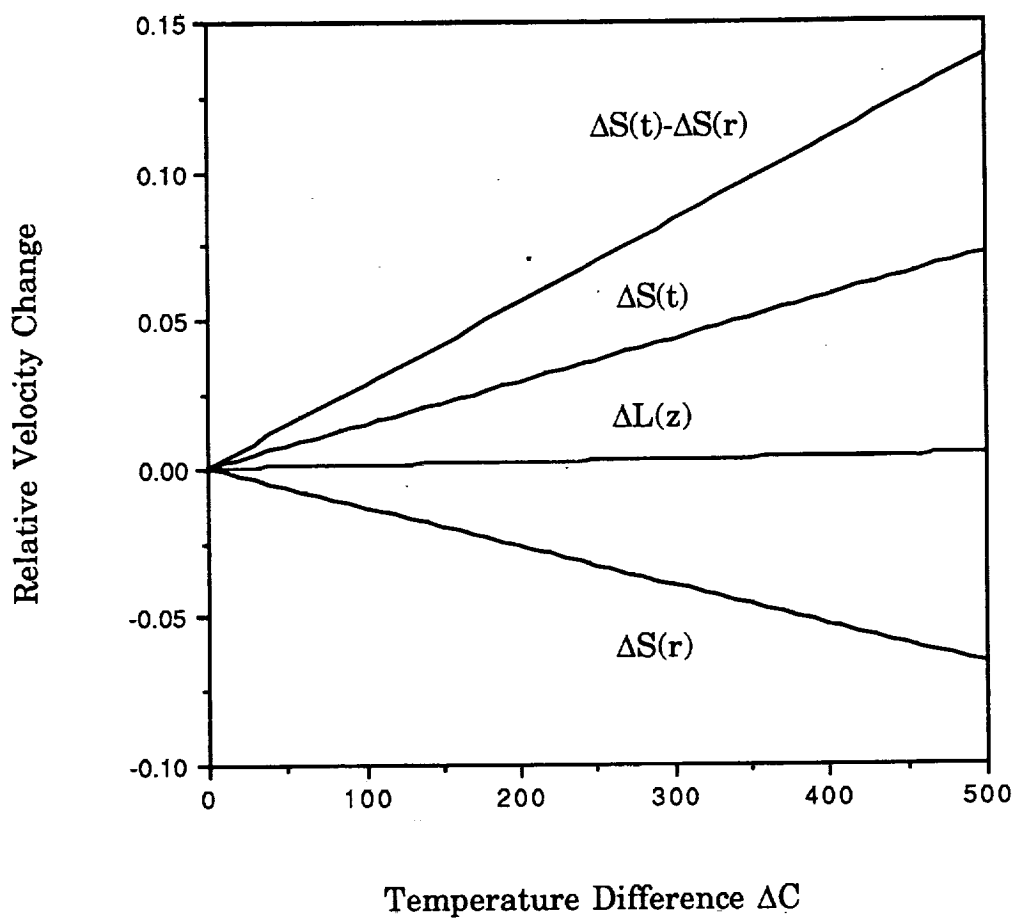
Fig. 5   Relative velocity changes as functions of temperature difference.
Notation same as those in Fig. 4.
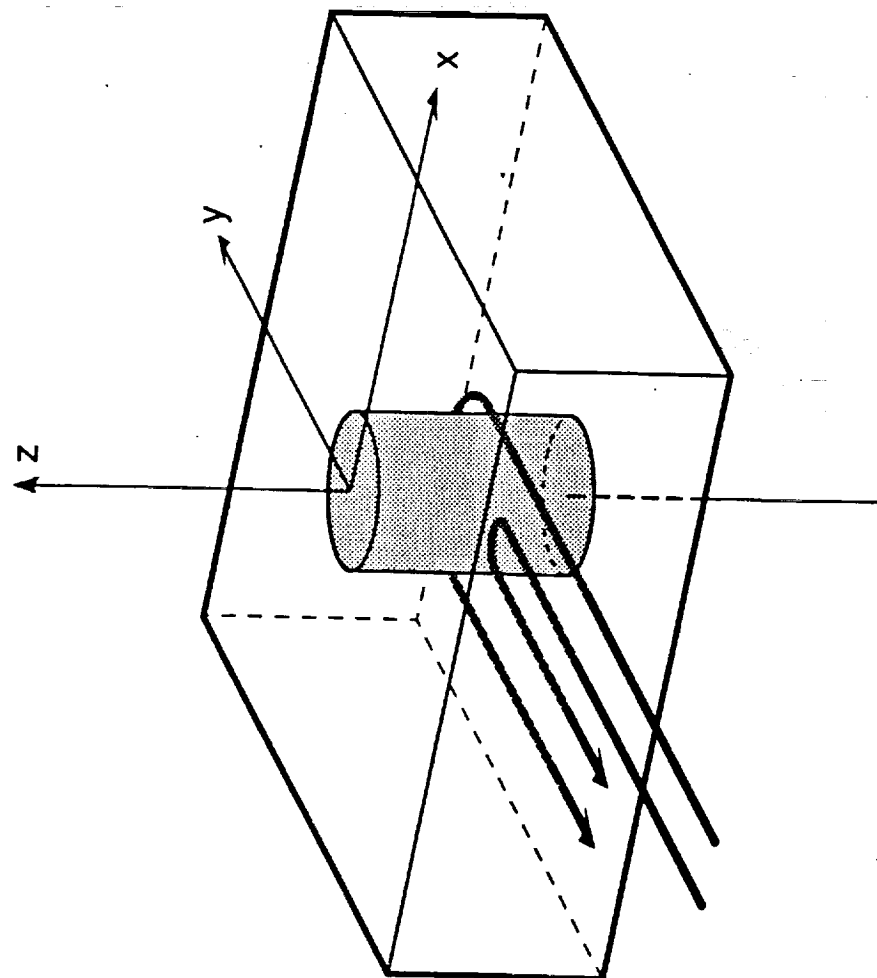
Fig. 6   Creeping ray setup.
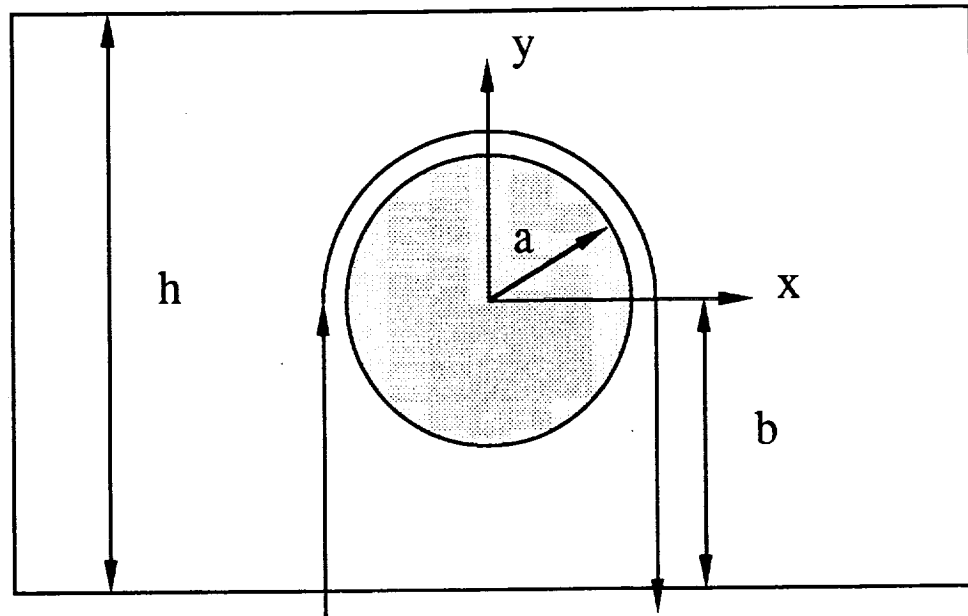
Fig. 7   Creeping ray path for a composite cell containing a single fiber.
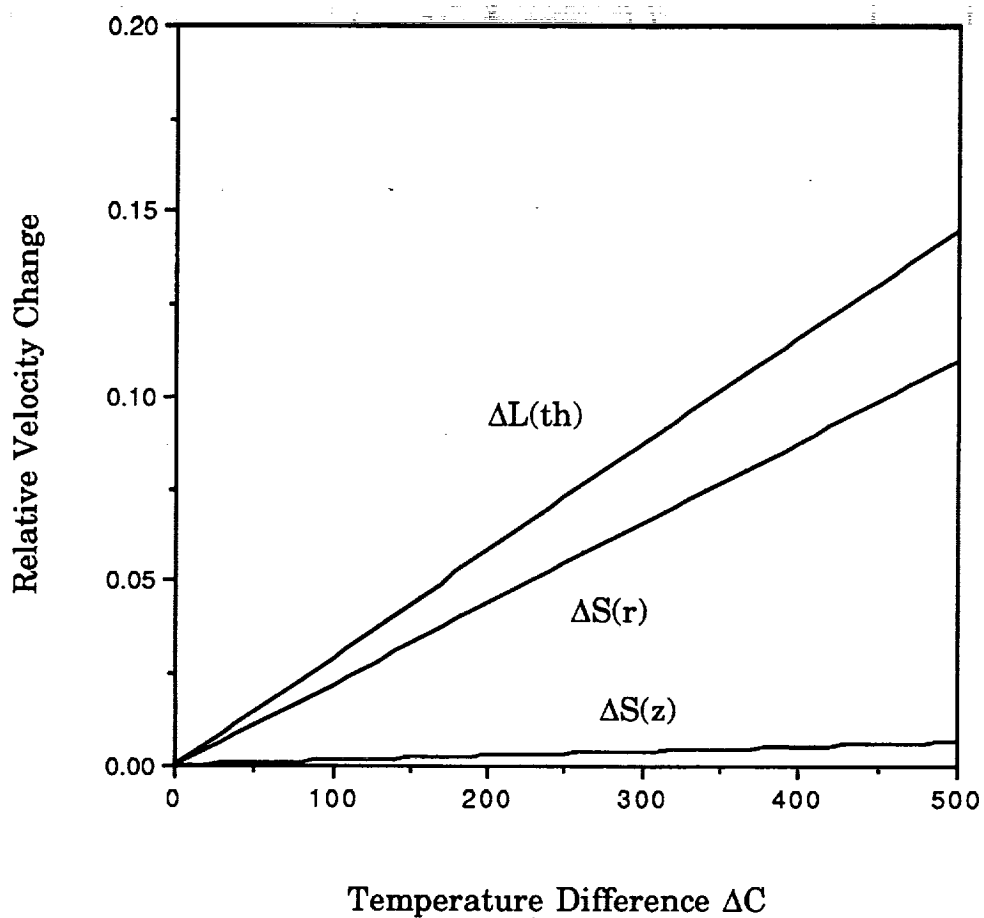
Fig. 8   Relative velocity changes for creeping rays as functions of

temperature difference; ΔL(th) is for the longitudinal wave mode

polarized in the circumferential direction, ΔS(r) and ΔS(z) are for the

shear wave modes polarized in the radial and the fiber axis

directions, respectively.
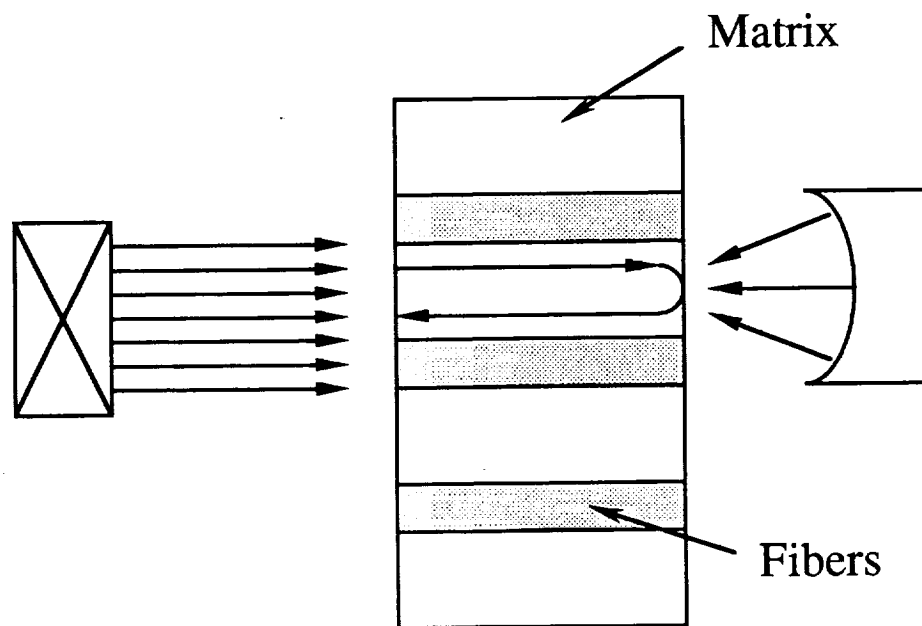
Fig. 9   A measurement setup for the use of focused transducers.

Appendix III - Lambda Research, Inc. Report on XRD

LAMBDA
RESEARCH

General Electric Company
GE Aircraft Engine Group
Evendale Plant
One Neumann Way
Mail Stop 87
Cincinnati, Ohio 45215-6301

X-RAY DIFFRACTION DETERMINATION
OF THE RESIDUAL STRESS DISTRIBUTIONS
IN ONE Ti-14-21 SCS-6 COMPOSITE
SPECIMEN GE 1770-000 PANEL 111B

REPORT: 0005-0449   ATTN: Mr. P.K. Wright
DATE: 10/02/90   AUTHORIZATION: 200-15-14Y97702

INTRODUCTION

One composite specimen was received from General Electric
Company for the purpose of determining the longitudinal and
transverse subsurface residual stress distributions. The
composite specimen, identified as Panel 111B, was reportedly
manufactured from Ti-14-21, and was nominally 1.4 x 1.6 x
0.05 in.

_____   _____
Keith A. Story   Perry W. Mason
Senior Laboratory Technician   Research Engineer

0005-0449

TECHNIQUE

X-ray diffraction residual stress measurements were made at the surface and at nominal depths of 1 and 3 x 10^{-3} in. Measurements were made in the longitudinal and transverse directions (with respect to the fibers) on both sides of the plate.

The samples were rocked through an angular range of +-2.5 deg. around the mean psi angles during measurement to integrate the diffracted intensity over more grains, minimizing the influence of the grain size.

X-ray diffraction residual stress measurements were performed using a two-angle sine-squared-psi technique, in accordance with GE specification 4013195-991 and SAE J784a, employing the diffraction of copper K-alpha radiation from the (423) planes of the HCP structure of the Ti-14-21. The diffraction peak angular positions at each of the psi tilts employed for measurement were determined from the position of the K-alpha 1 diffraction peak separated from the superimposed K-alpha doublet assuming a Pearson VII function diffraction peak profile in the high back-reflection region. [1] The diffracted intensity, peak breadth, and position of the K-alpha 1 diffraction peak were determined by fitting the Pearson VII function peak profile by least squares regression after correction for the Lorentz polarization and absorption effects, and for a linearly sloping background intensity.

Details of the diffractometer fixturing are outlined below:

Incident Beam Divergence:	0.10 in. circ. collimator
Detector :	Si(Li) set for 90% acceptance of the copper K-alpha energy
Psi Rotation :	0.0 - 45.0 deg.
E/(1 + v) :	9.95 +-0.2 x 10^7 psi
Irradiated Area :	0.13 in. circ. zone

The value of the x-ray elastic constant, E/(1 + v), required to calculate the macroscopic residual stress from the strain measured normal to the (423) planes of Ti-14-21 was previously determined empirically [2] employing a simple rectangular beam manufactured from Ti-14-21 loaded in four-point bending on the diffractometer to known stress levels and measuring the resulting change in the spacing of the (423) planes.

0005-0449

146

Material was removed electrolytically for subsurface measurement, minimizing possible alteration of the subsurface residual stress distribution as a result of material removal. All data obtained as a function of depth were corrected for the effects of the penetration of the radiation employed for residual stress measurement into the subsurface stress gradient. [3] The stress gradient correction applied to the last depth measured is based upon an extrapolation to greater depths, and may result in over correction at the last depth if the stress profile has been terminated in the presence of a steep gradient. Corrections for stress relaxation caused by layer removal [4] are applied as appropriate.

RESULTS AND DISCUSSION

The longitudinal and transverse residual stress distributions measured as functions of depth are presented in Tables I through IV, and are shown graphically in Figures 1 and 2. Compressive stresses are shown as negative values, tensile as positive, in units of ksi (10^3 psi) and MPa (10^6 N/m^2).

The results shown in each computer generated table of macroscopic residual stress data are given first as measured, then after correction for the penetration of the radiation employed for measurement into the subsurface stress gradient, and finally for stress relaxation which occurred as a result of removing layers of material by electropolishing for subsurface measurement and sectioning, as appropriate. It is the fully corrected data shown in the column titled, "Relaxation," that are plotted in the associated figure. For cylindrical samples from which complete shells were removed for subsurface measurement, the radial stress is calculated assuming a rotationally symmetrical residual stress distribution. The angular width of the (423) K-alpha 1 diffraction peak at half height is shown in the far right-hand column.

In each figure, the macroscopic residual stress distribution is plotted in the upper graph. The lower graph gives the (423) diffraction peak width distribution. The (423) diffraction peak width was calculated simultaneously with the macroscopic residual stress from the peak width in the psi = 0 orientation. The (423) diffraction peak width is a sensitive function of the chemistry, hardness, and the degree to which the material has been cold worked. In martensitic steels, it is commonly observed that plastic deformation produced by processes such as shot peening or grinding will

0005-0449

147

cause work softening, and a reduction in the peak width. In work hardening materials, the diffraction peak width increases significantly as a result of an increase in the average microstrain and the reduced crystallite size produced by cold working. The (423) diffraction peak width can be indicative of how the material may have been processed, and the depth to which it has been plastically deformed.

Details of the x-ray diffraction data reduction are shown in the computer printouts appended to this report. The error shown for each residual stress measurement is one standard deviation resulting from random error in the determination of the diffraction peak angular positions and in the empirically determined value of $E/(1 + v)$ in the $\langle 423 \rangle$ direction. An additional semi-systematic error on the order of $+-2$ ksi may result from sample positioning and instrument alignment errors. The magnitude of this systematic error was monitored using a powdered metal zero-stress standard in accordance with ASTM specification E915, and found to be $+1.6$ ksi during the course of this investigation.

CONCLUSIONS

The residual stress distribution in the longitudinal direction on side A is tensile for the depths examined with values between $+76$ ksi and $+48$ ksi. The results for the transverse direction have a surface compressive stress on the order of -15 ksi and subsurface values on the order of $+34$ ksi. The distribution crosses into tension at a nominal depth of 0.0005 in. The results for the longitudinal direction are of greater tensile magnitude as compared to the axial direction. The (423) peak width distributions are comparable and decrease in magnitude to nominally 0.0012 in.

The residual stress distributions in both directions on side B are tensile for the depths examined. Both distributions have maximum tensile values on the surface on the order of $+50$ ksi and $+110$ ksi for the longitudinal and transverse directions, respectively. The stresses are of greater tensile magnitude for the longitudinal direction beneath the surface. The (423) peak width distributions are comparable.

0005-0449

148

REFERENCES:

(1)   P. S. Prevey, ADV. IN X-RAY ANAL., Vol. 29, 1986,
      pp. 103-112.

(2)   P. S. Prevey, ADV. IN X-RAY ANAL., Vol. 20, 1977,
      pp. 345-354.

(3)   D. P. Koistinen and R. E. Marburger, Trans. ASM,
      Vol. 51, 1959, p. 537.

(4)   M.G. Moore and W. P. Evans, Trans. SAE, Vol. 66, 1958,
      p. 340.

RESIDUAL STRESS DISTRIBUTION

□ Long. Dir.   ▽ Trans. Dir.

(423) PEAK WIDTH DISTRIBUTION
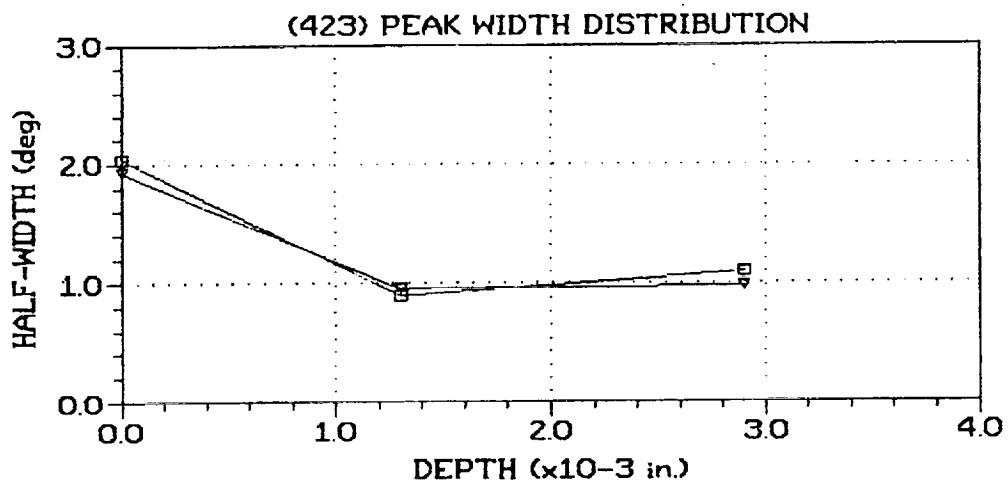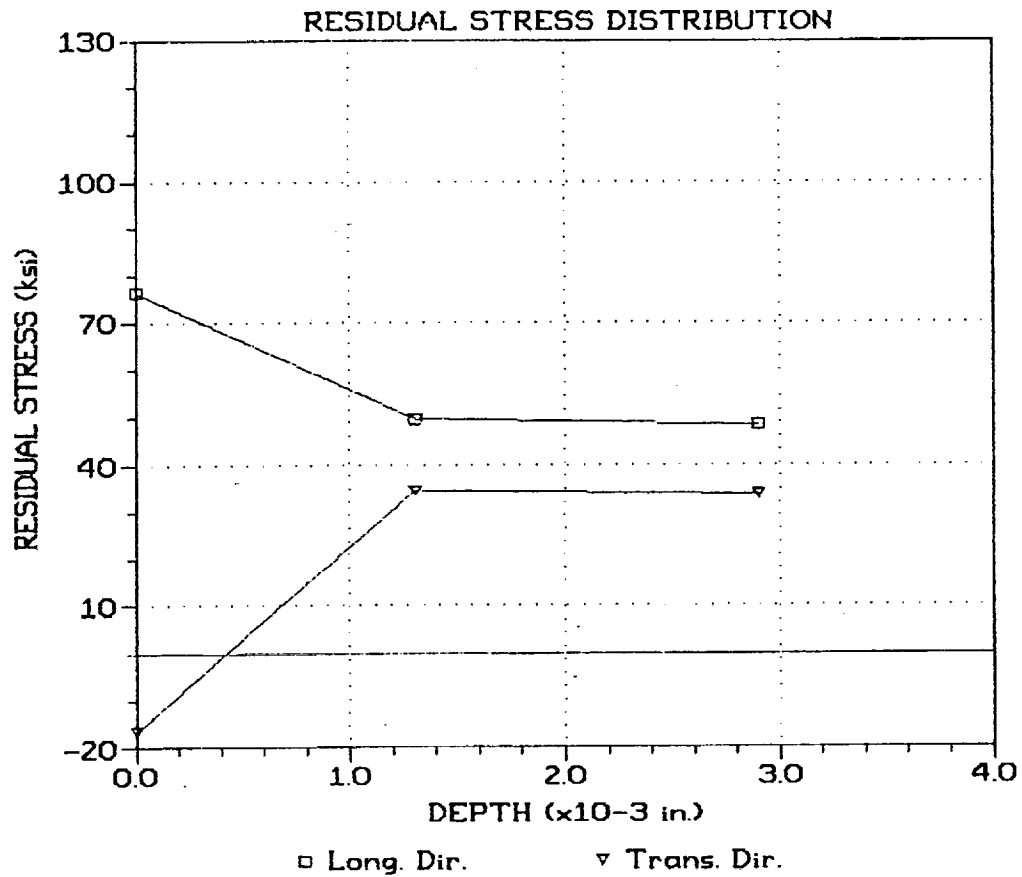
Ti-14-21 COMPOSITE SAMPLE
Specimen Panel 111B Side A Location

Figure 1

150

RESIDUAL STRESS DISTRIBUTION

□ Long. Dir.   ∇ Trans. Dir.

(423) PEAK WIDTH DISTRIBUTION
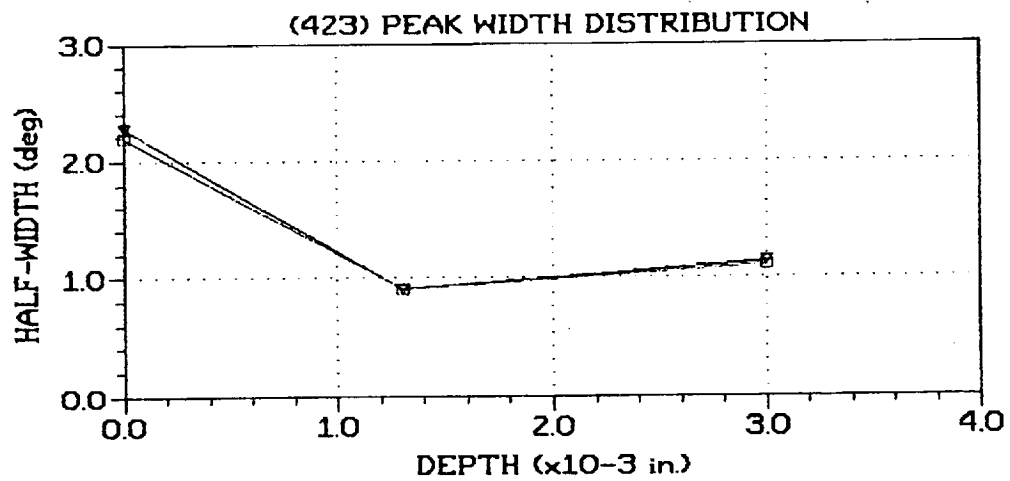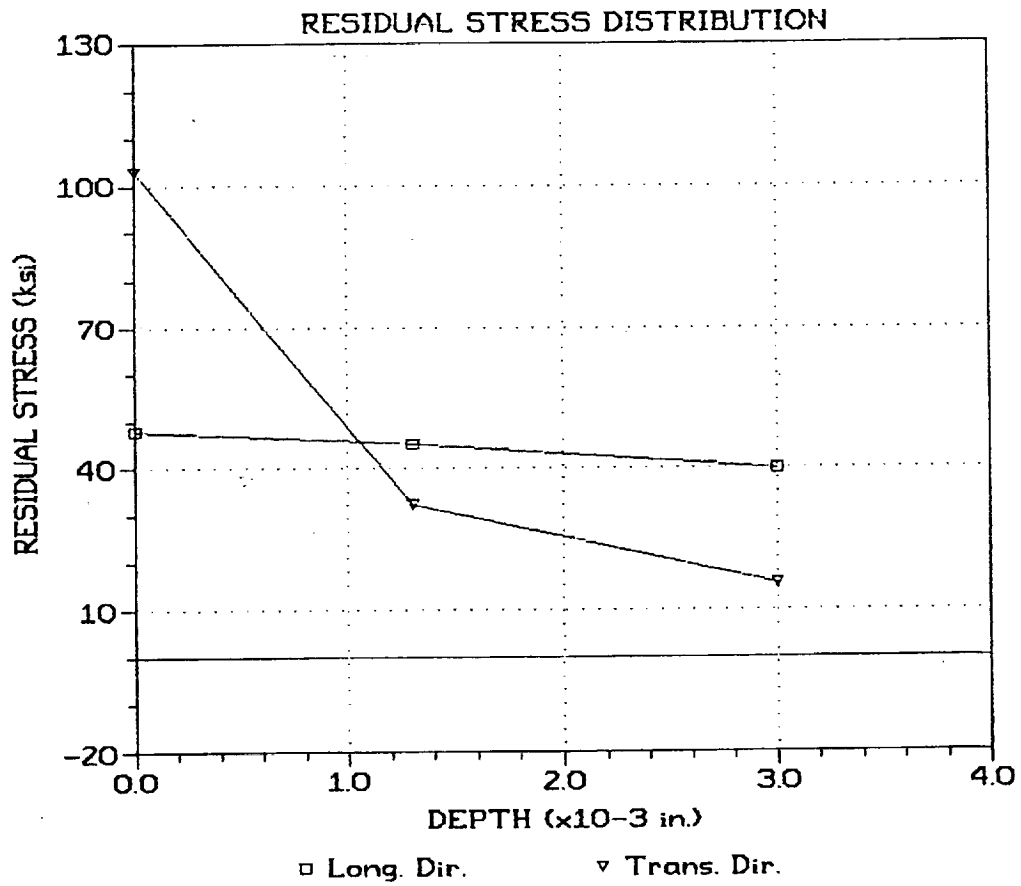
Ti-14-21 COMPOSITE SAMPLE
Specimen Panel 111B Side B Location

Figure 2

151

Lambda Research, Inc.
STRESS40.15

RESIDUAL STRESS DEPTH ANALYSIS

With Stress Gradient and Relaxation Corrections
and Diffraction Peak Width (B 1/2)

Ti-14-21 COMPOSITE LONGITUDINAL DIRECTION
Specimen Panel 111B Marked Side A Location

E/(1+v)=   9948. +- 159. ksi   1/2 S2 = 14.58 +- .23 x 10-6 1/MPa
MU= 2200. 1/in. (86.6 1/mm)   Sectioning Stress Relax. =   .0 ksi

| | DEPTH | | ---------------- RESIDUAL STRESS ksi (MPa) ---------------- | | | | | | B 1/2 |
	in.	(mm)	Measured				Gradient		Relaxation		(deg)
1	.0000(	.000)	70.5± 2.3 (	486.±	16.)	76.3(	526.)	76.3(	526.)		2.04
2	.0013(	.033)	55.0± 1.6 (	379.±	11.)	56.3(	388.)	49.7(	342.)		.89
3	.0029(	.074)	66.5± 1.7 (	459.±	12.)	62.1(	428.)	48.4(	334.)		1.09

TABLE I

152

Lambda Research, Inc.
STRESS40.15

RESIDUAL STRESS DEPTH ANALYSIS

With Stress Gradient and Relaxation Corrections
and Diffraction Peak Width (B 1/2)

Ti-14-21 COMPOSITE TRANSVERSE DIRECTION
Specimen Panel 111B Marked Side A Location

E/(1+v)=   9948, +- 159, ksi   1/2 S2 = 14.58 +- .23 x 10-6 1/MPa
MU= 2200, 1/in, (86.6 1/mm)   Sectioning Stress Relax. =   .0 ksi

| | DEPTH | | RESIDUAL STRESS ksi (MPa) | | | | | | B 1/2 |
	in.	(mm)	Measured		Gradient		Relaxation		(deg)
1	.0000(	.000)	-9.8± 1.4 (	-68.± 10.)	-16.7(	-115.)	-16.7(	-115.)	1.93
2	.0013(	.033)	38.7± 1.3 (	267.± 9.)	35.9(	247.)	34.4(	237.)	.95
3	.0029(	.074)	38.0± 1.3 (	262.± 9.)	40.7(	280.)	33.7(	232.)	.97

TABLE II

153

Lambda Research, Inc.
STRESS40.15

RESIDUAL STRESS DEPTH ANALYSIS

With Stress Gradient and Relaxation Corrections
and Diffraction Peak Width (B 1/2)

Ti-14-21 COMPOSITE LONGITUDINAL DIRECTION
Specimen Panel 111B Unmarked Side B Location

E/(1+ν)= 9948. +- 159. ksi   1/2 S2 = 14.58 +- .23 x 10-6 1/MPa
MU= 2200. 1/in. (86.6 1/mm)   Sectioning Stress Relax. =   .0 Ksi

| | DEPTH | | ---------------- RESIDUAL STRESS Ksi (MPa) ---------------- | | | | | B 1/2 |
	in.	(mm)	Measured		Gradient		Relaxation		(deg)
1	.0000(	.000)	43.9± 2.1 (	303.± 14.)	47.9(	330.)	47.9(	330.)	2.19
2	.0013(	.033)	49.0± 1.5 (	338.± 10.)	50.3(	347.)	45.2(	312.)	.90
3	.0030(	.076)	54.2± 1.6 (	374.± 11.)	51.6(	356.)	39.7(	274.)	1.10

TABLE III

RESIDUAL STRESS DEPTH ANALYSIS

With Stress Gradient and Relaxation Corrections
and Diffraction Peak Width (B 1/2)

Ti-14-21 COMPOSITE TRANSVERSE DIRECTION
Specimen Panel 111B Unmarked Side B Location

E/(1+v)=   9948. +- 159. ksi   1/2 S2 = 14.58 +- .23 x 10-6 1/MPa
MU= 2200. 1/in. (86.6 1/mm)   Sectioning Stress Relax. =   .0 ksi

| | DEPTH | | ---------------- RESIDUAL STRESS Ksi (MPa) ---------------- | | | | | B 1/2 |
	in.	(mm)	Measured		Gradient		Relaxation		(deg)
1	.0000(	.000)	88.0± 2.8 (	607.± 19.)	103.0(	710.)	103.0(	710.)	2.27
2	.0013(	.033)	32.9± 1.2 (	227.± 8.)	39.0(	269.)	32.2(	222.)	.90
3	.0030(	.076)	32.1± 1.2 (	222.± 9.)	25.9(	179.)	15.7(	109.)	1.13

TABLE IV

155

CAUCHY SEPARATED Ka1 DIFFRACTION PEAK STRESS ANALYSIS 1

E/(1+v) = 9948.+- 159. ksi   1/2 S2 = 14.58 +- .23 x 10-6 1/MPa

005449.d01   Spec. 111B Mark. Side A Loc. Surf. Long.   9009B12KDS

Psi	2-theta	1/I	1/Icor	Psi	2-theta	1/I	1/Icor
.00	144.38	91.15	446.21	33.21	143.71	165.94	3419.36
	145.10	57.34	175.90		144.31	136.56	877.75
	145.82	48.11	134.93		144.90	120.07	563.78
	146.78	54.93	169.82		146.60	144.66	1554.40
	147.74	78.94	359.62		148.30	151.91	3800.29
	140.00	161.77			140.00	191.83	
	150.00	125.04			150.00	155.54	

d = .80606 A
2θ= 145.718 +- .006 deg.

d = .80777 A
2θ= 144.939 +- .007 deg.

B 1/2 = 2.04 deg.
COLD WORK = .0 %
STRAIN = .002125
STRESS = 70.5 +- 2.3 ksi
       = 486. +- 16. (MPa)

DEPTH = .0000 in. (.000 mm)

005449.d01   Spec. 111B Marked Side A Loc. .0013 in. Long.   9009B12RJ

Psi	2-theta	1/I	1/Icor	Psi	2-theta	1/I	1/Icor
.00	144.49	59.59	208.00	33.21	143.89	69.95	179.02
	144.89	29.84	71.99		144.29	37.75	71.63
	145.29	21.54	47.93		144.69	28.72	51.05
	145.89	29.18	70.49		145.29	35.89	68.28
	146.49	43.48	124.64		145.89	54.88	125.94
	140.00	132.26			140.00	171.87	
	150.00	117.19			150.00	140.55	

d = .80714 A
2θ= 145.222 +- .004 deg.

d = .80848 A
2θ= 144.622 +- .004 deg.

B 1/2 = .89 deg.
COLD WORK = .0 %
STRAIN = .001658
STRESS = 55.0 +- 1.6 ksi
       = 379. +- 11. (MPa)

DEPTH = .0013 in. (.033 mm)

005449.d01   Spec. 111B Marked Side A Loc. .0029 in. Long.   9009B13KS

Psi	2-theta	1/I	1/Icor	Psi	2-theta	1/I	1/Icor
.00	144.74	127.70	342.56	33.21	143.83	83.05	230.09
	145.05	79.75	182.70		144.23	44.88	87.87
	145.38	65.39	143.73		144.63	32.74	58.88
	145.66	70.66	158.10		145.28	39.20	74.91
	145.94	83.56	194.95		145.93	62.92	150.11
	140.00	424.39			140.00	186.85	
	150.00	381.79			150.00	149.52	

d = .80685 A
2θ= 145.357 +- .003 deg.

d = .80847 A
2θ= 144.629 +- .004 deg.

B 1/2 = 1.09 deg.
COLD WORK = .0 %
STRAIN = .002005
STRESS = 66.5 +- 1.7 ksi
       = 459. +- 12. (MPa)

DEPTH = .0029 in. (.074 mm)

CAUCHY SEPARATED Ka1 DIFFRACTION PEAK STRESS ANALYSIS   1

E/(1+v) = 9948.+- 159. ksi   1/2 S2 = 14.58 +- .23 x 10-6 1/MPa

	005449.d02			Spec. 111B Mark. Side A Loc. Surf. Trans.				9009B12KS
Psi	2-theta	1/I	1/Icor	Psi	2-theta	1/I	1/Icor	
.00	144.39	75.59	368.18	33.21	144.12	112.97	1440.16	B 1/2 = 1.93 deg.
	145.24	44.38	130.29		145.17	76.01	292.22	COLD WORK = .0 %
	146.09	37.30	101.28		146.22	68.96	246.02	STRAIN = -.000296
	146.94	44.92	137.25		147.83	79.17	420.80	STRESS = -9.8 +- 1.4 ksi
	147.79	63.32	271.74		149.44	96.35	2222.88	= -68. +- 10. (MPa)
	140.00	133.39			140.00	146.08		
	150.00	105.56			150.00	100.68		
	d = .80590 A				d = .80566 A			
	2θ= 145.789 +- .006 deg.				2θ= 145.900 +- .008 deg.			DEPTH = .0000 in. (.000 mm)

	005449.d02			Spec. 111B Mark. Side A Loc. .0013 in. Trans.				9009B12RJ
Psi	2-theta	1/I	1/Icor	Psi	2-theta	1/I	1/Icor	
.00	144.57	52.43	180.33	33.21	144.12	68.35	168.65	B 1/2 = .95 deg.
	144.89	28.42	66.75		144.53	35.64	66.15	COLD WORK = .0 %
	145.20	20.32	44.30		144.93	27.84	49.03	STRAIN = .001166
	145.83	26.00	60.11		145.56	35.61	67.44	STRESS = 38.7 +- 1.3 ksi
	146.46	37.66	98.93		146.19	57.53	134.95	= 267. +- 9. (MPa)
	140.00	140.44			140.00	182.13		
	150.00	119.76			150.00	139.40		
	d = .80705 A				d = .80799 A			
	2θ= 145.264 +- .004 deg.				2θ= 144.940 +- .004 deg.			DEPTH = .0013 in. (.033 mm)

	005449.d02			Spec. 111B Mark. Side A Loc. .0029 in. Trans.				9009B13RJ
Psi	2-theta	1/I	1/Icor	Psi	2-theta	1/I	1/Icor	
.00	144.57	56.62	187.90	33.21	144.12	72.23	186.95	B 1/2 = .97 deg.
	144.98	29.42	70.55		144.44	43.78	86.85	COLD WORK = .0 %
	145.38	21.87	48.76		144.75	31.40	56.71	STRAIN = .001145
	146.01	28.38	67.91		145.47	34.32	64.25	STRESS = 38.0 +- 1.3 ksi
	146.64	44.91	130.97		146.19	50.76	139.51	= 262. +- 9. (MPa)
	140.00	134.73			140.00	177.69		
	150.00	116.76			150.00	142.37		
	d = .80693 A				d = .80785 A			
	2θ= 145.318 +- .004 deg.				2θ= 144.901 +- .004 deg.			DEPTH = .0029 in. (.074 mm)

E/(1+v) = 9948.+- 159. ksi   1/2 S2 = 14.58 +- .23 x 10-6 1/MPa

	005449.d03			Spec. 111B Unmark Side B Loc. Surf. Long.				9009B14KS
Psi	2-theta	1/I	1/Icor	Psi	2-theta	1/I	1/Icor		
.00	144.56	60.81	426.10	33.21	144.24	197.45	1453.76	B 1/2 =	2.19 deg.
	145.36	38.12	135.26		145.28	156.84	683.10	COLD WORK =	.0 %
	146.16	29.63	89.71		146.32	151.49	676.62	STRAIN =	.001324
	147.36	30.77	100.54		147.84	158.33	933.05	STRESS =	43.9 +- 2.1 ksi
	148.56	43.15	229.95		149.36	182.95	3493.78	=	303. +- 14. (MPa)
	140.00	100.57			140.00	284.32			
	150.00	60.62			150.00	193.10			
d =	.80472 A			d =	.80579 A				
2θ=	146.340 +- .007 deg.			2θ=	145.842 +- .009 deg.			DEPTH =	.0000 in. (.000 mm)

	005449.d03			Spec. 111B Unmark. Side B Loc. .0013 in. Long.				9009B14RJ
Psi	2-theta	1/I	1/Icor	Psi	2-theta	1/I	1/Icor		
.00	144.54	52.49	163.90	33.21	144.00	64.11	150.80	B 1/2 =	.90 deg.
	144.86	28.52	67.58		144.32	38.94	73.83	COLD WORK =	.0 %
	145.17	20.56	45.15		144.64	29.14	51.51	STRAIN =	.001478
	145.80	27.90	66.15		145.28	36.31	68.69	STRESS =	49.0 +- 1.5 ksi
	146.43	40.76	111.97		145.92	55.83	127.46	=	338. +- 10. (MPa)
	140.00	133.43			140.00	181.41			
	150.00	119.65			150.00	141.21			
d =	.80719 A			d =	.80838 A				
2θ=	145.200 +- .004 deg.			2θ=	144.664 +- .004 deg.			DEPTH =	.0013 in. (.033 mm)

	005449.d03			Spec. 111B Unmark. Side B Loc. .0030 in. Long.				9009B14RJ
Psi	2-theta	1/I	1/Icor	Psi	2-theta	1/I	1/Icor		
.00	144.48	66.26	206.09	33.21	143.92	77.92	199.97	B 1/2 =	1.10 deg.
	144.88	36.94	88.09		144.36	42.15	80.20	COLD WORK =	.0 %
	145.28	27.85	62.03		144.80	33.58	60.48	STRAIN =	.001634
	145.84	33.08	77.02		145.36	42.70	83.11	STRESS =	54.2 +- 1.6 ksi
	146.40	46.90	123.26		145.92	63.50	149.12	=	374. +- 11. (MPa)
	140.00	169.13			140.00	190.50			
	150.00	151.74			150.00	156.86			
d =	.80709 A			d =	.80841 A				
2θ=	145.245 +- .004 deg.			2θ=	144.652 +- .004 deg.			DEPTH =	.0030 in. (.076 mm)

CAUCHY SEPARATED Ka1 DIFFRACTION PEAK STRESS ANALYSIS   1

E/(1+v) = 9948.+- 159. ksi   1/2 S2 = 14.58 +- .23 x 10-6 1/MPa

005449.d04   Spec. 111B Unmark. Side B Loc. Surf. Trans.   9009B14KS

Psi	2-theta	1/I	1/Icor	Psi	2-theta	1/I	1/Icor
.00	144.72	111.64	596.72	33.21	144.00	299.77	8584.78
	145.44	73.68	245.44		144.50	247.28	1720.90
	146.16	60.18	178.53		145.20	221.35	1138.05
	147.36	62.47	198.12		147.40	263.40	3924.25
	148.56	90.17	462.43		149.80	265.25	9765.75
	140.00	204.76			140.00	342.40	
	150.00	131.09			150.00	275.52	

d = .80477 A   d = .80691 A
2θ= 146.318 +- .007 deg.   2θ= 145.330 +- .008 deg.

B 1/2 = 2.27 deg.
COLD WORK = .0 %
STRAIN = .002654
STRESS =   89.0 +- 2.8 ksi
       =   607. +- 19. (MPa)

DEPTH = .0000 in. (.000 mm)

005449.d04   Spec. 111B Unmark. Side B Loc. .0013 in. Trans.   9009B14RJ

Psi	2-theta	1/I	1/Icor	Psi	2-theta	1/I	1/Icor
.00	144.51	49.36	157.65	33.21	144.11	71.80	192.06
	144.86	25.56	60.29		144.51	36.74	69.87
	145.21	18.23	39.86		144.91	27.42	48.64
	145.81	25.17	59.61		145.51	34.88	66.54
	146.41	34.97	93.79		146.11	53.84	124.56
	140.00	123.76			140.00	169.67	
	150.00	106.23			150.00	135.88	

d = .80719 A   d = .80799 A
2θ= 145.200 +- .003 deg.   2θ= 144.840 +- .004 deg.

B 1/2 = .90 deg.
COLD WORK = .0 %
STRAIN = .000991
STRESS =   32.9 +- 1.2 ksi
       =   227. +- 8. (MPa)

DEPTH = .0013 in. (.033 mm)

005449.d04   Spec. 111B Unmark. Side B Loc. .0030 in. Trans.   9009B14RJ

Psi	2-theta	1/I	1/Icor	Psi	2-theta	1/I	1/Icor
.00	144.41	35.31	212.80	33.21	144.01	83.65	244.93
	144.86	37.42	91.85		144.46	43.99	87.23
	145.31	27.78	62.92		144.91	31.12	56.13
	145.96	33.39	79.72		145.56	36.49	69.45
	146.61	54.88	162.75		146.21	59.36	141.00
	140.00	156.04			140.00	177.82	
	150.00	140.61			150.00	144.96	

d = .80708 A   d = .80787 A
2θ= 145.249 +- .004 deg.   2θ= 144.896 +- .004 deg.

B 1/2 = 1.13 deg.
COLD WORK = .0 %
STRAIN = .000969
STRESS =   32.1 +- 1.2 ksi
       =   222. +- 9. (MPa)

DEPTH = .0030 in. (.076 mm)

Appendix IV - Derivation of In-Plane Shear Strength Model

The composite, represented by the square symmetry element shown in Figure IV-1, is divided into three subsections, **a**, **b**, and **c** as shown. Subsection **a** is a square representing the fiber and has fiber properties (subscript f) and subsections **b** and **c** and rectangles representing the matrix and have matrix properties (subscript m). The size of region **a** is represented by length a, and the overall symmetry element has a size of length l. For purposes of modeling subregions **a** and **b** together will at times be considered another subsection, designated **ab**. The volume fractions of the various subsections can be defined in terms of the overall volume fraction of the fiber, V_f, as follows:

$$V_a = (a^2)/(al) = a/l = \sqrt{V_f} \ . \qquad\qquad \text{(IV-1)}$$

$$V_b = (l-a)/(al) = 1 - a/l = 1 - \sqrt{V_f} \qquad\qquad \text{(IV-2)}$$

$$V_c = (l-a)l/l^2 = 1 - a/l = 1 - \sqrt{V_f} \qquad\qquad \text{(IV-3)}$$

$$V_{ab} = (la)/(l^2) = a/l = \sqrt{V_f} \qquad\qquad \text{(IV-4)}$$

The shear stress-strain response of the composite, τ_c-γ_c, can be divided into three regimes: Regime 1, Elastic fiber-elastic matrix-no interface slip; Regime 2, elastic fiber- elastic matrix- interface slip; Regime 3, elastic fiber-plastic matrix-interface slip; and Regime 4, elastic fiber-plastic matrix-no interface slip.

Regime 1: The derivation of shear modulus follows a mechanics of materials approach. (More accurate elastic models are available but this one is most compatable with the approach used in the inelastic Regimes 2, 3 and 4.) The subsections **a** and **b** are grouped together in parallel and the effective shear modulus of this pair is determined, and then subsections **ab** and **c** are grouped in series and the full composite modulus is determined:

$$G_{ab} = V_a G_a + V_b G_b \quad \text{(for subelements } \mathbf{a} \text{ and } \mathbf{b} \text{ in parallel)}$$

$$= V_f G_f + (1 - V_f) G_m, \ \text{(using Equations IV-1 and IV-2)} \qquad \text{(IV- 5)}$$

$$G_{comp} = \frac{1}{\dfrac{V_{ab}}{G_{ab}} + \dfrac{V_c}{G_c}} \quad \text{(for subelements } \mathbf{ab} \text{ and } \mathbf{c} \text{ in series)} \qquad \text{(IV- 6)}$$

With some rearranging and use of Eq. IV-3 and IV-4,

$$G_{comp} = \frac{G_m[G_f\sqrt{V_f} + G_m(1 - \sqrt{V_f})]}{[\sqrt{V_f} + (1 - \sqrt{V_f})^2]G_m + \sqrt{V_f}(1 - \sqrt{V_f})G_f} \quad \text{..................... (IV-7)}$$

with $\tau_{comp} = G_{comp}\, \gamma_{comp}$.
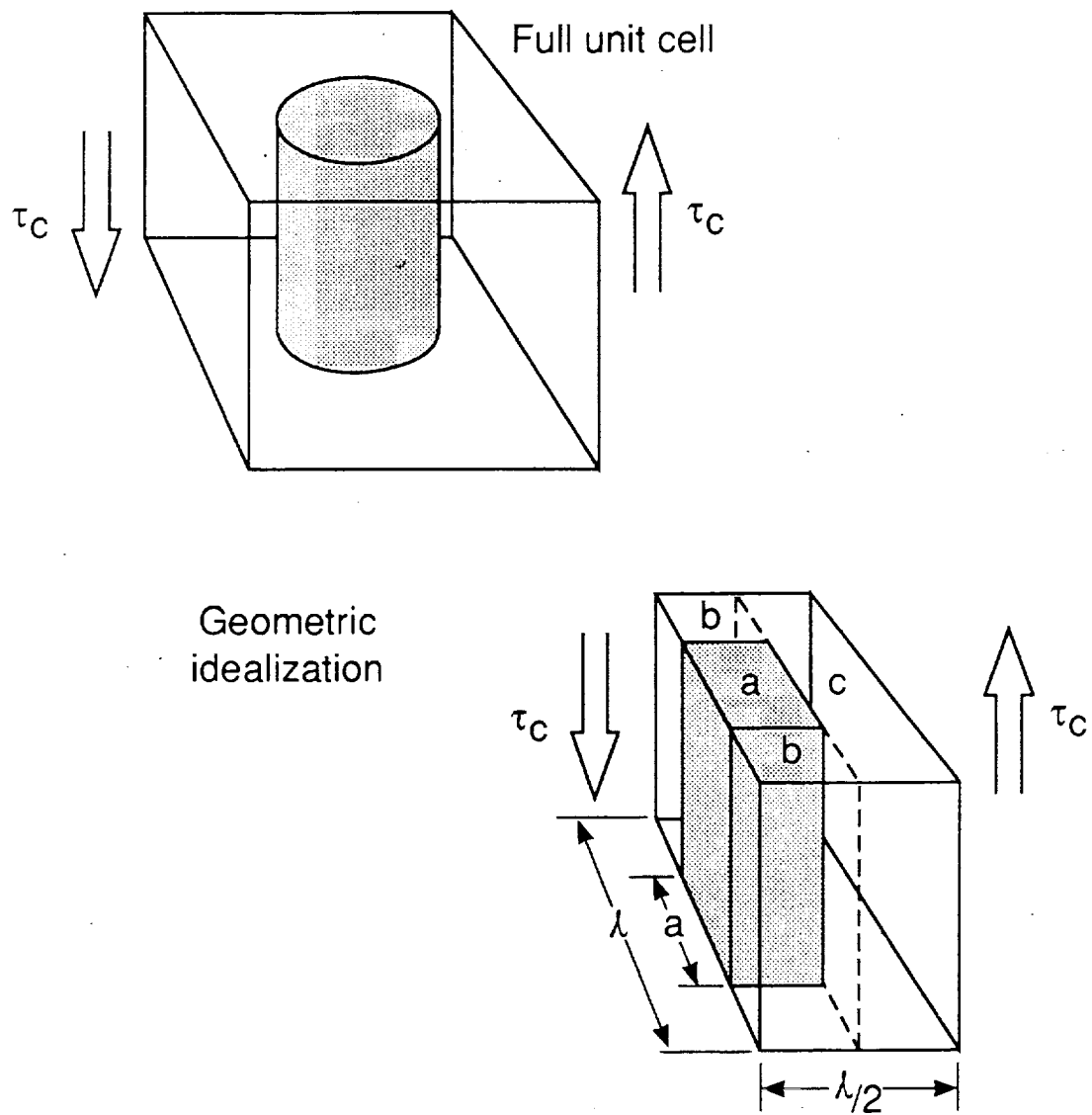
160

Figure IV-1. Geometric Model Used for In-Plane Shear Strength Model

Regime 2: In this regime, slip is allowed between the fiber (a) and the matrix (b and c). The total shear displacement, δ_{comp}, is composed of two parts in series, δ_{ab} from subsection ab, and δ_c from subsection c:

$$\delta_{comp} = \delta_{ab} + \delta_c \qquad \text{(IV-8)}$$

Rewriting in terms of shear strains and stresses:

$$\gamma_{comp} \; l = \gamma_{ab}(a) + \gamma_c(l\text{-}a) \qquad \text{(IV-9)}$$

$$= \frac{\tau_b}{G_m}(a) + \frac{\tau_{comp}}{G_m}(l - a) \qquad \text{(IV-10)}$$

Here $\dfrac{\tau_b}{G_m}$ is used for γ_{ab} since the full shear strain is only accomodated elastically by the matrix ligament, b. In the fiber subsection, a, the shear is partially accomodated by an unknown amount of interface slip. τ_b can be eliminated from this equation by noting that:

$$\tau_{comp} = \tau_a + \tau_b \qquad \text{(IV-11)}$$

and

$$\tau_a = 2\tau_i. \qquad \text{(IV-12)}$$

Equation IV-12 follows from a free body diagram of the fiber, a, with uniform frictional force τ_i acting on the three interface sides:

$$\tau_a \,[a] = \tau_i \,[a + 2(a/2)] \qquad \text{(IV-13)}$$

Substituting Eq. IV-12 into Eq. IV-11 and then into Eq. IV-10 gives for Regime 2:

$$\tau_{comp} = 2\tau_i\sqrt{V_f} + G_m\gamma_{comp} \qquad \text{(IV-14)}$$

Regime 3: In this regime the interface slips and the matrix is perfectly plastic, thus there is no unique value of shear displacement or strain for a given stress level. Rather, there is only the composite slip/yield stress to be determined. This can be done by equilibrium of forces along a plane throught the fiber center:

$$\tau_{comp} \; l = \tau_a \, a + \tau_b \, (l\text{-}a) \qquad \text{(IV-15)}$$

$$= 2\tau_i a + \tau_m \, (l\text{-}a) \qquad \text{(IV-16)}$$

$$\tau_{comp} = 2\tau_i \, (a/l) + \tau_m \, (l\text{-}a)/l \qquad \text{(IV-17)}$$

or, for Regime 3:

$$\tau_{comp} = 2\tau_i\sqrt{V_f} + \tau_m(1 - \sqrt{V_f}) \qquad \text{(IV-18)}$$

162

Regime 4: With no interface slip, the critical region is subsection c, the matrix region. Yielding occurs here when the composite stress reaches the matrix shear yield strength, τ_m. Thus in Regime 4:

$$\tau_c = \tau_m \qquad\qquad (\text{IV-19})$$

REPORT DOCUMENTATION PAGE

Public reporting burden for this collection of information is estimated to average 1 hour per response, including the time for reviewing instructions, searching existing data sources, gathering and maintaining the data needed, and completing and reviewing the collection of information. Send comments regarding this burden estimate or any other aspect of this collection of information, including suggestions for reducing this burden, to Washington Headquarters Services, Directorate for Information Operations and Reports, 1215 Jefferson Davis Highway, Suite 1204, Arlington, VA 22202-4302, and to the Office of Management and Budget, Paperwork Reduction Project (0704-0188), Washington, DC 20503.

1. AGENCY USE ONLY (Leave blank)	2. REPORT DATE	3. REPORT TYPE AND DATES COVERED
	September 1993	Final Contractor Report

4. TITLE AND SUBTITLE

Thermal Stress Effects in Intermetallic Matrix Composites

5. FUNDING NUMBERS

WU-510-01-50
C-NAS3-25790

6. AUTHOR(S)

P.K. Wright, M.D. Sensmeier, D.S. Kupperman, and H.N.G. Wadley

7. PERFORMING ORGANIZATION NAME(S) AND ADDRESS(ES)

GE Aircraft Engines
1 Newmann Way, G50
Cincinnati, Ohio 45215-6301

8. PERFORMING ORGANIZATION REPORT NUMBER

E-8127

9. SPONSORING/MONITORING AGENCY NAME(S) AND ADDRESS(ES)

National Aeronautics and Space Administration
Lewis Research Center
Cleveland, Ohio 44135-3191

10. SPONSORING/MONITORING AGENCY REPORT NUMBER

NASA CR-191191

11. SUPPLEMENTARY NOTES

12a. DISTRIBUTION/AVAILABILITY STATEMENT

Unclassified - Unlimited
Subject Category 38

12b. DISTRIBUTION CODE

13. ABSTRACT (Maximum 200 words)

Intermetallic matrix composites develop residual stresses from the large thermal expansion mismatch ($\Delta\alpha$) between the fibers and matrix. This work was undertaken to: establish improved techniques to measure these thermal stresses in IMC's; determine residual stresses in a variety of IMC systems by experiments and modeling; and, determine the effect of residual stresses on selected mechanical properties of an IMC. XRay Diffraction (XRD), Neutron Diffraction (ND), Synchrotron XRD (SXRD), and Ultrasonics (US) techniques for measuring thermal stresses in IMC were examined and ND was selected as the most promising technique. ND was demonstrated on a variety of IMC systems encompassing Ti- and Ni-base matrices, SiC, W, and Al_2O_3 fibers, and different fiber fractions (V_f). Experimental results on these systems agreed with predictions of a concentric cylinder model. In SiC/Ti-base systems, little yielding was found and stresses were controlled primarily by $\Delta\alpha$ and V_f. In Ni-base matrix systems, yield strength of the matrix and V_f controlled stress levels. The longitudinal residual stresses in SCS-6/Ti-24Al-11Nb composite were modified by thermomechanical processing. Increasing residual stress decreased ultimate tensile strength in agreement with model predictions. Fiber pushout strength showed an unexpected inverse correlation with residual stress. In-plane shear yield strength showed no dependence on residual stress. Higher levels of residual tension led to higher fatigue crack growth rates, as suggested by matrix mean stress effects.

14. SUBJECT TERMS

Nondestructive testing; Nondestructive evaluation; Neutron diffraction; Xray diffraction; Ultrasonics; Composites; Intermetallic matrix composites; Thermal stress; Residual stress

15. NUMBER OF PAGES

165

16. PRICE CODE

A08

17. SECURITY CLASSIFICATION OF REPORT	18. SECURITY CLASSIFICATION OF THIS PAGE	19. SECURITY CLASSIFICATION OF ABSTRACT	20. LIMITATION OF ABSTRACT
Unclassified	Unclassified	Unclassified	